MOLDOVA STATE UNIVERSITY

With the rights of manuscript

UDC: 539.21

ISACOVA CALINA

EXCITON AND PHONON PROPERTIES IN QUANTUM DOT NANOSTRUCTURES

131.04 - COMPUTATIONAL PHYSICS AND MODELLING OF PROCESSES

Doctor thesis in physics

Scientific supervisor: *Nica Denis, doctor habilitate in physics, associate professor, speciality 131.04*

Author:

CHIȘINĂU, 2023

UNIVERSITATEA DE STAT DIN MOLDOVA

Cu titlu de manuscris

CZU: 539.21

ISACOVA CALINA

PROPRIETĂȚILE EXCITONICE ŞI FONONICE ALE NANOSTRUCTURILOR FORMATE DIN PUNCTE CUANTICE

131.04 FIZICA COMPUTAŢIONALĂ ŞI MODELAREA PROCESELOR

Teză de doctor în științe fizice

Conducător ştiinţific: *Nica Denis, doctor habilitat în fizică, conferențiar cercetător, specialitatea 131.04*

Autor:

CHIȘINĂU, 2023

CUPRINS

ADNOTARE 5

SUMMARY 6

АННОТАЦИЯ 7

ABBREVIATIONS 8

INTRODUCTION 9

1. Cooperative phenomena in quantum dot nanostructures 21
   - ***1.1. Electrons, holes, excitons and photoluminescence in nanostructures*** 21
   - ***1.2. Phonons engineering in semiconductor nanostructures*** 34
   - ***1.3. Conclusions to Chapter 1 and objectives of the Thesis*** 45
2. Exciton processes in Si-based quantum dot nanostructures 46
   - ***2.1. Electron states is Si-based quantum dot nanostructures*** 46
   - ***2.2. Hole states in Si-based quantum dot nanostructures*** 56
   - ***2.3. Exciton states in Si-based quantum dot nanostructures*** 65
   - ***2.4. Calculation methods*** 83
   - ***2.5. Conclusions to Chapter 2*** 87
3. Thermal conductivity in 1D Si-based nanostructures 89
   - ***3.1. Phonons and thermal transport in Si-based one-dimensional quantum dot superlattices*** 89
     - ***3.1.1. Face-centred cubic cell model of lattice vibrations*** 91
     - ***3.1.2. Acoustic phonons in 1D Si-based nanostructures*** 96
   - ***3.2. Phonon thermal flux and phonon thermal conductivity*** 101
   - ***3.3. Phonons and thermal transport in multishell Si/SiO$_2$ nanotubes*** 115
   - ***3.4. Conclusions to Chapter 3*** 123

GENERAL CONCULSIONS AND RECOMMENDATIONS 126

REFERENCES 129

DECLARATION OF RESPONSIBILITY 143

Curriculum Vitae 144

ADNOTARE

Isacova Calina,
teza „Proprietățile electronice și fononice ale nanostructurilor formate din puncte cuantice” / pentru conferirea titlului de doctor în științe fizice, specialitatea 131.04 *Fizica computațională și modelarea proceselor*, elaborată în laboratorul de cercetări științifice „Fizica și ingineria nanomaterialelor „E. Pokatilov” al Universității de Stat din Moldova, or. Chișinău, R. Moldova, în anul 2023.

Structura lucrării: Lucrarea este formată din Introducere, trei capitole, Concluzii generale și Recomandări, Bibliografie din 157 titluri, 145 pagini, 79 figuri, 53 formule și 1 tabel. Rezultatele obținute în teză au fost publicate în 8 articole științifice și au fost prezentate 32 rapoarte la conferințe științifice internaționale și naționale.

Cuvinte-cheie: suprarețea unidimensională, Hamiltonian multizonal, exciton, fonon, conductibilitate termică.

Scopul și obiectivele: cercetarea influenței parametrilor materiali și geometrici ai suprarețelelor unidimensionale din puncte cuantice (1D-SRPC) Si/SiO_2 și Si/SiC asupra proprietăților electronice, de gol și excitonice; dezvoltarea modelului „face-centred cubic cell” al oscilațiilor rețelei cristaline pentru studierea proprietăților fononice și termoconductibile ale 1D-SRPC Si/Ge și Si/SiO_2, cât și a nanotuburilor multistrat (NTM) Si/SiO_2.

Noutatea științifică și originalitatea: Se arată, că descrierea cantitativă a stărilor excitonice în SRPC cercetate necesită utilizarea Hamiltonianului multizonal al golurilor, care permite de a ține cont de amestecarea golurilor grele, ușoare și de tip „split-off”; s-a stabilit faptul, că conductibilitatea termică a 1D-SRPC și NTM cercetate este semnificativ mai joasă decât a nanofirelor corespunzătoare datorită efectului de captare a modelor fononice și împrăștierea fononilor pe suprafețele interioare ale structurilor.

Problema științifică soluționată: au fost teoretic studiate detaliat proprietățile excitonice, fononice și termoconductibile ale 1D-SRPC Si/SiO_2 și Si/SiC, cât și transportul de căldură în NTM Si/SiO_2.

Valoarea teoretică: au fost dezvoltate modelele teoretice ale stărilor excitonice și fononice în 1D-SRPC și NTM.

Valoarea aplicativă a lucrării: implementarea practică a rezultatelor obținute va contribui la apariția unei clase noi de nanomateriale, având perspective promițătoare în aplicațiile optoelectronice, termoelectrice și de izolare termică.

SUMMARY

Isacova Calina, “Exciton and phonon properties in quantum dot nanostructures”,
Ph. D. thesis in physics,
speciality 131.04 *Computational physics and modelling of processes*, was elaborated
in “E. Pokatilov laboratory of Physics and Engineering of Nanomaterials”,
Moldova State University, Chișinău, R. Moldova, 2023.

Work structure: The Thesis consists of an Introduction, 3 Chapters, General conclusions and recommendations, 157 references, 145 pages, 79 figures, 53 equations, and 1 table. The results presented in the work are published in 8 scientific articles and presented at 32 international and national conferences.

Keywords: one-dimensional quantum dot superlattice, multi-band Hamiltonian, exciton, phonon, thermal conductivity

Goals and objectives: the study of material and geometrical parameters’ influence on electronic, holes’, and excitonic properties in one-dimensional quantum dot superlattice (1D-QDSL) Si/SiO$_2$ and Si/SiC; development of face-centred cubic cell (FCC) lattice dynamic model for studying phonon and thermal properties in Si/Ge and Si/SiO$_2$ 1D-QDSL, as well as in Si/SiO$_2$ multishell nanotube (MNT)

Scientific novelty and originality: it was demonstrated, that three-band Hamiltonian for holes, which takes into account the mixing of the heavy, light, and split-off holes’ states, is required for more accurate quantitative description of exciton states in 1D-QDSL; it was theoretically shown that thermal conductivity of the Si-based 1D-QDSL and Si/SiO$_2$ MNT is significantly lower than that in corresponding silicon nanowires due to the trapping of phonon modes in nanostructure’s segments and phonon scattering at interfaces of the QDSL.

Solved scientific problem: it has been carried out a detailed theoretical study of the exciton, phonon and thermal properties in the Si/Ge, Si/SiC and Si/SiO$_2$ QDSLs as well as of phonon and thermal properties in the Si/SiO$_2$ MNTs

Theoretical importance is related to development of the theoretical model of the exciton and phonon states in 1D-QDSLs

Practical significance: practical implementation of the obtained results may lead to the appearance of new nanomaterials promising for optoelectronic, thermoelectric and thermal insulating applications

АННОТАЦИЯ

Исакова Калина,
диссертация «Экситонные и фононные свойства квантовоточечных наноструктур»
на соискание ученой степени доктора физических наук по специальности
131.04 *Вычислительная физика и моделирование процессов*, выполненная в
лаборатории «Физика и инженерия наноматериалов имени Е. Покатилова»
Государственного университета Молдовы, г. Кишинев, Р. Молдова, в 2023 году.

Структура работы: Работа состоит из Введения, трех глав, Общих выводов и рекомендаций, Библиографии из 157 названий, 145 страниц, 79 рисунков, 53 формул и 1 таблицы. Полученные результаты опубликованы в 8 научных работах и представлены на 32 международных и национальных конференциях.

Ключевые слова: одномерная сверхрешетка, многозонный гамильтониан, экситон, фононы, теплопроводность

Цели и задачи: исследование влияния материальных и геометрических параметров одномерных квантовоточечных сверхрешеток (1D-КТСР) Si/SiO_2 и Si/SiC на электронные, дырочные и экситонные свойства; развитие “face-centred cubic cell” модели колебаний кристаллической решетки для изучения фононных и теплопроводящих свойств одномерных квантовоточечных сверхрешеток Si/Ge и Si/SiO_2, а также многослойных нанотрубок (МНТ) Si/SiO_2.

Научная новизна и оригинальность: показано, что для количественного описания экситонных состояний в рассматриваемых 1D-КТСР необходимо использовать многозонный дырочный гамильтониан, который позволяет учесть перемешивание тяжелых, легких и “split-off” дырок; установлено, что теплопроводность 1D-КТСР и МНТ значительно ниже теплопроводности соответствующих нанонитей благодаря эффекту захвата фононных мод в сегментах этих наноструктур и рассеянию фононов на внутренних интерфейсах

Решенная научная задача: проведено подробное теоретическое изучение экситонных, фононных и теплопроводящих свойств 1D-КТСР Si/Ge и Si/SiO_2, а также теплового транспорта в МНТ Si/SiO_2.

Теоретическая значимость: развиты модели экситонных и фононных состояний в 1D-КТСР и МНТ.

Практическая ценность работы: практическое внедрение полученных результатов будет способствовать появлению нового класса наноматериалов перспективных для оптоэлектронных, термоэлектрических и теплоизоляционных применений.

ABBREVIATIONS

APGV – average phonon group velocity

CA – continuum approach

DFT – density functional theory

DOS – density of states

DTPQD – double truncated pyramidal quantum dot

FCC – face-centred cubic cell

HRTEM – high-resolution transmission electron microscopy
LA – longitudinal acoustic

MNT – multi-shell nanotubes

MP– mean path

nc – nanocrystals

NT – nanotubes

NW – nanowire

TA – transversal acoustic

TBM – tight-binding model

QD – quantum dot

QDSL – quantum dot superlattice

1D-QDSL – one-dimensional quantum dot superlattice

1D-C-QDSL – one-dimensional quantum dot superlattice with constant cross-section

1D-M-QDSL – one-dimensional quantum dot superlattice with modulated cross-section

PL – photoluminescence

RT – room temperature

TC – thermal conductivity
TEM – transmission electron microscopy

INTRODUCTION

For the last decades, semiconductor nanostructures remain the object of close attention of researchers. Their characteristic feature is confinement, which causes quantization of the energy spectrum of charge carriers and phonons [1–12]. Silicon, being the second most abundant element on earth and having excellent mechanical and electronic properties, has become the main material in microelectronics with the advent of microelectronics. semiconductor industry and is likely to remain so for the foreseeable future. Silicon quantum dots (QDs) (nanocrystals) have demonstrated different unique physical properties [2], [3], [13], [14], allowing their applications in optoelectronics (light-emitting diodes (LEDs), single electron transistors, or memory devices), in photonics (different energy sources) as well as in biomedicine for photosensitization of singlet oxygen [15]. Qualitative and quantitative information about the optical, exciton, phonon, and thermal properties of silicon-based nanostructures is necessary for the improvement of the characteristics of silicon-based devices.

Optimization of thermal transport in nanoscale structures is one of the priority tasks in modern nanoelectronics. Efficient heat management at the nanoscale can prevent overheating of electronic chips and may lead to an increase of their operation speed. The low thermal conductivity of nanoscale structures makes them potentially promising for thermoelectric applications, since the quality factor of thermoelectric conversion ZT contains thermal conductivity in the denominator: $ZT = \frac{S^2\sigma T}{(\kappa_{ph} + \kappa_{el})}$, where S is the Seebeck coefficient, σ is the electrical conductivity, T is the absolute temperature, κ_{ph} and κ_{el} are the phononic and electronic thermal conductivity, respectively. At the same time, efficient heat removal from micro- and nanosized electronic chips requires nanomaterials with high thermal conductivity. Thus, the theoretical and experimental search for different ways to both reduce and increase thermal conductivity continues [16], [17]. Phonon engineering, i.e. improving of electrical, and thermal properties of nanostructures by changing their phonon properties was found as a powerful tool for the optimization of thermal, electric and thermoelectric properties at the nanoscale [6], [18], [19]. It has been shown that phonon engineering is particularly effective in nanostructured materials composed of layers or segments of different shapes, sizes, and/or materials. A strong drop of lattice thermal conductivity (up to one order of magnitude) has been demonstrated both experimentally and theoretically in silicon nanolayers containing germanium quantum dots [20], in silicon nanowires with rough surfaces [21], in Si/Ge nanowires of constant and variable cross sections [7], [8], [22], [23], as well as in segmented nanowires [23–28]. At the same time, there is some lack of investigation of the physical properties of quasi-one-dimensional quantum dot superlattices, i.e. arrays of quantum dots ordered in one spatial dimension. Such structures combine the possibility of free moving of charge carriers or phonons in one direction with strong spatial confinement in the other two directions. In this Thesis, we theoretically investigate the exciton, phonon, and thermal properties of Si-based one-dimensional quantum dot superlattices and Si/SiO$_2$ multi-shell nanotubes and discuss optimization of their parameters for optical, energy transfer, and thermal management applications.

Goal and objectives:

- Development of theoretical models for electron, hole, and exciton states in Si-based 1D-QDSLs;
- Investigation of electron, hole, exciton, and photoluminescence properties of Si-based 1D-QDSLs and their optimization for optical and energy transfer applications;
- Development of theoretical models for phonon states and thermal conductivity in Si-based QDSLs and Si/SiO$_2$ multi-shell nanotubes;
- Investigation of phonon and thermal properties of Si-based 1D-QDSLs and Si/SiO$_2$ MNTs and their optimization for heat management applications.

Research hypothesis:

- Three-band Bart's Hamiltonian should be used for the quantitate description of exciton states in Si quantum dots;
- The broadening of photoluminescence lines in Si QDs can be theoretically explained by the dispersion of QD's shapes and sizes;
- Thermal transport in Si/Ge 1D-QDSLs is significantly suppressed due to trapping of many phonon modes in nanostructure segments and phonon scattering at Si/Ge interfaces;
- *L*-fold drop of the thermal conductivity in a wide temperature range from $50\,\mathrm{K}$ to $400\,\mathrm{K}$ is predicted for Si/SiO$_2$ MNTs with *L* shells in comparison with one-shell Si/SiO$_2$ NT.

Scientific research methodology

Exciton properties:

1. *Effective-mass approach* with *three-band hole Hamiltonian* for the theoretical investigation of the electron, hole, and exciton states. This approach has also taken into account anisotropy of the electron and hole effective masses and self-actions;
2. *Finite differences method* for numerical solution of Schrodinger equations
3. *Davidson-Liu method* [29] for diagonalization of huge matrix (up to 10^7 elements).

4. *An iterative method of Jacobi-Seidel* for numerical calculation of Coulomb potentials in the considered nanostructures.

   Phonons and thermal conductivity:

5. *Face-centred-cubic cell model of lattice vibrations* for theoretical investigation of phonon modes in Si-based 1D-QDSLs and Si/SiO_2 MNTs.
6. *Boltzmann transport equation approach within relaxation time approximation* [30–33] for the theoretical study of thermal fluxes in Si-based 1D-QDSLs and Si/SiO_2 MNTs. All main mechanisms of phonon scattering in QDSLs and MNTs were taken into consideration: three-phonon Umklapp scattering, boundary, and impurity scatterings [31–38].

The scientific novelty of the work is related to the comprehensive theoretical study of exciton, phonon, and thermal properties of the recently-discovered class of nanostructures: Si-based one-dimensional quantum-dot superlattices and Si/SiO_2 multi-shell nanotubes. The following new theoretical results have been obtained:

- An increase in the potential barrier height leads to an enhancement of electron and hole spatial confinement and the corresponding increase of their energies and distance between energy levels;
- Both binding energy and total exciton energy decrease with the rise of QD's volume due to the weakening of the spatial confinement of electrons and holes;
- The shape of the Si QDs strongly influences electron, hole, and exciton states. It has been shown that conical QDs possess lower values of ground exciton energy in comparison with the cuboid and pyramidal QDs for volumes $V < 32\,\mathrm{nm}^3$, while for $V > 32\,\mathrm{nm}^3$ cuboid QDs demonstrate lower values of ground exciton energy;
- The outer media parameters influence the electron and hole ground energy only for Si QDs with narrow SiC shell with thickness < 1 nm because maximal penetration of hole and electron wave functions into barrier media in considered Si/SiC/air or Si/SiC/water QDs is about 1 nm .
- The large broadening of PL bands in Si QDs as well as the dependence of exciton energy on annealing temperature reported recently in experimental works [13], [39], [40] can be theoretically explained by the dispersion of QD's shapes and sizes.
- Phonon modes in Si/Ge 1D-QDSLs are trapped in their segments due to an acoustical mismatch of materials. The slope of the phonon dispersion in 1D-QDSLs is smaller than in Si nanowires. Many high energy modes in Si/Ge QDSLs are dispersionless and possess low group velocities close to 0 value.

- The average phonon group velocities in Si/Ge 1D-QDSLs are significantly lower than those in nanowires for all phonon energies in 1D-M-QDSLs and for phonon energies $\hbar\omega > 5\,\text{meV}$ in 1D-C-QDSLs. The effect of APGV drop is stronger in the case of 1D-M-QDSLs due to the interplay between segmentation and cross-section modulation.
- Thermal transport in Si/Ge 1D-QDSLs is significantly suppressed due to phonon deceleration and reinforcement of phonon scattering at Si/Ge interfaces. Up to 7-times (13.5-times) drop of TC was demonstrated for C-QDSLs (M-QDSLs) as a function of temperature. At room temperature, the thermal conductivity in Si/Ge 1D-C-QDSLs is by a factor of 2.6 – 2.9 lower than that in silicon nanowires with the same cross-section.
- Phonon average group velocities in multi-shell Si nanotubes are close to 0 for phonon energies $\hbar\omega > 10\text{ meV}$.
- A large number of phonon modes in Si/SiO$_2$ MNTs are scattered on Si/SiO$_2$ interfaces. As a result, an *L*-fold drop of the thermal conductivity in a wide temperature range from $50\,\text{K}$ to $400\,\text{K}$ is predicted for Si/SiO$_2$ MNTs with *L* shells in comparison with one-shell Si/SiO$_2$ NT.

Structure of the Thesis

The Thesis consists of an Introduction, 3 Chapters, and General conclusions and Recommendations. The Thesis contains 157 references, 145 pages, 79 figures, 53 equations, and 1 table.

The **Introduction** presents a general analysis of the thesis, argues the relevance of the researched topic, and describes the state of research on this topic in the world. The Introduction elucidates the scientific novelty of the obtained results, and the theoretical and practical importance of the research is highlighted. The main scope and objectives of the work are also defined.

Chapter 1 contains a review of scientific papers published in the literature on the problem under study and methods of solution. We analysed works that study, both theoretically and experimentally, excitonic, photoluminescence, and thermal properties of the different nanostructures and the comparison of these properties with analogical bulk materials. The presented works are dedicated to the Si/SiO$_2$ QDs and their PL properties, and the influence of the sample tailoring conditions on PL energy, line form, and its intensity. There are described practical applications of the QD of different origins, especially of the non-radiative energy transfer from QDs. The methods of the theoretical study of the electron, hole, and exciton properties of the QD are described, as well. The second part elucidates research in the field of phonon engineering and thermal transport. It provides details about different approaches to the theoretical study of the thermal flux in heterogeneous nanostructures, such as multi-layered planar structures, and heterowires.

Chapter 2 describes the theoretical study of the electron, hole, exciton, and PL properties of the Si QD embedded in a dielectric matrix. The electron and hole spectra were calculated in the framework of the effective mass approach, taking into account self-action energy, finite potential barrier, and anisotropy of the effective mass in Si. Holes energy states were calculated using one-zone Hamiltonian and non-symmetric three-band Bart's Hamiltonian. Hole levels calculated via Bart's Hamiltonian have lower energy and less energy distance between levels than the heavy hole levels calculated using one-zone Hamiltonian. Exciton energies were calculated taking into account the mixing of charge carriers levels with higher energies. Mixing electron and hole levels, and using Bart's Hamiltonian gives lower energy of the exciton levels, which gives us better concordance with the experimental results, and makes our model applicable for predicting exciton energies even for small QD, with diameters $\leq 2\ \text{nm}$. We studied the influence of the QD shape and dimensions on electron, hole, and exciton states. It was shown that the energy of states decreases with the increase of the QD size, due to weaker spatial confinement of electrons and holes. The QDs of the spherical form have lower energies because of the uniform distribution of the wave function inside QD and less spatial confinement. The dependence on the potential barrier demonstrates the rise of the electron, hole, and exciton energies. The binding energy decreases by module while QD dimensions increase because the exciton effective radius is getting larger. Here we study the possible reasons for the PL band broadening in Si/SiO$_2$ QDs. We demonstrated that the size dispersion of the QDs in the samples and their coupling can be the reason for PL energy dependencies to take a Gaussian-like shape. The study of the Si/SiC QDs placed into water or air medium demonstrates that varying the QD size and shell thickness can adjust exciton levels energy distances to make the transition between them more effective for non-radiative energy transition.

The topic of **Chapter 3** is the thermal properties of the Si-based one-dimensional superlattices. We studied the possibility of thermal conductivity reducing in 1D-QDSL with a constant and periodically modulated cross-section with and without a shell using principles of *phonon engineering*. Phonon spectra were calculated within the lattice dynamic model Face-centred cubic cell, which considers replacing the real crystal lattice of the Si or Ge with one face-centred cubic lattice with double mass in its node. This approach excludes optic oscillations from calculations, however, we do not have any fitting parameters and demonstrated a good qualitative description of the effects. We derived equations of the phonon spectrum within the FCC model for 1D-QDSL with a modulated cross-section. We studied spectra and velocities of the 1D-QDSL. It was demonstrated that modulated cross-section amplifies the effect of the acoustical mismatch of the materials and reduces thermal transport more effectively. It is demonstrated that contact of the acoustic mismatch materials leads to the redistribution of the phonon density of states toward lower energies. Together with phonon deceleration, it results in a reduction of the thermal transport. Thermal flux was calculated using the Boltzmann transport equation within the approximation of the relaxation time. In order to provide more accurate results, we used a one-dimensional density of states. We took into account three basic mechanisms of scattering: Umklapp, boundary, and impurity. It was shown that manipulation of such geometrical parameters as a cross-section, the difference between QDs' cross-section in M-QDSL, translation period can enhance thermal drop in 1D-QDSL.

Publications and approval of the obtained results

The results of the current work were published in 8 articles, including 4 in international press visible in ISI Web of science/SCOPUS. The results presented in this work were discussed at 32 international and national conferences. Two articles and two conference abstracts were published without co-authors.

1. NIKA, D.L., COCEMASOV, A.I., **ISACOVA, C.I.**, BALANDIN, A.A., FOMIN, V.M., SCHMIDT, O.G. Suppression of phonon heat conduction in cross-section-modulated nanowires. In: *Physical Review B*. 2012, vol. 85, p. 205439. DOI: 10.1103/PhysRevB.85.205439
2. **ISACOVA, C.**, COCEMASOV, A., NIKA D. L., FOMIN, V. M. Phonons and thermal transport in Si/SiO_2 multishell nanotubes: atomistic study. In: *Appl. Sci*. 2021, vol. 11(8), p. 3419. DOI: 10.3390/app11083419
3. COCEMASOV, A.I., **ISACOVA, C.I.**, NIKA, D.L. Thermal transport in semiconductor nanostructures, graphene, and related two-dimensional materials. In: *Chinese Physics B*. 2018, vol. 27(5), p. 056301. DOI: 10.1088/1674-1056/27/5/056301
4. FOMIN, V.M.; NIKA, D.L.; COCEMASOV, A.I.; **ISACOVA, C.I**.; SCHMIDT, O.G. Strong reduction of the lattice thermal conductivity in superlattices and quantum dot superlattices. In: *AIP Conference Proceedings*. 2012, vol. 1449, p. 33-36. DOI: 10.1063/1.4731490
5. **ИСАКОВА, К**. Падение фононной теплопроводности в сегментированных Si/Ge нанонитях. In: *Studia Universitatis. Seria științe exacte și economice.* 2015, nr. 2 (82), pp. 65-71. ISSN 1857-2073.

6. **ИСАКОВА, К.** Электронные, дырочные и экситонные состояния в кремниевых квантовых точках, помещенных в диэлектрическую среду оксида кремния. In: *Studia Universitatis Moldaviae. Seria științe exacte și economice.* 2011, nr. 7 (47), pp. 66-72. ISSN 1857-2073

7. **ИСАКОВА, К.**, НИКА, Д., ПОКАТИЛОВ, Е. Экситонные состояния в квантовых точках Si/SiO$_2$. In: *Studia Universitatis Moldaviae. Seria Ştiinţe Reale şi ale Naturii.* 2008, nr. 2(12), pp. 232-236. ISSN 1814-3237

8. **ИСАКОВА, К.,** НИКА, Д., АСКЕРОВ, А., ЗИНЧЕНКО, Н., ПОКАТИЛОВ, Е. Исследование кулоновского взаимодействия в квантовой точке Si/SiO$_2$. In: *Studia Universitatis Moldaviae. Seria Ştiinţe Reale şi ale Naturii.* 2007, nr. 7, pp. 280-284 ISSN 1814-3237.

The results presented in this work were discussed at 32 international and national conferences:

1. **ИСАКОВА, К.**, КОЧЕМАСОВ, А., НИКА, Д. Фононная инженерия в одномерных наноструктурах. In: *Rezumatele ale comunicărilor, Științele exacte, Științele ale naturii Conferinţa ştiinţifică naţională cu* participare *internaţională „Integrare prin cercetare şi inovare”,* 10-11 Noiembrie, 2022. Chişinău, Moldova, pp. 293-296. ISBN 978-9975-152-48-8

2. **ИСАКОВА, К.**, КОЧЕМАСОВ, А., НИКА, Д. Фононная инженерия в нанонитях и нанотрубках на основе кремния. In: *Rezumatele ale comunicărilor, Științele exacte, Științele ale naturii Conferinţa ştiinţifică naţională cu participare internaţională „Integrare prin Cercetare şi Inovare”, dedicată aniversării a 75-a a Universității de Stat din Moldova,* 10-11 noiembrie, 2021. Chișinău, Moldova, pp. 194-196. ISBN 978-9975-152-48-8.

3. **ISACOVA, C.**, COCEMASOV, A., NIKA, D., FOMIN, V. Thermal transport in Si/SiO$_2$ nanoshell nanotubes. In: *CMD2020GEFES, European Physical Society*, 31 August – 4 September, 2020. (online): https://www.cmd2020gefes.eu/_files/_event/_28512/_editorFiles/file/Scientific%20Program_CMD2020GEFES.pdf.

4. **ISACOVA, C.I.**, COCEMASOV, A.I., NIKA, D.L., SCHMIDT, O.G., FOMIN, V.M. Phonon modes and thermal conductivity in Si/SiO$_2$ multishell nanotubes. In: *DPG Spring Meeting*, 31 March – 05 April, 2019, Regensburg, Germany, DS 10.3.

5. **ISACOVA, C.I.**, COCEMASOV, A.I., NIKA, D.L. Suppression of the thermal flux in Si/Ge and Si/SiO_2 crosssection modulated nanowires. In: *Book of abstracts of the 4th Central and Eastern European Conference on Thermal Analysis and Calorimetry (CEEC-TAC4).* 28−31 August 2017. Chisinau, Moldova, p. 84. ISBN 978-9975-9787-1-2.

6. **ИСАКОВА, К.Я.**, КОЧЕМАСОВ, А.И., НИКА, Д.Л. Зависимость теплопроводности сегментированных нанонитей на основе кремния от их геометрии и физических параметров материалов. In: *Abstract book of the 18-th International Conference "Modern information and electronic technologies"*, 22-26 May, Odessa, Ukraine, 2017, pp. 69-70. ISSN: 2308-8060

7. **ИСАКОВА, К.** Падение теплопроводности в сегментированных Si/Ge нанонитях с переменным сечением. In: *Rezumatele ale comunicărilor, Ştiinţele exacte, Ştiinţele ale naturii Conferința științifică națională cu participarea internațională „Integrarea prin cercetare și inovare"*, 9-10 Noiembrie, 2017, Chișinău, Moldova, pp. 232-236. ISBN 978-9975-71-701-4

8. **ISACOVA, C.I.**, COCEMASOV, A.I., NIKA, D.L. Strong suppression of the lattice thermal conductivity in silicon-based segmented nanowires. In: *Abstracts of the 8th Int. Conf. on Materials Science and Condensed Mater Physics, MSCMP 2016*, September 12-16, 2016, Chisinau, Moldova, p. 202. ISBN 978-9975-9787-1-2.

9. **ISACOVA, C.**, COCEMASOV, A., NIKA, D. Suppression of phonon heat conduction in cross-section, modulated nanowires. *In: Book of Abstracts of the 3rd International Conference on Nanotechnologies and Biomedical Engineering*, September 23-26, 2015, Chisinau, Moldova, S1-P.51. ISBN: 978-981-287-735-2

10. **ISACOVA, C.**, COCEMASOV, A., NIKA, D. Suppression of phonon heat conduction in cross-section modulated nanowires. In: *Rezumatele ale comunicărilor, Ştiinţele exacte, Ştiinţele ale naturii Conferința științifică națională cu participarea internațională „Integrarea prin cercetare și inovare"*, 10-11 Noiembrie, 2015, Chișinău, Moldova, pp. 147-148. ISBN: 978-9975-74-705-2

11. **ИСАКОВА, К.Я.**, НИКА, Д.Л. Теплопроводность сегментированных Si/Ge нанонитей. In: *Труды 14-ой Международной научно-практической конференции «Современные информационные и электронные технологии».* Май, 27-31, 2013, Одесса, Украина, pp. 158-159. ISBN 978-966-2666-04-5

12. **ИСАКОВА, К.** Экситонные и фотолюминесцентные свойства кремниевых квантовых точек. In: *Rezumatele ale comunicărilor Conferinţei ştiinţifice cu participare internaţională "Interferenţe universitare – integrare prin cercetări şi inovare"*, Septembrie 25-26, 2012, Chişinău, Moldova, p.154-156. ISBN: 978-9975-71-267-5

13. **ISACOVA, C.I.**, COCEMASOV, A.I., NIKA, D.L., BALANDIN, A.A., FOMIN, V.M., SCHMIDT, O.G. Reduction of thermal conductivity in cross-section modulated silicon nanowires. In: *Conference Proceedings of the "Modern information and electronic technologies"*, June 4-8, 2012, Odessa, Ukraine, p. 295.

14. FOMIN, V.M., NIKA, D.L., COCEMASOV, A.I., **ISACOVA, C.I.**, CRISMARI, D.V., BALANDIN, A.A., Schmidt, O.G. Phonon heat conduction in one-dimensional quantum-dot superlattices and cross-section modulated nanowires. In*: 2012 EMN Open Access Week*, October 22-24, 2012, Chengdu, China, p. 39-40.

15. NIKA, D.L., COCEMASOV, A.I., **ISACOVA, C.I.**, CRISMARI, D.V., BALANDIN, A.A., FOMIN, V.M., SCHIMDT, O.G. Suppression of phonon heat conduction in undulated nanowires. In*: 76th Annual Meeting of the DPG and DPG Spring Meeting*, March 25-30, 2012, Berlin, Germany, DS 33.4.

16. **ИСАКОВА, К.Я.,** КОЧЕМАСОВ, А.И. Падение решёточной теплопроводности в нанонитях переменного сечения. In: *Материалы XIX международной научной конференции студентов, аспирантов и молодых учёных «Ломоносов»,* 9-13 апреля, 2012, Москва, Россия, Секция «Физика», Подсекция «Физика твердого тела», с. 46. https://lomonosov-msu.ru/archive/Lomonosov_2012/1880/29294_c41c.doc. ISBN: 978-5-317-04041-3

17. **ISACOVA, C.IA.**, NIKA, D.L., POKATILOV, E.P. Exciton states of Si quantum dots. In: *Proceedings of the XIth International Young Scientists' Conference on Applied Physics*, June 15-18, 2011, Kyiv, Ukraine, pp. 117-118.

18. **ИСАКОВА, К.Я.** Экситонные состояния в кремниевых точках. In: *Материалы XVIII международной научной конференции студентов, аспирантов и молодых учёных «Ломоносов»,* 11-15 апреля, 2011, Москва, Россия, Секция «Физика» Подсекция «Физика твердого тела», с. 19-20. ISBN 978-5-317-03634-8

19. NIKA, D.L., ZINCENCO, N.D., **ISACOVA, C.IA.**, POKATILOV, E.P., FOMIN, V.M., BALANDIN, A.A. Ultra-low lattice thermal conductivity of one-dimensional quantum dot Si/Ge superlattices. In: *Book of Abstracts of the 5th International Conference on Material Science and Condensed Matter Physics*, 13–17 September, 2010, Chişinău, Moldova, p. 206. ISBN 978-9975-66-190-4

20. **ИСАКОВА, К.Я.**, НИКА, Д.Л., ПОКАТИЛОВ, Е.П. Экситонные состояния в квантовых точках кристаллов кремния, помещенных в водную и воздушную среду. In: *Труды 11-ой международной научно-практической конференции «Современные информационные и электронные технологии»*, 24–28 Мая, 2010, Одесса, Украина, часть 2, p. 103.

21. **ИСАКОВА, К.**, НИКА, Д., ПОКАТИЛОВ, Е. Экситонные состояния и полосы фотолюминесценции в Si-квантовых точках в диэлектрической матрице SiO_2. In: *VII-th Scientific Abstracts of the International conference of young researchers,* 5-6 November 2009, Chisinau, Moldova, p. 91. ISBN 978-9975-62-196-0.

22. **ИСАКОВА, К.**, ПОКАТИЛОВ, Е., НИКА, Д., ТИМОШЕНКО, В. Экситонные состояния в кремниевых точках. In*: Proceedings of conference of Moldovan physicists*, 26-28 November 2009, Chisinau, Moldova, p.143.

23. **ISACOVA, C.IA.**, NIKA, D.L., POKATILOV, E.P. Exciton states in Si quantum dots imbedded into SiO_2 dielectric matrix. In: *Труды 10-ой международной научно-практической конференции «Современные информационные и электронные технологии»,* 18–22 May, 2009, Ukraine, Odessa, часть 2, p. 103.

24. **ИСАКОВА, К.Я.**, НИКА, Д.Л., ПОКАТИЛОВ, Е.П. Экситонные состояния и полосы фотолюминесценции в Si – квантовых точках в диэлектрической матрице SiO_2. In: *Тезисы докладов XVII Республиканской научной конференции аспирантов, магистрантов и студентов «Физика Конденсированного Состояния»,* 16 – 17 Апреля, 2009, Гродно, Беларусь, pp. 114 – 115. ISBN 978-985-515-135-8

25. **ISACOVA, C.**, NIKA, D., POKATILOV, E. Exciton states in Si quantum dots imbedded into the dielectric matrix. In: *Scientific abstracts of International conference of young researchers*, 6-7 November, 2008, Chişinău, Republic of Moldova, p. 113. ISBN 978-9975-62-196-0

26. **ISACOVA, C.**, NIKA D., POKATILOV, E. Exciton states in Si quantum dots imbedded into SiO_2 dielectric matrix. In: *Abstracts of the 4th International Conference "Material Science and Condense Matter Physics",* 23-25 September, 2008, Chisinau, Republic of Moldova, p. 218.

27. **ISACOVA, C.IA.**, NIKA, D.L., POKATILOV, E.P. Development of charge-carriers states theory for Si quantum dots. In: *Труды 9-ой международной научно-практической конференции «Современные информационные и электронные технологии»*, 19-23 Мая, 2008, Одесса, Украина, часть 2, p. 106.

28. **ISACOVA, C.Ia.**, NIKA, D.L., POKATILOV, E.P. Development of charge-carriers states theory for Si quantum dots. In: *Тезисы докладов XVI Республиканской научной конференции аспирантов, магистрантов и студентов «Физика Конденсированного Состояния»*, 23-25 April, 2008, Гродно, Беларусь, часть 2, pp. 116-117. ISBN 978-985-515-102-0

29. **ISACOVA, C.**, NIKA, D., POKATILOV, E. Exciton states in rectangular Si quantum dots, Scientific abstracts, In: *Scientific abstracts of international conference of young researchers*, November, 9, 2007, Chisinau, Moldova, p. 123. ISBN 978-9975-62-196-0

30. NIKA, D., POKATILOV, E., **ISACOVA, C.**, TIMOSHENKO, V. Electron and hole states in Si quantum dots imbedded into dielectric medium: Role of the quantum dot shape and size. In: *Proceedings of conference of Moldovan physicists,* 11-12 October, 2007, Chisinau, Moldova, p. 17.

31. NIKA, D., POKATILOV, E., **ISACOVA, C.** Charge-carriers states in Si quantum dots with rectangular, conical and tetrahedral shapes. In: *Scientific abstracts of international conference of young researchers*, November, 9, 2007, Chisinau, Moldova, p. 125. ISBN 978-9975-62-196-0

32. **ISACOVA, C.**, NIKA, D., ZINCENCO, N., POKATILOV, E. Exciton states in rectangular Si quantum dots. In: *Conference Proceedings of the Second annual international conference of young scientists "Computer Science and Engineering - 2007",* 4-6 October, 2007, Lviv, Ukraine, p.231-233

ACKNOWLEDGEMENTS

The author wishes to extend sincere gratitude to their esteemed scientific advisor, Associate Professor D.L. Nika, for the invaluable guidance, unwavering assistance, and consistent encouragement generously provided throughout the entirety of this scholarly pursuit and its subsequent phases.

The recognition of indebtedness is also extended to the esteemed memory of the late Professor E.P. Pokatilov, whose enduring legacy serves as an abiding source of motivation for scientific inquiry. The author expresses gratitude to the late Associate Professor S. I. Boldirev, whose scientific discussions and support also positively influenced the research.

Furthermore, the author conveys heartfelt appreciation to their esteemed colleagues at the “E. Pokatilov Laboratory of Physics and Engineering of Nanomaterials” at Moldova State University: A.A. Cliucanov, G.S. Korotcenkov, V.I. Brinzari, A.I. Cocemasov, A.S. Ascherov, N.I. Gaiu, L.I. Rosca, L.V. Tarakanova. The scholarly camaraderie and intellectually stimulating discussions offered by this group have undoubtedly contributed to the refinement of the author's insights and perspectives. The collaborative and enriching environment fostered by their collective efforts deserves sincere recognition and gratitude.

The author would like to thank Professor V.M. Fomin for a valuable experience at the Institute for Integrative Nanosciences – Dresden. Fruitful collaboration and co-authorship are greatly recognized.

1. Cooperative phenomena in quantum dot nanostructures

Spatial conferment of charge carriers and phonons in quasi 0D, 1D and 2D nanostructures strongly influence their conduction, thermal and optical properties as compared with bulk materials [6], [41], [42]. The unique physical properties of nanostructures ensure their wide applications in optoelectronic, thermoelectric, sensory and thermal management systems [6], [41–45].

1.1. Electrons, holes, excitons and photoluminescence in nanostructures

Production of silicon nanocrystals

Silicon and silver nanodots (nanocrystals) are attracted a particular attention as non-toxic and biologically compatible nanopartclies [9–12]. More over, silicon nanodots are also complementary metal-oxide semiconductor (CMOS) compatible [9–11]. The production of silicon QD currently are produced mainly by electrochemical etching of bulk silicon [46], laser-driven - pyrolysis of silane [47], gas phasesynthetics [48], [49], microemulsion synthesis [50], [51], wet chemistry techniques [52]. In the work [53] authors demonstrated hydrothermal synthesis using as silicon source (3-aminopropyl) trimethoxysilane (APTES) and sodium ascorbate as a reduction reagent to obtain water-dispersible and fluorescent Si-QDs. The transmission electron microscopy (TEM) and high-resolution transmission electron microscopy (HRTEM) analysis of these Si QD samples demonstrates the narrow size distribution (see Fig. 1.1), the diagram fits to Gaussian peak with relative standard deviation 17.5 %. The size $<5\,\mathrm{nm}$ makes them good for biomedical applications *in vivo* [54].

Authors affirm that Si QDs PL shows stability in intensity, position and shape for six months because of the stable surfaces. Provided samples are not sensitive for pH in range of 2-12 and preserve 90 % of PL intensity after 2 hours UV irradiation with $364\,\mathrm{nm}$ light.

Silicon nanocrystals is used to enhance photoluminescence properties of the other materials. For example, in [55] silicon NC are used to increase the photoluminescence intensity peak of Er^{3+} ions. Authors obtained SiO_2 films with the embedded Si nanocrystals and doped with Er^{3+} ions by co-sputtering of Si, SiO_2 and Er_2O_3 pellets. Films had thickness $\sim 1\,\mu\mathrm{m}$ and were deposited onto quartz plates. After deposition, samples were annealed at $1100^\circ\mathrm{C}$.

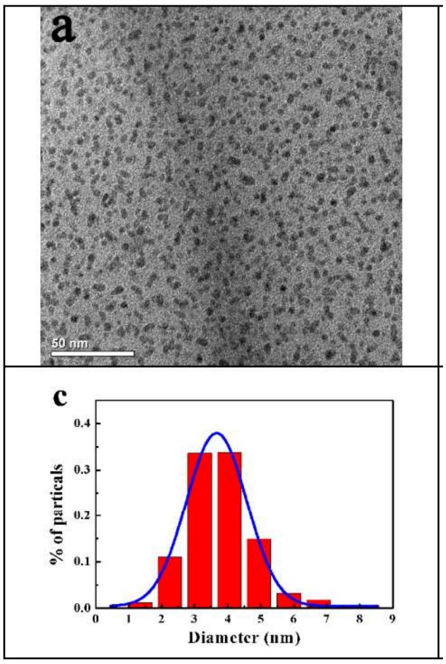

Fig. 1.1. TEM images of SI QDs;

The diameter distribution of the Si QDs derived from several TEM images.

Figure is adopted from Ref. [53]

The easy synthesis, solubility, pH and photo stability, and good PL properties make Si QD produced by one-step hydrothermal procedure prospective candidates for biomedical application.

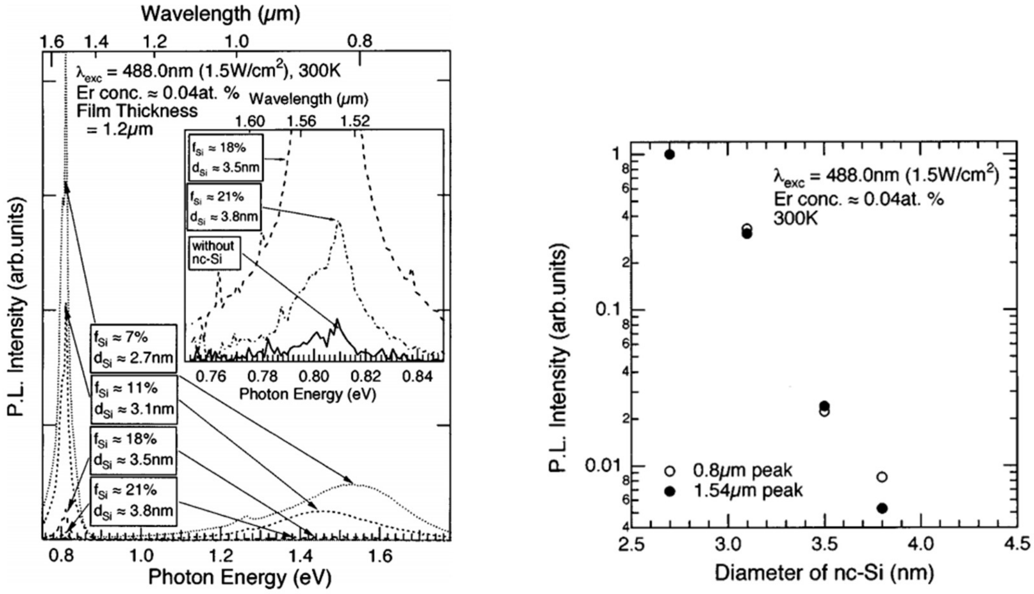

(a) **(b)**

Fig. 1.2. Photoluminescence intensity of nc-Si and Er^{3+} ions for different nc-Si concentrations.

(a) as function of the photon energy and **(b)** as function of the nc-Si diameter

Figure is adopted from Ref. [55]

In Fig. 1.2 (a) the photoluminescence intensity dependencies are shown. In volume fraction of the silicon nanocrystals has varied between 0 – 21 %, while the concentration of the Er^{3+} were fixed at 0.04 %. As fraction of Si varied from 7 % to 21 % nanocrystals diameter changed from 2.7 nm to 3.8 nm. Film thickness were constant and has a value of $1.2\,\mu m$. Samples within porous silicon (without nanocrystals) have a very weak peak at $1.5\,\mu m$ that corresponds to the intra-*4f* transition of Er^{3+} ${}^4I_{13/2} - {}^4I_{15/2}$. It was shown PL intensity increases drastically by adding silicon nanocrystals and has maximum when volume fraction of silicon nanocrystals becomes 7 % ($d_{Si} \approx 2.7\,\mathrm{nm}$). The further increase of d_{Si} from $2.7\,\mathrm{nm}$ to $3.8\ \mathrm{nm}$ leads to decrease of PL intensity. The samples with nc-Si shows a peak at $\sim 0.8\ \mu m$ (see Fig. 1.2(a)) that can be explained by recombination of the electron-hole pair [56] The high-energy shift of this peak with decreasing of Si nc size is caused by the widening of the band gap due to the quantum size effects. The PL intensity at $0.8\ \mu m$ increases due to increase of the oscillator strength [57] and decrease of nonradiative Auger recombination process [58]. In Fig. 1.2(b) the intensities of the $1.54\ \mu m$ and $0.8\ \mu m$ peaks as a function of d_{Si}. The intensities were normalized at their maximum intensities obtained for $d_{Si} \approx 2.7\,\mathrm{nm}$. We can see that intensity of PL of Er^{3+} ($1.54\ \mu m$)as well as the PL peak ($0.8\ \mu m$) of nc-Si as d_{Si} decreases become more intensive. Although the intensity ratio of the $1.54\,\mu m$ and $0.8\ \mu m$ peaks does not depend on the size, it depends strongly on Er^{3+} concentration. Authors assume energy transfer from Si nanocrystals to Er^{3+}. The excitation light is absorbed mainly by Si nc and electron-hole pairs are generated in ncs. A part of the recombination energy transfers to ions. The amount of the energy transferred from electron-hole pairs to Er^{3+} increases together with Er^{3+} concentration. The energy transfer is limited by the concentration of the optically active Er^{3+} ions, so intensity of $1.54\ \mu m$ peak does not depend linearly on nc Si size.

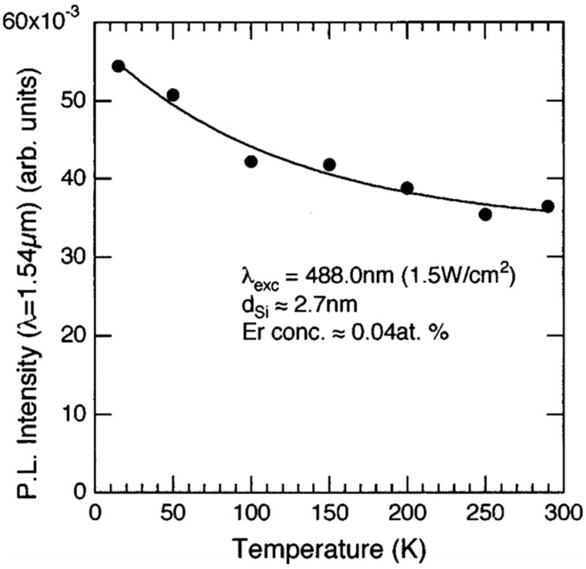

Fig. 1.3. The PL intensity of the 1.54 μm peak as a function of a temperature.

Figure is adopted from Ref. [55]

In Fig. 1.3 the intensity of the $1.54\ \mu m$ peak as a function of a temperature is shown. The degree of thermal quenching is only about $30\ \%$ in the large temperature range (from 15K to $290\,K$). This value is much smaller than that reported for the Er-doped bulk-Si crystal [59]. Very small thermal quenching has been observed for all the samples.

Therefore, authors conclude that two main features of the quantum size effect of nc-Si, i.e., the band gap widening and the increases in the PL intensity with decreasing the nc size, improves room temperature PL efficiency of Er^{3+} ions.

Bulk Si is widely used in electronics, but it has poor optical properties. But porous and nanocrystalline Si shows photoluminescence at visible wavelength at room temperature, which origin/provenience is not clear: highly located defect states or quantum confinement. In the work [60] authors report about classification and control of the photoluminescence origin in Si nc.

They studied Si nanocrystals embedded in SiO_2, that was formed after annealing of the SiO/SiO_2 superlattice deposited on a Si substrate. Conform transmission electron microscopy annealed samples consists of 37 bilayers, layers with Si nanocrystals have thickness of $\sim 1.5\,\text{nm}$ and dioxide layers have $\sim 3\,\text{nm}$ thickness. High-resolution TEM (HRTEM) showed that most nanoparticles have oblate form with $\sim 3\,\text{nm}$ in-plane diameter and $\sim 1.5\,\text{nm}$ dimension in direction perpendicular to layers. The images clearly show a crystalline Si core (see Fig. 1.4).

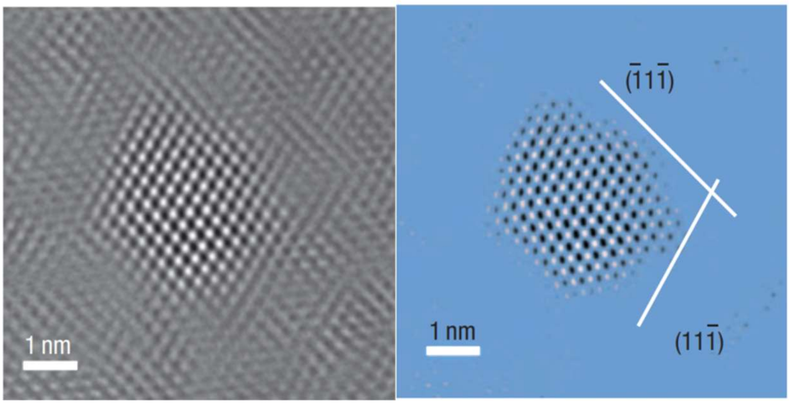

(a) **(b)**

Fig. 1.4. Images of Si nanocrystals embedded into SiO$_2$ matrix.

Figure is adopted from Ref. [60]

(a) Image of a single Si nanoparticle along the [011] zone axis;

(b) Bragg filtered image after subtraction of the background. This clearly highlights the <111> faceting of this nanoparticle.

Photoluminescence origin

In order to determine the origin of the PL, two types of experimented were conducted electron spin resonance (ESR) and magneto-PL. Two different defect centres were identified by ESR analysis, which are characteristic of Si/SiO$_2$ interfaces. These type of defects are deep non-radiative recombination centres, which reduce the PL Si nc in the $1.4\,\text{eV} - 2.2\text{ eV}$ range [61]. The estimated fraction of non-defect optically active Si nc is at least $30\ \%$.

Next, authors investigated the influence of UV irradiation of samples' defects. After irradiation with UV light with UV light of $\sim 362\,\text{nm}$ for $71\,\text{h}$ by xenon lamp with interference filter the ESR was performed the signals from SiO$_2$ specific centres. Then, the filter was removed and sample was irradiated with the same lamp with the full UV spectrum centred 8.2 eV for 10 h . the intensity of these centres increased drastically. The interface defect signals did not change after UV irradiation and they are fully activated. The ESR investigation shows that samples have a large number of defects, but none of them is PL-active. But this fact cannot exclude the defect origin of PL because interface defects are weakly observed in ESR [62–65]. To determine origin of the PL the experiments in pulsed magnetic field up to $50\ T$ were carried out at $85\ K$. The applied magnetic field has an associated length scale $l = \sqrt{\frac{\hbar}{eB}}$, where $\hbar$ is the reduced Planck constant and e is the electron charge, which confines the wave function of the state under study before recombination, and hence increases the PL energy. The smaller the extent of the wave function, the smaller the diamagnetic shift of the centre of mass of the PL: $\Delta E_{CM} = \frac{e^2 \langle \rho^2 \rangle}{8\mu} B^2$, where μ is the reduced effective mass and $\langle \rho^2 \rangle^{1/2}$ is the average wave function extent in the plane perpendicular to the applied field. The energy shift should be significant so we can distinguish between a state confined to a few nanometres within a Si nanocrystal and a highly localized defect state. If the shift is very small, the QC origin of the PL cannot be excluded. In order to increase the shift authors have passivated the sample in 1 atm of pure hydrogen for 30 min at a temperature of $400°\mathrm{C}$. This temperature does not influence the size and nature of the Si nanocrystals [66]. Then the ESR and PL measurements were repeated. After the passivation all traces of any defects have been removed, the only part that remains being the Si:P marker signal. The intensity of the PL signal has increased, consistent with the removal of the P_b defects. Authors assume that the passivation has also eliminated the ESR-inactive defects and PL has entirely QC origin. This can be seen in (Fig. 1.5 a) a parabolic shift of about 1.5 meV was observed during the second magneto-PL experiment. After illumination for 8 h near $95\ \%$ of the interface defects being reactivated and the PL became totally of interface-defect origin, even if their PL may still be quenched by the reintroduction of P b-type defects Fig. 1.5. (b).

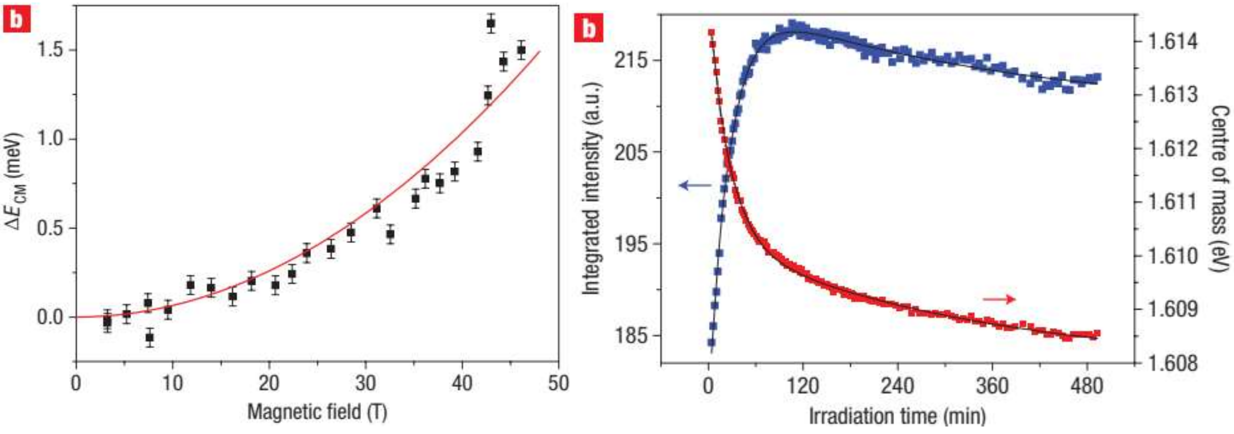

Fig. 1.5. PL in Si nanocrystals embedded into SiO_2 matrix

(a) Shift of the centre of mass of the PL peak (ΔE_{CM}) as a function of magnetic field at $85\mathrm{K}$ after passivation the solid line shows the parabolic fit;

(b) Effect of UV irradiation on a passivated sample Time dependence of the centre of mass (right-hand axis) and integrated intensity (left-hand axis) of the PL, after passivation and during irradiation with the UV lines of an unfocused Ar^+ laser. The lines are fitted to the data using double exponential functions.

Figure is adopted from Ref. [60]

It was shown that high magnetic fields can be used to distinguish defects generated PL from quantum confinement PL in Si nanocrystals embedded SiO_2. Authors switched from defect-related PL, to QC PL, and back in a single sample by a combination of passivation to remove defects and UV irradiation to reintroduce them.

In PL and influence of the exciton migrations on it were studied in the work [67]. Authors obtained Si nc by evaporation of the SiO superlattice and subsequent thermally induced phase separation. The nc-Si were prepared by alternative evaporation of SiO powder in either vacuum or oxygen atmosphere to create a SiO/SiO_2 superlattice [68]. Thickness of the SiO layers was in the range $1\,\mathrm{nm}-6\,\mathrm{nm}$, while SiO_2 layers thickness was $4\,\mathrm{nm}$. The evaporated samples were annealed at $1100^{\circ}\mathrm{C}$ in N_2 atmosphere. This method allows size-control synthesis of Si-nc completely passivated with SiO_2.

Photoexcited Si has inefficient light emission due to the indirect band gap in the bulk Si. In the case of the Si nc the probability of the indirect transition increases with the decries of the nc size due to the spatial confinement. At the same time the electron, hole and exciting binding energies increase, too (see Fig. 1.6). It results in the blueshift of the PL energy [61], [69–72]. The exciton energy is split into triplet and singlet states. The radiative lifetime of the electron-hole recombination represents the thermal equilibrium of the lifetime of the triplet and singlet state [69].

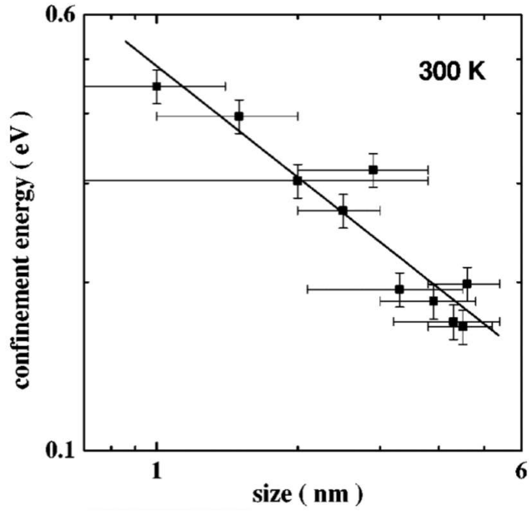

Fig. 1.6. Dependence of confinement energy

(the sum of the difference between electron and hole confined energies and electron-hole interaction) on Si crystal size measured by XRD for PL measured at $300\,\mathrm{K}$.

Figure is adopted from Ref. [67]

Besides radiative or non-radiative recombination the exciton migration between adjacent ncs influences its optical properties in the case of the extremely long radiative lifetimes of excitons in Si in large temperature range. This mechanism of exciton migration together with Gaussian size distribution explain the stretched exponential time decay of the PL signal [73–75]: $I(t)=I_0\exp\left[-\left(\frac{t}{\tau}\right)^b\right]$, where $I(t)$ stands for PL intensity at the time t and b is the dispersion factor. This mechanism is used for porous Si and shows qualitatively the same trends for Si nc embedded in SiO_2 matrix [70], [75], [76]. Quantitative difference can be explained by the fact that in nc exciton migrates into more energetically favourable low state. The temperature dependencies of the PL peak and full width at half maximum (FWHM) indicate a significant influence of the excitonic migration on the optical properties of layers (see Fig. 1.7). Though, the thermalization of the exciton could not fully explain difference between PL in porous silicon [71] and Si nc, especially at low temperatures. Measurements made at low temperature indicate on the existence of the intermediate layer with lower potential barrier. The formation of a SiO shell around Si nc is probable during the phase separation of the SiO_x into Si and SiO_2. A lower band gap of the surrounding matrix leads also to a higher migration probability and very strong migration effects.

The described effects could be explained by electron-hole recombination. The smaller band gap of dielectric matrix and very high density of Si nc increase migration probability of the excitons between the crystals. This can explain the quantitative size dependence of the different confinement effects.

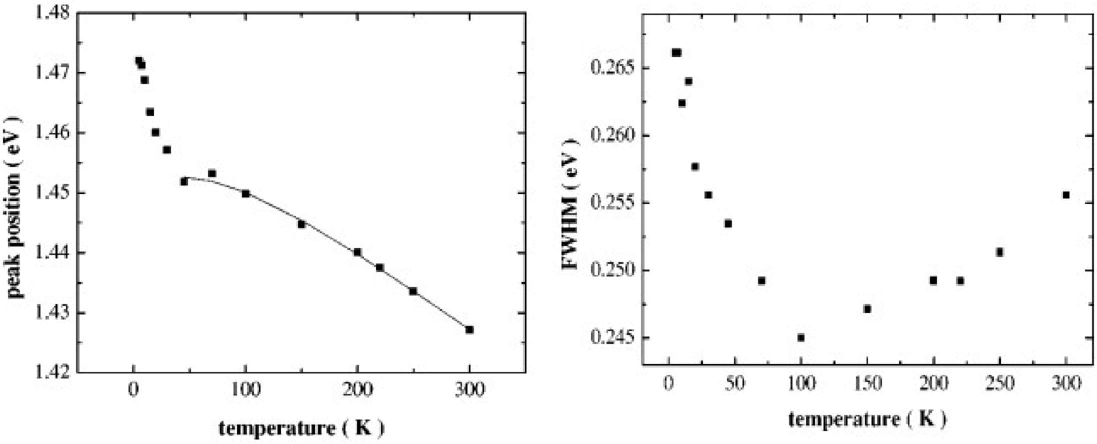

Fig. 1.7. Temperature dependencies of PL

(a) PL peak position as a function of temperature for the sample with a 4-nm-thick SiO layer. The solid line shows the best fit to the experimental data from 50 K to 300 K according to $I(t)$ equation;

(b) FWHM of the PL signal as a function of temperature for the sample with a 4-nm-thick SiO layer.

Figure is adopted from Ref. [67]

Silver nanodots applications

The PL engineering and control in nanostructures give wide spectra of silver nanodots' application that were impossible for analogic bulk materials. In the work [77] authors reported about developing of silver nanodots for biological applications. Silver nanodots (Ag ND) are the class of fluorophores with photophysical properties similar to semiconductor quantum dots. Ag NDs have various applications as photoluminescent and electroluminescent materials, probes and biolabels due to high luminescence quantum yields, large molar extinctions, and excellent photostability. Silver NDs produce higher emission rates and molecular brightness than available organic dyes [78]. Silver emitters in different energy ranges show significant improvement of the two-photon absorption cross sections in comparison with the organic ones even for smaller Ag QD, this fact make them promising candidates for optical *in vivo* imaging [79], [80]. The experiments demonstrate high photostability, persistent emission rates and brightness of Ag ND [78], [80], [81]. The first problem of the Ag ND creation is the propensity of silver clusters toward oxidation and their vulnerability to other electron acceptors. Besides that, silver atoms demonstrate tendency to agglomerate, preventing formation of nanoclusters.

The solid matrices formed from glasses [82] and zeolite [83], [84] act as a shield for Ag ND from their oxidation and agglomeration. Silver ND can be formed on different surfaces by thermal, chemical or photo-reduction. Silver clusters formed on silver halide microcrystals show luminescence on cryogenic temperatures with emission bands at $550\ \text{nm}$, $590\ \text{nm}$, $640\ \text{nm}$ [85], [86], which is lost at the room temperature. The room temperature emission is shown for Ag nanoclusters formed on photo-reduced surfaces of silver oxides [87]. The nanoclusters formed on oxyfluoride show large emission wave range (see Fig. 1.8).

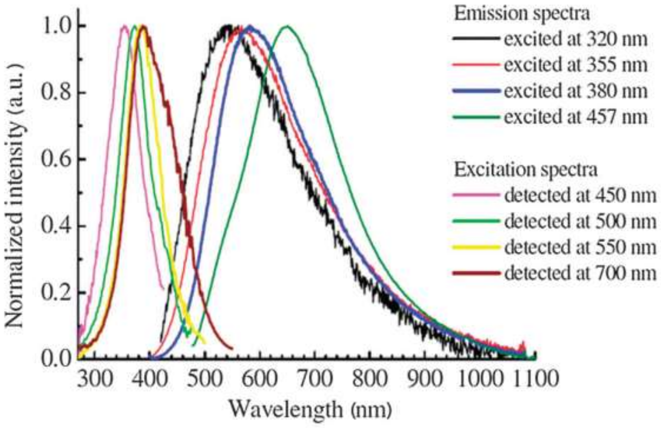

Fig. 1.8. Normalized emission and excitation spectra of the oxyfluoride glass doped with 5 wt% $AgNO_3$.

Figure is adopted from Ref. [82]

The emission bands in type A zeolite (Agx, K-A) depend on the silver loading ratio x. For silver content $x < 3$, the zeolite samples show a broad emission band in the range $530\,\mathrm{nm} - 580\,\mathrm{nm}$. As the silver content increases up to $x < 6$ the emission band shifts to $690\,\mathrm{nm}$. In the case if x takes values 7–10 the band near $550\,\mathrm{nm}$ disappear. For saturated zeolites (x = 11 to 12) the main emission band blue-shifts from $690\,\mathrm{nm}$ to $590\,\mathrm{nm}$ [84]. Silver nanoclusters in solid matrices are promising candidates for information storage and light emitting materials.

For bioapplications the Si nanodots should be soluble and stable as well. Silver nanodots were produces by photoactivation in as a core in polyglycerol-block-poly-acrylic acid. The sample showed stable emission during more than 9 hours of the continuous irradiation [88]. The mixture of silver ions poly(methacrylic acid) shows microseconds lifetimes if are irradiated with visible light instead of UV light. The increase of silver-methacrylic molar ratio leads to the red-shift of the absorption and emission peaks [89].

Reports on peptide-protected nanodots sample shows excellent stability under physiological conditions [90–92], see Fig. 1.9. The stability of silver nanodots depends on peptide sequence: for peptide with short sequence chemical lifetime is 3 days at room temperature, but longer peptide sequences can extend it up to 2 weeks in deionized water and 5 weeks in phosphate buffered saline.

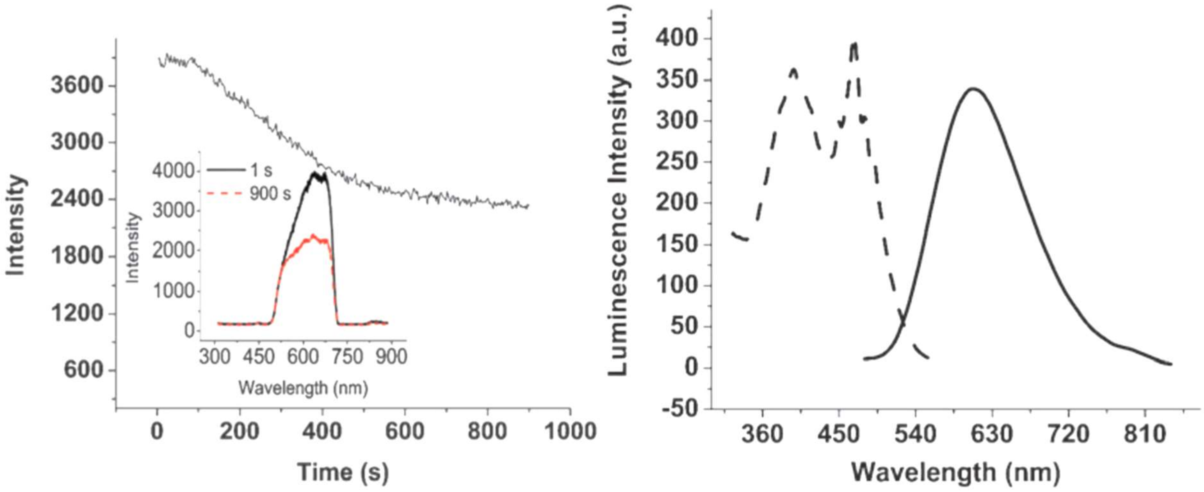

Fig. 1.9. PL intensity in the protein/peptide-protected silver nanodots.

(a) Argyrophilic proteins are good templates for the generation of silver nanodots. These nanodots are quite photostable, with a low photobleaching rate after an initial decrease in emission intensity

(b) The peptide-protected silver nanodots show red emission with large Stokes shift

Figure is adopted from Ref. [80].

The photoluminescence properties of silver ND strongly depend on how scaffold protect them from environment interactions, which van enhance or quench emission. This fact makes silver nanodots good candidates for sensors. The DNA-encapsulated silver nanodots demonstrate PL quenching for low concentrations of Hg^{2+} [78]. Also, they have good selectivity: ions Co^{2+}, Ni^{2+}, Pb^{2+} and Zn^{2+} do not affect the emission intensity of the nanodots, but others, such as Cu^{2+}, Fe^{2+}, Fe^{2+}, Mn^{2+} cause slight quenching of emission. In the work [93] the detection of Cu^{2+} by Si ND embedded in PMAA shield. The intensity of emission drastically falls at copper concentration 4.5 10 × M. Other ions such as Co^{2+}, Ni^{2+} and Fe^{3+} do not reduce intensity such significantly. DNA-encapsulated nanodots demonstrate increase of the PL in the presence of the Cu^{2+} [94]. Authors demonstrated good selectivity and sensitivity of DNA-protected Ag ND (see Fig. 1.10) after introducing of 3-mercaptopropionic acid (MPA). The PL responds strongly to a concentration of 0.5 mM Cu^{2+} ions, while the respond is weak to the other metal ions with the concentration 50 mM.

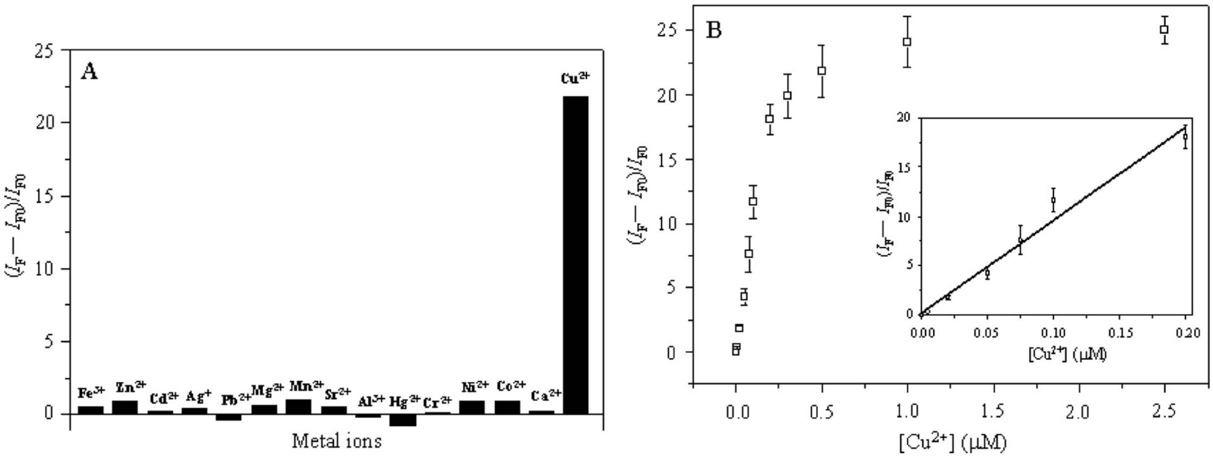

Fig. 1.10. Detection of copper(II) by DNA/Ag/Cu.

(a) Selectivity towards copper(II);

(b) Sensitivity demonstration. I_{F0} and I_F are the PL intensities of the in the absence and presence of copper cations, respectively. Inset: linear range of the plot of $(I_{F0} - I_F)/I_{F0}$ as a function of Cu^{2+} concentration (0–0.2 μM)

Figure is adopted from Ref. [94].

The theoretical study of the exciton in nanostructures

Different theoretical approaches have been employed to study exciton and photoluminescence properties of nanostructures: effective mass approach [34], [95–99], tight-binding [100–102] and density functional theories [103], [104]. Although these models can predict different values of exciton energies in nanostructures, they made qualitatively identical conclusions regarding blue-shift of exciton energy and basic mecanisms of photoluminescence. It has been established that EMAs with multi-band hamiltonians predict exciton energies in a good agrement with existing experimental data for different nanostructures if their lateral dimensions exceed 2 nm [34], [96], [97], [105], [106].

In the work [34] authors theoretical analysis of the exciton states in AlGaN/GaN quantum well heterostructures using asymmetric six-band Hamiltonian for holes and one-band Hamiltonian for electron.

The electron states in QD one band Schrodinger equation:

$$\hat{H}_e = \hat{H}_s\left(\vec{r}_e\right) + V_P\left(z_e\right) + H^{(\varepsilon)}\left(\vec{r}_e\right) + \Delta E_c\left(z_c\right) + V_{SA}\left(z_e\right), \tag{1.1}$$

where $\hat{H}_s\left(\vec{r}_e\right)$ is the kinetic part, $V_{SA}\left(z_h\right)$ is the hole self-interaction energy [105], $\Delta E_c\left(z_e\right)$ height of potential barrier.

The replacement of the six-band Hamiltonian with the one-band Hamiltonian for heavy, light, and split-off holes lacks sufficient justification, as the binding energy of the ground exciton level depends on the effective mass of all three types of holes [106]. The one-band Hamiltonian only yields fully symmetrical s-like hole and exciton ground states, while a multiband Hamiltonian can provide a solution with a p-like ground state. The symmetry of the exciton state is crucial for selection rules and the interpretation of photoluminescence (PL) experimental data. By considering the nonsymmetric six-band Hamiltonian, the mixing of light, heavy, and spin-orbit split-off holes is appropriately accounted for.

The six-band Hamiltonian has form

$$\hat{H}_h = \begin{vmatrix} \hat{H}_{XYZ}\left(\vec{r}_h\right) + \hat{H}_h^e & 0 \\ 0 & \hat{H}_{XYZ}\left(\vec{r}_h\right) + \hat{H}_h^e \end{vmatrix} + \hat{H}_{S-O} + eFz_h\hat{I} + \Delta E_h\left(z_h\right)\hat{I} + V_{SA}\left(z_h\right)\hat{I}, \tag{1.2}$$

where $\Delta E_h\left(z_h\right)$ is hole barrier height, $V_{SA}\left(z_h\right)$ is the hole self-interaction energy [105], $\hat{I}$ is the 6 × 6 unit matrix, $\hat{H}_{S-O}$ is the spin-orbit Hamiltonian [107], $\hat{H}_h^e$ is the deformation interaction Hamiltonian [107], H_{XYZ} is the 3 × 3 matrix representing the kinetic energy in the Hamiltonian for unit cell in the basis $\left|X\right\rangle$, $\left|Y\right\rangle$, $\left|Z\right\rangle$ and depends on Rashba-Sheka-Pikus parameters of the valence band [108].

The exciton Hamiltonian

$$\hat{H}_{exc} = \hat{H}_e\left(\vec{r}_e\right) + \hat{H}_h\left(\vec{r}_h\right) + V_C\left(\vec{r}_e - \vec{r}_h, z_e, z_h\right)\hat{I} \tag{1.3}$$

includes electron and holes Hamiltonian and energy of the electron-hole Coulomb interaction.

In Fig. 1.11 the comparison of the theoretical and experimental exciton energies in the $Al_{0.24}Ga_{0.76}N$/GaN heterostructure are shown. Inset shows the difference between theoretical energies calculated in the six-band approach [34] and one-band approach [109]

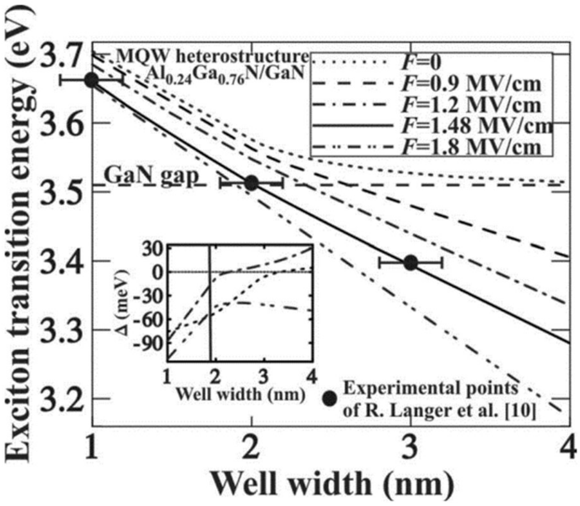

Fig. 1.11. Well-width dependence of the calculated exciton transition energies in an $Al_{0.24}Ga_{0.76}N$/GaN heterostructure and the experimental peak positions.

Inset: Deviations D of the present results from those calculated in Ref. [109].

Figure is adopted from Ref. [109]

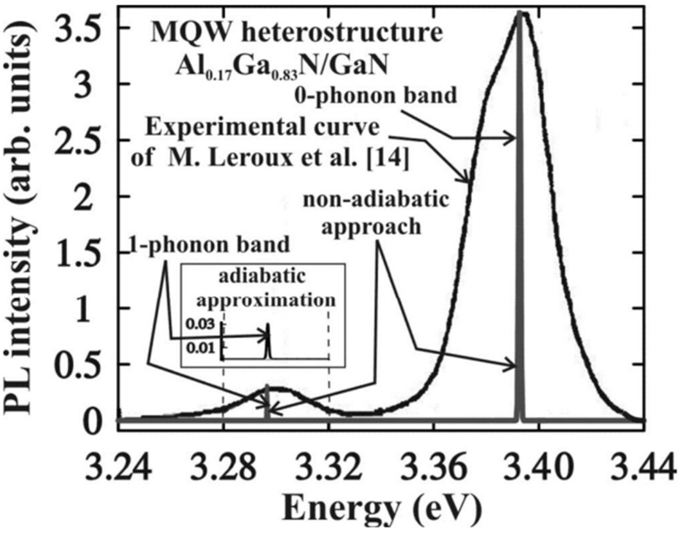

Fig. 1.12. Photoluminescence spectra of an $Al_{0.17}Ga_{0.83}N$/GaN MQW heterostructure with four 16 ML QWs and 30 nm barriers.

Figure is adopted from Ref. [109]

In Fig. 1.12 the PL as function of the energy is shown. The positions of the PL peaks and their relative intensities obtained theoretically are in fair agreement with the experiment of Ref. [110]

1.2. Phonons engineering in semiconductor nanostructures

Phonons play an important role in the majority of physical processes in semiconductor materials: they interact with charge carriers and limit their mobility, affects optical properties and carry heat [1]. Spatial confinement of phonons in nanostructures significantly change phonon properties in comparison with bulk materials because the phonon mean free path in nanostructures become comparable to nanostructure spatial sizes (thickness or length) [1], [5], [18], [111–113]. S. Rytov [113] has demonstrated that in planar lamellar medium folded phonon modes appear. Further investigations have revealed strong modification of phonon energy spectra and phonon group velocities in planar nanostructures and nanowires which affects all phonon-assisted processes.

Continuum model for phonons in nanostructures

Initial theoretical investigations of phonon confinement in homogeneous films and nanowires as well as in multilayered planar heterostructures and core-shell nanowires were undertaken employing continuum approach. In the framework of this approach the equation of motion for elastic vibrations can be written as [114], [115]:

$$\rho\frac{\partial^2 U_m}{\partial t^2} = \frac{\partial \sigma_{mi}}{\partial x_i}, \qquad (1.1)$$

where $\vec{U}(U_1, U_2, U_3)$ is the displacement vector, ρ is the mass density of the material, σ_{mi} is the elastic stress tensor given by $\sigma_{mi} = c_{mikj}U_{kj}$, $U_{kj} = \frac{1}{2}\left(\frac{\partial U_k}{\partial x_j} + \frac{\partial U_j}{\partial x_k}\right)$ is the strain tensor, i=1,2,3 and m = 1,2,3.

In the non-uniform media the elastic modules are the piece-wise functions of $\vec{r}$:

$$c_{mikj} = c_{mikj}(\vec{r}). \qquad (1.2)$$

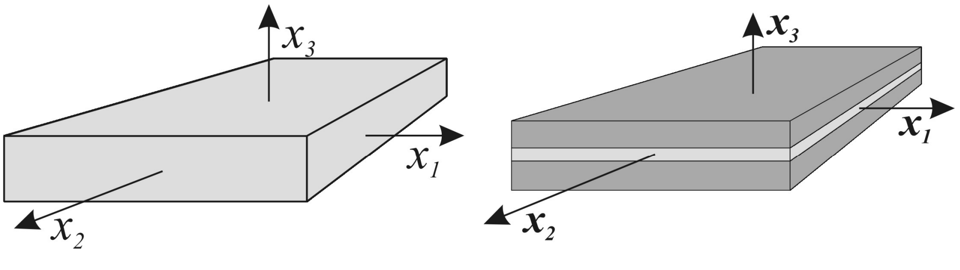

(a) (b)

Figure 1.13. The schematic view of the researched
(a) thin film and **(b)** three-layered heterostructure
Figure is adopted from Ref. [111]

For planar nanostructures (see Figure 1.13) Eq. 1.1 splits into a system of two interrelated differential equations for the amplitudes u_1 and u_3 and a separate differential equation for the amplitude u_2 [111], [116]:

$$-\rho\omega^2 u_2(x_3) = c_{44}\frac{d^2u_2(x_3)}{dx_3^2} + \frac{dc_{44}}{dx_3}\cdot\frac{du_2(x_3)}{dx_3} - c_{66}q^2u_2(x_3), \qquad (1.3)$$

$$-\rho\omega^2 u_1(x_3) = -q^2c_{11}u_1(x_3) + c_{44}\frac{d^2u_1(x_3)}{dx_3^2} +$$

$$+q(c_{13}+c_{44})\frac{du_3^{'}(x_3)}{dx_3} + \frac{dc_{44}}{dx_3}\left(\frac{du_1(x_3)}{dx_3} + qu_3^{'}(x_3)\right)$$

$$-\rho\omega^2 u_3^{'}(x_3) = -q^2c_{44}u_3^{'}(x_3) + c_{33}\frac{d^2u_3^{'}(x_3)}{dx_3^2} +$$

$$+\frac{dc_{33}}{dx_3}\frac{du_3^{'}(x_3)}{dx_3} - q\left[(c_{13}+c_{44})\frac{du_1(x_3)}{dx_3} + \frac{dc_{13}}{dx_3}u_1(x_3)\right] \qquad (1.4)$$

In Eqs. (1.3 - 1.5) $u_3^{'} = -\mathbf{i}u_3$ and **i** is imaginary unit. We note here that Eqs. 1.2-1.3 were derived in the following assumptions:

- axis X_1 and axis X_2 of the Cartesian coordinate system are in the plane of the layers;
- acoustic waves propagate along axis X_1;
- four indexes (*mikj*) of elastic modules are converted into two indexes (*nl*) according to the prescription: (1111)→(11); (2222)→(22); (3333)→(33); (1122)→(12); (1133)→(13); (1313)→(44); (2323)→(55) and (1212)→(66);
- crystal lattice of layer's materials possesses hexagonal symmetry, i.e. there are only five independent elastic constants $c_{11}, c_{12}, c_{13}, c_{33}$ and c_{44}:

$$c_{ij}^{wurtzite} = \begin{pmatrix} c_{11} & c_{12} & c_{13} & 0 & 0 & 0 \\ c_{12} & c_{11} & c_{13} & 0 & 0 & 0 \\ c_{13} & c_{13} & c_{33} & 0 & 0 & 0 \\ 0 & 0 & 0 & c_{44} & 0 & 0 \\ 0 & 0 & 0 & 0 & c_{44} & 0 \\ 0 & 0 & 0 & 0 & 0 & c_{66} = \frac{c_{11}-c_{12}}{2} \end{pmatrix}.$$

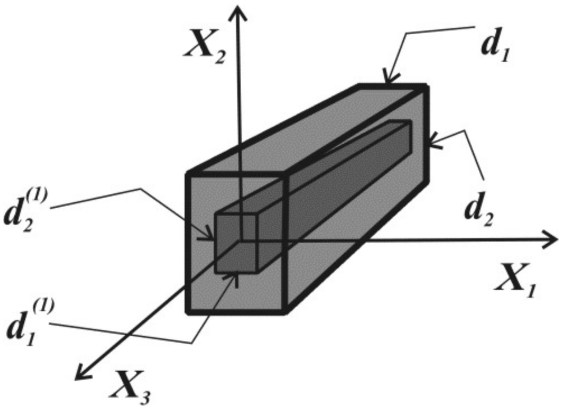

Fig. 1.14. Schematic view of a rectangular core/shell nanowire.

Figure is adopted from Ref. [117]

In the case of rectangular nanowires when axis X_3 is directed along nanowire axis (see Fig. 1.14) Eq. 1.2 can be re-written as follows [117]:

$$
\begin{aligned}
\left(c_{44}q^2-\omega^2\rho\right)u_1 &= c_{11}\frac{\partial^2 u_1}{\partial x_1{}^2}+c_{66}\frac{\partial^2 u_1}{\partial x_2{}^2}+\frac{\partial c_{11}}{\partial x_1}\frac{\partial u_1}{\partial x_1}+\\
&+\frac{\partial c_{66}}{\partial x_2}\frac{\partial u_1}{\partial x_2}+\left(c_{12}+c_{66}\right)\frac{\partial^2 u_2}{\partial x_1\partial x_2}+\frac{\partial c_{12}}{\partial x_1}\frac{\partial u_2}{\partial x_2}+\\
&+\frac{\partial c_{66}}{\partial x_2}\frac{\partial u_2}{\partial x_1}+q\left(c_{13}+c_{44}\right)\frac{\partial u_3}{\partial x_1}+q\frac{\partial c_{13}}{\partial x_1}u_3,
\end{aligned}
\tag{1.5}
$$

$$
\begin{aligned}
\left(c_{44}q^2-\omega^2\rho\right)u_2 &= c_{66}\frac{\partial^2 u_2}{\partial x_1{}^2}+c_{11}\frac{\partial^2 u_2}{\partial x_2{}^2}+\\
&+\frac{\partial c_{66}}{\partial x_1}\frac{\partial u_2}{\partial x_1}+\frac{\partial c_{11}}{\partial x_2}\frac{\partial u_2}{\partial x_2}+\left(c_{12}+c_{66}\right)\frac{\partial^2 u_1}{\partial x_1\partial x_2}+\\
&+\frac{\partial c_{66}}{\partial x_1}\frac{\partial u_1}{\partial x_2}+\frac{\partial c_{12}}{\partial x_2}\frac{\partial u_1}{\partial x_1}+q\left(c_{13}+c_{44}\right)\frac{\partial u_3}{\partial x_2}+q\frac{\partial c_{13}}{\partial x_2}u_3,
\end{aligned}
\tag{1.6}
$$

$$
\begin{aligned}
\left(q^2c_{33}-\omega^2\rho\right) &= c_{44}\left(\frac{\partial^2 u_3}{\partial x_1^2}+\frac{\partial^2 u_3}{\partial x_2^2}\right)+\frac{\partial c_{44}}{\partial x_1}\frac{\partial u_3}{\partial x_1}+\\
&+\frac{\partial c_{44}}{\partial x_2}\frac{\partial u_3}{\partial x_2}-q\left(c_{13}+c_{44}\right)\left(\frac{\partial u_1}{\partial x_1}+\frac{\partial u_2}{\partial x_2}\right)-q\left(\frac{\partial c_{44}}{\partial x_1}u_1+\frac{\partial c_{44}}{\partial x_2}u_2\right).
\end{aligned}
\tag{1.7}
$$

The system of two-dimensional differential equations Eqs. 1.5-1.7 can be simplified in the case of cylindrical nanowires (see Fig. 1.15) [118] to the system of one-dimensional differential equations:

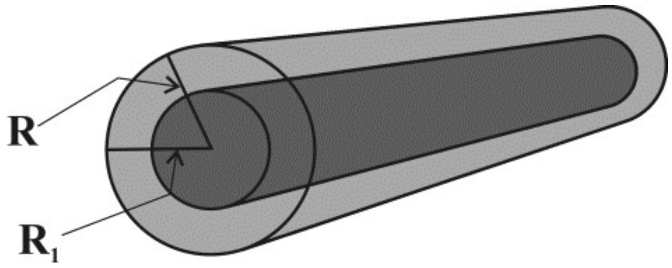

Fig. 1.15. A schematic view of a core/shell cylindrical nanowire.
Figure is adopted from Ref. [118].

$$\begin{aligned}
&\left(c_{44}q^2-\rho\,\omega^2\right)u_r = c_{11}\frac{d^2u_r}{dr^2}+\left(\frac{c_{11}}{r}+\frac{dc_{11}}{dr}\right)\frac{du_r}{dr}\\
&+\left(\frac{1}{r}\frac{dc_{12}}{dr}-\frac{c_{11}}{r^2}-\frac{m^2c_{66}}{r^2}\right)u_r+m\left(\frac{1}{r}\frac{dc_{12}}{dr}-\frac{c_{11}+c_{66}}{r^2}\right)u_\varphi+\\
&+\frac{m\left(c_{11}-c_{66}\right)}{r}\frac{du_\varphi}{dr}+q\left(c_{13}+c_{44}\right)\frac{du_z}{dr}+q\frac{dc_{13}}{dr}u_z,
\end{aligned}\tag{1.8}$$

$$\begin{aligned}
&\left(c_{44}q^2-\rho\,\omega^2\right)u_\varphi = c_{66}\frac{d^2u_\varphi}{dr^2}+\left(\frac{c_{66}}{r}+\frac{dc_{66}}{dr}\right)\frac{du_\varphi}{dr}-\\
&-\left(\frac{c_{66}}{r^2}+\frac{1}{r}\frac{dc_{66}}{dr}+\frac{c_{11}m^2}{r^2}\right)u_\varphi-\frac{m\left(c_{11}-c_{66}\right)}{r}\frac{du_r}{dr}-\\
&-m\left(\frac{c_{11}+c_{66}}{r^2}+\frac{1}{r}\frac{dc_{66}}{dr}\right)u_r-\frac{mq\left(c_{13}+c_{44}\right)}{r}u_z,
\end{aligned}\tag{1.9}$$

$$\begin{aligned}
&\left(c_{33}q^2-\rho\,\omega^2\right)u_z = c_{44}\frac{d^2u_z}{dr^2}+\left(\frac{c_{44}}{r}+\frac{dc_{44}}{dr}\right)\frac{du_z}{dr}-\\
&-\frac{c_{44}m^2}{r^2}u_z-q\left(\frac{c_{13}+c_{44}}{r}+\frac{dc_{44}}{dr}\right)u_r-\\
&-q\left(c_{13}+c_{44}\right)\frac{du_r}{dr}-\frac{qm\left(c_{13}+c_{44}\right)}{r}u_\varphi.
\end{aligned}\tag{1.10}$$

Two opposite types of boundary conditions were employed in Refs. [111], [116–118] both for planar nanostructures and nanowires: free external boundaries (FES) and clamped external boundaries (CES). Free external boundaries correspond to free-standing nanostructures [112], [119], [120] when force on the external surfaces is equal to 0, i.e. force components $P_1=P_2=P_3=0$. Clamped external surfaces represent a theoretical limit when external surfaces are immovable (this limit cannot be experimentally reached): $u_1=u_2=u_3=0$.

Phonon properties of three-layer planar nanostructures with GaN inner layer and core/shell nanowires with GaN core were investigated in Refs. [18], [111], [116–118], [121], using elastic continuum approach. Authors have demonstrated that phonon energy spectra in nanostructures consisting of layers from different acoustic materials (like GaN and AlN or Si and Ge) strongly differs from those in homogeneous slabs or wires. It has been theoretically established the following peculiarities of energy spectra in multi-layer nanostructures:

- Depending of the wave-vector q phonon modes demonstrates behavior similar to transversal acoustic or longitudinal acoustic modes of corresponding bulk materials. For example, in AlN/GaN/AlN planar heterostructure or GaN/AlN core/shell nanowires phonon modes can be (GaN, TA) bulk-type, (GaN, LA) bulk-type, (AlN, TA) bulk-type and (AlN, LA) bulk type. Similarly, in Ge/Si/Ge nanostructures modes can be divided into four groups: (Si, TA) bulk type, (Si, LA) bulk-type, (Ge, TA) bulk-type and (Ge, LA) bulk-type phonons.
- Evident straight lines combining segments of energy curves with close slope appears in the phonon energy spectra (see lines L, L’ in Fig. 1.16 and Fig. 1.19).
- For large values of q all phonon modes become (GaN, TA) bulk-like in the case of AlN/GaN/AlN heterostructures or GaN/AlN core/shell nanowires and (Ge, TA) bulk-like in the case of Ge/Si/Ge heterostructures or Si/Ge nanowires (see Fig. 1.17 and Fig. 1.20).
- Phonon group velocities for all phonon branches demonstrates non-monotonic behaviour and possess values between bulk v_{LA} and v_{TA} values of corresponding materials. At large q phonon velocities tends to v_{TA} (GaN) in nanostructures with GaN-channel and to v_{TA}(Ge) in nanostructures with Si-channel.
- Claddings/shell made from material with lower sound velocity than in the internal layer (core) decrease average phonon group velocity of nanostructure; claddings/shell made from material with higher sound velocity demosntrate an opposite effect and increase average phonon group velocity of nanostructure in wide energy range. This effect is illustrated in Fig. 1.20, where dependence of average phonon group velocity on phonon energy is shown from GaN nanowires, GaN/AlN and GaN. Plastic (Pl) core/shell nanowires. Average velocity in GaN nanowire with plastic shell is substantially lower that that in bare nanowire, while average velocity in GaN nanowire with AlN shell is higher than that in the bare nanowire for energy ranges: $\hbar\omega < 4$ meV and $\hbar\omega > 7$ meV phonons.

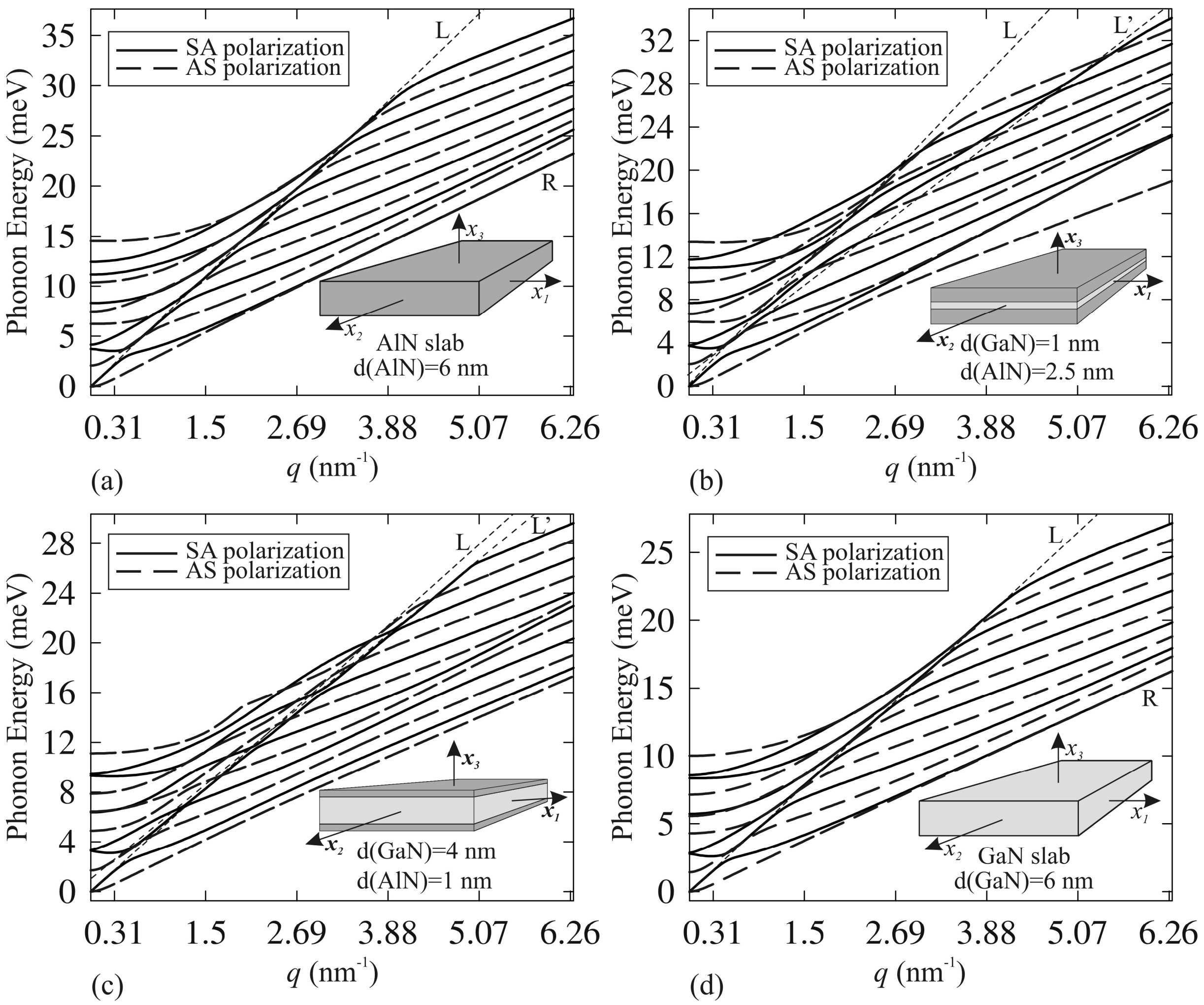

Fig. 1.16. Energy dispersion of the SA and AS acoustic phonon modes in slabs and heterostructures.

(a) homogeneous GaN slab with thickness of 6 nm ;

(b) AlN/GaN/AlN heterostructure with dimensions 2.5 nm / 1.0 nm / 2.5 nm ;

(c) AlN/GaN/AlN heterostructure with dimensions 1.0 nm / 4.0 nm / 1.0 nm ;

(d) AlN slabs with thickness of 6 nm ; Insets show the geometry of the slab and three-layered structure.

Figure is adopted from Ref. [111].

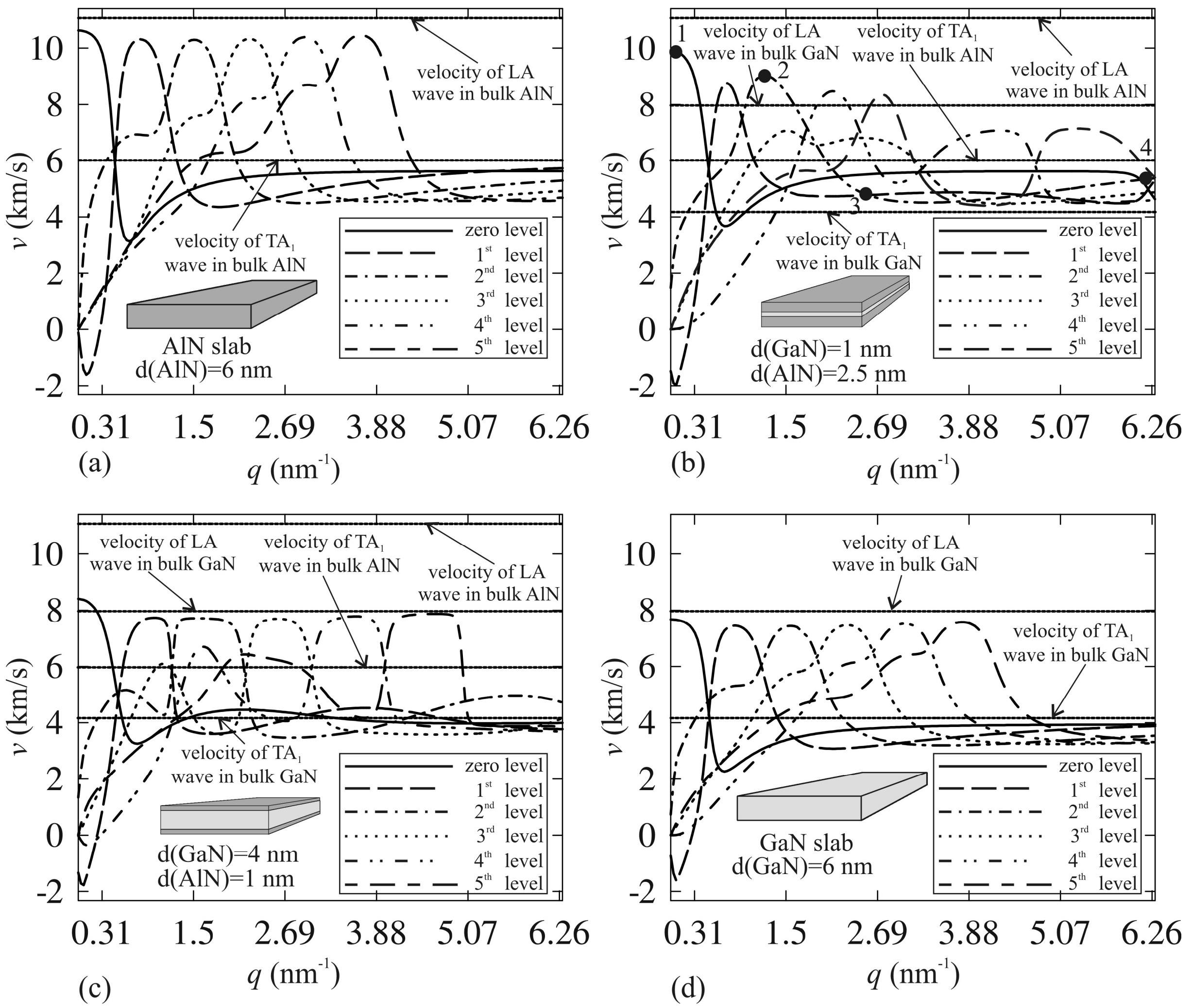

Fig. 1.17. **Phonon group velocities as a function of phonon wave vector for the SA acoustic phonon modes in AlN/GaN/AlN heterostructure**

(a) homogeneous GaN slab with thickness of $6\ \mathrm{nm}$;

(b) AlN/GaN/AlN heterostructure with dimensions $2.5\ \mathrm{nm}$ / $1.0\ \mathrm{nm}$ / $2.5\ \mathrm{nm}$;

(c) AlN/GaN/AlN heterostructure with dimensions $1.0\ \mathrm{nm}$ / $4.0\ \mathrm{nm}$ / $1.0\ \mathrm{nm}$;

(d) AlN slabs with thickness of $6\ \mathrm{nm}$ **;** Insets show the geometry of the slab and three-layered structure.

Figure is adopted from Ref. [111].

Despite the fact that numerous studies have employed continuum approach for modelling of phonon and thermal properties in nanostructures both qualitatively and quantitatively, the applicability of this approach has important limitations: (1) it does not take into account an atomistic structure of investigated material; (2) the number of continuum phonon modes is formally infinite and it is necessary to artificially cut off the maximal phonon energy spectra; (3) at large values of q velocities of continuum phonon modes are not zero and tend to transversal acoustic sound velocity.

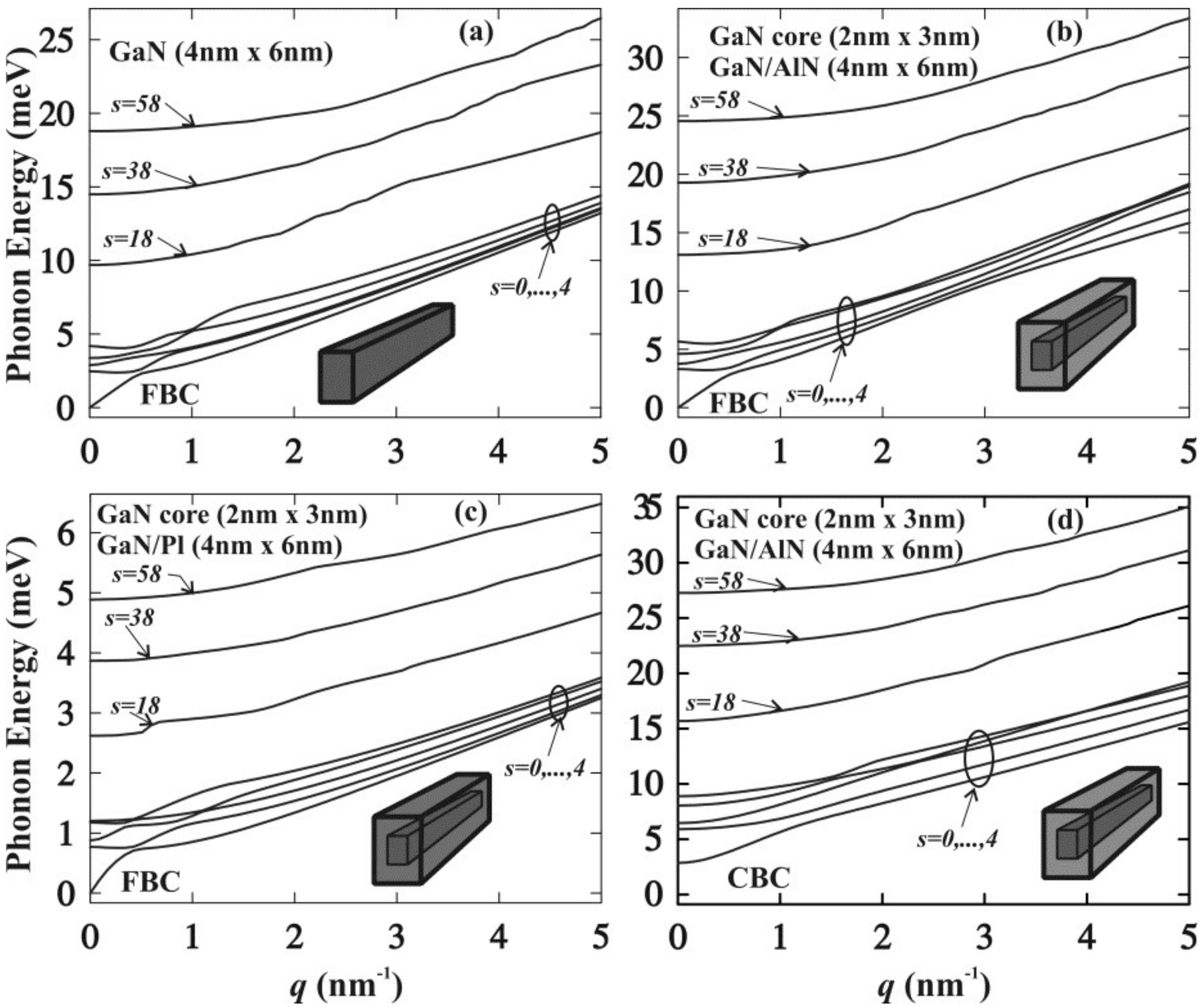

Fig. 1.18. Phonon dispersions for the dilatational modes for free-surface (a–c) and clamped-surface (d) boundary conditions at the external barrier boundaries.

(a) The results are shown for GaN nanowire of the $4\ \mathrm{nm} \times 3\ \mathrm{nm}$ cross section without the barriers;

(b) GaN nanowire with acoustically fast AlN barriers of the $4\ \mathrm{nm} \times 6\ \mathrm{nm}$ and $2\ \mathrm{nm} \times 3\ \mathrm{nm}$ GaN nanowire cross sections;

(c) GaN nanowire with acoustically slow barriers of the $4\ \mathrm{nm} \times 6\ \mathrm{nm}$ and $2\ \mathrm{nm} \times 3\ \mathrm{nm}$ GaN nanowire cross sections.

(d) GaN nanowire with acoustically fast AlN barriers of the $4\ \mathrm{nm} \times 6\ \mathrm{nm}$ and $2\ \mathrm{nm} \times 3\ \mathrm{nm}$ Figure is adopted from Ref. [117].

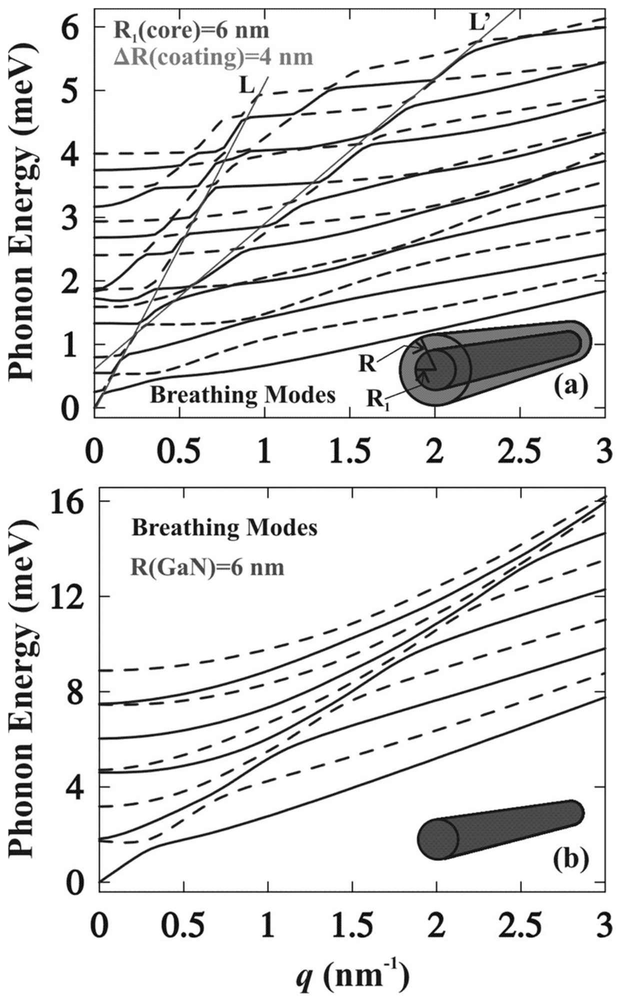

Fig. 1.19. Phonon energy as a function of the phonon wave vector *q* for the breathing modes (*m* = 0).

(a) GaN nanowire with the „acoustically soft" barrier layer ($R_1\left(GaN\right)=6\ \text{nm}$ and $R=10\ \text{nm}$);

(b) GaN nanowire without the barrier layer ($R=6\ \text{nm}$). The insets show the geometry of the nanostructures.

Figure is adopted from Ref. [118].

Limitations of continuum approach have stimulated theoretical investigations of phonon-assisted processes using dynamic models of lattice vibrations, molecular dynamic simulations or density-functional theory [7], [22], [122–126].

The detailed comparison between phonon energies, phonon group velocities and thermal conductivities in Si nanolayers calculated using continuum approach and face-centred-cubic cell model of lattice vibrations is presented in Ref. [32]. It has been established that both energies of phonon modes and behavior of phonon energy curves calculated in the framework of FCC model is different from those calculated using CA (see Fig. 1.21). Authors also found that the CA overestimates the values of the thermal conductivity for medium and high temperatures in comparison with FCC model due to an overestimation of phonon group velocities near the Brillouin zone boundary.

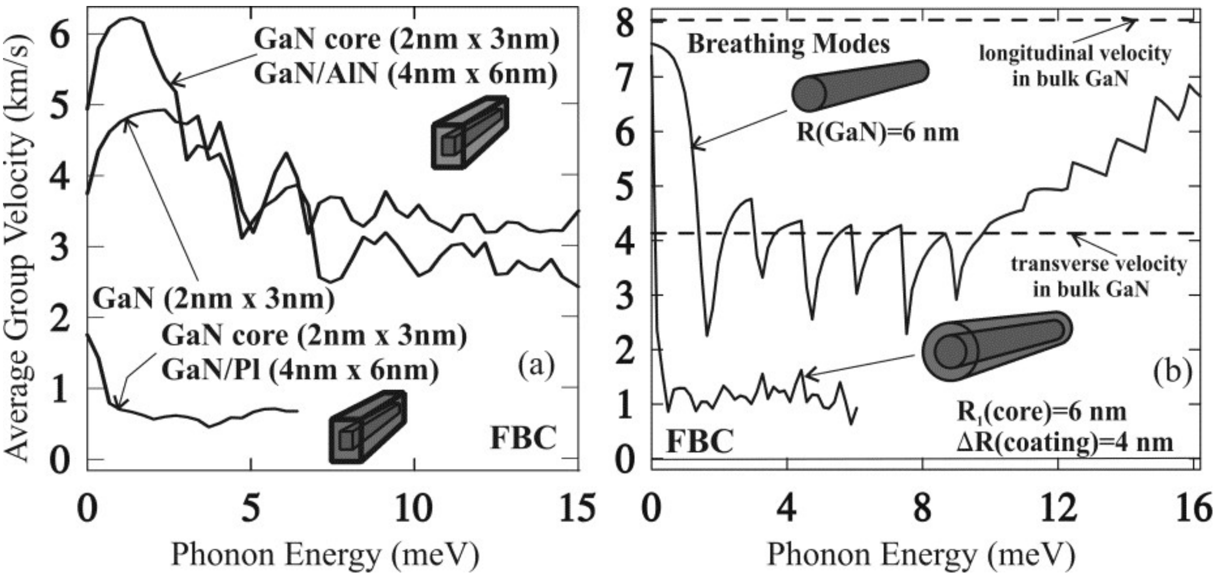

Fig. 1.20. Average phonon group velocity as a function of the phonon frequency

(a) for dilatational modes in rectangular GaN, GaN/AlN and GaN/Plastic nanowires;

(b) for breathing modes in cylindrical uncoated GaN nanowire and GaN nanowire with acoustically soft barrier.

Figure is adopted from Refs. [117], [118].

A study of phonon and thermal properties of three-layered planar structures with an inner silicon layer using the FCC model is reported in Ref. [38]. It has been demonstrated that similarly to CA the claddings strongly influence on thermal flux. Diamond claddings with higher sound velocity than in silicon enhance thermal flux by a ratio of 3, while plastic claddings (with sound velocity smaller than in silicon) decrease thermal flux by a ratio of 1.2 – 1.4. This effect is illustrated in Fig. 1.22 where phonon thermal flux is shown as a function of temperature for different Si-based planar nanostructures. Qualitatively similar results have been reported for core/shell Si/Ge nanowires, using FCC and VFF models of lattice vibrations as well as molecular dynamics [7], [8], [22], [125]. Thus, multi-layer nanostructures provide a good opportunity for engineering of their phonon and thermal properties.

Other prospective candidates for efficient phonon engineering are cross-section-modulated and segmented nanowires. Using both FCC and BVK models of lattice vibrations it has been demonstrated that phonon thermal flux can be sufficiently suppressed in such nanowires [23–25].

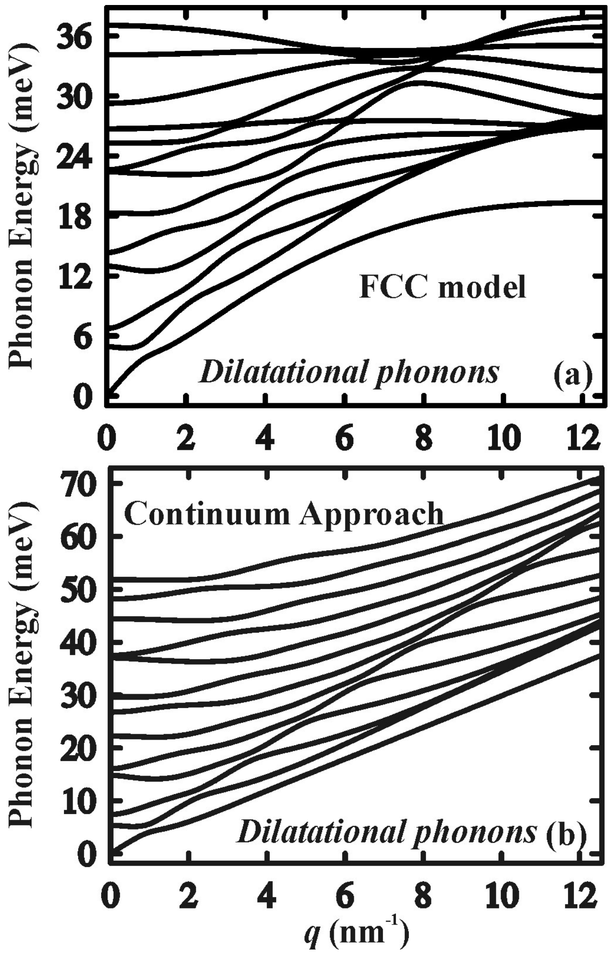

Fig. 1.21. Phonon energies as the functions of the phonon wavevector for Si layer with *d* =3.258 nm plotted for

(a) FCC-model and **(b)** continuum approach.

Figure is adopted from Ref. [118].

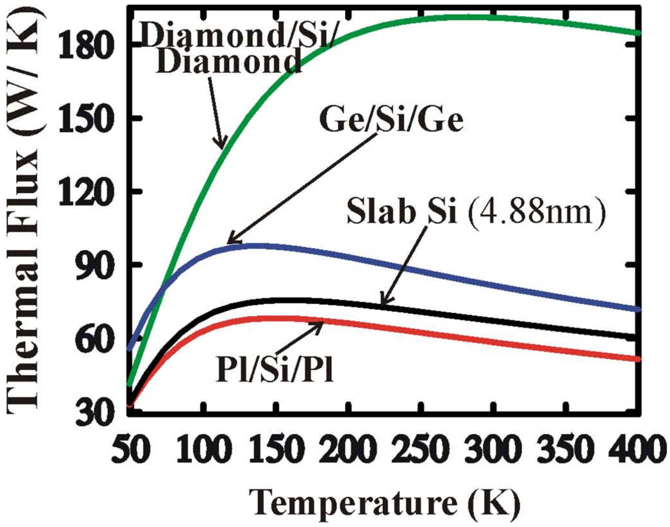

Fig. 1.22. Thermal Flux as the function of temperature for Si slab and three-layered planar nanostructures with inner Si layer.

Figure is adopted from Ref. [38].

1.3. Conclusions to Chapter 1 and objectives of the Thesis

Different nanostructures continue to attract significant attention from the research community due to their unique optical, transport, and sensing properties. Superlattices with Si quantum dots have been particularly demonstrated as CMOS-compatible and non-toxic sources of energy for both radiative and non-radiative energy transfer. For investigation of exciton and optical properties of nanostructures both effective mass approach and tight-binding models were widely employed. The theoretical investigation of phonon modes and thermal transport in nanostructures was undertaken using the continuum approach, FCC and VFF models of lattice vibrations, molecular dynamics, and density functional theory. It has been demonstrated that multi-layer nanostructures possess wide possibilities for charge-carrier or phonon engineering by tuning their shape and size as well as layer materials. At the same time, there is some lack of investigation of exciton and phonon processes in quasi-one-dimensional quantum dot superlattices.

The main goal of the Thesis is a comprehensive theoretical investigation of exciton, phonon, and thermal properties of quasi-one-dimensional Si-based nanostructures (1D-QDSL and core/shell nanotubes) and their optimization for optical, energy transfer, and thermal management applications. To achieve this goal, the following objectives are formulated:

- Development of theoretical models for electron, hole, and exciton states in Si-based 1D-QDSL;
- Investigation of electron, hole, exciton, and photoluminescence properties of Si-based 1D-QDSL and their optimization for optical and energy transfer applications;
- Development of theoretical models for phonon states and thermal conductivity in Si-based QDSL and Si/SiO_2 multi-shell nanotubes;
- Investigation of phonon and thermal properties of Si-based 1D-QDSL and Si/SiO_2 MNTs and their optimization for heat management applications.

The following **methods and approaches are used in the Thesis:**

1) Multi-band effective-mass approximation for the investigation of electron, hole, and exciton states

2) Face-centred-cubic cell model of lattice vibrations for the investigation of phonon states;

3) Boltzmann transport equation with relaxation time approximation for the investigation of thermal transport.

2. Exciton processes in Si-based quantum dot nanostructures

In this Chapter, we investigate confined electron, hole, and exciton properties in silicon-based quantum dots (QDs) of different shapes embedded in the dielectric matrix using effective mass approximation. One-band $k \times p$ Hamiltonian for electrons and one- and three-band $k \times p$ Hamiltonians for holes are employed for calculations of the charge carriers' energy spectra. Our model also takes into account both finite the height of a potential barrier at QD interfaces and the strong anisotropy of an electron effective mass in silicon. We analyze the impact of heavy, light, and spin-off holes mixing on the exciton energies and compare our results with experimentally available data. Taking into account a possible size distribution of nanocrystals we interpret the broadening of exciton PL peaks and dependence of its position on an annealing temperature reported experimentally in Refs. [13], [127], [128]. The discussions in this Chapter mostly follow the author's original articles [98], [129].

2.1. Electron states is Si-based quantum dot nanostructures

The electron energy states in QDs were obtained from the Schrodinger equation. Its general form is:

$$\hat{H}^{(e)}\Psi_n^{(e)}\left(\vec{r}_e\right) = E_n^{(e)}\Psi_n^{(e)}\left(\vec{r}_e\right), \tag{2.1}$$

where $\hat{H}^{(e)}$ – is the Hamilton operator, $E_n^{(e)}$ is the electron energy and $\Psi_n^{(e)}$ is the electron wave function. Index *n* corresponds to number of energy level.

In the effective-mass approximation Hamiltonian takes form:

$$\hat{H}^{(e)} = -\frac{\hbar^2}{2}\left(\frac{\partial}{\partial x}\frac{1}{m_x\left(\vec{r}_e\right)}\frac{\partial}{\partial x} + \frac{\partial}{\partial y}\frac{1}{m_y\left(\vec{r}_e\right)}\frac{\partial}{\partial y} + \frac{\partial}{\partial z}\frac{1}{m_z\left(\vec{r}_e\right)}\frac{\partial}{\partial z}\right) + V_b^{(e)}\left(\vec{r}_e\right) + V_{SA}^{(e)}, \tag{2.2}$$

where, $\Psi_n^{(e)}$ and $E_n^{(e)}$ are the electron wave function and electron energy in n-*th* state, correspondingly; $m_i\left(\vec{r}_e\right)$ is the electron effective mass where index $i = x, y, z$, $\hbar$ is the Planck's constant, $V_b^e\left(\vec{r}_e\right)$ is the electron barrier potential, $V_{SA}^{(e)}\left(\vec{r}_e\right)$ is electron self-energy. Eq. 2.2 was solved using finite difference method.

Different effective masses along x, y and z axes in Eq. (2.2) take into account peculiarities of conduction band in bulk Si that possess 3 not degenerated energetic subbands. Position of the absolute minima determines bottom of the conduction band. In the silicon it lies along [100] direction, so there are 6 equivalent energy minima (see Fig. 2.1) [15]. These minima are also called valleys. Isoenergetic surfaces represent ellipsoids that rotates about its major axis and have the form:

$$E(k) = E(k_0)$$

$$E(k) = E(k_0) + \frac{\hbar^2 (k_x - k_{0x})^2}{2m_x} + \frac{\hbar^2 (k_y - k_{0y})^2}{2m_y} + \frac{\hbar^2 (k_z - k_{0z})^2}{2m_z} = \\ = \frac{\hbar^2 (k_x - k_{0x})^2 + \hbar^2 (k_y - k_{0y})^2}{2m_t} + \frac{\hbar^2 (k_z - k_{0z})^2}{2m_l}, \quad (2.3)$$

where $m_x = m_y = m_t = 0.19m_0$ is transversal component of the effective mass; while $m_z = m_l = 0.98m_0$ is longitudinal component, m_0 is the electron effective mass.

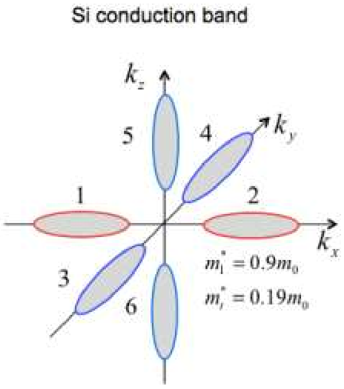

Fig. 2.1. Schematic view of silicon ellipsoids in the conduction band.

Figure is adopted from Ref. [130]

In the case of the semiconductor QD embedded in dielectric media electron barrier energy $V_b^{(e)}\left(\vec{r}^{(e)}\right)$ depends on electron position and can be presented by the stepwise function:

$$V_b^{(e)} = \begin{cases} 0, \text{inside QD} \\ V, \text{outside QD} \end{cases}, \quad (2.4),$$

where V is the height of potential barrier at the interface between QD and surrounding media. Electron's potential self-energy $V_b^{(e)}\left(\vec{r}^{(e)}\right)$ appears due to the interaction between electron and medium polarized by it:

$$V_{SA}\left(\vec{r}^{(e)}\right) = -\frac{1}{2} \lim_{\vec{r} -> \vec{r}^{(e)}} \left(V_{Coulomb}\left(\vec{r} - \vec{r}^{(e)}\right) - \frac{e^2}{4\pi\varepsilon\left(\vec{r}_e\right)\varepsilon_o \mid \vec{r} - \vec{r}^{(e)} \mid} \right), \quad (2.5)$$

where $V_{Coulomb}$ is the Coulomb interaction energy, $\vec{r}_e$ is the electron radius-vector, e is the electron charge, ε_0 is the vacuum permittivity and $\varepsilon(\vec{r})$ is the dielectric constant.

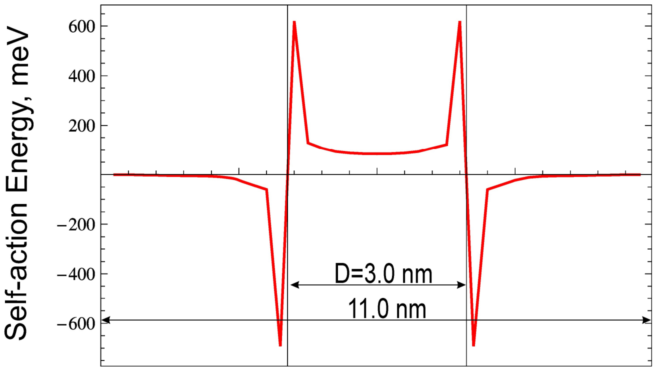

Fig. 2.2. Distribution of the self-action energy values along OX.

Taking into account the charge self-action energy at the interface between a semiconductor and a dielectric is important for a quantitative description of the electronic properties of semiconductor/dielectric systems. Self-interaction leads to a modification of the energy spectra and wave functions of electrons and holes. It can affect the distance between different energy levels and can influence the emission and absorption spectra.

The distribution of the self-action energy along OX axis is shown in the Fig. 2.2 for the spherical Si QD with the diameter $D = 3.0\,\text{nm}$. It is clearly seen that near the QD/shell interface, self-action energy changes its sign due to the different electrical permittivity of the materials (it means than attraction is changed to repulsion and wise versa).

Electron states in individual quantum dots: role of shapes and material parameters

The dependence of the electron energy in cuboid QD on potential barrier height is depicted in Fig. 2.3. The electron levels are presented for QD with dimensions $L_x = L_y = L_z = 3\,\text{nm}$. We consider here two of six energy ellipsoids (see Fig. 2.1) with light transversal effective masses $m_t = 0.19 m_0$ along OX and OY axes and hard longitudinal one $m_l = 0.98 m_0$ along OZ axis. Qualitatively similar results can be obtained for the rest four ellipsoids.

In the Fig. 2.3 five lowest electron levels are shown. Model barrier material possesses the same effective electron mass as in SiO2 $m = m_0$. The barrier energy varies in the range $400\text{ meV} - 4000\text{ meV}$. The levels with quantum numbers $n_x = 2$, $n_y = 1$, $n_z = 1$ and $n_x = 1$, $n_y = 2$, $n_z = 1$ are two-fold degenerated because QD facets have equal dimensions and equal effective electron masses along OX and OY axes. The electron energy increases together with the potential barrier V_b for all energy levels. The curve's slope is smaller for energies higher than $\sim 1000\text{ meV}$. The energy distance between levels also increases with rise of V_b. These effects take place due to reinforcement of spatial confinement for electrons.

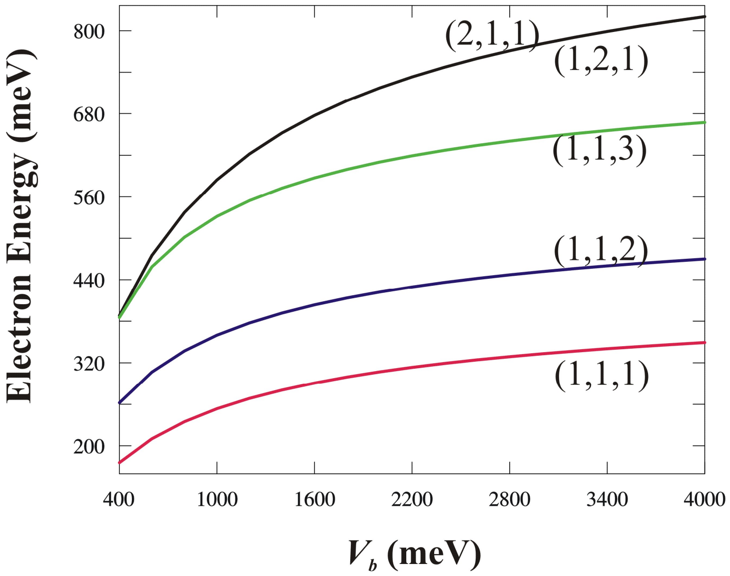

Fig. 2.3. Electron energy states in dependence on the height of the potential barrier in Si cuboid QD.

The shape of the QDs strongly influences the electron energy spectra. In Fig. 2.4 the electron energy and electron wave functions for different QD shapes are depicted. In panel (a) the electron levels are shown for spherical QDs, while electron spectra of double truncated pyramidal QDs (DTPQD) are depicted in panel (b). Electron levels for cuboid, pyramidal, and conical QDs are provided in panel (c). The height of non-spherical QDs is directed along OZ axes, and their cross-section are in the XOY plane. The electron energies in panels (a) and (b) are shown as a function of the spherical QD's diameter, while in panel (c) as a function of QDs' volume. In the case of the double truncated pyramidal QDs (panel (b)) diameter D corresponds to spherical QDs with the same volume. In order to obtain the same volume for non-spherical QDs in Fig. 2.4(c) we fixed the base of pyramidal or conical QDs and varied their height. The considered volume range $4\,\mathrm{nm}^3 - 36\,\mathrm{nm}^3$ approximatively corresponds to the volumes of spherical QDs with diameter from $2\,\mathrm{nm}$ to $4\ \mathrm{nm}$.

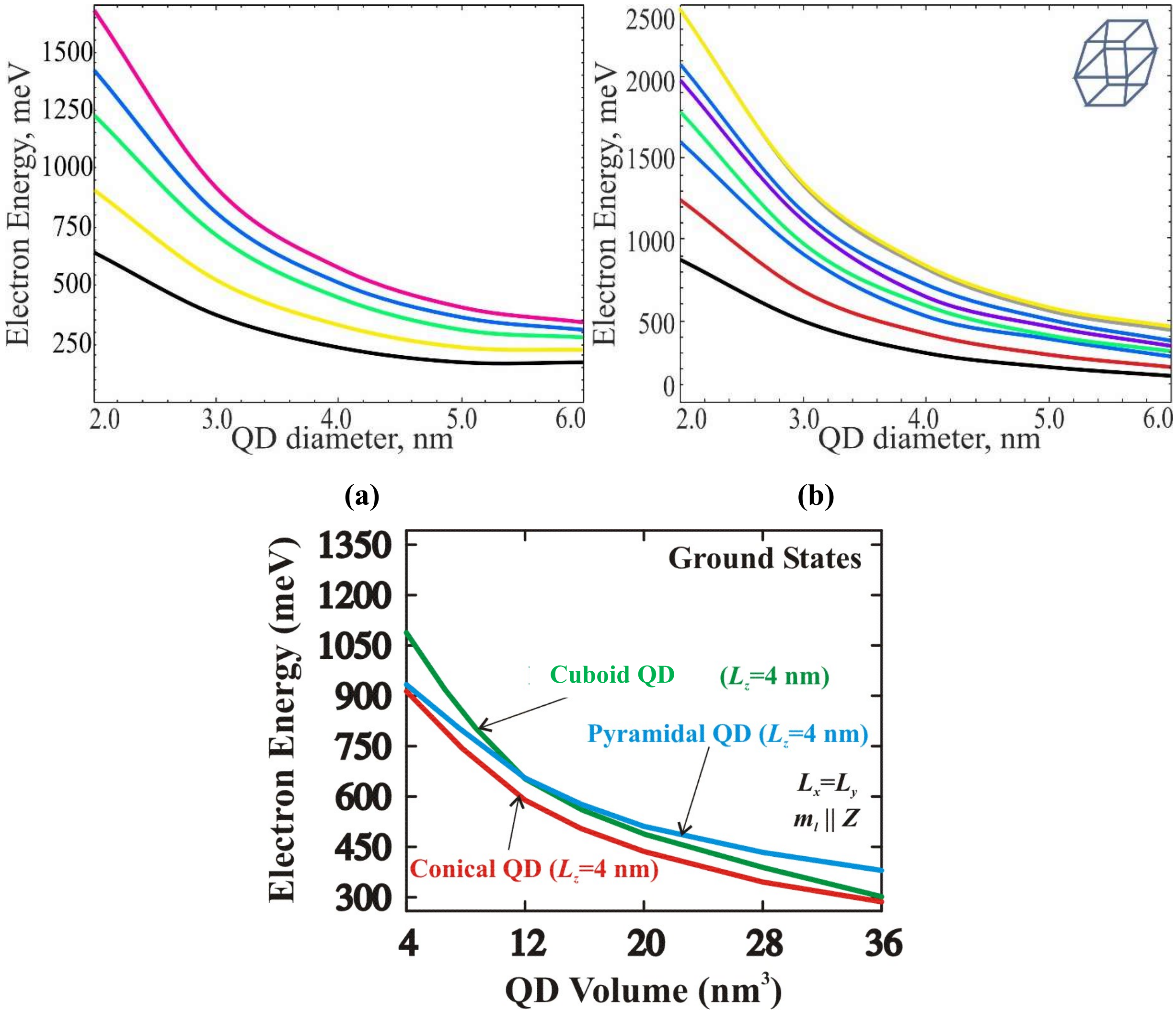

(a) **(b)**

(c)

Fig. 2.4. Electron energy diameter and electron wave function in Si QDs of different shapes.

(a) in spherical QD; **(b)** In DTPQD; **(c)** in cuboid, pyramidal and conical QDs.

The 7 lowest electron levels for spherical and double truncated pyramidal Si QDs are shown in panel (a) and (b), respectively. For cuboid, pyramidal, and conical QD only ground electron level are depicted. In the spherical QD pairs of 4 – 5 and 6 – 7 levels are twofold degenerated due to the spherical symmetry of QD and 2 identical effective mass components $m_t = 0.19m_0$. The energy of electrons and energy distance between their levels decrease while QD's dimensions increase because the confinement of the electrons becomes weaker. The ground level of the spherical QD is lower than in the QD of the other forms. Ground level has approximatively the same values in the conical and DTP QD and is lower than in the cuboid and pyramidal QDs for the presented volume range. The ground state energy of the cuboid QDs is higher than that in the pyramidal QDs for volumes lower than $12\,\text{nm}^3$, while for larger volumes the opposite situation takes place and ground electron energy in cuboid QDs are lower than that in pyramidal QDs. The later can be explained by the images presented in Fig. 2.5 where the electron's wave functions in cuboid (panel (a)), pyramidal (panel (b)), and conical (panel (c)) QDs of the same volumes are provided. The QD dimensions are as follows: the height for all QDs is directed along the OZ and equal to $3\ \text{nm}$, $L_x = L_y = 1\ \text{nm}$ for the cuboid QD and $L_x = L_y = 1.73\ \text{nm}$ for pyramidal QD; the radius of the conical QD is $R = 1\ \text{nm}$. Surfaces containing $75\ \%$ of electron wave function are depicted for all shapes. It is clearly seen that the wave functions reflect the form of the QDs. In conical and pyramidal QDs wave functions are concentrated near their base, while in cuboid QD – in the central region. The area of the base in conical QDs is larger than in pyramidal QD, and larger than the cross-section area of cuboid QD of the same volume. Therefore, electron confinement for ground level wave function is weaker in conical QDs and electron energy is smaller in all dimension range despite the fact that confinement in the Z-direction is stronger in conical QDs. The intersection in energy curves for cuboid and pyramidal QDs is explained by the interplay of two factors: weaker confinement in the XOY-plane in pyramidal QD accompanied by stronger confinement in the Z-direction. The first factor plays a decisive role for small QDs with volumes lower than $12\ \text{nm}^3$, so ground level energy is smaller in pyramidal QD. While in the case of QDs with volumes larger than $12\ \text{nm}^3$, the second factor becomes decisive and electron energy in cuboid QDs becomes smaller than in pyramidal QDs.

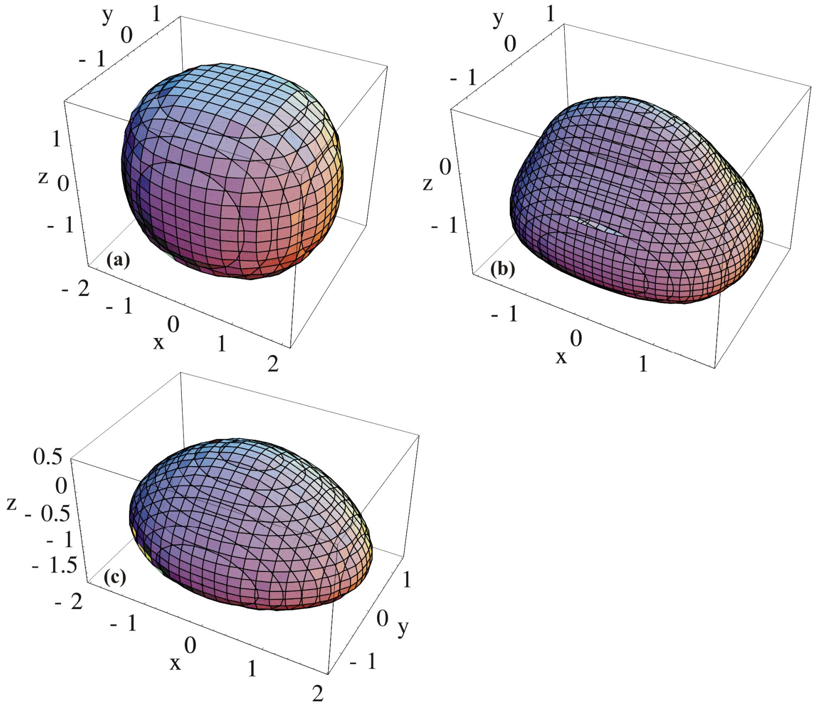

Fig. 2.5. Electron wave function in QDs.

(a) in cuboid QD; **(b)** in pyramidal QD and **(c)** in conical QD.

In the case of the infinite potential barrier electrons/holes do not penetrate in the outer dielectric medium. The wave function is concentrated only inside QD. Normalization condition are given by the following equation:

$$\int\limits_{QD volume} \left|\Psi\left(\vec{r}\right)\right|^2 dV = 1. \tag{2.6}$$

In our calculations we took into account the finiteness of the barrier between Si QD and dielectric media. In this case, the electron and hole wave functions can penetrate throw the potential barrier into dielectric media. So Eq. 2.6 takes the form:

$$\int\limits_{QD volume + barrier volume} \left|\Psi\left(\vec{r}\right)\right|^2 dV = 1. \tag{2.7}$$

The part of the integral inside the barrier medium shows us the probability to find a particle beyond QD:

$$\int\limits_{barrier volume} \left|\Psi_e\left(x, y, z\right)\right|^2 dV. \tag{2.8}$$

In order to obtain correct numerical results, it is important to consider a wide enough dielectric shell allowing free decay of wave function without additional artificial confinement. To satisfy this condition in all cases considered below (including the calculation of electron hole energy spectra) we determined such thickness of the shell so that its growth no longer affects the result of the calculation. So, in our calculations, we added at least a 2 nm shell for QDs.

The dependences of the electron wave function penetration into the barrier medium for the QDs of the different shapes are shown in Fig. 2.6. In panel (a) dependence on the potential barrier for cubic QD with dimensions: $L_x = L_y = L_z = 3\ \text{nm}$ is shown for the first 5 electron energy levels (levels 4 - 5 are degenerated). The penetration into the barrier increases with the electron energy and is significant enough ($8\ \% - 10\ \%$) for all considered levels at $V_b < 1000\ \text{meV}$. In panel (b) the dependence of ground level electron wave function penetration on the QD volume is presented for cuboid, pyramidal, and conical QDs. The volumes of QDs varied between $4\ \text{nm}^3 - 36\ \text{nm}^3$. The penetration is significant for small QD volumes because the energy of the electrons due to the stronger confinement is higher and closer to the barrier energy. In the case of spherical QDs penetration of ground level wave function is smaller than that in complex-shaped QDs due to smaller ground energy of electrons (see Fig. 2.4 (a) and (c)).

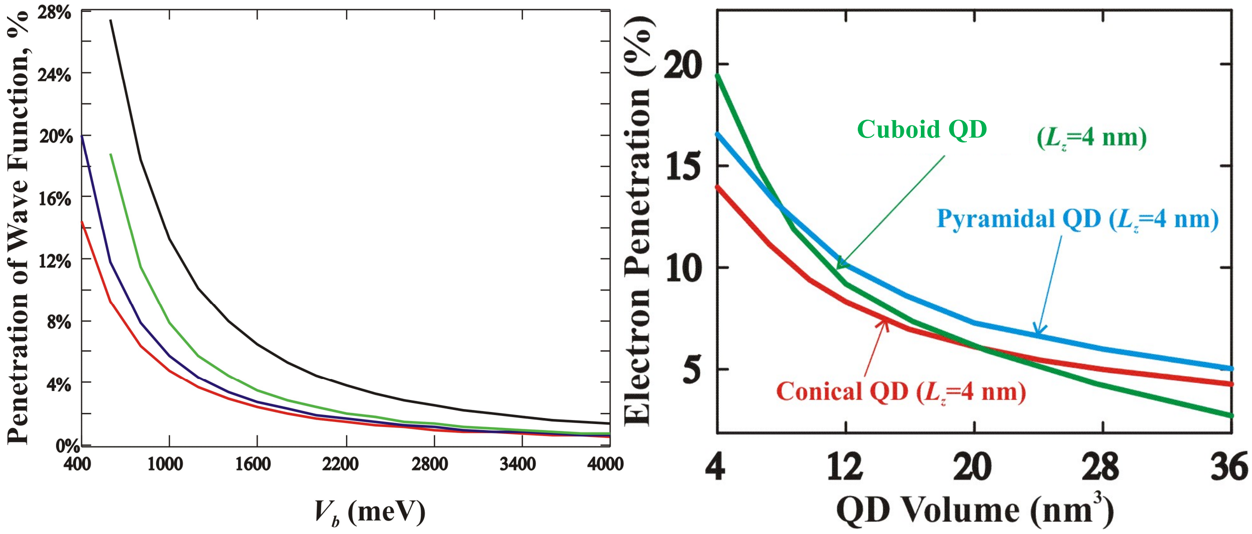

(a) (b)

Fig. 2.6. Electron wave function penetration into the dielectric matrix

(a) for cubic QD in dependence on potential barrier;

(b) for cuboid, pyramidal and conical QDs as a function of their volume

The electron wave function distribution for the three lowest energy levels along axis X in the spherical Si QD is shown in Fig. 2.7. For the ground level $n_e = 1$ wave function possesses a maximum in the centre of the spherical QD. The wave function of the second electron level $n_e = 2$ demonstrates two maxima, placed anti-symmetrically inside the QD, while the wave function for $n_e = 3$ has three maxima: one in the centre of the QD, and two closer to the barrier. All wave functions penetrate into the barrier medium by $\sim 0.3\text{ nm} - 0.5\text{ nm}$ (the inner Si conduction channel is shown by straight dashed lines in Fig. 2.7). The penetration of wave function reinforces with rise of n_e.

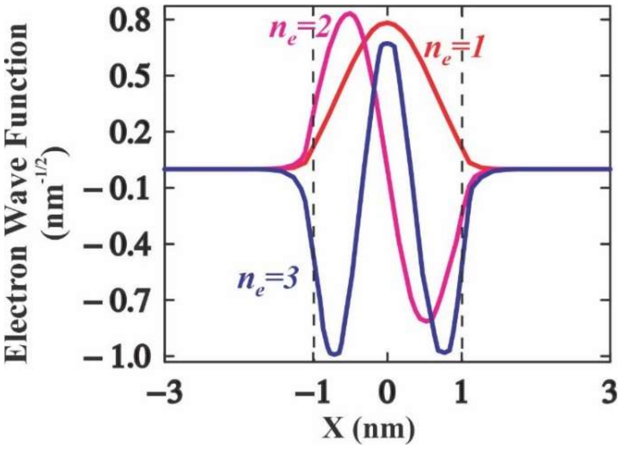

Fig. 2.7. Electron wave function distribution along OX in Si/SiO$_2$ QDs

We also studied electron energy spectra in spherical Si QDs embedded in SiC dielectric shell placed in water or air media (see Fig. 2.8). The effective mass for SiC and barrier energies are taken as follows: $m_x = m \ = 1.47 m_0$, $m_y = m_z = m \ = 4.00 m_0$, $V_b^e(x,y,z) = 2400\,\text{meV}$ at the Si/SiC interfaces, $V_b^e(x,y,z) = 1000\ \text{meV}$ and $V_b^e(x,y,z) = 4600\,\text{meV}$ at the SiC/H_2O and SiC/air interfaces, respectively. The dependence of electron energy on shell thickness is depicted in Fig. 2.8 for different QD's radii. The increase of the shell thickness decreases the electron energies due to deeper penetration of the wave function in SiC shell and softening of the electron spatial confinement. The outer medium influences electron energy for QDs with thin shell only ($d < 1\,nm$) because in this case wave function penetrates into outer medium. Rise of d decreases its penetration into air or water and electron energies become independent of outer medium material.

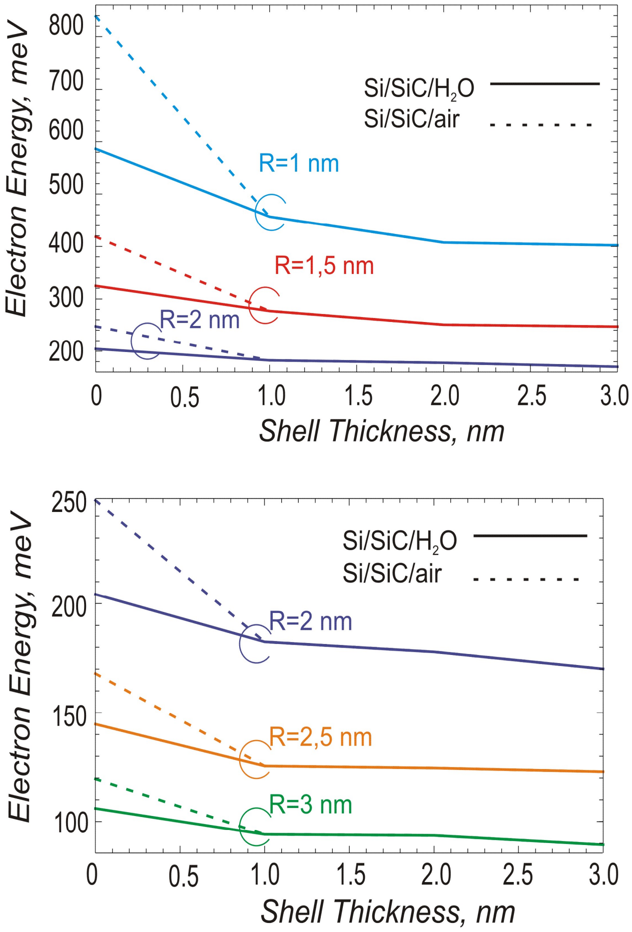

Fig. 2.8. Electron states in Si/SiC QD embedded in water or air media

Electron states in Si/SiO₂ one-dimensional quantum dot superlattices

The electron energy spectra in one-dimensional superlattices of Si QDs in SiO_2 medium were calculated from Eq. 2.2 with applying periodic boundary conditions along superlattice axis OZ: $\vec{\Psi}_e^{n_e}(x,y,z+L) = \vec{\Psi}_e^{n_e}(x,y,z)\,exp\left[ik_e L\right]$, where k_e is the hole wave number,

$\bar{\Psi}_e^{n_e}(x,y,z+L)$ is the electron wave function outside the chosen translation element, $\bar{\Psi}_e^{n_e}(x,y,z)$ is the hole wave function inside the translation element and L is the translation period.

In Fig. 2.9 the electron dispersions in 1D-QDSL with different QD shapes and translation periods are shown. QDs of all shapes possess the same volume. Panel (a) demonstrates ground electron energy dispersion for cuboid QDs with $d = 0.3$ nm and $d = 0.5$ nm. For $d = 0.3$ nm electron wave function strongly penetrates in dielectric medium and electrons from different QDs are strongly coupled. The latter is confirmed by formation of electron miniband with a width of ~ 40 meV. For larger $d = 0.5$ nm penetration of wave function beyond QDs becomes weaker and miniband width decreases to 4 meV. Further growth of d leads to further decoupling of electrons from different QDs and to further decrease of miniband width. Panel (b) and (c) show the electron energy dispersions for QDSLs with different shapes: cuboid, pyramidal, cylindrical, and spherical. Ground energy dispersions are shown in panel (b), while the dispersions of 3 lowest energy levels are presented in panel (c). It is clearly seen from Fig. 2.9(b) that QD shape affects the width of miniband: QDSLs with spherical and pyramidal QDs demonstrate narrow miniband as compared with QDSL from cuboid or cylindrical QDs. In the case of $d = 0.5$ nm (panel (c)), all 3 lowest minibands are narrow enough both for QDSLs from cuboid and pyramidal QDs. Nevertheless, in the case of pyramidal QDs miniband width is smaller than 1 meV, while for QDSL with cuboid QDs, it is ~ 4 meV $-$ 6 meV. It is also important to note that QD shape strongly influences the distance between energy minibands. In the case of QDSL with pyramidal QDs the distance between ground and the second miniband is by a factor of ~ 4 larger than that in QDSL with cuboid QDs.

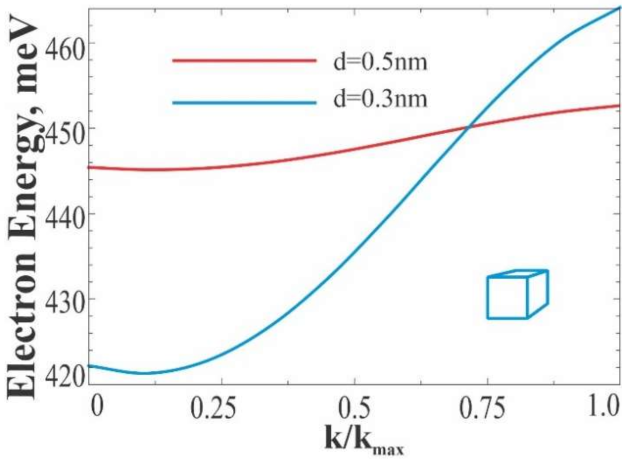

(a)

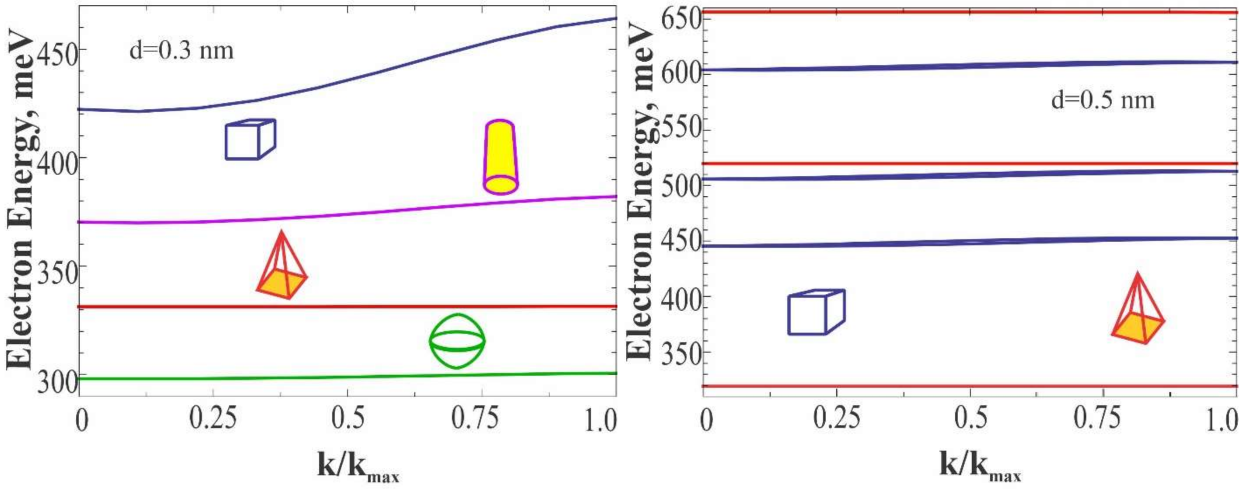

(b) **(c)**

Fig. 2.9. Dispersions of the electron states in Si/SiO$_2$ QDSL

(a) Ground electron energy dispersion for cuboid QDs

(b) Ground electron energy dispersion for QDs with different shapes

(c) 3 lowest electron levels' energy dispersion for cuboid and pyramidal QDs

2.2. Hole states in Si-based quantum dot nanostructures

The valence band in Si is anisotropic: there are three valleys with heavy, light and split-off holes. The valence zone energy maxima is in the centre of the of Brillouin zone $k_0 = 0$. All three valleys have maxima at the centre of the of Brillouin zone $k_0 = 0$ (see Fig. 2.10): one double degenerated energy level (from heavy and light holes bands) and one non-degenerated level from split-off holes band which possesses smaller energy due to spin-orbital interaction. The isoenergetic surfaces have complex form [131]. The schematic view of the holes' valleys and energetic scheme is provided in Fig. 2.10 [130].

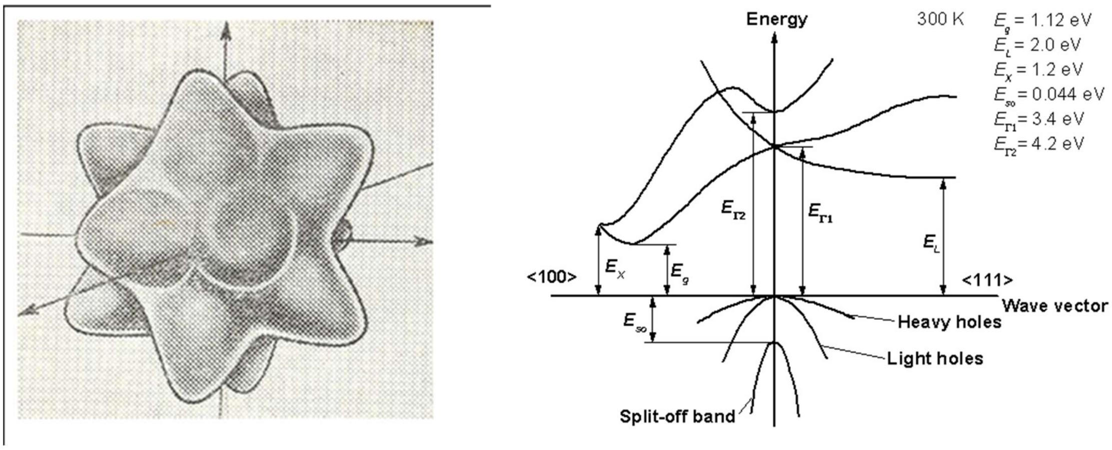

Fig. 2.10. Holes valleys in Si

Hole states have been calculated using Schrodinger equation, taking into account self-action energy:

$$\widehat{H}^{(h)}\Psi_n^{(h)}\left(\vec{r}_h\right)=E_n^{(h)}\Psi_n^{(h)}\left(\vec{r}_h\right),$$

where

$$\widehat{H}^{(h)}=E_k+V_b^{(h)}+V_{SA}^{(h)}. \tag{2.9}$$

In our calculations, we used two different approaches for the holes: one-band Hamiltonian and three-band Bart's Hamiltonian. One-band Hamiltonian has the following form:

$$\hat{H}^{(h)}=-\frac{\hbar^2}{2}\left(\frac{\partial}{\partial x}\frac{1}{m_x\left(x,y,z\right)}\frac{\partial}{\partial x}+\frac{\partial}{\partial y}\frac{1}{m_y\left(x,y,z\right)}\frac{\partial}{\partial y}+\frac{\partial}{\partial z}\frac{1}{m_z\left(x,y,z\right)}\frac{\partial}{\partial z}\right)+V_b^{(h)}\left(x,y,z\right)+V_{SA}^{(h)}, \tag{2.10}$$

$$V_{SA}\left(\vec{r}^{(h)}\right)=-\frac{1}{2}\lim_{\vec{r}->\vec{r}^{(h)}}\left(V_{Coulomb}\left(\vec{r}-\vec{r}^{(h)}\right)-\frac{e^2}{4\pi\varepsilon_{material}\varepsilon_o\,|\,\vec{r}-\vec{r}^{(h)}\,|}\right), \tag{2.11}$$

where, $\Psi_n^{(h)}$ and $E_n^{(h)}$ is the hole wave function and energy for state *n*, respectively; $m_i\left(i=x,y,z\right)$ is the effective mass of the hole, $\hbar$ is the Planck constant, $V_b^e\left(x,y,z\right)$ is the potential barrier for hole, $V_{SA}^{(e)}$ is the self-action energy, $V_{Coulomb}$ is the Coulomb energy of electron-hole interaction, $\vec{r}^{(e)}$ is the radius-vector of the hole, *e* is the electron electric charge, $\varepsilon_0=8.85\times10^{-12}$ F·m^{-1} is the vacuum permittivity, $\varepsilon_{material}=\varepsilon_{Si}$ is the dielectric permittivity of the silicon QD, $\varepsilon_{material}=\varepsilon_{SiO_2}$ is the dielectric permittivity of the SiO$_2$ barrier material. One-band Hamiltonian does not take into account mixing of heavy, light and split-off holes. Thus we carried out calculations for all these three types of holes separately, substituting effective mass of heavy, light or split-off hole in Eq. 2.10.

Hole states in individual quantum dots (one-band hamiltonians): role of shapes and material parameters

The energies of the heavy and light holes' levels are presented in Fig. 2.10 (a) and (b), respectively. The dependences are shown for the cuboid Si QD with dimensions: $L_x = L_y = L_z = 3\,\text{nm}$. The values of the potential barrier energy varied between $400\,meV$ and $4000\,meV$. Five curves are presented in Fig. 2.10 (a) for heavy holes' energy levels. The heavy holes levels with quantum numbers (i) $n_x = 1$, $n_y = 2$, $n_z = 1$, $n_x = 2$, $n_y = 1$, $n_z = 1$, $n_x = 1$, $n_y = 1$, $n_z = 2$ and (ii) $n_x = 1$, $n_y = 2$, $n_z = 2$, $n_x = 2$, $n_y = 1$, $n_z = 2$, $n_x = 2$, $n_y = 2$, $n_z = 1$ are three-fold degenerated, due to the cubic form of the QD and because their effective mass are equal along the axes OX, OY, OZ. The three lowest energy branches of the light holes are depicted in Fig 2.10 (b). The light holes' energy levels with the same quantum numbers as indicated for heavy ones are three-fold degenerated, too. The energy levels of the light holes are higher than the corresponding levels of the heavy holes. The hole's levels energy and energy distance between them increase with the increase of the potential barrier energy both for heavy and light holes because of the reinforcement of spatial confinement of the electron for higher values of the barrier energy V_b.

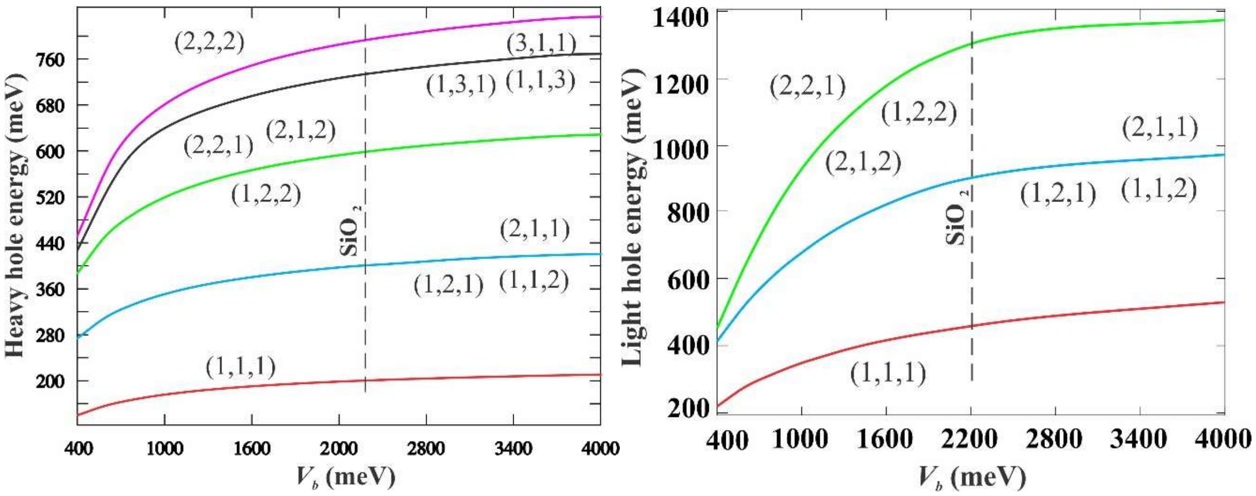

(a) **(b)**

Fig. 2.11. Hole energy levels in cuboid Si QD in dependence on potential barrier

The **(a)** heavy holes' and **(b)** light holes' energy levels in dependence on the potential barrier.

In Fig. 2.12 the penetration dependence on the potential barrier for the hole's wave function is shown. The energy levels are the same as in Fig. 2.11: the first eleven energy levels for heavy holes and the first seven levels for the light ones. The dashed line corresponds to the value of the hole's potential barrier on the Si and SiO_2 interface. The growth of the potential barrier leads to the diminution down to the $0-2\%$ wave function penetration for the heavy hole (see Fig. 2.12 (a)). The penetration of the light holes (see Fig. 2.12 (b)) is decreasing, too, but is still significant for ground level 4% and up to $\sim 20\,\%$ for higher energy levels. The smaller effective mass of the light hole leads to its higher values of the energy levels and percentage of wave function penetration into barrier material.

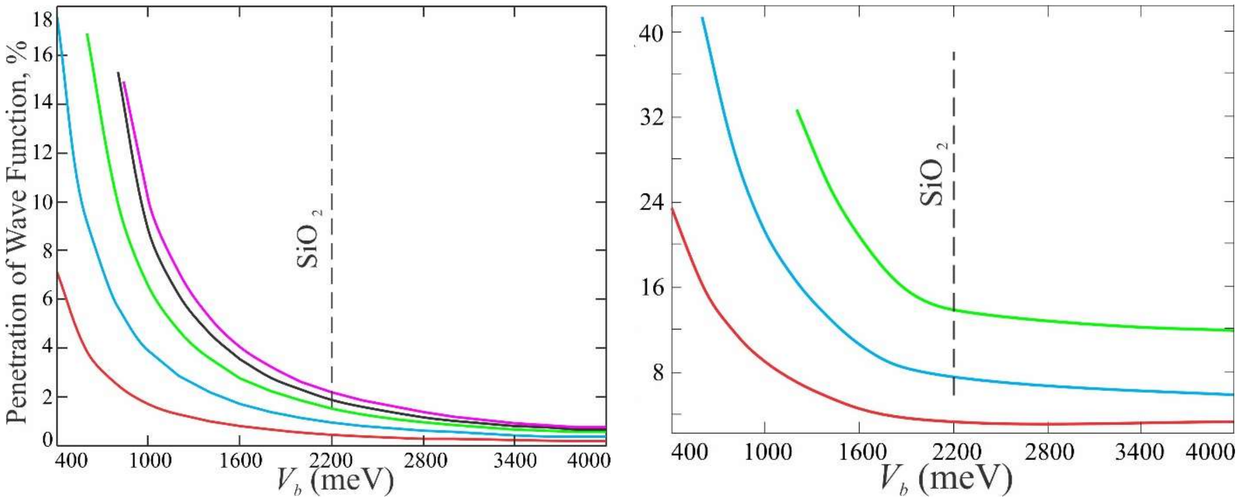

(a) **(b)**

Fig. 2.12. The penetration of the hole's wave function as a dependence on the potential barrier.

(a) penetration of heavy holes wave function; **(b)** penetration of light holes wave function

The ground hole energy levels for the QDs with different shapes: cuboid, conical, and pyramidal are depicted in Fig. 2.13. Notations '*hh*', '*sh*', and '*lh*' correspond to heavy, split-off, and light holes. We fixed the height and changed the cross-section square in the way to obtain an equal QD volume. The heavy, split-off, and light hole ground levels are distributed in the same way for all QD's shapes: the heavy holes have the lowest energy, but light holes have the highest energy. All types of holes possess the same behaviour in dependence on QD volume. The energy of the ground levels in conical QDs is higher than in pyramidal QDs for all calculated QDs' volumes. In cuboid QD the energy of the hole is higher for the small QDs' volume (up to $\sim 10\ \mathrm{nm}^3$) and lower hole energy for larger QDs.

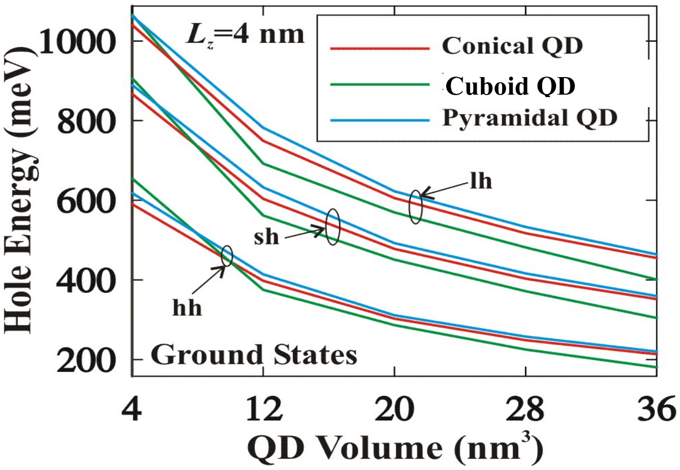

Fig. 2.13. Hole's ground energy states in Si QDs with different shapes: pyramidal, cuboid, and conical, in dependence on the QD's volume.

Penetration of the ground wave function in the barrier medium for heavy and light holes is presented in Fig. 2.14. Since light holes possess higher energy their penetration is stronger for all considered QD's shapes. The crossing of penetration curves for different shapes reflects the crossing of the corresponding energy curves (see Figure 2.13).

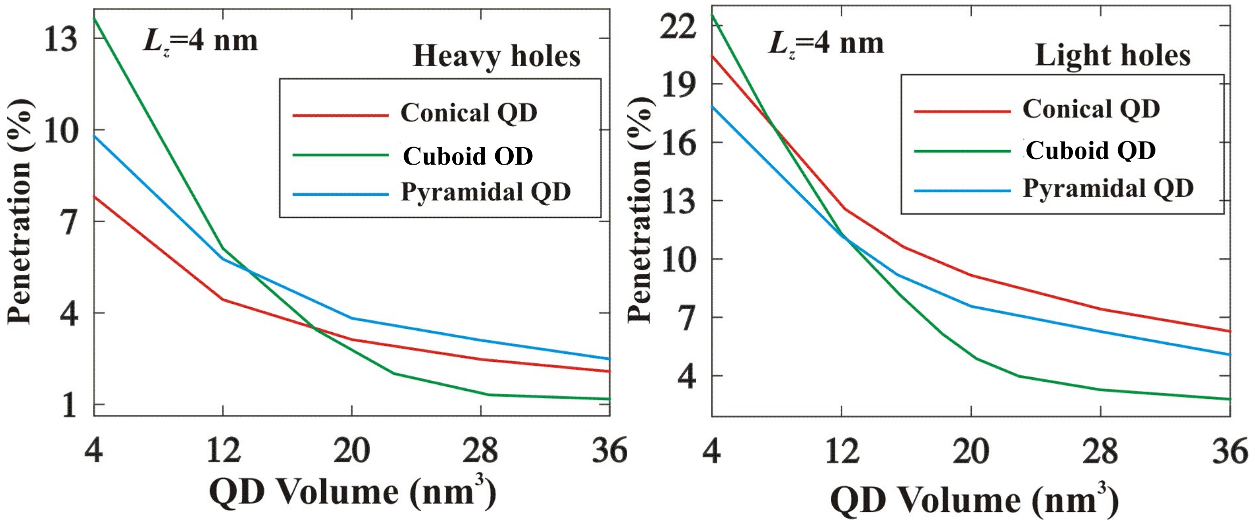

(a) **(b)**

Fig. 2.14. Penetration of the hole wave function in Si QD of the different shapes in dependence on QDs' volume:

(a) of the heavy holes and **(b)** of the light holes.

In the second approach hole's energy spectra calculations were done on the base non-symmetrized three-band Bart's Hamiltonian. This Hamiltonian describes more accurately the valence band of the Si and allows us to take into account hole mixing [34], [132]. The Hamiltonian takes the following form, while the resultant hole wave function represents the superposition of three wave function, corresponding to the number of the holes' types:

$$\hat{H}_h \vec{\Psi}_h^{n_h} = E_h^{n_h} \vec{\Psi}_h^{n_h}, \ \vec{\Psi}_h^{n_h} = \left(\Psi_1^{n_h}, \Psi_2^{n_h}, \Psi_3^{n_h} \right),$$

$$\hat{H}_h = \begin{pmatrix} \hat{k}_x \beta_l \hat{k}_x + \hat{\mathbf{k}}_x^{\perp} \beta_h \hat{\mathbf{k}}_x^{\perp} & 3\left(\hat{k}_x \gamma_3^{+} \hat{k}_y + \hat{k}_y \gamma_3^{-} \hat{k}_x\right) & 3\left(\hat{k}_x \gamma_3^{+} \hat{k}_z + \hat{k}_z \gamma_3^{-} \hat{k}_x\right) \\ 3\left(\hat{k}_x \gamma_3^{-} \hat{k}_y + \hat{k}_y \gamma_3^{+} \hat{k}_x\right) & \hat{k}_y \beta_l \hat{k}_y + \hat{\mathbf{k}}_y^{\perp} \beta_h \hat{\mathbf{k}}_y^{\perp} & 3\left(\hat{k}_y \gamma_3^{+} \hat{k}_z + \hat{k}_y \gamma_3^{-} \hat{k}_x\right) \\ 3\left(\hat{k}_x \gamma_3^{-} \hat{k}_z + \hat{k}_z \gamma_3^{+} \hat{k}_x\right) & 3\left(\hat{k}_y \gamma_3^{-} \hat{k}_z + \hat{k}_y \gamma_3^{+} \hat{k}_x\right) & \hat{k}_z \beta_l \hat{k}_z + \hat{\mathbf{k}}_z^{\perp} \beta_h \hat{\mathbf{k}}_z^{\perp} \end{pmatrix} + V_b^h\left(x, y, z\right) + V_{SA}, \quad (2.12)$$

where $\hat{\mathbf{k}}_i^{\perp} = \hat{\mathbf{k}} - \hat{\mathbf{k}}_i$, $\left(i = x, y, z \right)$, $\hat{\mathbf{k}} = -\mathbf{i}\nabla$ – impulse operator, $\beta_l = \gamma_1 + 4\gamma_2$, $\beta_h = \gamma_1 - 2\gamma_2$, $\gamma_3^{+} = \left(2\gamma_2 + 6\gamma_3 - \gamma_1 - 1\right)/3$, $\gamma_3^{-} = \left(-2\gamma_2 + \gamma_1 + 1\right)/3$ – parameters, which are expressed with Luttinger parameters $\gamma_1, \gamma_2, \gamma_3$. Energy barrier was $5919.6 \ \mathrm{meV}$ for holes.

Hole states in individual quantum dots (3-band Hamiltonian): role of shapes and material parameters

In Fig. 2.15 we compare hole energies calculated using 1-band Hamiltonian for heavy and light holes with those calculated within 3-band Hamiltonian. The first 3 lowest energy curves are depicted for all types of considered holes: heavy, light, and 3-band. The black lines correspond to the 3-band holes, while blue lines are for the holes calculated in the one-band approach: dash-dotted lines are heavy holes energy levels and continuous lines for the light holes spectrum. The ground level of the 1-band Hamiltonian approach, i.e. ground level of heavy holes possesses smaller energy than the ground level of 3-band holes. Higher energy levels of 3-band holes demonstrate similar behaviour with higher levels of heavy or light holes. However, the energy difference reaches $\sim 20 \ \mathrm{meV}$ in dependence on QD's radius.

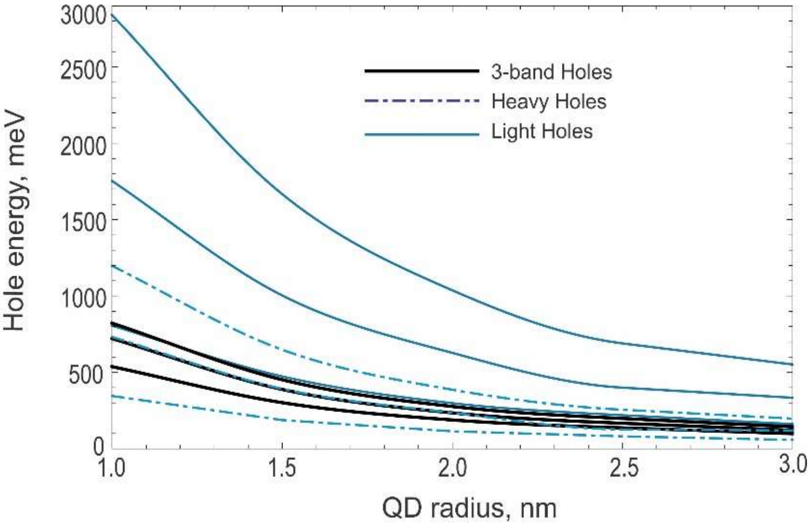

Fig. 2.15. Comparison of the 3 lowest hole energy levels calculated within 3-band and 1-band Hamiltonian approaches

The hole energy spectra in dependence on the QD diameter in spherical and double-truncated pyramidal QDs is presented in Fig. 2.16 (a) and (b). Energy levels in the spherical QDs with quantum numbers (i) $n_x = 1$, $n_y = 2$, $n_z = 1$, $n_x = 2$, $n_y = 1$, $n_z = 1$, $n_x = 1$, $n_y = 1$, $n_z = 2$ and (ii) $n_x = 1$, $n_y = 2$, $n_z = 2$, $n_x = 2$, $n_y = 1$, $n_z = 2$, $n_x = 2$, $n_y = 2$, $n_z = 1$ are three-fold degenerated, due to spherical symmetry of QD. The hole energy decreases with QD's size due to the weakening of spatial confinement for holes. The slope of the curves and energy distance between energy also becomes smaller with the increasing of QD size. In the case of double-truncated pyramidal QDs (see Figure 2.16 (b)) indicated radii correspond to radii of spherical QDs with the same volume. The hole's energy levels in the TDP QDs are not degenerated because there is no geometric symmetry. The energies of the hole's levels in DTP QDs decrease with QDs' volume, but they are higher than those in spherical QDs due to stronger confinement.

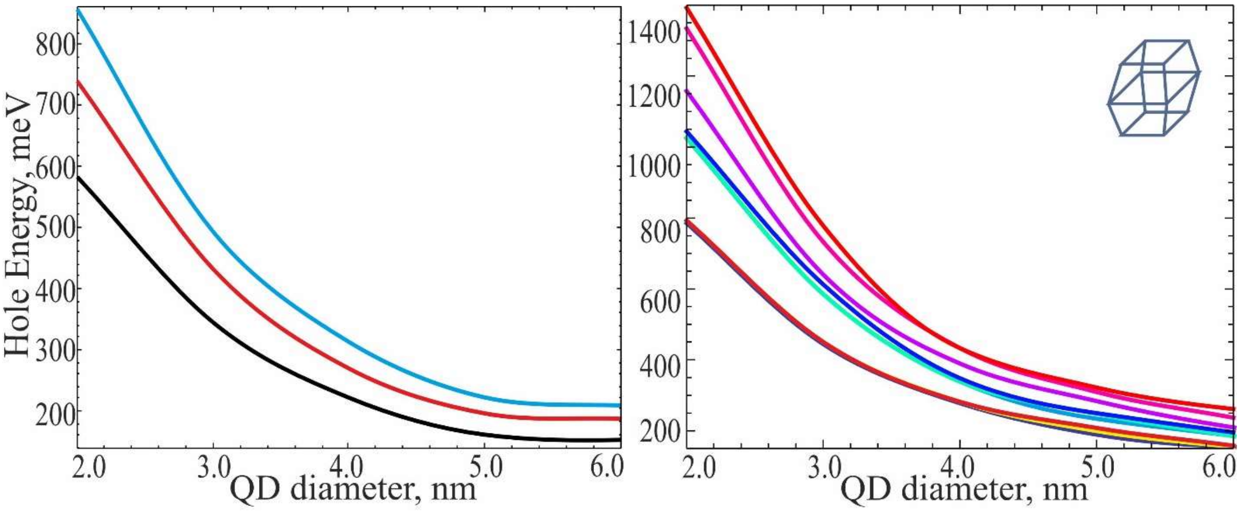

(a) **(b)**

Fig. 2.16. Hole energy spectra in dependence on QD diameter:

(a) in spherical QD and **(b)** in DTPQD

In Fig. 2.17 the hole wave functions distribution along axis X in the spherical Si QD is shown. Fig. 2.17 (a) corresponds to the ground hole energy level, while the panels (b) and (c) correspond to the 3rd and 21st levels, respectively. Different colours (red, blue, green) are used for depicting different wave-function components of a 3-band hole: Ψ_1, Ψ_2, Ψ_3. Straight dashed lines mark interfaces between QD and dielectric media. One can see, that the wave function with higher a quantum number penetrates stronger in the barrier because the probability of finding the hole outside the QD increases together with the energy level.

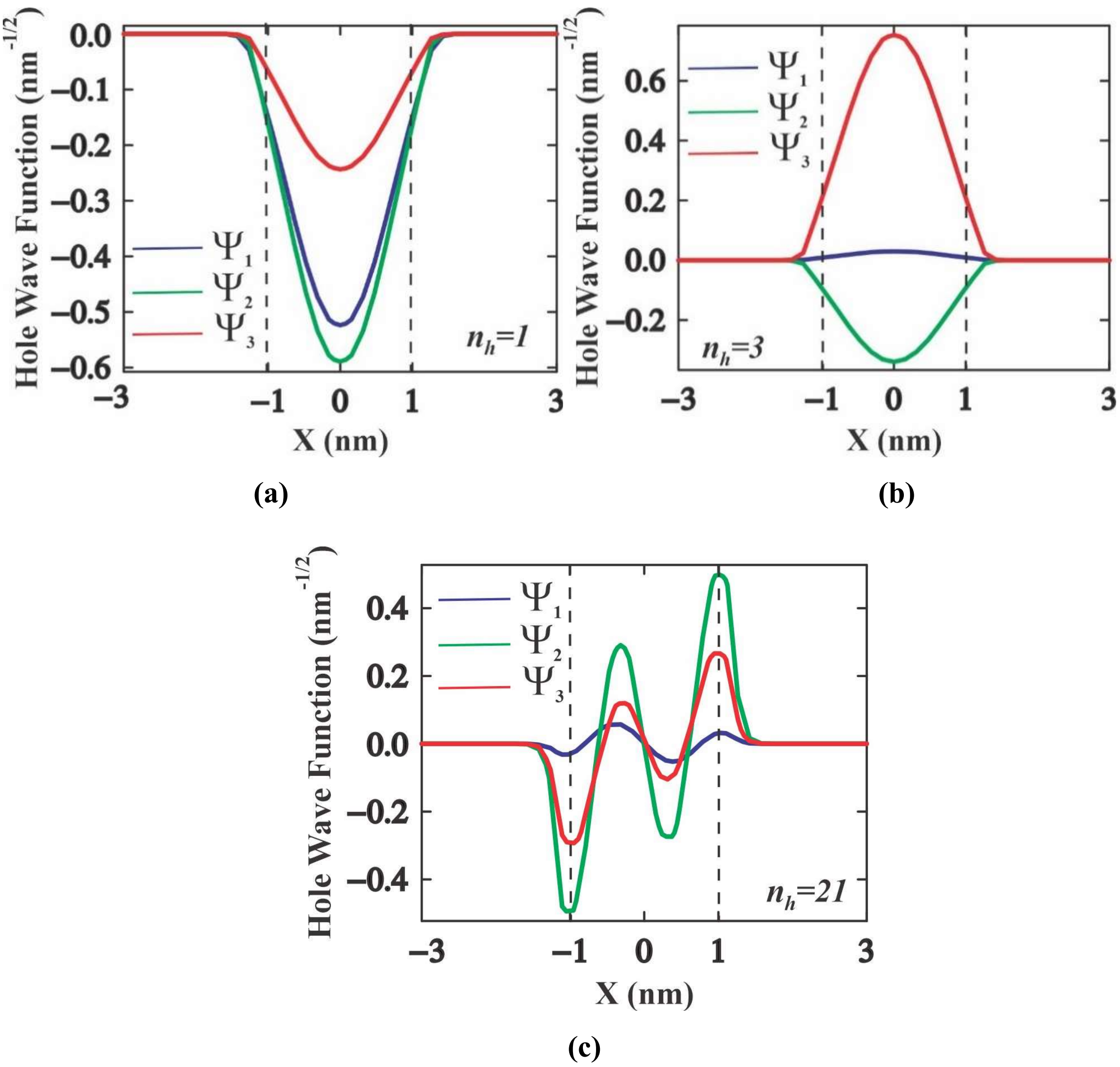

(a) **(b)**

(c)

Fig. 2.17. Distribution of the hole wave function along axe X:

(a) 1st energy level; **(b)** 3rd energy level **(c)** 21th energy level

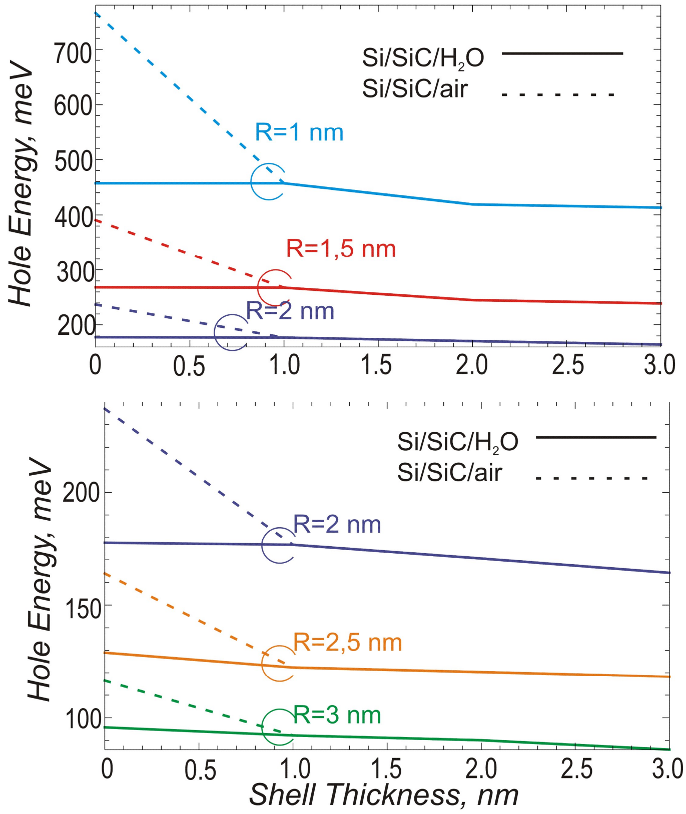

Fig. 2.18. Distribution of the hole wave function along axe X

To emphasize possibility of wide engineering of hole states in Si-based QDs we also studied hole spectra in spherical Si QDs embedded in SiC dielectric shell placed in water or air media (see Fig. 2.18). The holes were calculated using 3-band Bart Hamiltonian with parameters: $\gamma_1(Si)=4.22$, $\gamma_2(Si)=0.53$, $\gamma_3(Si)=1.38$, $\gamma_1(SiC)=1.00$, $\gamma_2(SiC)=0.00$, $\gamma_3(SiC)=0.00$ and $\gamma_1(medium)=0.00$, $\gamma_2(medium)=0.00$, $\gamma_3(medium)=0.00$. The barrier energy values were between Si and SiC $V_b^e(x,y,z)=2400$ meV, and $V_b^e(x,y,z)=1000\,\text{meV}$, and $V_b^e(x,y,z)=4600\,\text{meV}$ at the SiC/H_2O and SiC/air interfaces, respectively [133]. In Fig. 2.18 thickness of the SiC shell varies from 0 to 3 nm. The results are qualitatively similar to the electron case (see Fig. 2.8): the increase of shell thickness leads to a smaller decrease of the hole energy due to a deeper propagation of wave function into the shell (increase of shell thickness shifts higher SiC/air or SiC/water barrier further away from QD). For shell thickness $>1\,\text{nm}$ hole wave function only weakly penetrates into the dielectric medium and hole energies for the case of air medium or water medium coincide with each other.

Hole states in Si/SiO_2 one-dimensional quantum dot nanostructures

The hole dispersions in Si/SiO_2 1D-QDSLs were calculated using Hamiltonian from Eq. 2.10 and with applying periodic boundary conditions along superlattice axis OZ:

$\vec{\Psi}_h^{n_h}\left(x,y,z+L\right)=\vec{\Psi}_h^{n_h}\left(x,y,z\right)exp\left[ik_hL\right]$, where k_h is the hole wave number, $\vec{\Psi}_h^{n_h}\left(x,y,z+L\right)$ is the hole wave function outside the chosen translation element, $\vec{\Psi}_h^{n_h}\left(x,y,z\right)$ is the hole wave function inside the translation element and L is the translation period.

In Fig. 2.19 the hole dispersions of the ground level in the QDSL with different QD shapes are shown. The results are presented for heavy holes. All QDs have the same volume. The distance between QDs is $d=0.3\,nm$. Ground level in QDSL with spherical QDs has the lowest values. The hole ground level in QDSL with cylindrical QDs is very close to the spherical. The ground level of the cuboid and pyramidal QD are higher with approximately $\sim 50\,meV$. Dependencies corresponding to the QDSL with cylindrical and pyramidal QDs have a slight slope, while ones corresponding to the QDSL with cuboid QD and spherical QD are almost flat.

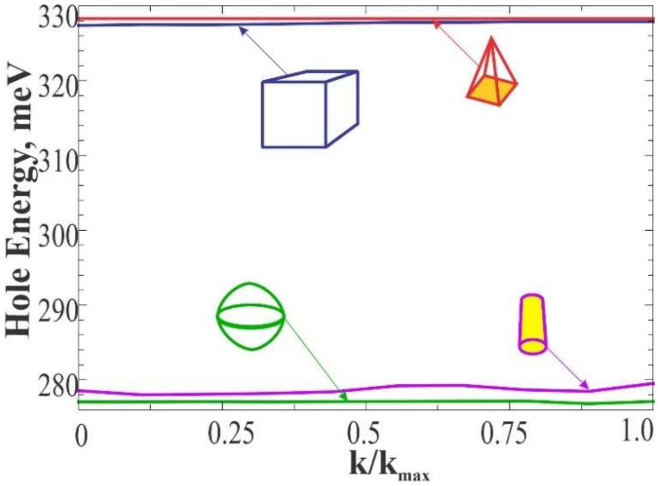

Fig. 2.19. Dispersions of the hole states in Si/SiO2 QDSL

2.3. *Exciton states in Si-based quantum dot nanostructures*

Exciton Hamiltonian can be represented in the following form:

$$H_{exc}(\vec{r}_e,\vec{r}_h)\Phi^n_{exc}(\vec{r}_e,\vec{r}_h)=E^n_{exc}\Phi^n_{exc}(\vec{r}_e,\vec{r}_h)\,, \qquad (2.13)$$

where:

$$H_{exc}\left(\vec{r}_e,\vec{r}_h\right)=H^{SA}_e\left(\vec{r}_e\right)+H^{SA}_h\left(\vec{r}_h\right)+V_{Coulomb}\left(\left|\vec{r}_e-\vec{r}_h\right|\right), \qquad (2.14)$$

where $\Phi^n_{exc}(\vec{r}_e,\vec{r}_h)$ are exciton wave functions, $H_e\left(\vec{r}_e\right)$ and $H_h\left(\vec{r}_h\right)$ are electron and hole Hamiltonians respectively, (see Eq. 2.2 and 2.10), $V_{Coulomb}$ is the Coulomb interaction potential.

We are looking for the exciton wave function in the form of an expansion in series by products of size-quantized electron and hole functions found from Eqs. 2.2 and 2.10 (number of functions in the basis is $n_e^{\max}$, $n_h^{\max}$):

$$\Phi_{exc}^{n}\left(\vec{r}_e,\vec{r}_h\right)=\sum_{i=1}^{n_e^{\max}}\sum_{j=1}^{n_h^{\max}}C_{i,j}^{n}\Psi_{e}^{i}\left(\vec{r}_e\right)\phi_{h}^{i}\left(\vec{r}_h\right) \tag{2.15}$$

where $\Psi_e^i\left(\vec{r}_e\right)$ is the wave function of *i*-th electron level found from Eq. 2.2, $\phi_h^i\left(\vec{r}_h\right)$ is the wave function of j-th hole level found from Eq. 2.10, $n_e^{\max}$ and $n_h^{\max}$ is the number of electron and hole wave functions in the basis, respectively.

Multiplying Eq. 2.13 to wave-functions from Eq. 2.15 one can obtain a system of homogeneous linear equations for coefficients $C_{i,j}^n$:

$$\begin{aligned}&\Phi_{exc}^{n'}\left(\vec{r}_e,\vec{r}_h\right)H_{exc}\left(\vec{r}_e,\vec{r}_h\right)\Phi_{exc}^{n}\left(\vec{r}_e,\vec{r}_h\right)=\sum_{i_1}^{n_e^{\max}}\sum_{j_1}^{n_h^{\max}}C_{i_1,j_1}^{n'}\Psi_e^{i_1}\left(\vec{r}_e\right)\phi_h^{j_1}\left(\vec{r}_h\right)\\&\left\{H_e\left(\vec{r}_e\right)+H_h\left(\vec{r}_h\right)+V_{Coulomb}\left(\left|\vec{r}_e-\vec{r}_h\right|\right)\right\}\sum_{i}^{n_e^{\max}}\sum_{j}^{n_h^{\max}}C_{i,j}^{n}\Psi_e^{i}\left(\vec{r}_e\right)\phi_h^{j}\left(\vec{r}_h\right)=\\&=\sum_{i_1}^{n_e^{\max}}\sum_{j_1}^{n_h^{\max}}\sum_{i}^{n_e^{\max}}\sum_{j}^{n_h^{\max}}\Big(C_{i_1,j_1}^{n'}C_{i,j}^{n}\left\{E_e^i\delta_i^{i_1}\delta_j^{j_1}+E_h^j\delta_i^{i_1}\delta_j^{j_1}+\right.\\&\left.+\int\Psi_e^{i_1}\left(\vec{r}_e\right)\phi_h^{j_1}\left(\vec{r}_h\right)V_{Coulomb}\left(\left|\vec{r}_e-\vec{r}_h\right|\right)\Psi_e^{i}\left(\vec{r}_e\right)\phi_h^{j}\left(\vec{r}_h\right)d\vec{r}_e d\vec{r}_h\right\}\Big).\end{aligned} \tag{2.16}$$

Let's denote integral as:

$$A_{i,j}^{i_1,j_1}=\int\Psi_e^{i_1}\left(\vec{r}_e\right)\phi_h^{j_1}\left(\vec{r}_h\right)V_{Coulomb}\left(\left|\vec{r}_e-\vec{r}_h\right|\right)\Psi_e^{i}\left(\vec{r}_e\right)\phi_h^{j}\left(\vec{r}_h\right)d\vec{r}_e d\vec{r}_h\,. \tag{2.17}$$

By substituting Eq. (2.17) into Eq. (2.16), one can re-write a system of linear equation in the following form:

$$\sum_{i_1}^{n_e^{\max}}\sum_{j_1}^{n_h^{\max}}\sum_{i}^{n_e^{\max}}\sum_{j}^{n_h^{\max}}\left(C_{i_1,j_1}^{n'}C_{i,j}^{n}\left\{E_e^i\delta_i^{i_1}\delta_j^{j_1}+E_h^j\delta_i^{i_1}\delta_j^{j_1}+A_{i,j}^{i_1,j_1}\right\}\right)=\sum_{i_1}^{n_e^{\max}}\sum_{j_1}^{n_h^{\max}}\sum_{i}^{n_e^{\max}}\sum_{j}^{n_h^{\max}}\left(C_{i_1,j_1}^{n'}C_{i,j}^{n}\delta_i^{i_1}\delta_j^{j_1}\delta_n^{n'}E_{exn}^{n}\right). \tag{2.18}$$

Let's expand sums, taking into account Kronecker delta symbols:

$$\sum_{i_1}^{n_e^{\max}}\sum_{j_1}^{n_h^{\max}}\sum_{i}^{n_e^{\max}}\sum_{j}^{n_h^{\max}}\left(C_{i_1,j_1}^{n'}C_{i,j}^{n}\left\{E_e^i\delta_i^{i_1}\delta_j^{j_1}+E_h^j\delta_i^{i_1}\delta_j^{j_1}+A_{i,j}^{i_1,j_1}\right\}\right)=\sum_{i_1}^{n_e^{\max}}\sum_{j_1}^{n_h^{\max}}\sum_{i}^{n_e^{\max}}\sum_{j}^{n_h^{\max}}\left(C_{i_1,j_1}^{n'}C_{i,j}^{n}\delta_i^{i_1}\delta_j^{j_1}E_{exn}^{n}\right). \tag{2.19}$$

If we switch to the excitonic state index n $\left(n=1,2,...,N_{\max},N_{\max}=n_e^{\max}n_h^{\max}\right)$, which combines pair of *i* and *j* indices, we obtain:

$$\sum_{n_1=1}^{N_{\max}}\sum_{n=1}^{N_{\max}}\left(C_{n_1}C_n\left\{E_e^i\delta_n^{n_1}+E_h^j\delta_n^{n_1}+A_n^{n_1}\right\}\right)=E_{exn}^{n}\sum_{n_1=1}^{N_{\max}}\sum_{n=1}^{N_{\max}}\left(C_{n_1}C_n\delta_n^{n_1}\right), \tag{2.20}$$

where each n corresponds to the pair (i,j), and n_1 corresponds to the pair (i_1,j_1), so $A_n^{n_1} = A_{i,j}^{i_1,j_1}$, $\delta_n^{n_1} = \delta_i^{i_1}\delta_j^{j_1}$.

Let's bring Eq. 2.20 into the following form:

$$\sum_{n_1=1}^{N_{\max}} C_{n_1} \sum_{n=1}^{N_{\max}} C_n \left\{ E_e^i \delta_n^{n_1} + E_h^j \delta_n^{n_1} + A_n^{n_1} \right\} = \sum_{n_1=1}^{N_{\max}} C_{n_1} \sum_{n=1}^{N_{\max}} E_{exn}^n C_n \delta_n^{n_1} . \tag{2.21}$$

The Eq. 2.21 implies that for any fixed value of $n = 1,\ldots,N_{\max}$ the following equation must hold:

$$\sum_{n_1=1}^{N_{\max}} \left\{ E_e^i \delta_n^{n_1} + E_h^j \delta_n^{n_1} + A_n^{n_1} \right\} C_{n_1} = E_{exn}^n C_n . \tag{2.22}$$

Exactly, we obtained standard problem of linear algebra: $M\vec{x} = E\vec{x}$, where E represents the exciton energy, and $\vec{x}$ is a vector of unknown coefficients for the expansion of $C_n : \left(C_1, C_2, \ldots, C_{N_{\max}}\right)$. Matrix elements will take the form:

$$M_{n,n_1} = E_e^i \delta_n^{n_1} + E_h^j \delta_n^{n_1} + A_n^{n_1} .$$

The indices i and j can be uniquely determined based on index n, while $A_n^{n_1}$ is the integral of Coulomb energy and wave functions:

$$A_n^{n_1} = A_{i,j}^{i_1,j_1} = \int \Psi_e^{i_1}(\vec{r}_e)\phi_h^{j_1}(\vec{r}_h) V_{Coulomb}\left(\left|\vec{r}_e - \vec{r}_h\right|\right) \Psi_e^{i}(\vec{r}_e)\phi_h^{j}(\vec{r}_h)\, d\vec{r}_e d\vec{r}_h . \tag{2.23}$$

So, first we calculate:

$$R_i^{i_1}(\vec{r}_h) = \int \Psi_e^{i_1}(\vec{r}_e) V_{Coulomb}\left(\left|\vec{r}_e - \vec{r}_h\right|\right) \Psi_e^{i}(\vec{r}_e)\, d\vec{r}_e .$$

Thereafter matrix elements $A_n^{n_1}$ were calculated according:

$$A_{i,j}^{i_1,j_1} = \int \phi_h^{j_1}(\vec{r}_h) R_i^{i_1}(\vec{r}_h) \phi_h^{j}(\vec{r}_h)\, d\vec{r}_h .$$

Exciton energy can be calculated on the base of the ground size-quantized states without mixing of higher energy levels. In this case problem reduces to the integration:

$$E_{bind}^{ml} = \iiint_V \iiint_V \Psi_{el}^{m} \Psi_{el}^{m*} \Psi_h^{l} \Psi_h^{l*} E_{coul}\left(x_{el}, y_{el}, z_{el}, x_h, y_h, z_h\right) dx_{el} dy_{el} dz_{el} dx_h dy_h dz_h , \tag{2.24}$$

where E_{bind}^{ml} — exciton binding energy in silicon QD, E_{coul} — electrostatic Coulomb interaction energy, x_{el}, y_{el}, z_{el} and x_h, y_h, z_h are electron's and hole's coordinates, respectively. We have integrated Eq. 2.24 on all computational space.

In order to obtain Coulomb interaction, we solved numerically Maxwell equation:

$$div\left(\varepsilon \operatorname{grad} \varphi\right) = -4\pi\rho , \tag{2.24b}$$

where ε is the dielectric permittivity, φ is the field potential, ρ is the electric charge density. In the case of the QD embedded into dielectric matrix permittivity is not constant, so the Coulomb interaction was calculated taking into account the difference of the dielectric permittivity in different materials.

Total exciton energy has the following form:

$$E_{exc}^{n} = E_{h}^{m} + E_{el}^{l} + E_{bind}^{ml} + E_{gap}. \tag{2.25}$$

In order to demonstrate how different dielectric permittivities influence electrostatic potential in Fig. 2.20 and Fig. 2.21 we show the electrostatic potential distribution in the spherical Si QD along the OX axis. In Fig. 2.20, the distribution for charge placed in the centre, near the centre, and places at the distance $d = 0.75\,\mathrm{nm}$ from the QD surface are depicted in panel (a), panel (b), and panel (c), respectively. Solid lines represent Coulomb potential calculated using different permittivities, while dotted and dashed lines represent Coulomb potential calculated with Si and SiO_2 dielectric permittivities, respectively. In panels (a) and (b) solid lines tend to the dotted lines inside the QDs and to the dashed lines in the dielectric medium. However, in the case of the charge placed outside the QD (see panel (c)), dependency is very close to the SiO_2 potential in all coordinates range.

In Fig. 2.21 the dependence of the Coulomb potential on QD's sizes and permittivities is illustrated. The charge was placed in the centre of the QD for all dependencies presented in Fig. 2.21. Panel (a) demonstrates distribution of the potential for different dielectric permittivity inside the QD. Calculations were carried out for $\varepsilon_{medium} = 12.0$, and two values of the $\varepsilon_{QDot} = 8.5$ (dotted line) and $\varepsilon_{QDot} = 12.0$ (dashed line). Higher permittivity of the QD leads to the higher values of the potential. Panel (b) demonstrates distribution of the potential for different QD dimensions: thick solid line corresponds to the QD with diameter $D = 1\,\mathrm{nm}$, while thin solid line is for $D = 1.5\,\mathrm{nm}$. The potential is lower inside the QD with the smaller dimensions. In the dielectric medium potential values for both dimensions are very close.

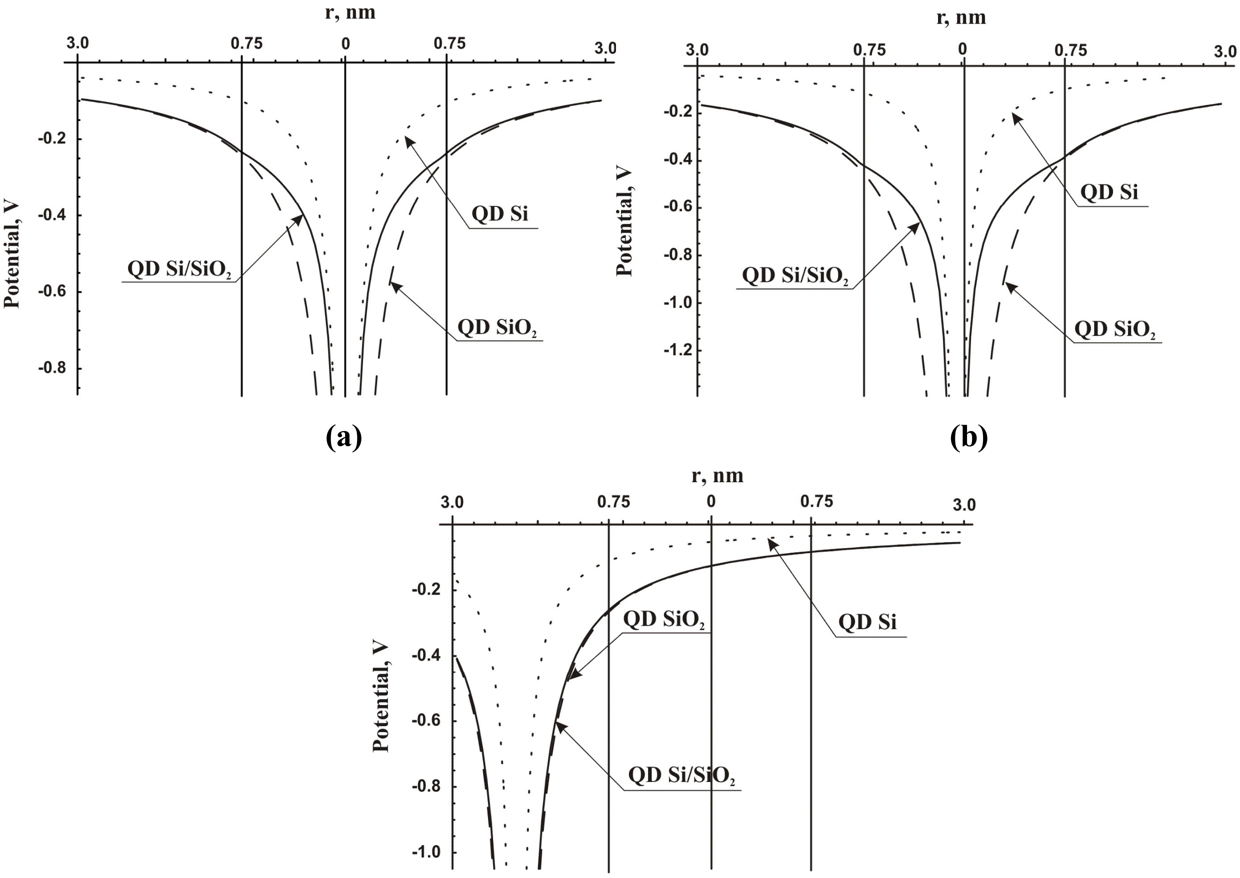

(a) **(b)**

(c)

Fig. 2.20. Distribution of the Coulomb potential in Si/SiO2 QDSL for different charge location

(a) charged is placed in the centre of the QD**;** **(b)** charged is placed near the centre of the QD

(a) charged is placed outside of the QD

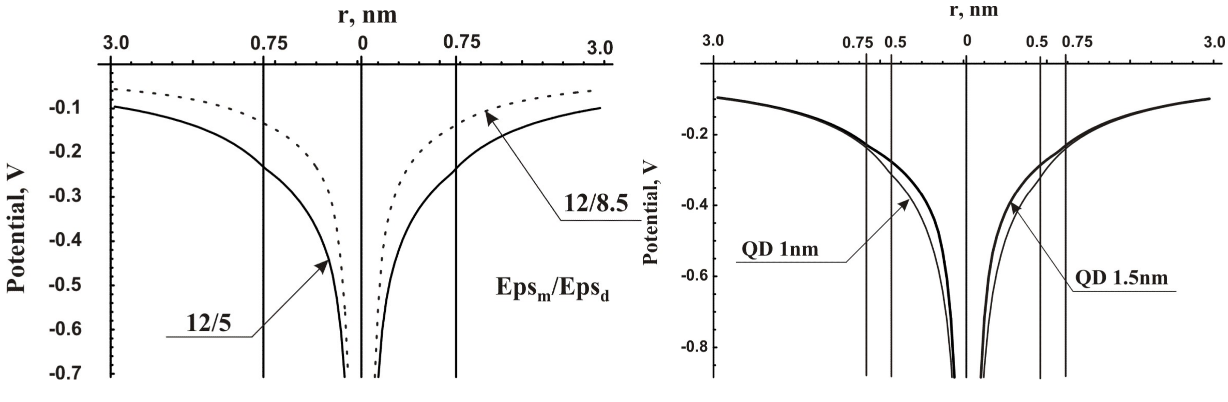

(a) **(b)**

Fig. 2.21. Distribution of the Coulomb potential in Si/SiO2 QDSL

(a) for different QD dielectrical permittivity; **(b)** for different QD dielectrical radius

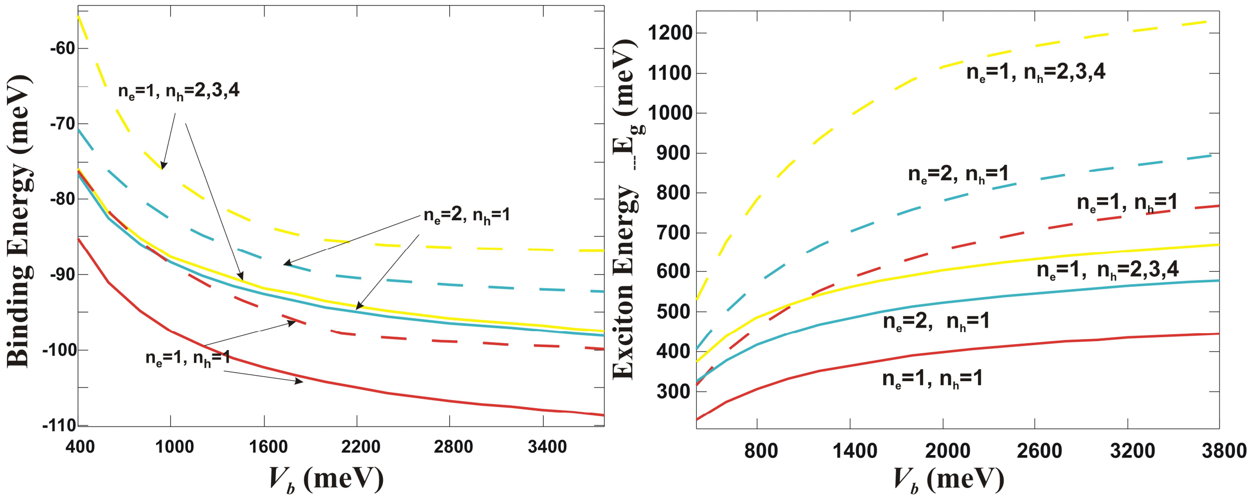

(a) **(b)**

Fig. 2.22. Exciton energy dependence on the potential barrier in Si QDs.

(a) binding energy and **(b)** full exciton energy in dependence on QD volume.

In Fig. 2.22 the dependences of binding energy (a) and total exciton energy (b) on potential barrier height are shown. The Si QD possesses the form of a cuboid with dimensions: $L_x = L_y = L_z = 3\text{ nm}$. The values of the potential barrier energy vary between $400\,\text{meV}$ and 3800 meV. Continues lines represent exciton states calculated using heavy holes' spectrum, and dashed lines are calculated using energies of the light ones; n_e and n_h are quantum numbers for electron and hole, respectively. Holes energies were calculated using Eq. 2.10, while exciton binding energy was calculated from Eq. 2.24. The corresponding levels' quantum numbers are indicated in the graph. Exciton levels 3-5 with quantum numbers $n_e = 1$ and $n_h = 2,3,4$ (corresponds to $n_{hx} = 2$, $n_{hy} = 1$, $n_{hz} = 1; n_{hx} = 1$, $n_{hy} = 2$, $n_{hz} = 1$; $n_{hx} = 1$, $n_{hy} = 1$, $n_{hz} = 2$) are three fold degenerated, due to the symmetry of hole's effective mass. Light holes demonstrate higher exciton energy than the heavy ones for all levels. Excitons formed by electrons and holes with higher energy have smaller binding energy due to larger exciton radius. In spite of this fact, exciton energy continuously increases with the potential barrier because increase of charge carrier energy is more significant than drop of binding energy.

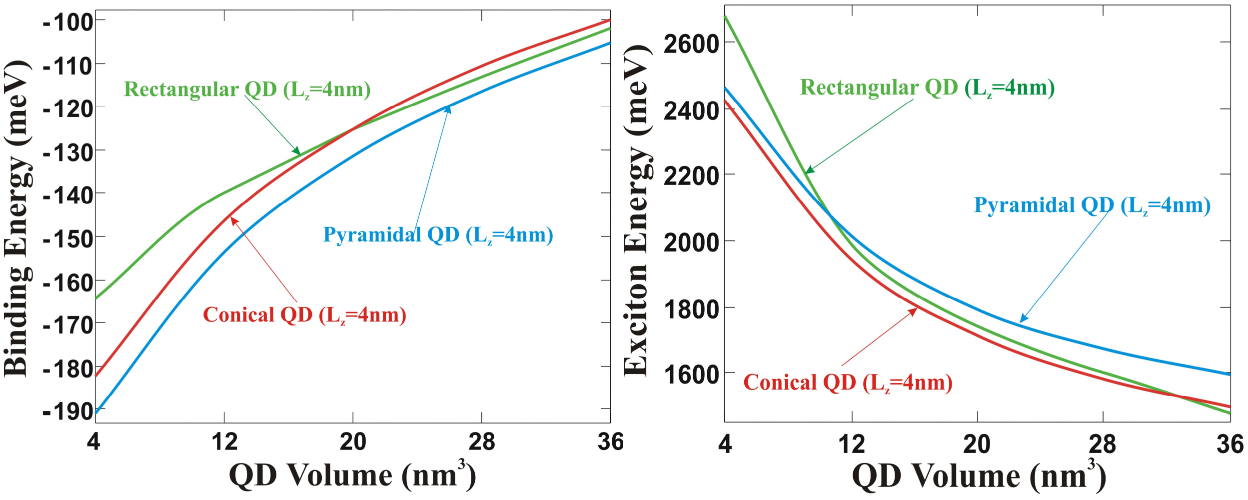

(a) **(b)**

Fig. 2.23. Influence of the QD shape on exciton energy

(a) binding energy and **(b)** full exciton energy in dependence on QD volume.

The influence of QD's shape on the binding energy of exciton (panel (a)) and on total exciton energy (panel (b)) is illustrated in Fig. 2.23 for Si/SiO$_2$ QDs. Energy curves are depicted as a function of QD volume. In both panels energies for the pyramidal QDs are represented with blue curves, for the conical QDs with red curves, and for the cuboid QDs with green ones. The binding energy increases together with QD volume. In the pyramidal QDs, its value is smaller than that in conical and cuboid QDs for all considered QD volumes presented in the figure. For the cuboid and conical QDs binding energy curves are crossed: $E^{ground}_{bind,conical\,QD} < E^{ground}_{bind,cuboid\,QD}$ for volumes $V <$ 20 nm^3 and $E^{ground}_{bind,conical\,QD} > E^{ground}_{bind,cuboid\,QD}$ for $V >$ 20 nm^3.

Total exciton energy (see Fig. 2.23 (b)) decreases with increase QD size due to decrease of electron and hole energy with the weakening of the spatial confinement. All exciton energy curves are crossed: for volumes in the range of $4\,\text{nm}^3 - 36\,\text{nm}^3$ the conical QDs demonstrate the lowest energy values, while for $V > 36\,\text{nm}^3$ energy in cuboid QDs becomes smaller than that in conical or pyramidal QDs. The behaviour of energy curves is explained by behaviour of both the electron and hole energy curves (see Figs. 2.4. and 2.13) as well as by dependence of binding energies on volume V (see Fig. 2.23 (a)).

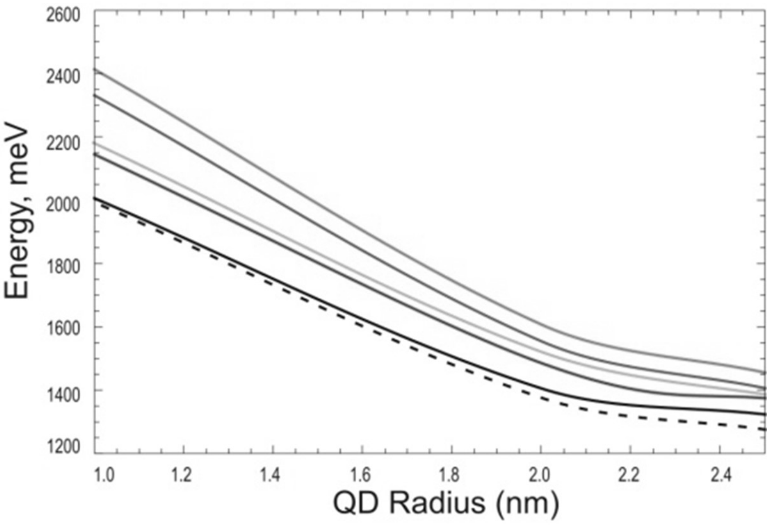

Fig. 2.24. Exciton energy with and without mixing of levels in spherical Si QDs

In Fig. 2.24 dependence of exciton energy on QD's size is presented. Continuous lines – exciton energy calculated taking into account electron and hole higher energy levels. Dashed line – exciton energy for heavy holes without "mixing" of higher states. The calculations for exciton energy were carried out taking into account the non-symmetrized three-band Bart's Hamiltonian for holes (Eq. 2.12) and *mixing* of higher levels for electrons and holes (Eq. 2.22). The continuous lines represent exciton energy levels calculated taking into account *mixing* levels. The dashed line indicates the energy of the first exciton level, calculated without taking into account *mixing*. Exciton ground states energy calculated without *mixing* is lower than energy calculated taking into account high energy levels. The difference between ground levels calculated within different approaches increases simultaneously with the dimensions of QD because the energy distance between electron and hole levels becomes smaller and the influence on ground exciton levels increases. Total exciton energy is lower for larger QDs because charge carrier energies are lower and electron-hole interaction in the exciton is less too, due to a larger exciton radius.

In Fig. 2.25 the binding energy (panel (a)) and the exciton states (panel (b)) in the spherical QD in dependence on QD diameter are depicted. The dependencies are shown for the 1-8 lowest exciton energies. Levels are degenerated due to the symmetry of the spherical shape. The binding energy decreases by module because effective exciton radius becomes more and Coulomb interaction between electron and hole diminishes. Exciton energy levels behaviour is determined by the behaviour of the charge carriers' states, which energy decreases with the increase of the QDs volume.

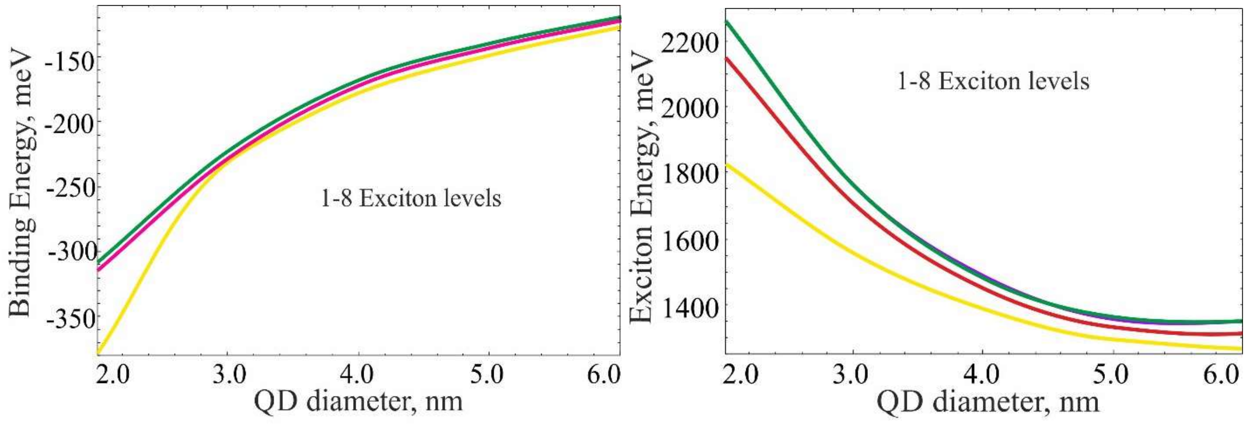

(a) **(b)**

Fig. 2.25. Exciton states in spherical Si QDs

(a) binding energy and **(b)** full exciton energy in dependence on QD diameter.

In Fig. 2.26 binding energy (panel (a)) and the exciton states (panel (b)) in the double truncated pyramidal QD in dependence on QD diameter are depicted. The indicated diameter corresponds to the diameter with spherical QD with the same volume. The dependencies are shown for the 1-4 lowest exciton energies. The binding energy increases together with the diameter of the QD, while the exciton energy decreases. The behaviour of the exciton energy dependency is determined by the behaviour of the charge carriers' states, just like in the case of the spherical QDs. The binding energy in DTCPQD is less than in spherical QD by module. Exciton energy in DTCPQD is higher because the electron and hole space confinement is stronger due to the shape of QD.

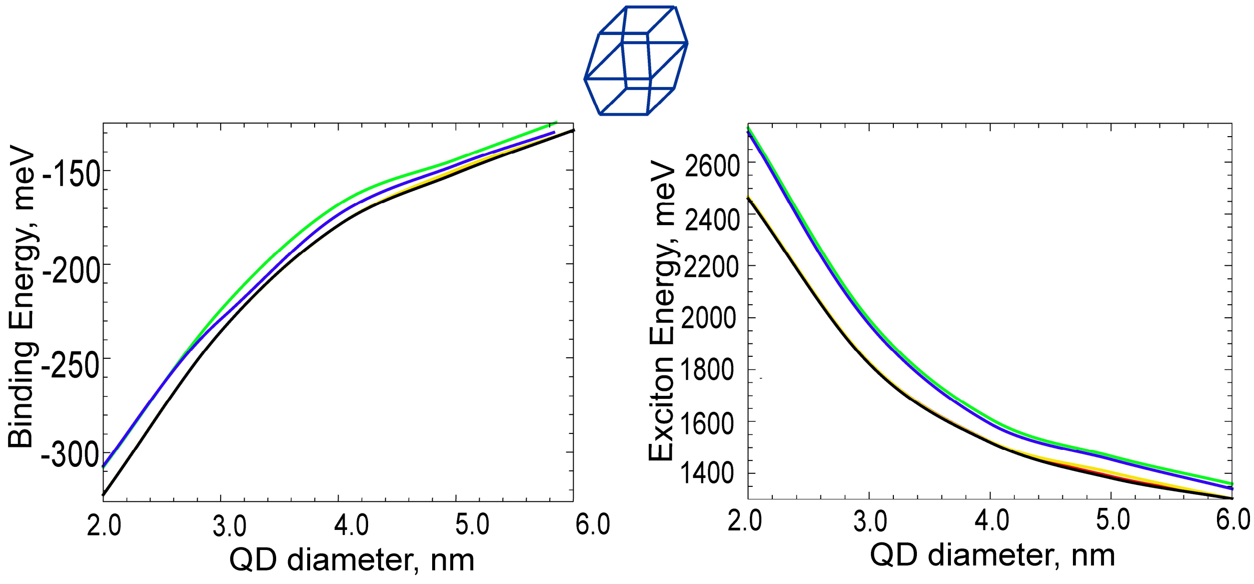

(a) **(b)**

Fig. 2.26. Exciton states in doubled truncated pyramidal Si QDs

(a) binding energy and **(b)** full exciton energy in dependence on QD volume.

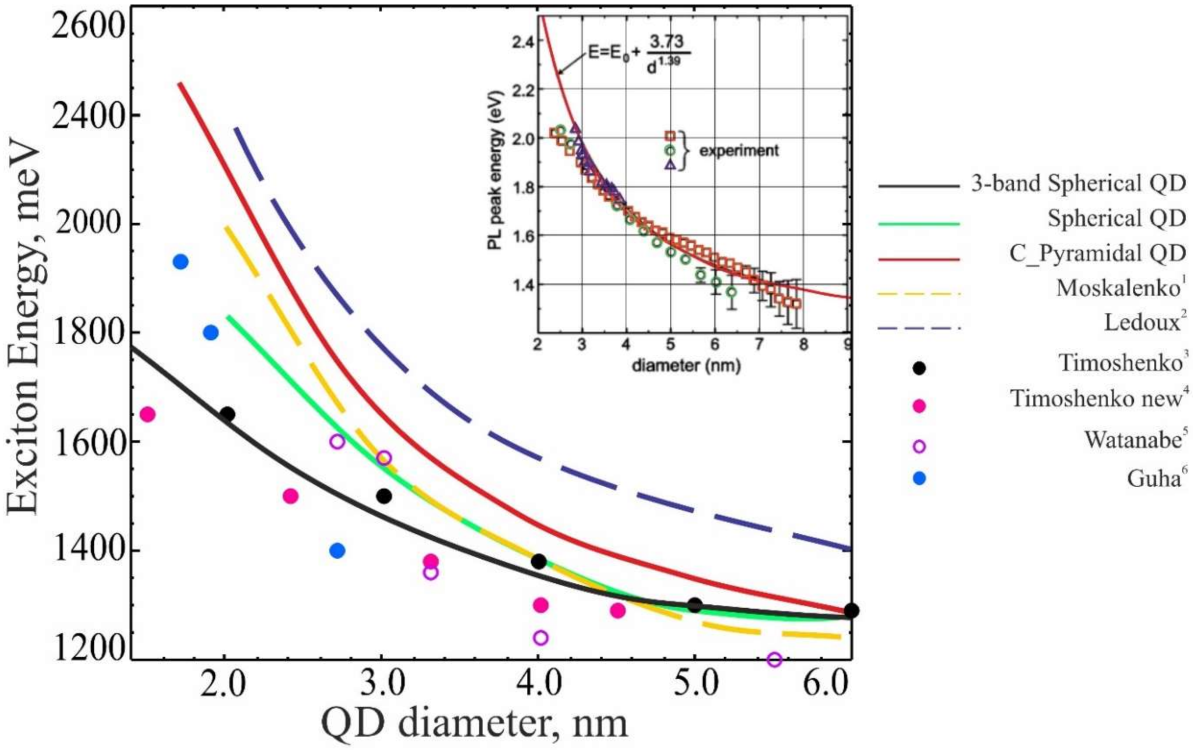

Fig. 2.27. Comparison of the theoretical calculations and the experimental values of the exciton energies in Si QDs.

In Fig. 2.27 the comparison of experimental and theoretical results for exciton energy is depicted. Solid lines represent theoretical calculations made in this Thesis. The green line corresponds to the spherical QDs in the approach of 1-band Hamiltonian for holes (Eq. 2.10) and without mixing levels for exciton (Eq. 2.24). The black line is for spherical QD too, but the hole's spectra are calculated using a 3-band Hamiltonian for holes (Eq. 2.12) and taking into account mixing (Eq. 2.22) of energy levels for exciton. The exciton energy of DTPQD is shown with a red line. Dependence was calculated using taking into account the 3-band Hamiltonian and mixing high energy levels of charge carriers. Dashed lines represent theoretical calculations from other works: the yellow line represents theoretical calculations of spherical QD exciton energy from work Ref. [134], and the blue line represents theoretical calculations effectuated by Ledoux et al. in Ref. [76], (same as in inset). Black dots, magenta dots and circles, and cyan dots represent experimental results obtained for exciton energy in works [40], [39], [135], [14], respectively. In the presented experiments Si nanocrystals were embedded into the dielectric matrix SiO_2, in the work of Watanabe Ref. [135] the Er^+ ions were also present in the dielectric matrix. Inset is taken from Ref. [76]. It shows theoretical and experimental data of exciton energy in dependence on QD size.

It is clearly seen that all theoretical curves for spherical QDs have higher energy than experiment data for QD's diameter $<3\,\text{nm}$, but are in good accordance with measured PL for larger QDs. The best agreement with the experimental data demonstrates theoretical calculations carried out for spherical QD within a 3-band Hamiltonian approach taking into account the mixing of size-quantized electron and hole energy levels. The larger difference between theoretical and experimental results for small QDs can be explained by the following reasons: (experimental difficulties in obtaining QDs of the same shape and size as well as insufficient accuracy of QD's size/form determination and size/form dispersion in an experiment, which strongly affects spectra of QDs with $d<3\,\text{nm}$ [13]; and (ii) limited applicability of the continual approach for QDs with $d<3\,\text{nm}$ (the validity of the continual approach is quite discussible in this case).

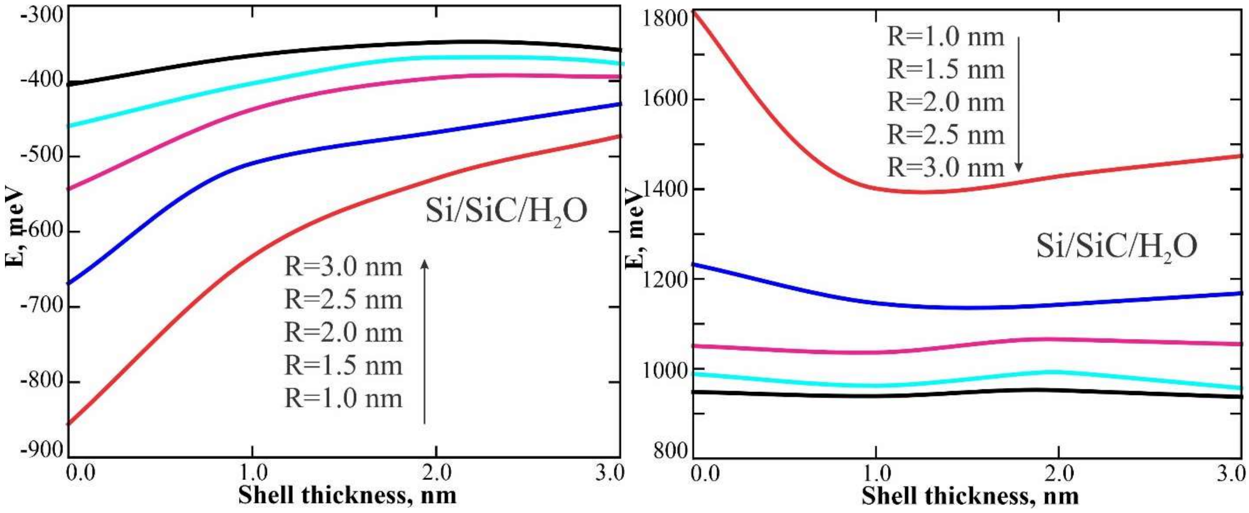

(a) **(b)**

Fig. 2.28. Exciton energy in Si/SiC/medium QDs in dependence of SiC shell thickness **(a)** binding energy and **(b)** full exciton energy in dependence on shell thickness.

In Fig. 2.28 the dependencies of binding energy and total exciton energy in Si/SiC/H_2O QDs on SiC shell thickness for different QD radii are presented. The binding energy is smaller by the module for QD with a thicker shell because the spatial confinement of the charge carriers is less, while penetration of charge carrier wave functions into barrier medium is stronger (see Fig. 2.27) and, as follows, increases of the effective exciton radius. However, at the thicknesses $\geq 2\,\text{nm}$ binding energy value saturates because the spatial confinement of the charge carriers does not increase anymore, and the effective exciton radius does not increase, as well. The inverse relation between QD size and exciton energy is valid as in the case of QD Si/SiO_2. Shell dependencies show the decay of the exciton energy for shell thicknesses in the range

$0\,\text{nm} - 1\,\text{nm}$. This decay is more prominent for smaller QD radii. The continuous increase of the shell leads to the slight growth of the exciton energy, due to the contribution of the binding energy.

Fig. 2.29 shows the penetration of the electron wave function in Si/SiC/H_2O QD as a function of the SiC shell thickness. Penetration saturates with the growth of the shell thickness and has lower values for the QD with a larger size.

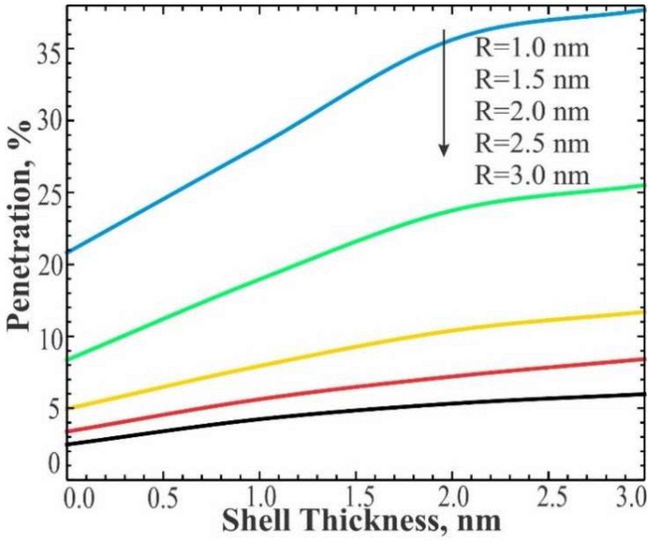

Fig. 2.29. Electron ground level wave function penetration in Si/SiC/H_2O QD in dependence on shell thickness

Photoluminescence in Si/SiO_2 quantum dot nanostructures

Photoluminescence curves of the QDs ensemble which have the same dimension and shape should have the form of sharp peaks. But conform experiments presented in Ref. [39] photoluminescence spectra of a spherical QD Si/SiO_2 have the form of Gaussian curves, but not of sharp peaks (See Fig.2.30(b)). In Fig, 2.30 we can see **(a)** a TEM cross-sectional image of an nc-Si/SiO_2 structure with 3.5 nm Si nanocrystals **(b)** PL spectra of not-doped nc-Si/SiO_2 structures [39]; **(c)** Photoluminescence spectra of QD ensembles before (as-deposited) and after thermal annealing at temperatures indicated above the respective curves [13]

It is clearly seen from Fig. 2.30 (a) reproduced from Ref. [39] that QDs have different sizes and irregular forms and also there are dots without clear boundaries (See Fig.2.30(a)). In Ref. [13] authors affirm that, however, the formation of larger Si-NCs is preferential at relatively low annealing temperatures, while at higher annealing temperatures smaller Si-NCs can be formed. Authors argue that the low-energy shift of PL can be explained by two main effects: exciton migration through a percolative network and Ostwald phenomena when larger nanocrystals grow at the cost of the small one increasing the standard deviation of size distribution.

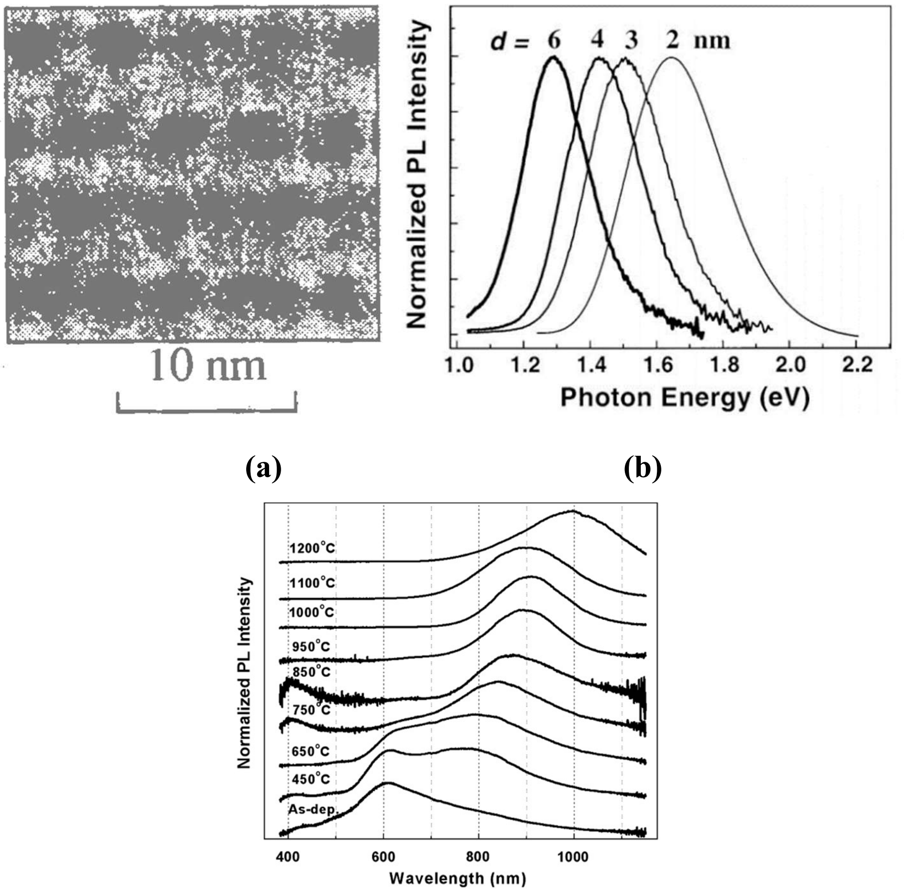

(a) **(b)**

(c)

Fig. 2.30. Photoluminescence of Si-nc embedded into dielectric SiO_2 matrix.

(a) TEM cross-sectional image of an nc-Si/SiO_2 structure with 3.5 nm Si nanocrystals;

(b) Typical PL spectra of undoped nc-Si/SiO_2 structures formed from a-Si/SiO_2 superlattices with different thicknesses of SiO layer (labeled at corresponding curves).

(c) Normalized PL spectra of silicon-rich silicon oxide films before (as-deposited) and after thermal annealing at temperatures indicated above the respective curves

Figure is adopted from Refs. [13] and [39].

In our theoretical investigation, we assume two main possible reasons for photoluminescence band broadening: size dispersion and QDs merge.

For our calculations, we have used Gauss distribution by radius in the case of size distribution and Gauss distribution by the distance between QDs centres for the QDs merge case. In order to take into account the merge of QDs we analysed the following system: we joined centres of 2 spherical QDs with virtual axis and moved them together, i.e. the distance between centres of QDs changed from $2R_0$ to zero:

$$N(K) = NW(K) ,$$

$$W(K)=Ae^{-a\left(\frac{K-K_0}{K_0}\right)^2}, \quad (2.26)$$

where coefficient A has been found from the normalization condition:

$$\int_0^\infty W(K)dK=1$$

and is equal to:

$$A=\frac{1}{K_0\left(\frac{1}{2}\sqrt{\frac{\pi}{a}}+\int_0^1 e^{-ax^2}dx\right)}. \quad (2.27)$$

Theoretical modelling of photoluminescence lines has been done conform the following equation:

$$I_{PL}\left(\varepsilon\left(K\right)\right)=I_{PL}\left(\varepsilon_{\max}\right)e^{-a\left(\frac{K(\varepsilon_\pm)-K_0(\varepsilon_{\max})}{K_0(\varepsilon_{\max})}\right)^2}, \quad (2.28)$$

where, K_0 – initial radius of QD or maximal distance between the centres of QD, $\varepsilon_{\max}$ – exciton energy of QD with K_0, a – parameter, describing dispersion, and is calculated conform the following expression:

$$\left\langle\left(x^2\right)\right\rangle=\frac{\int_{-1}^\infty x^2e^{-ax^2}dx}{\int_{-1}^\infty e^{-ax^2}dx}, \quad (2.29)$$

where $x=\frac{K-K_0}{K_0}$.

In Fig. 2.31 the comparison of theoretical and experimental curves of photoluminescence intense distribution in dependence on PL energies for different QD sizes is shown. Red continuous lines represent experimental photoluminescence curves, black dashed lines are dependencies obtained via theoretical modelling of QD’s size dispersion, while yellow dash-n-dot lines demonstrate the results of theoretical modelling of QD’s merging. In Fig. 2.31 (a) the photoluminescence for QD with diameter $3\ \mathrm{nm}$ is shown with dispersion value $\left\langle\left(x^2\right)\right\rangle=0.0324$. One can see that the theoretical curve for size distribution almost coincides with experimental data (size dispersion is equal to $18\ \%$ from the QD radius). For the QD with a diameter of $4\ \mathrm{nm}$ (see Fig. 2.31 (b)), the dispersion was taken the same as for QD with $D=3\ \mathrm{nm}$, $\left\langle\left(x^2\right)\right\rangle=0.0324$. But in this case, there is a difference between the size dispersion curve and experimental data at the low-energy region. For QD with diameter $5\ \mathrm{nm}$ dispersion was increased to $\left\langle\left(x^2\right)\right\rangle=0.0484$.

Even for greater dispersion value, the theoretical curve coincides with the experimental one only in high-energy region. This occurs because exciton energy increases more slowly with increasing QDs size, the size distribution curve is asymmetric, and it’s narrow at the low-energy region, even for size dispersion up to $a = 80\%$ from the QD diameter.

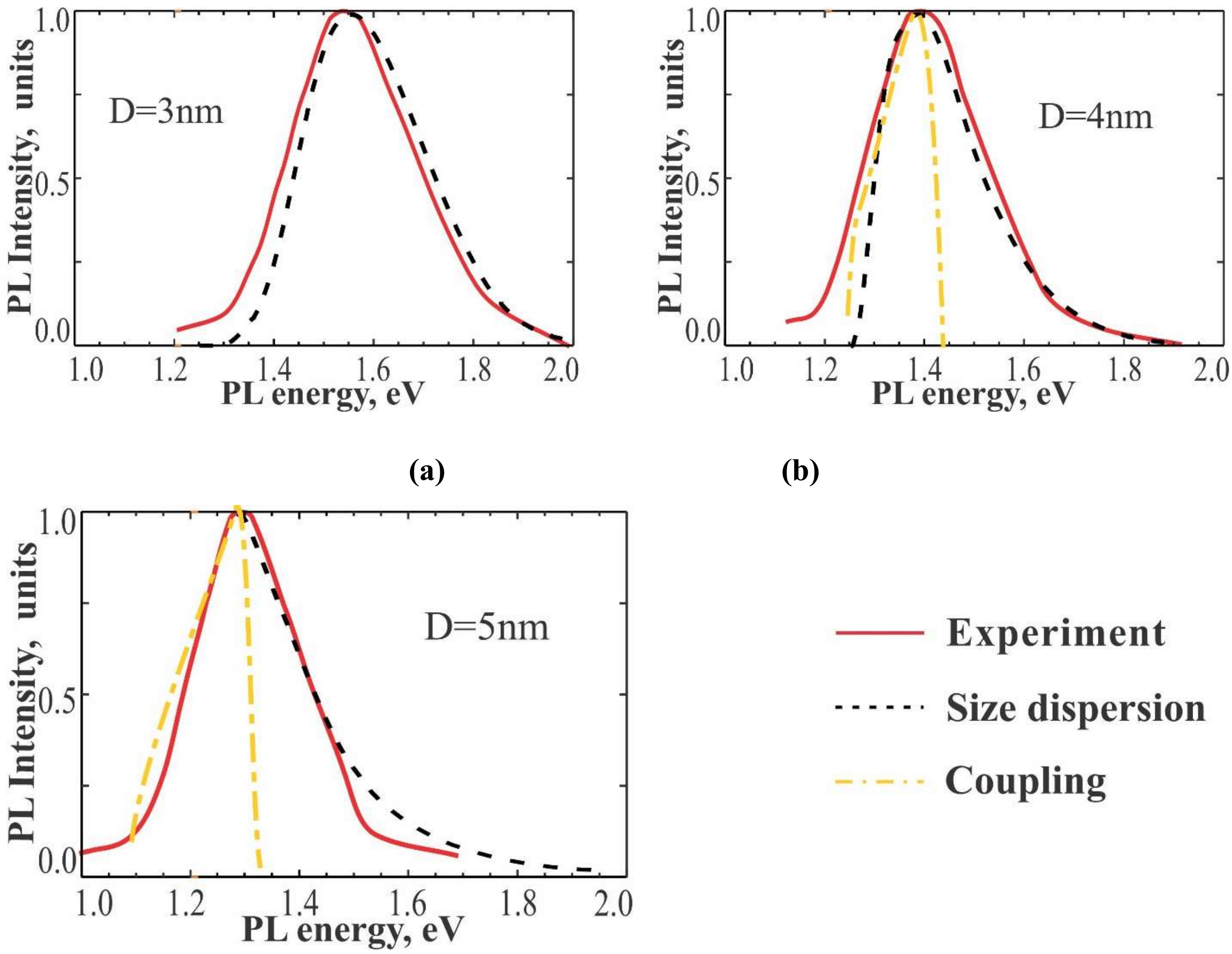

(a) **(b)**

(c)

Fig. 2.31. Theoretical PL intensity distribution in Si/SiO$_2$ in dependence on PL energy for QDs **(a)** with diameter 3 nm; **(b)** with diameter 4 nm and **(c)** with diameter 5 nm

To explain photoluminescence band broadening we have examined the merge of the QDs. Due to the lower exciton energy of the merged QDs, we have obtained good accordance of our theoretical calculations with the experiment, as is seen in Fig. 2.31 (c). Therefore, size distribution allows us to explain the broadening of the photoluminescence band in the range of high energies, at the same time merge of the QDs can be a reason for the broadening in low-energy region. In the case of QD diameter $D = 3\,\text{nm}$ the percentage of merged QD is nearly zero and the photoluminescence curved is determined only by the effect of QD size dispersion. In evidence of our theory about the QDs merging on photoluminescence and exciton energy, we have compared theoretically obtained exciton energy with an experiment from Ref. [13].

In Fig. 2.32 the electron and hole energies for ground levels for coupled spherical QDs as a function of the distance between QD centres for the initial QD radius $R = 1.0$ nm . Calculations have been done in the way that the volume of merged QDs has been equal to the total volume of two QDs. Both dependencies have a minimum in the interval $d = 1$ nm $- 1.5$ nm . At this distance, QD has a maximum diameter. The continuous increase of the distance between the centres leads to the reinforcement of the special confinement due to the QD shape. At the distance $d=2$ nm QDs separate one from another, however, the electron and hole energies do not reach their initial values. It happens because electron and hole wave functions penetrate into the dielectric medium, so the energies are lower with $\sim 12\%$ for electrons, and $\sim 3\%$ for holes. The difference in electron energies is more significant because the penetration of the electron wave function is more than that of the holes (18% for electrons and 6% for holes).

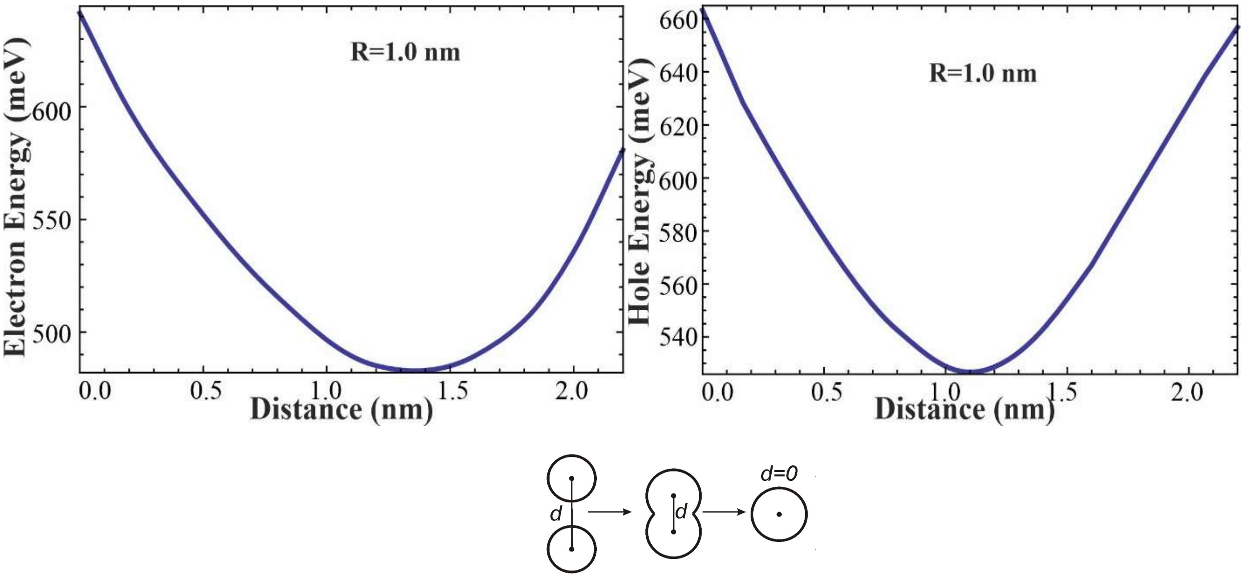

(a) **(b)**

Fig. 2.32. Electron and hole energies in dependence on the distance between QDs centres

(a) electron ground energy level; **(b)** hole ground energy level

In Fig. 2.33 the exciton energy dependence on the distance between centres of merged QDs is shown. The continuous line represents theoretical calculations of exciton energy in coupled QDs in dependence on the distance between their centres (the scheme is presented in the inset). Dots represent experimental photoluminescence energy for different annealing temperatures. Dots in the graphic correspond to the exciton energies of the sample in dependence on annealing temperature [13]. The dependence of the exciton energy on the distance between QD centres of the coupled QDs is shown for QDs with $R = 2$ nm . The exciton energy decreases up to 10% with increasing distance. Experimental points shown on the graph are taken from Ref. [13] for different annealing temperatures.

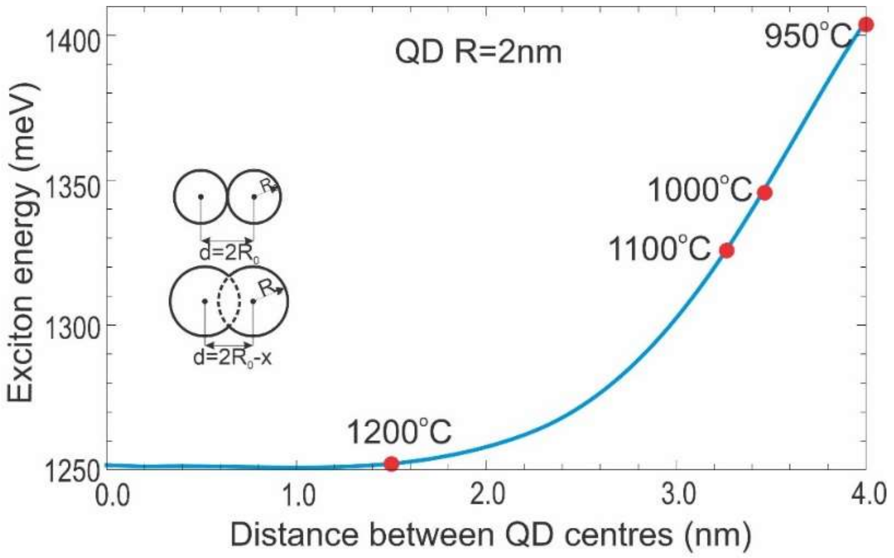

Fig. 2.33. Exciton energy in the coupled QD

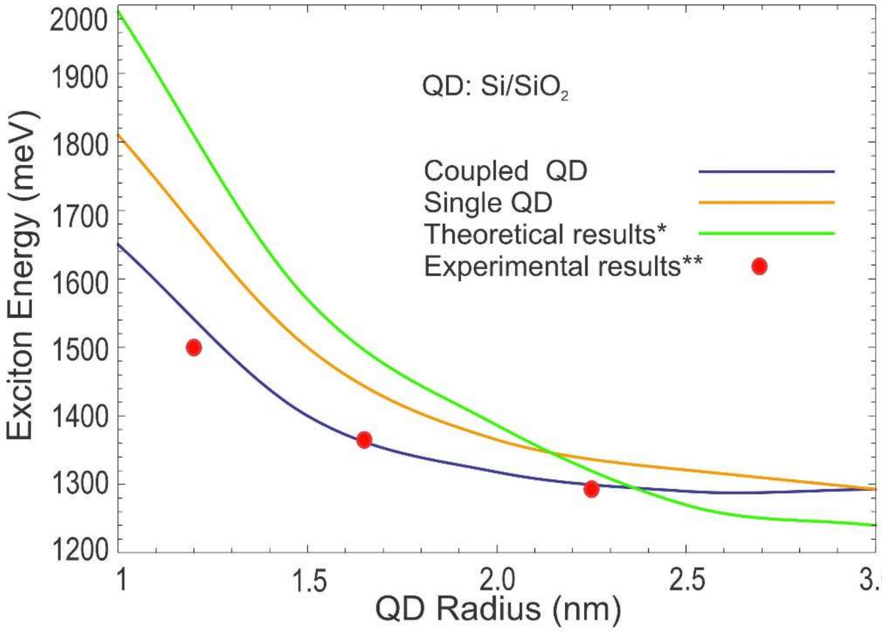

Fig. 2.34. Exciton energy in the coupled QD

In Fig. 2.34 the comparison of the theoretical results obtained in Ref. [134] (green line) and out results for single spherical QD (orange line), coupled QD (blue line) with the same radius and distance d between coupled centres equal $d = 0.75D$, where D is diameter of the QD, and experimental data from Ref. [13] (red points). It is seen that coupling of the QD causes the exciton energy drop, and is closer to the experimental results, especially at radii $R < 2$ nm. However, exciton energy for QD with radii $R > 2.5$ nm is lower than the energy for single QD.

Exciton states engineering in Si/SiC/H_2O quantum dot nanostructures

Energy transfer between QD and impurities embedded in dielectric media is an effective mechanism to pump photons in Er^{3+}-ions [39] or to obtain a singlet state of O_2 from triplet ground level [136], [137]. Exciting of O_2 from biologically passive ground state to biologically active excited state is important for photo-dynamic cancer therapy [136], [137]. In this case, the Auger [136] process of energy transfer takes place. The Auger energy transfer is more efficient if the exciton transit from a higher energy level to the lower one. In Fig. 2.35 the scheme of excitation of the singlet oxygen state is presented. Absorbed by Si QDs radiation excites oxygen molecules from the ground triplet state to the first excited singlet state by non-radiative energy transfer ($\approx 977\,\mathrm{meV}$).

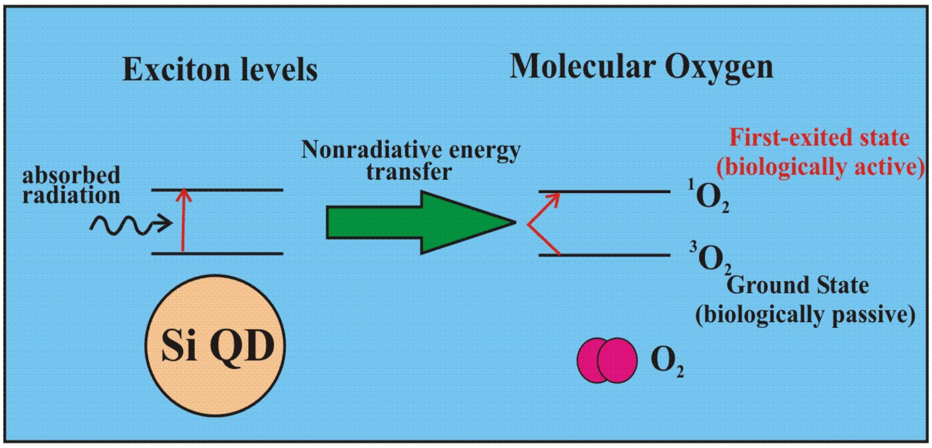

Fig. 2.35. Excitation of oxygen molecule

In our theoretical study of Si/SiC/medium QDs, we show that it is possible to obtain the energy distance between exciton energy levels closer to the oxygen excitation energy by change of quantum dot and shell sizes. In Fig. 2.36 the scheme of exciton energy levels for different QD radii and shell thickness are shown. Arrows indicate exciton state transition that may cause resonant energy transfer to an oxygen molecule (energy difference is close to the oxygen excitation energy). For different Si QD radius resonant transition takes place between different exciton energy levels. Modifying of the shell thickness may adjust the energy distance to be closer to the oxygen excitation energy. In the case of the transition energy greater/less than the excitation energy process may go with phonon emission/absorption. The obtained results may be useful for photodynamic cancer therapy [138] and other application of photosensitizing agents.

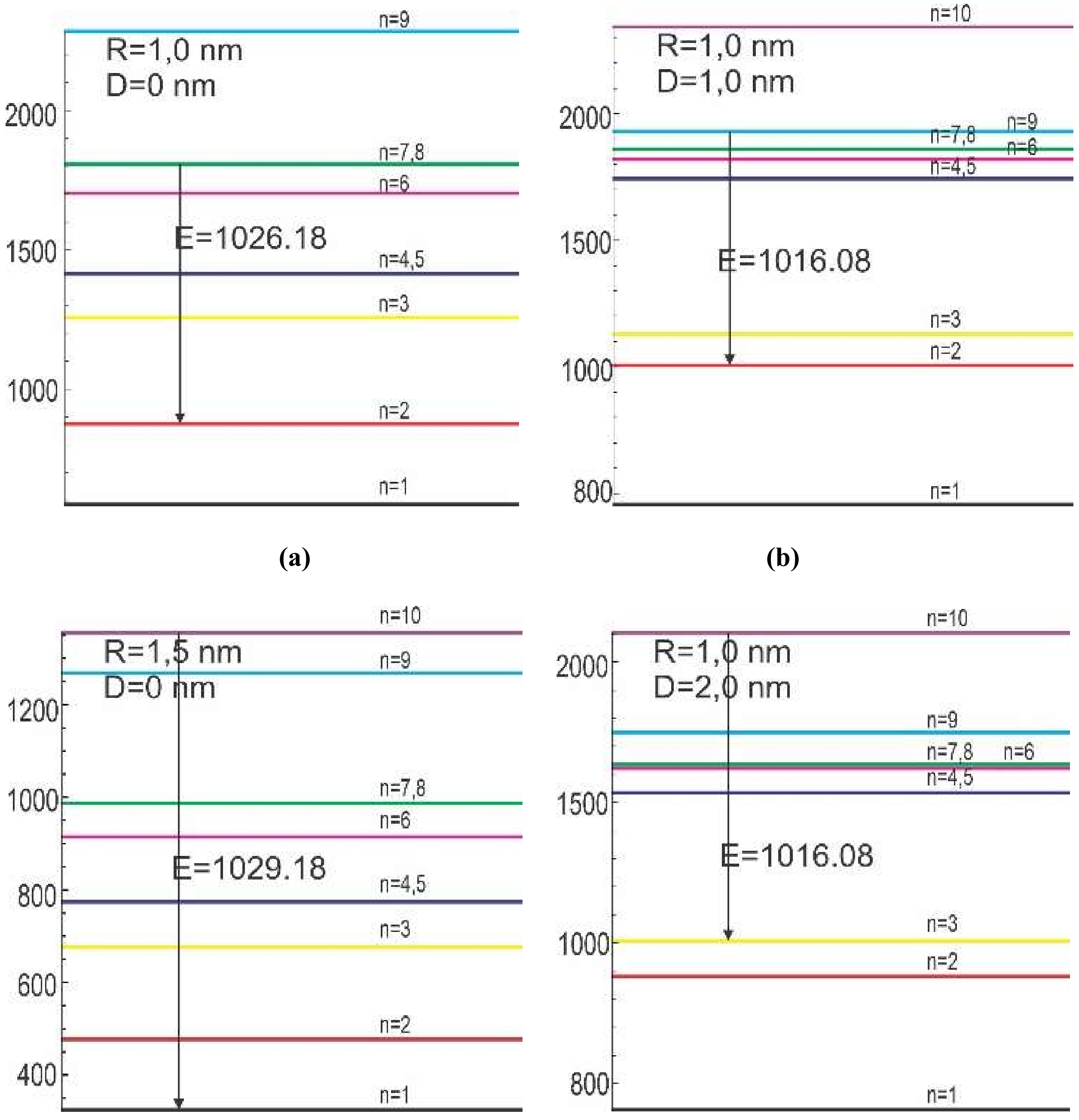

(a) **(b)**

(c) **(d)**

Fig. 2.36. Exciton states in Si/SiC/H2O QDSL.

(a) - **(d)** QD Radius (R) and Shell thickness (D) are as labelled in the panels.

2.4. Calculation methods

General information

Electron effective mass in silicon has three components: two transverse $m_{t,Si} = 0.19m_e$ and one longitudinal $m_{l,Si} = 0.98m_e$, while in a dielectric matrix effective mass components take the same values $m_{l,SiSiO_2} = m_{t,SiSiO_2} = m_e$. Components of effective mass are directed along axes OX, OY, and OZ. The longitudinal effective mass component direction is chosen along axis OZ and along QD height. For non-spherical QDs axes were directed as follows: OZ – along the height of the QD through the centre of the shape base, OX and OY in the base plane. The thickness of dielectric matrix should assure a smooth fade of the wave function. We verified empirically that the minimal thickness of the dielectric matrix is equal to $2\ \mathrm{nm}$. The total length of the structure is equal to $L = D + 2l$, where D – diameter or maximal of the QD's linear dimensions, l is the thickness of the dielectric matrix. We took into account the difference between the material parameters of QD and the dielectric matrix. Electron and hole Hamiltonians were solved by the finite difference method. Eigenvectors and eigenvalues were found using the Davidson-Liu method for monster matrices [29]. We have taken into account different effective masses in QD and dielectric medium.

Average parameters

In real structures, material parameters (effective mass, dielectric permittivity, etc.) do not change abruptly on the interface between QD and dielectric matrix, due to the formation of layers with mixed properties. Material parameters for any point $\vec{r} = (i, j, k)$ from this layer were calculated by averaging on volume V. We took the cube with the centre in point $\vec{r} = (i, j, k)$ and with the edge length a (see Fig. 2.37). In order to improve the accuracy of the calculation we used a smaller calculation step h_2 inside the cube. Points of the cube situated inside or outside QD have a value of material parameter equal to the value of this material parameter in Si or SiO_2, respectively.

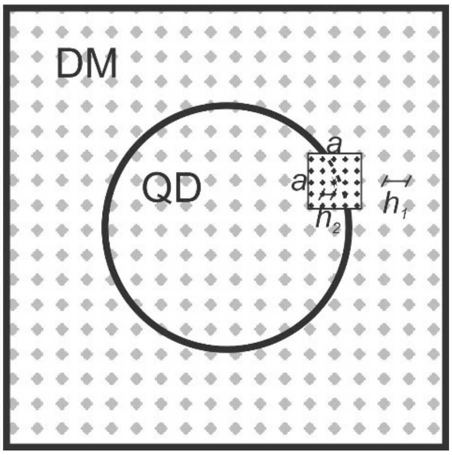

Fig. 2.37. Scheme for the method of the average material parameters.

The material parameter in $\vec{r}=(i,j,k)$ point can be written as follows:

$$\bar{g}=\int_{\Delta V} g(\vec{r})dV\cdot\frac{1}{\Delta V} \tag{2.29}$$

where $g(\vec{r})$ is the value of the parameter in the point with radius-vector $\vec{r}$, ΔV – volume of cube, $\bar{g}$ – average value of the parameter.

The advantage of this method: it can be used for any form of QD. The precision of the method depends on the step of calculation h_2 inside the cube. This method was used to average effective mass and permittivity on interfaces QD/shell, shell/medium.

Finite difference method

The Hamiltonians for electrons and holes were resolved by using the finite difference method. We approximate derivatives with finite difference implicit method, the presented formula for the electron is written as an example:

$$\begin{aligned}&-\frac{\hbar^2}{2}\left[M_x\cdot\frac{\Psi_{i+1}-2\Psi+\Psi_{i-1}}{\Delta x^2}+\frac{M_x}{\Delta x}\cdot\frac{\Psi_{i+1}-\Psi_{i-1}}{2\Delta x}+\right.\\&+M_y\cdot\frac{\Psi_{j+1}-2\Psi+\Psi_{j-1}}{\Delta y^2}+\frac{M_y}{\Delta y}\cdot\frac{\Psi_{j+1}-\Psi_{j-1}}{2\Delta y}+\\&\left.+M_z\cdot\frac{\Psi_{k+1}-2\Psi+\Psi_{k-1}}{\Delta z^2}+\frac{M_z}{\Delta z}\cdot\frac{\Psi_{k+1}-\Psi_{k-1}}{2\Delta z}\right]=E\Psi,\end{aligned} \tag{2.30}$$

where $M_x=\frac{1}{m_x}, M_y=\frac{1}{m_y}, M_z=\frac{1}{m_z}$ $\Delta x, \Delta y, \Delta z$ are the steps of discretization along axes *X, Y,* and *Z*, respectively.

In the case of the Hamiltonians, we obtain the Hermitian matrix. The eigenvalues and eigenvectors of this matrix represent the energy levels and wave functions of the charge carriers, respectively. The charge carrier's spectrum in the QDs discrete. Only the eigenvalues smaller than the potential barrier possess physic sense. Hence, we don't need all matrix solutions, but only several with values less the potential barrier between materials. The continuous model means that we can enhance the accuracy of the results we should use a smaller discretization step, which leads to an increase in matrix's size. The Davidson-Liu's method described in Ref. [29]. It is an iterative method, which allows us to find only a certain number of the lowest charge-carrier energy levels. The approximation of the derivatives for Coulomb potential results in a system of linear equations. The Maxwell law Eq. 2.24 can be rewritten as:

$$\frac{\partial\varepsilon_x}{\partial x}\frac{\partial\varphi_x}{\partial x}+\varepsilon\frac{\partial^2\varphi_x}{\partial x^2}+\frac{\partial\varepsilon_y}{\partial y}\frac{\partial\varphi_y}{\partial y}+\varepsilon\frac{\partial^2\varphi_y}{\partial y^2}+\frac{\partial\varepsilon_z}{\partial z}\frac{\partial\varphi_z}{\partial z}+\varepsilon\frac{\partial^2\varphi_z}{\partial z^2}=-4\pi\rho\,. \tag{2.31}$$

In the finite difference approach Eq. 2.31 takes the form:

$$\begin{aligned}
&\frac{\varepsilon(i+1,j,k)-\varepsilon(i-1,j,k)}{2\Delta x}\frac{\varphi(i+1,j,k)-\varphi(i-1,j,k)}{2\Delta x}+\\
&+\varepsilon\frac{\varphi(i+1,j,k)-2\varphi(i,j,k)+\varphi(i-1,j,k)}{\Delta x^2}+\\
&+\frac{\varepsilon(i,j+1,k)-\varepsilon(i,j-1,k)}{2\Delta y}\frac{\varphi(i,j+1,k)-\varphi(i,j-1,k)}{2\Delta y}+\\
&+\varepsilon\frac{\varphi(i,j+1,k)-2\varphi(i,j,k)+\varphi(i,j-1,k)}{\Delta y^2}+\\
&+\frac{\varepsilon(i,j,k+1)-\varepsilon(i,j,k-1)}{2\Delta z}\frac{\varphi(i,j,k+1)-\varphi(i,j,k-1)}{2\Delta z}+\\
&+\varepsilon\frac{\varphi(i,j,k+1)-2\varphi(i,j,k)-\varphi(i,j,k-1)}{\Delta z^2}=-4\pi\rho(i,j,k).
\end{aligned} \tag{2.32}$$

This system was resolved numerically by the Jacobi-Seidel iterative method.

The result of the calculation of the Coulomb potential distribution in Si QD with $d = 3$ nm embedded in SiO2 dielectric medium is presented in Fig. 2.38. The distribution of potential along the OX axis is depicted for the electron charge placed at a distance of 0.375 nm from the QD centre. Permittivity near the interface Si/SiO2 changed in the way described above in this paragraph. For comparison, spherical Coulomb potentials with $\varepsilon=\varepsilon_{Si}$ and $\varepsilon=\varepsilon_{SiO_2}$ are also shown by dotted and dashed lines, respectively. From Fig. 2.38 it is obvious that taking into account the difference in permittivities of QD and surrounded media is crucial for an accurate calculation of Coulomb potential.

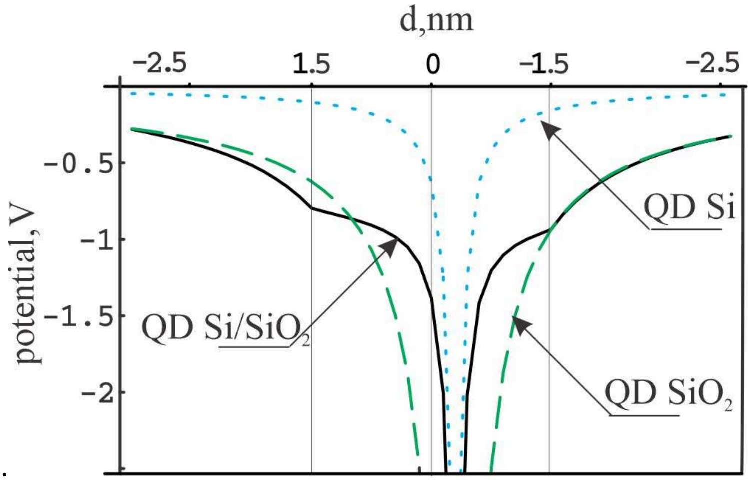

Fig. 2.38. Distribution of the Coulomb potential for charge placed near the centre of the QD.

2.5. Conclusions to Chapter 2

In this Chapter, we discussed electron, hole, and exciton states in the Si/SiO$_2$, Si/SiC/air, and Si/SiC/water QDs. Electron and hole spectra were calculated using the effective mass approach, taking into account both the anisotropy of effective electron mass in Si and the possible mixing of different types of holes: heavy, light, and split-off. The calculation of hole and exciton states using both 1-band and 3-band Hamiltonians is performed to elucidate the effect of holes' mixing. The effect of the potential barrier height and QD shapes on the charge carriers' and exciton states is investigated. The following conclusions can be formulated based on the obtained results:

- An increase in the potential barrier height leads to an enhancement of electron and hole spatial confinement and the corresponding increase of their energies and distance between energy levels.
- Both binding energy and total exciton energy decrease with the rise of QD's volume due to the weakening of the spatial confinement of electrons and holes.
- The shape of the Si QDs strongly influences electron, hole, and exciton states. It has been shown that conical QDs possess the lower values of ground exciton energy in comparison with cuboid and pyramidal QDs for the volumes $V < 32\ \mathrm{nm}^3$, while for $V > 32\ \mathrm{nm}^3$ cuboid QDs demonstrate the lower values of ground exciton energy.
- The outer media parameters influence the electron and hole ground energy only for Si QDs with narrow SiC shells with thickness $< 1\ \mathrm{nm}$ because maximal penetration of hole and electron wave functions into barrier media in considered Si/SiC/air or Si/SiC/water QDs is about $1\ \mathrm{nm}$.

- The obtained theoretical results were compared with the existing theoretical [76], [134], and experimental results [14], [39], [40], [135] of the other groups. Exciton energies calculated in this work are closer to the experiment values in comparison with other theoretical results obtained within similar approaches, even for the QDs with a radius $< 2\ \mathrm{nm}$ where the applicability of effective mass theory may require additional confirmations. The difference between the theoretical and experimental values for the QDs with the $r \approx 1.5\ \mathrm{nm}$ is about 8% . A better agreement with the experimental results has been obtained within the 3-band Hamiltonian approach with taking into possible mixing of electron and hole states.
- The large broadening of PL bands in Si QDs as well as the dependence of exciton energy on annealing temperature reported recently in experimental works [13] can be theoretically explained by the dispersion of QD's shapes and sizes.

3. Thermal conductivity in 1D Si-based nanostructures

In this Chapter we study phonon and thermal properties of Si-based quasi-one-dimensional quantum dot superlattices. We consider here both superlattices with constant (1D-C-QDSL) and modulated (1D-M-QDSL) cross-sections. The influence of both geometrical and materials parameters of QDSLs on phonon spectra, phonon group velocities and thermal conductivity is investigated. We also provide comparative analysis of phonon and thermal properties of multi-shell silicon nanotubes. The presented results are based on the original author's works [24], [139–141].

The efficient heat management is one of the crucial problems of nowadays/modern electronics. Thermal properties of nanodevices and nanostructures are widely investigated both experimentally and theoretically [6], [112], [119], [120], [140], [142]. Optimization and precise control of thermal properties is the main goal of the phonon engineering [5], [6], [140]. Nanomaterials with high thermal conductivity are promising candidates as heat spreaders and interconnectors, while nanomaterials with low thermal conductivity are prospective for thermoelectric applications since the efficiency of the thermoelectric energy conversion, figure of merit *ZT*, is directly proportional to the electrical conductivity and inversely proportional to the total thermal conductivity: $ZT = \frac{S^2 \sigma T}{\kappa_{ph} + \kappa_{el}}$, where S is the Seebeck coefficient, σ is the electrical conductivity, T is the absolute temperature, and κ_{ph} and κ_{el} are the phonon and electron thermal conductivities, respectively.

Acoustic phonons are the main heat carriers in bulk semiconductors at room temperature (RT) and above. So tuning their properties one can influence the thermal flux.

3.1. Phonons and thermal transport in Si-based one-dimensional quantum dot superlattices

Quasi-one-dimensional quantum dot superlattices can be divided into two types: superlattices with constant cross-section and superlattices with periodically modulated cross-section. Sometimes, in the literature, QDSLs with constant cross-section are referred as segmented nanowires [25], [143], while QDSLs with modulated cross-section are referred as cross-section modulated nanowires [23], [24], [26]. Nevertheless, in this work we follow initial QDSL notation, i.e.: C-QDSL and M-QDSL. The schematic view of investigated nanostructures is presented in Fig. 3.1: 1D-QDSL with constant cross-section (Fig. 3.1 a); 1D-QDSL with modulated cross-sections (Fig. 3.1 b), where QDSL segments are formed from the two different materials; 1D-QDSL formed from quantum dots with and without coating (Fig. 3.1 c) and QDSL formed from quantum dots with a different thickness coating (Fig. 3.1 d). The *X* and *Y* axes of the Cartesian coordinate system are located in the cross-sectional plane of the 1D-QDSL and are parallel to its sides, while the *Z* axis is directed along the structure axis. The origin of the coordinates is set at the centre of the nanowire cross-section. All structures have square cross-section and periodic structure along OZ. We assume that investigated 1D-structures are infinite along the *Z* axis. The sides of 1D-C-QDSL with the constant cross-sections are denoted as d_x and d_y. The narrow and wide segments of 1D-M-QDSL possess dimensions $d_{x,1} \times d_{y,1} \times d_{z,1}$ and $d_{x,2} \times d_{y,2} \times d_{z,2}$, respectively. In the case of the QDSL with coated QD total cross-section is denoted with $d_{x,1t} \times d_{y,1t}$ for narrow segments and $d_{x,2t} \times d_{y,2t}$ for the wide ones. The core dimensions are $d_{x,1} \times d_{y,1} \times d_{z,1}$ and $d_{x,2} \times d_{y,2} \times d_{z,2}$ for small and large QDs, respectively. In the case of the partially coated QDSL $d_{x,1} = d_{x,1t}$ and $d_{y,1} = d_{y,1t}$. The length period for 1D-QDSL of all types is $d_z = d_{z,1} + d_{z,2}$. The external surfaces of the nanostructures under consideration are assumed to be free [5], [25], [117]. The number of monolayers is denoted as *N*; the index behind it corresponds to the notations indicated for the length *d*.

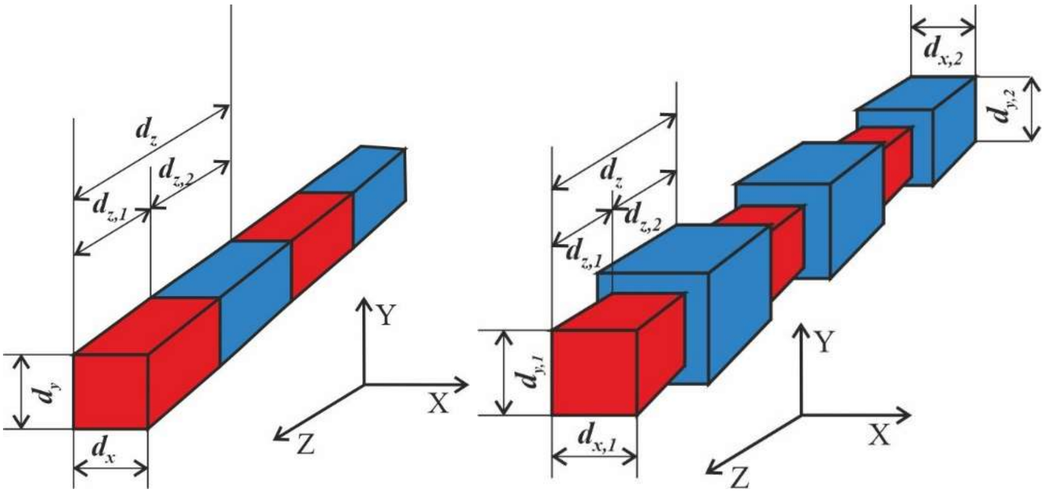

(a) **(b)**

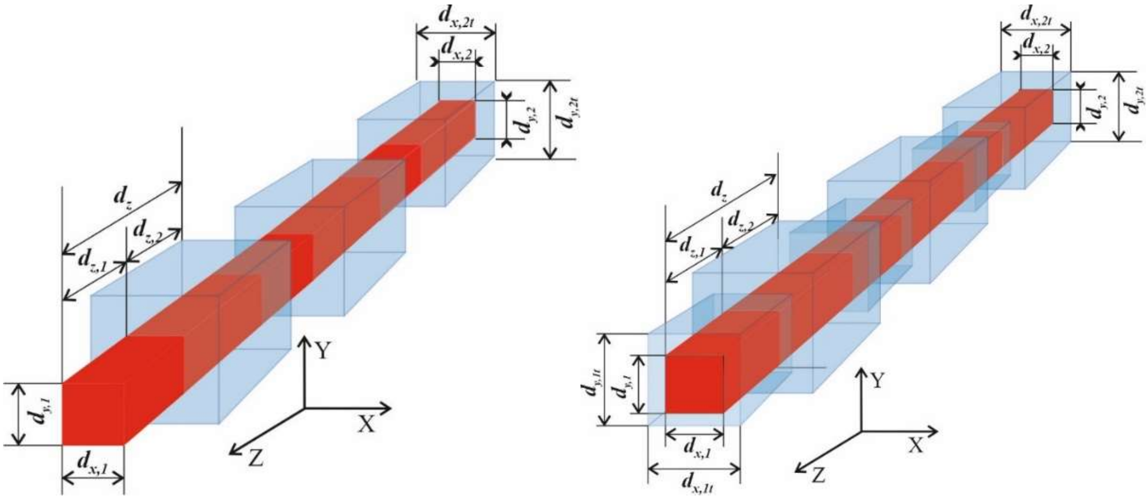

(c) **(d)**

Fig. 3.1. Schematic view of the investigated 1D-QDSL

(a) 1D quantum dot superlattice with constant cross-section (C-QDSL);

(b) 1D segmented quantum dot superlattice with a modulated cross-section (M-QDSL);

(c) 1D partially coated QDSL with the constant core;

(d) 1D modulated coated QDSL with the constant core

3.1.1. Face-centred cubic cell model of lattice vibrations

The phonon energy spectra are calculated using an atomistic Face-Centred Cubic Cell (FCC) [144] model of lattice dynamics. The real crystal lattice of Si and Ge consists of two face-centred cubic Bravais sublattices, which are shifted along the main diagonal of a unit cell by 1/4 of its length. The real crystal lattice of Si or Ge is replaced with one face-centred cubic lattice with atoms possessing double mass in its nods. The schematic view is presented in Fig. 3.2. The atoms of the second sublattice are denoted with blue colour. This approach considers only acoustic oscillations, neglecting relative motion of the atoms of the different sublattices. Since the main heat carriers in silicon and germanium [145] are acoustic phonons, our simplification is quite reasonable and justified.

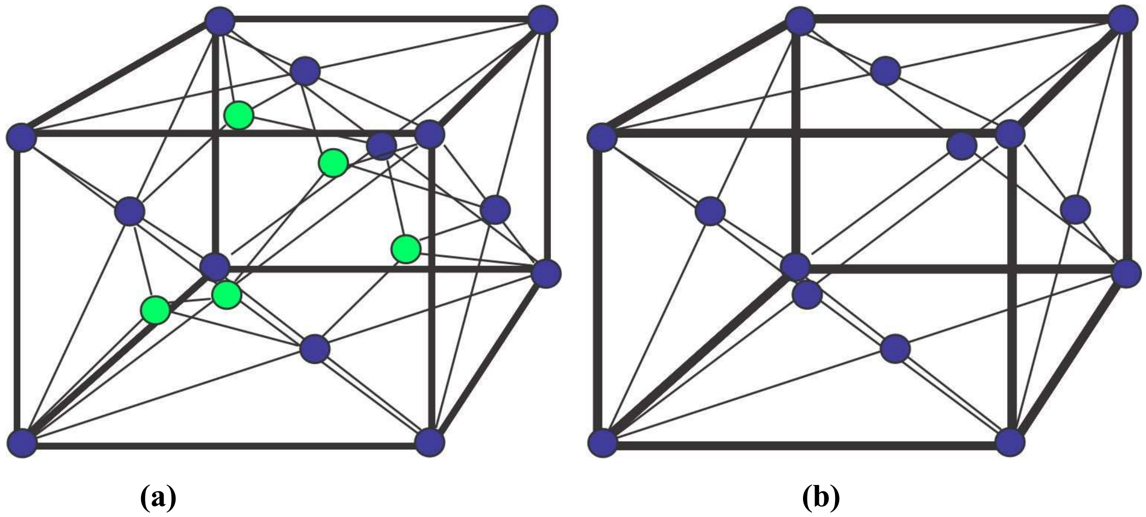

Fig. 3.2. Crystal lattice of Si and Ge:

(a) Real; **(b)** FCC-model.

Figure is adopted from Ref. [19]

In order to obtain the acoustic phonon in 1D-QDSL we have derived equation of motions for QDSL period and resolved it taking into account periodic boundary conditions along QDSL's axis. All atoms from QDSL period are translation independent; their displacement differs by phase and amplitude.

Using the force matrix, second Newton law for the atom with radius-vector $\vec{r}$ is given by:

$$m(r)\omega^2 U_\alpha(r,q) = -\sum_{(r'),\beta} \Phi_{\alpha\beta}(r,r')U_\beta(r',q) \text{ where } \alpha,\beta = x,y,z. \tag{3.1}$$

In Eq. (3.1) $m(r)$ – is the double mass of the crystal lattice cell node $m(r)=\frac{\rho(r)a^3}{4}$, $\rho(r)$ is the material density, ω is the phonon frequency, $U_\alpha(r_i,q)$ is the component of the displacement vector for the atom $m(r_i)$, $\Phi_{\alpha\beta}(r,r')$ is the interaction potential between atom with radius-vector (r) and atom with radius-vector (r'). The summation in Eqs. (3.1) is performed over all the nearest and second-nearest atoms for atom with (r'). In the case of silicon, the atom at $\vec{r}$ has 4 nearest neighbours at $\vec{r}_n' = \vec{r} + \vec{h}_n^I$ (n=1,…,4) and 12 second-nearest neighbours at $\vec{r}_n' = \vec{r} + \vec{h}_n^{II}$ (n=1,..,12).

Let's find solution of differential Equations 3.1 in the form Bloch functions for each atom (r): $U_\alpha(r') = u_\alpha(r')\exp(\mathbf{i}\omega t)$, where $u_\alpha(r')$ – is amplitude of atom (r') displacement. We substitute this solution into system of differential equations Eqs. (3.1) and will obtain system of linear homogeneous algebraic equation for amplitudes $u_\alpha(r)$:

$$m(i,j,k)\omega^2 u_\alpha(i,j,k) = \sum_{(i',j',k'),\beta} \Phi_{\alpha\beta}(i,j,k,i',j',k')u_\beta(i',j',k'). \tag{3.2}$$

Interaction with nearest neighbours (atoms are placed at the distance $\frac{a}{\sqrt{2}}$) is central-symmetric, that's why this interaction between atom with radius-vector (r) and atom with radius-vector (r') can be described by only one force constant $\kappa_1(i',j',k',i,j,k)$ and can be written as: $\Phi^{(1)}_{\alpha\beta}\left(\vec{h}^{(k)},i',j',k',i,j,k\right) = \frac{-\kappa_1(i',j',k',i,j,k)h^{(k)}_\alpha h^{(k)}_{\beta 1}}{\left|\vec{h}^{(k)}\right|^2}$, where $\vec{h}^{(k)}$ is coordination vector of the first sphere. Interaction with second-nearest neighbours (atoms are placed at the distance a) is described by to force constants $\kappa_2(i',j',k',i,j,k)$ and $\kappa_3(i',j',k',i,j,k)$ [141]:

for atoms with coordinates ($\pm a$,0,0):

$$\Phi^{(2)}_{\alpha\beta}\left(\vec{h}^{(k)},i',j',k',i,j,k\right) = \begin{pmatrix} \kappa_2(i',j',k',i,j,k) & 0 & 0 \\ 0 & \kappa_3(i',j',k',i,j,k) & 0 \\ 0 & 0 & \kappa_3(i',j',k',i,j,k) \end{pmatrix},$$

for atoms with coordinates (0,$\pm a$,0):

$$\Phi^{(2)}_{\alpha\beta}\left(\vec{h}^{(k)},i',j',k',i,j,k\right) = \begin{pmatrix} \kappa_3(i',j',k',i,j,k) & 0 & 0 \\ 0 & \kappa_2(i',j',k',i,j,k) & 0 \\ 0 & 0 & \kappa_3(i',j',k',i,j,k) \end{pmatrix}, \tag{3.3}$$

for atoms with coordinates (0,0, $\pm a$):

$$\Phi^{(2)}_{\alpha\beta}\left(\vec{h}^{(k)},i',j',k',i,j,k\right) = \begin{pmatrix} \kappa_3(i',j',k',i,j,k) & 0 & 0 \\ 0 & \kappa_3(i',j',k',i,j,k) & 0 \\ 0 & 0 & \kappa_2(i',j',k',i,j,k) \end{pmatrix}.$$

Three independent force constants κ_1, κ_2 and κ_3 can be expressed through the elastic moduli c_{11}, c_{12} and c_{44} of a bulk cubic crystal: $\kappa_1 = \frac{a(c_{12}+c_{44})}{2}$, $\kappa_2 = \frac{a(c_{11}-c_{12}-c_{44})}{2}$, $\kappa_3 = \frac{a(c_{44}-c_{12})}{8}$, where a is the lattice constant.

Using the explicit form of the dynamic matrix coefficients and replacing $u_3 = \mathbf{i}u_3$ one can obtain the system of 3 equations of motion for the components of the displacement vector for each atom with coordinates $\left(i,j,k\right)$ in the case of 1D-QDSL with constant and modulated cross-sections [141]:

$$
\begin{aligned}
&m\left(i,j,k\right)\omega^2 u_1\left(i,j,k\right)=\\
&=\left[\frac{\kappa_1\left(i+1,j+1,k\right)+\kappa_1\left(i-1,j+1,k\right)+\kappa_1\left(i+1,j-1,k\right)+\kappa_1\left(i-1,j-1,k\right)}{2}+\right.\\
&+\frac{\kappa_1\left(i+1,j+1,k+1\right)+\kappa_1\left(i-1,j+1,k+1\right)+\kappa_1\left(i+1,j-1,k+1\right)+\kappa_1\left(i-1,j-1,k+1\right)}{2}\\
&+\kappa_2\left(i+2,j,k\right)+\kappa_2\left(i-2,j,k\right)+\kappa_3\left(i,j,k+2\right)+\kappa_3\left(i,j,k-2\right)+\\
&\left.\kappa_3\left(i,j+2,k\right)+\kappa_3\left(i,j-2,k\right)\right]u_1\left(i,j,k\right)-\\
&-\kappa_3\left(i,j,k+2\right)u_1\left(i,j,k+2\right)-\kappa_3\left(i,j,k-2\right)u_1\left(i,j,k-2\right)-\kappa_2\left(i+2,j,k\right)u_1\left(i+2,j,k\right)-\\
&-\kappa_2\left(i-2,j,k\right)u_1\left(i-2,j,k\right)-\kappa_2\left(i,j+2,k\right)u_1\left(i,j+2,k\right)-\kappa_2\left(i,j-2,k\right)u_1\left(i,j-2,k\right)-\\
&-\frac{\kappa_1\left(i+1,j,k+1\right)}{2}u_1\left(i+1,j,k+1\right)-\frac{\kappa_1\left(i-1,j,k+1\right)}{2}u_1\left(i-1,j,k+1\right)-\\
&-\frac{\kappa_1\left(i+1,j,k-1\right)}{2}u_1\left(i+1,j,k-1\right)-\frac{\kappa_1\left(i-1,j,k-1\right)}{2}u_1\left(i-1,j,k-1\right)-\\
&-\frac{\kappa_1\left(i+1,j+1,k\right)}{2}u_1\left(i+1,j+1,k\right)-\frac{\kappa_1\left(i-1,j+1,k\right)}{2}u_1\left(i-1,j+1,k\right)-\\
&-\frac{\kappa_1\left(i+1,j-1,k\right)}{2}u_1\left(i+1,j-1,k\right)-\frac{\kappa_1\left(i-1,j-1,k\right)}{2}u_1\left(i-1,j-1,k\right)-\\
&-\frac{\kappa_1\left(i+1,j+1,k\right)}{2}u_2\left(i+1,j+1,k\right)+\frac{\kappa_1\left(i-1,j+1,k\right)}{2}u_2\left(i-1,j+1,k\right)+\\
&+\frac{\kappa_1\left(i+1,j-1,k\right)}{2}u_2\left(i+1,j-1,k\right)-\frac{\kappa_1\left(i-1,j-1,k\right)}{2}u_2\left(i-1,j-1,k\right)+\\
&+\left[\frac{\kappa_1\left(i+1,j+1,k\right)-\kappa_1\left(i+1,j-1,k\right)-\kappa_1\left(i-1,j+1,k\right)+\kappa_1\left(i-1,j-1,k\right)}{2}\right]u_2\left(i,j,k\right)-\\
&-\frac{\kappa_1\left(i+1,j,k+1\right)}{2}u_3\left(i+1,j,k+1\right)+\frac{\kappa_1\left(i+1,j,k-1\right)}{2}u_3\left(i+1,j,k-1\right)+\\
&+\frac{\kappa_1\left(i-1,j,k+1\right)}{2}u_3\left(i-1,j,k+1\right)-\frac{\kappa_1\left(i-1,j,k-1\right)}{2}u_3\left(i-1,j,k-1\right)+\\
&+\left[\frac{\kappa_1\left(i-1,j,k-1\right)-\kappa_1\left(i+1,j,k-1\right)-\kappa_1\left(i-1,j,k+1\right)+\kappa_1\left(i+1,j,k+1\right)}{2}\right]u_3\left(i,j,k\right),
\end{aligned}
\tag{3.4a}
$$

$$
\begin{aligned}
&m\left(i,j,k\right)\omega^2 u_2\left(i,j,k\right)= \\
&=-\frac{\kappa_1\left(i+1,j+1,k\right)}{2}u_1\left(i+1,j+1,k\right)+\frac{\kappa_1\left(i-1,j+1,k\right)}{2}u_1\left(i-1,j+1,k\right)+ \\
&+\frac{\kappa_1\left(i+1,j-1,k\right)}{2}u_1\left(i+1,j-1,k\right)-\frac{\kappa_1\left(i-1,j-1,k\right)}{2}u_1\left(i-1,j-1,k\right)+ \\
&+\left[\frac{\kappa_1\left(i+1,j+1,k\right)-\kappa_1\left(i+1,j-1,k\right)-\kappa_1\left(i-1,j+1,k\right)+\kappa_1\left(i-1,j-1,k\right)}{2}\right]u_1\left(i,j,k\right)- \\
&-\left[\frac{\kappa_1\left(i+1,j+1,k\right)+\kappa_1\left(i-1,j+1,k\right)+\kappa_1\left(i+1,j-1,k\right)+\kappa_1\left(i-1,j-1,k\right)}{2}+\right. \\
&+\frac{\kappa_1\left(i,j+1,k+1\right)+\kappa_1\left(i,j-1,k+1\right)+\kappa_1\left(i,j+1,k-1\right)+\kappa_1\left(i,j-1,k-1\right)}{2}+\kappa_2\left(i,j+2,k\right) \\
&\left.+\kappa_2\left(i,j-2,k\right)+\kappa_3\left(i+2,j,k\right)+\kappa_3\left(i-2,j,k\right)+\kappa_3\left(i,j,k+2\right)+\kappa_3\left(i,j,k-2\right)\right]u_2\left(i,j,k\right) \\
&-\kappa_2\left(i,j+2,k\right)u_2\left(i,j+2,k\right)-\kappa_2\left(i,j-2,k\right)u_2\left(i,j-2,k\right)- \\
&-\kappa_3\left(i,j,k+2\right)u_2\left(i,j,k+2\right)-\kappa_3\left(i,j,k-2\right)u_2\left(i,j,k-2\right)- \\
&-\kappa_3\left(i+2,j,k\right)u_2\left(i+2,j,k\right)-\kappa_3\left(i-2,j,k\right)u_2\left(i-2,j,k\right)- \\
&-\frac{\kappa_1\left(i,j+1,k+1\right)}{2}u_2\left(i,j+1,k+1\right)-\frac{\kappa_1\left(i,j-1,k+1\right)}{2}u_2\left(i,j-1,k+1\right)- \\
&-\frac{\kappa_1\left(i,j+1,k-1\right)}{2}u_2\left(i,j+1,k-1\right)-\frac{\kappa_1\left(i,j-1,k-1\right)}{2}u_2\left(i,j-1,k-1\right)- \\
&-\frac{\kappa_1\left(i+1,j+1,k\right)}{2}u_2\left(i+1,j+1,k\right)-\frac{\kappa_1\left(i-1,j+1,k\right)}{2}u_2\left(i-1,j+1,k\right)- \\
&-\frac{\kappa_1\left(i+1,j-1,k\right)}{2}u_2\left(i+1,j-1,k\right)-\frac{\kappa_1\left(i-1,j-1,k\right)}{2}u_2\left(i-1,j-1,k\right)- \\
&\frac{\kappa_1\left(i,j+1,k+1\right)}{2}u_3\left(i,j+1,k+1\right)+\frac{\kappa_1\left(i,j-1,k+1\right)}{2}u_3\left(i,j-1,k+1\right)+ \\
&+\frac{\kappa_1\left(i,j+1,k-1\right)}{2}u_3\left(i,j+1,k-1\right)-\frac{\kappa_1\left(i,j-1,k-1\right)}{2}u_3\left(i,j-1,k-1\right)+ \\
&+\left[\frac{-\kappa_1\left(i,j+1,k+1\right)+\kappa_1\left(i,j-1,k+1\right)+\kappa_1\left(i,j+1,k-1\right)-\kappa_1\left(i,j-1,k-1\right)}{2}\right]u_3\left(i,j,k\right),
\end{aligned}
\tag{3.4b}
$$

$$
\begin{aligned}
&m\left(i,j,k\right)\omega^{2}u_{3}\left(i,j,k\right)=\\
&=-\frac{\kappa_{1}\left(i+1,j,k+1\right)}{2}u_{1}\left(i+1,j,k+1\right)-\frac{\kappa_{1}\left(i-1,j,k+1\right)}{2}u_{1}\left(i-1,j,k+1\right)\\
&+\frac{\kappa_{1}\left(i-1,j,k+1\right)}{2}u_{1}\left(i+1,j,k-1\right)-\frac{\kappa_{1}\left(i-1,j,k-1\right)}{2}u_{1}\left(i-1,j,k-1\right)+\\
&+\left[\frac{\kappa_{1}\left(i+1,j,k+1\right)-\kappa_{1}\left(i-1,j,k+1\right)-\kappa_{1}\left(i+1,j,k-1\right)+\kappa_{1}\left(i-1,j,k-1\right)}{2}\right]u_{1}\left(i,j,k\right)-\\
&-\frac{\kappa_{1}\left(i,j+1,k+1\right)}{2}u_{2}\left(i,j+1,k+1\right)+\frac{\kappa_{1}\left(i,j-1,k+1\right)}{2}u_{2}\left(i,j-1,k+1\right)+\\
&+\frac{\kappa_{1}\left(i,j+1,k-1\right)}{2}u_{2}\left(i,j+1,k-1\right)-\frac{\kappa_{1}\left(i,j-1,k-1\right)}{2}u_{2}\left(i,j-1,k-1\right)+\\
&+\left[\frac{-\kappa_{1}\left(i,j+1,k+1\right)+\kappa_{1}\left(i,j-1,k+1\right)+\kappa_{1}\left(i,j+1,k-1\right)-\kappa_{1}\left(i,j-1,k-1\right)}{2}\right]u_{2}\left(i,j,k\right)\\
&-\Bigg[\frac{\kappa_{1}\left(i,j+1,k+1\right)+\kappa_{1}\left(i,j-1,k+1\right)+\kappa_{1}\left(i,j+1,k-1\right)+\kappa_{1}\left(i,j-1,k-1\right)}{2}\\
&+\frac{\kappa_{1}\left(i+1,j,k+1\right)+\kappa_{1}\left(i-1,j,k+1\right)+\kappa_{1}\left(i+1,j,k-1\right)+\kappa_{1}\left(i-1,j,k-1\right)}{2}\\
&+\kappa_{2}\left(i,j,k+2\right)+\kappa_{2}\left(i,j,k-2\right)+\kappa_{3}\left(i,j+2,k\right)+\kappa_{3}\left(i,j-2,k\right)+\\
&+\kappa_{3}\left(i+2,j,k\right)+\kappa_{3}\left(i-2,j,k\right)\Big]u_{3}\left(i,j,k\right)-\\
&-\frac{\kappa_{1}\left(i,j+1,k+1\right)}{2}u_{3}\left(i,j+1,k+1\right)-\frac{\kappa_{1}\left(i,j-1,k+1\right)}{2}u_{3}\left(i,j-1,k+1\right)-\\
&-\frac{\kappa_{1}\left(i,j+1,k-1\right)}{2}u_{3}\left(i,j+1,k-1\right)-\frac{\kappa_{1}\left(i,j-1,k-1\right)}{2}u_{3}\left(i,j-1,k-1\right)-\\
&-\frac{\kappa_{1}\left(i+1,j,k+1\right)}{2}u_{3}\left(i+1,j,k+1\right)-\frac{\kappa_{1}\left(i-1,j,k+1\right)}{2}u_{3}\left(i-1,j,k+1\right)-\\
&-\frac{\kappa_{1}\left(i+1,j,k-1\right)}{2}u_{3}\left(i+1,j,k-1\right)-\frac{\kappa_{1}\left(i-1,j,k-1\right)}{2}u_{3}\left(i-1,j,k-1\right)-\\
&-\kappa_{2}\left(i,j,k+2\right)u_{3}\left(i,j,k+2\right)-\kappa_{2}\left(i,j,k-2\right)u_{3}\left(i,j,k-2\right)-\\
&-\kappa_{3}\left(i+2,j,k\right)u_{3}\left(i+2,j,k\right)-\kappa_{3}\left(i-2,j,k\right)u_{3}\left(i-2,j,k\right)-\\
&-\kappa_{3}\left(i,j+2,k\right)u_{3}\left(i,j+2,k\right)-\kappa_{3}\left(i,j-2,k\right)u_{3}\left(i,j-2,k\right).
\end{aligned}
\tag{3.4c}
$$

3.1.2. Acoustic phonons in 1D Si-based nanostructures

We calculated phonon energy spectra in 1D nanostructures by solving the Eqs. (3.4) numerically taking into account free-surface boundary conditions in the XY-plane and periodic boundary conditions along axis Z, $u_{i}\left(k\pm N_{z},q\right)=u_{i}\left(k,q\right)Exp\left[\pm\mathbf{i}q\ d_{z}\right]$, where N – is the number of monolayers in the translation period, values of the wave vector q_z belong to the interval $\left(0,\frac{\pi}{d_z}\right)$ for 1D-QDSL and $\left(0,\frac{\pi}{a}\right)$ for NW. Diagonalization of the matrix from Eqs (3.4) was performed using LAPACK library [146] under GCC 8.4 compiler [147].

The influence of the acoustical mismatch on phonon dispersions are shown in Fig. 3.3. In order to compare phonon dispersions of different type of 1D structures we consider Si nanowire and Si/Ge 1D-C-QDSL of the same cross-sections. In order to obtain the same number of phonon branches we treat Si NW as QDSL, which consist of QDs of the same material and dimensions. Both structures have the same geometric parameters: cross-section dimensions $2.70\,\text{nm}\times 2.70\,\text{nm}$ ($10\text{ ML}\times 10\text{ ML}$) and translation period $d_z = 8$ ML, segments of Si and Ge/Si have the same length $d_{z,1} = d_{z,2} = 4$ ML. Similarly to rectangular nanowires [148], phonon modes in 1D-C-QDSL can be classified into four types according to the spatial symmetry of the displacement vector components: *Dilatational*, *Flexural1*, *Flexural2* and *Shear*. For both structures we show phonon branches of Dilatational polarization with numbers s = 0 - 10, 30, 50, …,490, 500, 520, …, 1120. The total number of modes in Si NW and in Si/Ge 1D-C-QDSL is *4332*, and the number of *Dilatational* branches is *1120*. The slope of dispersions in 1D-C-QDSL is less than in the Si NW nearly uniformly in all energy interval. In Fig. 3.3(b) one can see that a lot of phonon modes are concentrated at lower energy values (below green dashed line in Fig. 3.3(b)). It happens because maximal energy of acoustic phonons in Ge (dashed line in Fig. 3.3(b)) is lower than in Si. So, the number of high-energy Si-like modes in QDSL is smaller than that in Si NW. Besides, the slope of the phonon modes with energy higher than ~ 16 meV in 1D-C-QDSL is also smaller than that in NW, especially for energies higher than maximal phonon energy in Ge. Therefore, high energy Si-liked modes become "trapped" in the Ge segments of 1D-C-QDSL due to acoustical mismatch and do not contribute to the thermal transport [23], [24]. Thus 1D-C-QDSL operates like phonon filter, which decreases number of common phonon modes that participate in thermal transport.

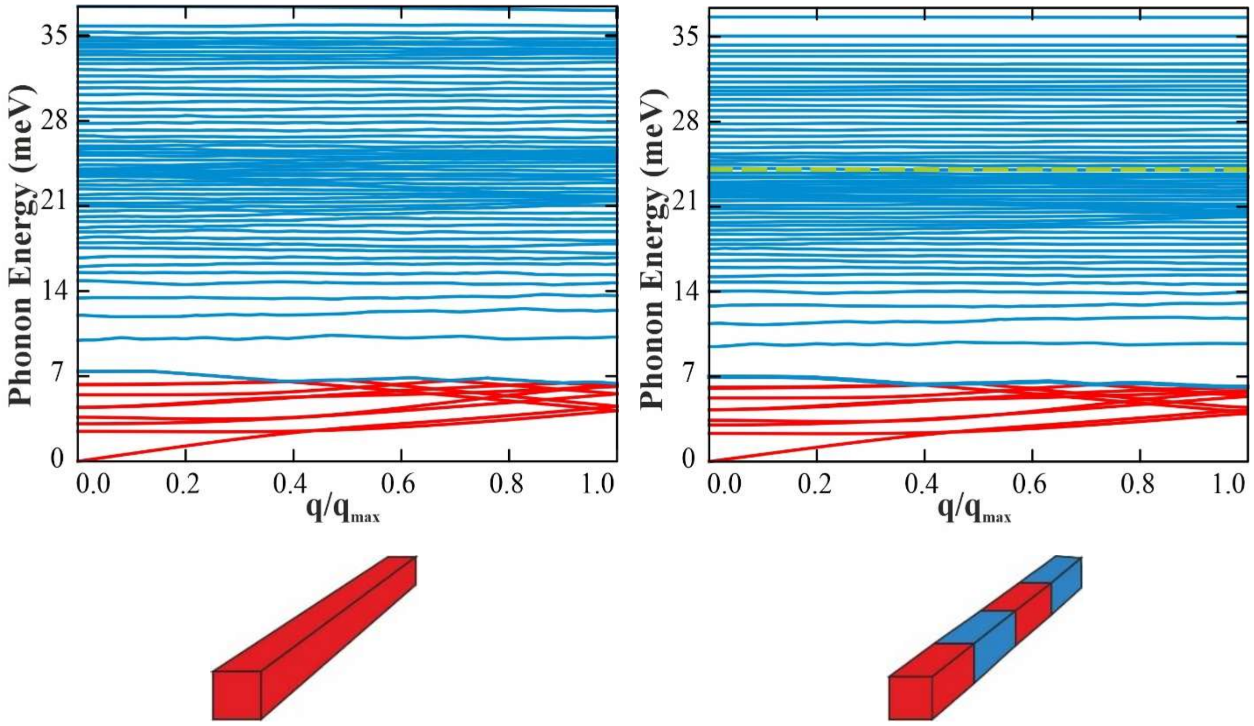

(a) **(b)**

Fig. 3.3. Dilatational modes of acoustic phonon spectra in 1D-C-QDSL

(**a**) Phonon dispersions in homogeneous silicon NW with cross-section dimensions $2.70\ \text{nm} \times 2.70\ \text{nm}$ $(10\ \text{ML} \times 10\ \text{ML})$.

The branches with quantum numbers s = 0-10, 30, 50, …, 490, 500, 520, …, 1120 are shown.

(**b**) Phonon dispersions in Si/Ge 1D-C-QDSL with cross-section dimensions $2.70\ \text{nm} \times 2.70\ \text{nm}$ $(10\ \text{ML} \times 10\ \text{ML})$

The branches with quantum numbers s = 0-10, 30, 50, …, 490, 500, 520, …, 1120 are shown.

The next type of the investigated 1D-QDSL is M-QDSL formed from Si and Ge QDs with different cross-sections, but same length along OZ. In Fig. 3.4 we depicted phonon modes of all polarization types. In the case of the M-QDSL we cannot obtain quite the same number the phonon modes, so in order to make comparison more fair we took Si homogeneous NW with the same cross-section as have Si QDs in M-QDSL and had same translation period as M-QDSL. The phonon dispersions with different polarization are shown for Si NW with cross-section $10\ \text{ML} \times 10\ \text{ML}$ and translation period in Fig. 3.4 (a). The dependencies for Si/Ge 1D-M-QDSL with following geometric parameters: Si QDs $d_{x,1} = d_{y,1} = 10$ ML and $d_{z,1} = 2$ ML, Ge QDs $d_{x,2} = d_{y,2} = 12$ ML and $d_{z,2} = 2$ ML are presented in Fig. 3.4 (b). For the Si NW, we show phonon branches with following numbers for *Dilatational*: s = 1-9, 10, 15, 20 -70, 80, …, 130; *Shear*: s = 1-9, 10, 15, 20, …, 70, 80-110; *Flexural1*: s = 1-9, 10, 13, 16, …, 48, 58, …, 118 and

Flexural2: s = 1-9, 10, 14, 18, …, 48, 58, 61, 64, …, 121 polarizations. The total number of modes in Si NW is 2166. For the Si/Ge M-QDSL, we show phonon branches with following numbers for *Dilatational*: s = 1-9, 10, 12, 14, …, 50, 51, 54, …, 105; *Shear*: s = 1-9, 10, 12, 14, …, 50, 51, 53, ..., 89; *Flexural1:* s = 1-9, 10, 13, 16, …, 48, 58, 60, …, 98; and *Flexural2:* s = 1-9, 10, 14, 18, …, 48, 58, 61, …, 97. Total number of modes in the presented Si/Ge 1D-M-QDSL is 2670. Number of the phonon modes in 1D-M-QDSL is higher because of the higher number of atoms in the translation element. Likewise, in the case of 1D-C-QDSL, one can see many nearly horizontal dispersion curves for higher energies in comparison with Si NW. However, in the case of the M-QDSL this effect takes place starting from energies $\hbar\omega > 5\text{ meV}$. In Ref. [24] it has been demonstrated that in the case of the homogeneous undulated (modulated) nanowires the phonon modes in the wide segments represent standing waves that do not propagate along the nanowire. This fact leads to an increase of the number of dispersionless modes trapped in QDSL segments and amplifies the effect of acoustical mismatch.

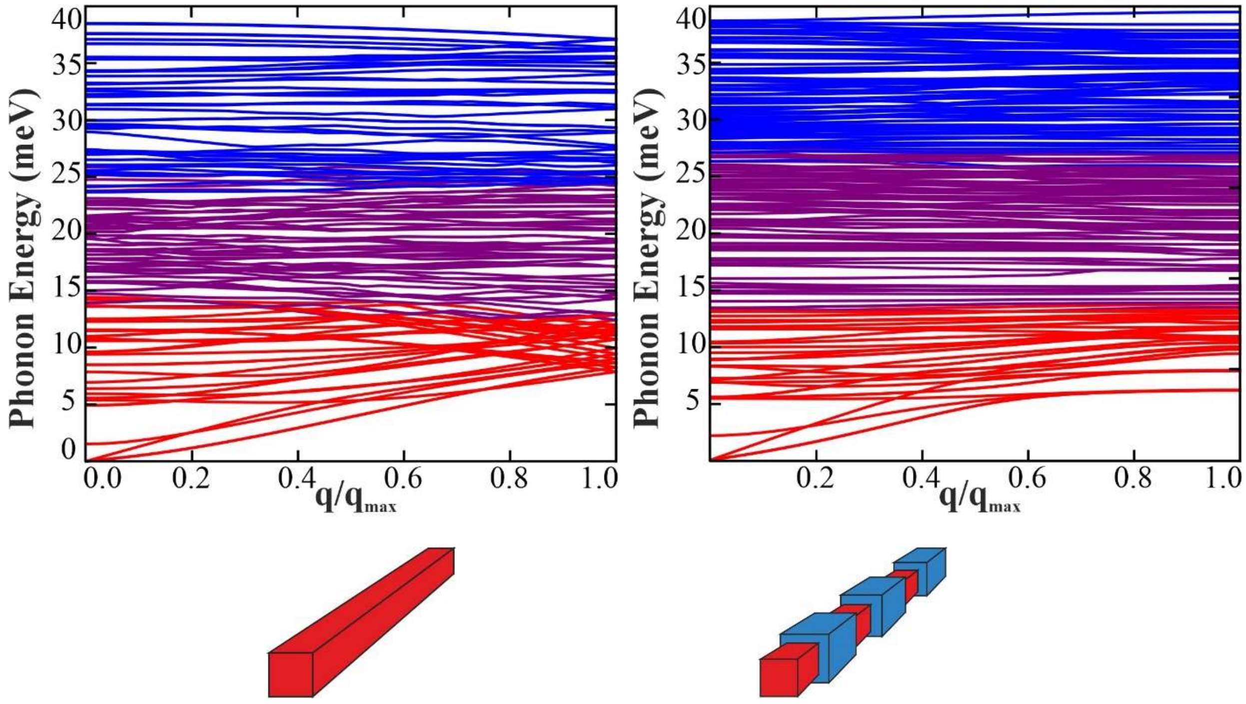

(a) **(b)**

Fig. 3.4. Acoustic phonon spectra in 1D-M-QDSL.

(a) Si $10ML\times 10ML$ *Dilatational*: 1-9, 10, 15, 20 -70, 70, 80-130; *Shear*: 1-9, 10, 15, 20-70, 70, 80-110; *Flexural1*: 1-9, 10, 13, 16 -48, 48, 58-118; *Flexural2*: 1-9, 10,14,18 -48, 58, 61-121;
(b) SiGe $9\text{ ML}\times 9\text{ ML}\times 2\text{ ML}-11\text{ ML}\times 11\text{ ML}\times 2\text{ML}$: *Dilatational*: 1-9, 10, 12, 14 -50, 51, 54-105; *Shear*: 1-9, 10, 12, 14-50, 51, 53-89; *Flexural1*: 1-9, 10, 13, 16 -48, 58, 60 -98; *Flexural2*: 1-9, 10, 14, 18-48, 58, 61-97.

The effect of phonon deceleration due to the influence of the phonon confinement is known for different nanostructures, including 1D structures [117], [118]. The phonon engineering can be used to enhance the drop of a phonon group velocity. The acoustical mismatch of materials and varying geometric parameters of the 1D-QDSL allows one to decrease velocity more significant. To demonstrate the effect of the phonon deceleration we calculated APGV in Si/Ge 1D-C-QDSL and 1D-M-QDSL. The average phonon group velocity was calculated by formula:

$$\langle v\rangle(\omega)=\frac{g(\omega)}{\sum_{s(\omega)}\left(dq_z/d\omega_s\right)} \qquad (3.5)$$

The result of the calculations is depicted in Fig. 3.5. The comparison of the APGV of the phonon energy in Si NW and Si/Ge 1D-C-QDSL are shown in Fig. 3.5 (a). Red line corresponds to Si NW, while the green one is for Si/Ge 1D-C-QDSL. Both structures have same cross-section $19\ \mathrm{ML}\times 19\ \mathrm{ML}$. Translation period for 1D-C-QDSL is $d_z = 8\ \mathrm{ML}$. The provided curves demonstrate the influence of the acoustical mismatch of materials on phonon properties. The APGV in Si/Ge 1D-C-QDSL is lower than in Si NW in all energy interval, it is more visible starting from energies greater than $\sim 5\,\mathrm{meV}$, when the velocity drops in ~ 1.7 times. For energies lower than $15\ \mathrm{meV}$ APGV is oscillating in the range $0-0.5\ \mathrm{km/s}$. Such character of the APVG dependency demonstrate the exclusion of the high-energy phonon levels from the phonon transport.

The effect of the APGV drop due to acoustical mismatch of the materials can be amplified by geometric parameters of the 1D-QDSL. In Fig. 3.5 (b) the comparison of the APVG energy dependencies in Si NW (red line) and Si/Ge 1D-M-QDSL (blue line) is shown. The cross-section of the Si NW was $9\ \mathrm{ML}\times 9\ \mathrm{ML}$. Geometric parameters of the Si/Ge 1D-M-QDSL were as follows: cross-section of the Si QD was $9\ \mathrm{ML}\times 9\ \mathrm{ML}$, equal to the cross-section of the NW, cross-section of the Ge elements was $15\ \mathrm{ML}\times 15\ \mathrm{ML}$; along the OZ the lengths of the QDs were $d_{z,Si} = d_{z,Ge} = 8\ \mathrm{ML}$, total length of the translation period was $d = 16\ \mathrm{ML}$. The bulk sound velocity values are not reached even for Si NW, maximum PGVs in Si are longitudinal $v_l = 8.48\ \mathrm{km/s}$ and transversal $v_t = 5.86\ \mathrm{km/s}$ [19]. In the case of the Si/Ge 1D-C-QDSL PGV is lower than its maximum values in the bulk Ge, $v_l = 5.13\ \mathrm{km/s}$ and $v_t = 3.36\ \mathrm{km/s}$ [19]. The confinement of the phonon leads to the more explicit drop of the APGV even for low energy range $0-5\ \mathrm{meV}$. Values become close to 0 starting from energies greater than $\sim 12\ \mathrm{meV}$.

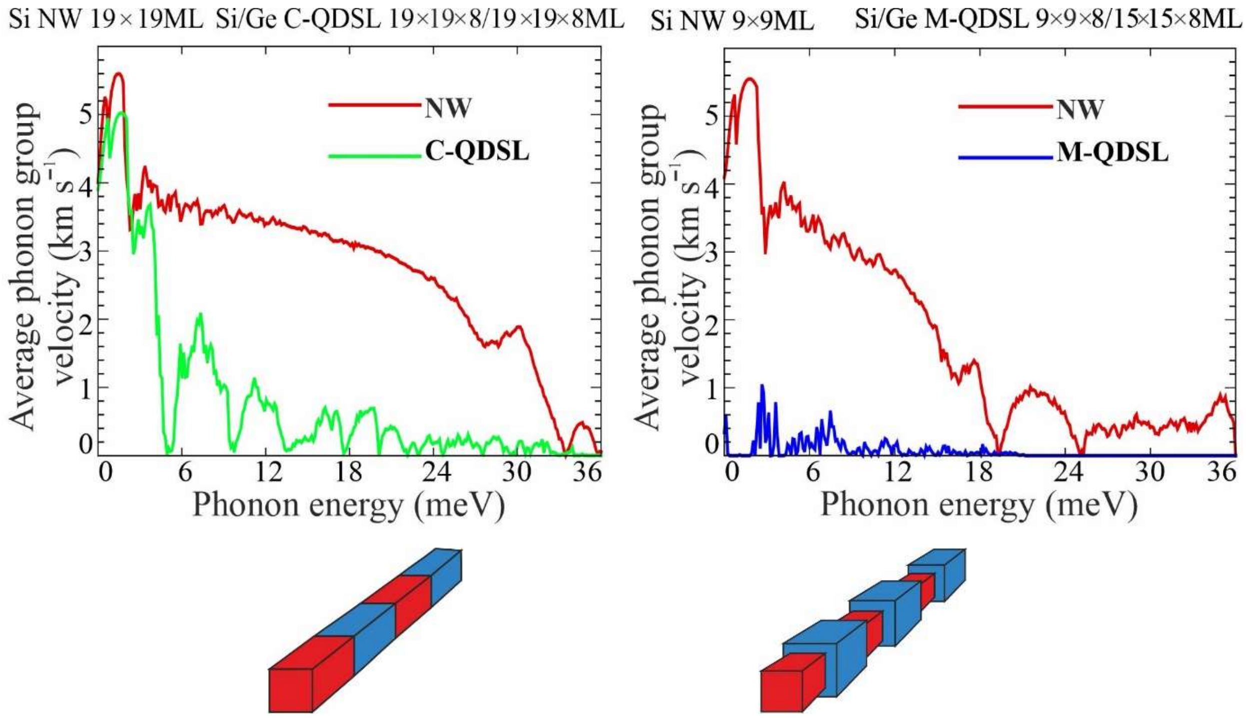

(a) **(b)**

Fig. 3.5. Average phonon group velocities in
(a) 1D-C-QDSL; **(b)** 1D-M-QDSL**.**

The maximum APGV of the Si/Ge 1D-M-QDSL is nearly 5.5 times lower than the maximum one in the Si NW, and nearly 5.0 times lower then maximum in Si/Ge 1D-C-QDSL. Velocity becomes less than $1\ {}^{\mathrm{km}}\!/_{\mathrm{s}}$ starting from $3\ \mathrm{meV}$ in Si/Ge 1D-M-QDSL and from energies greater than $10\ \mathrm{meV}$ in Si/Ge 1D-C-QDSL, so more phonon modes with the higher energies are excluded from the phonon transport. All these facts show that phonon confinement enhances the effect of the acoustical mismatch and leads to the drastically drop of APGV.

3.2. Phonon thermal flux and phonon thermal conductivity

For calculation of the phonon thermal flux in 1D nanostructures, we used the following expression, which was derived from the Boltzmann transport equation within the relaxation time approximation [30–33] taking into account one-dimensional density of phonon states

$$\Theta = \frac{1}{2\pi k_B T^2} \sum_{s=1,\dots,3N} \int_0^{q_{\max}} \left(\hbar\omega_s\left(q_z\right)\upsilon_{z,s}\left(q_z\right)\right)^2 \tau_{tot,s}\left(q_z\right) \frac{\exp\left(\frac{\hbar\omega_s\left(q_z\right)}{k_B T}\right)}{\left(\exp\left(\frac{\hbar\omega_s\left(q_z\right)}{k_B T}\right)-1\right)^2} dq_z\,. \tag{3.6}$$

Here $\tau_{tot,s}$ is the total phonon relaxation time, *s* is the number of a phonon branch, k_B is the Boltzmann constant, $\hbar$ is the Planck constant and *T* is the absolute temperature, *ω* is phonon frequency, υ_Z is the *Z*-th component of the phonon group velocity.

According to the Matthiessen's rule, the total phonon relaxation time is given by:

$$\frac{1}{\tau_{tot,s}(q_z)} = \sum \frac{1}{\tau_{mechanism}(q_z)}, \tag{3.7}$$

where $\tau_{mechanism}$ is the relaxation time specific for scattering mechanism.

Lattice thermal conductivity for 1D-C-QDSL were calculated as

$$\kappa_{ph}^{NW,NT} = \frac{\Theta}{S_{NW,NT}}, \tag{3.8a}$$

while for 1D-M-QDSL

$$\kappa_{ph}^{M-QDSL} = \frac{\Theta(l_1 + l_2)}{\left(d_{x,1} d_{y,1} l_1 + d_{x,2} d_{y,2} l_2\right)}. \tag{3.8b}$$

We have taken into account all basic mechanisms of phonon scattering: three-phonon Umklapp scattering, boundary and impurity scatterings [31–38]. Umklapp-scattering was calculated using following expression [31], [149]:

$$\frac{1}{\tau_{U,s}(q_z)} = B(\omega_s(q_z))^2 T \exp(-C/T); \tag{3.9a}$$

impurity scattering [25], [31] was taken as:

$$\frac{1}{\tau_{imp,s}(q_z)} = A(\omega_s(q_z))^4; \tag{3.9b}$$

while boundary scattering calculation formula in the case of 1D structures with the constant cross-section: NW and 1D-C-QDSL took form:

$$\frac{1}{\tau_{B,s}(q_z)} = \frac{1-p}{1+p} \frac{|\upsilon_{z,s}(q_z)|}{2} \left(\frac{1}{d_x} + \frac{1}{d_y}\right), \tag{3.9c}$$

while in the case of a 1D-M-QDSL it is

$$\begin{aligned} \frac{1}{\tau_{B,s}(q_z)} = \frac{1-p}{1+p} \frac{|\upsilon_{z,s}(q_z)|}{2} \Bigg(& \left(\frac{1}{d_{x,1}} + \frac{1}{d_{y,1}}\right) \int_{-d_{x,1}/2}^{d_{x,1}/2} \int_{-d_{y,1}/2}^{d_{y,1}/2} \int_{0}^{l_1} \left|\vec{w}_s(x,y,z;q_z)\right|^2 dx dy dz + \\ & + \left(\frac{1}{d_{x,2}} + \frac{1}{d_{y,2}}\right) \int_{-d_{x,2}/2}^{d_{x,2}/2} \int_{-d_{y,2}/2}^{d_{y,2}/2} \int_{l_1+a/4}^{l_1+l_2} \left|\vec{w}_s(x,y,z;q_z)\right|^2 dx dy dz \Bigg). \end{aligned} \tag{3.9d}$$

Parameters A, B and C from Eqs (3.9a-3.9b) were fitted from a comparison of the thermal conductivity calculated for bulk silicon with experimental data [24], [25], [28], [150]. The following values of parameters are used for relaxation rate calculations (see Eqs. (3.9a-3.9b)): $A = 1.32\times10^{-9}\ \mathrm{s}^3$, $B = 1.88\times10^{-19}\ \mathrm{s/K}$, and $C = 137.39\ \mathrm{K}$. In Eqs. (3.9c-3.9d) $\upsilon_{z,s}\left(q_z\right) = \dfrac{d\omega_s\left(q_z\right)}{dq_z}$ is the phonon group velocity along the nanowire axis, p is the specularity parameter of the boundary scattering, and $\vec{w}_s(x, y, z; q_z)$ is a displacement vector. Specularity parameters p varies from 0 (strong pure diffusive scattering) to 1 (no boundary scattering, pure phonon specular). Equations (3.9c-3.9d) provide an extension of the standard formula for the rough edge scattering [151] to the case of a rectangular NW or 1D-M-QDSL. In Eq. (3.9d) we take into account the fact that a part of the phonon wave corresponding to the mode $\left(s, q_z\right)$, concentrated in the 1D-M-QDSL segment *1* with geometry dimensions $d_{x,1}\times d_{y,1}\times d_{z,1}$ scatters on the boundaries of this segment, while the rest of this wave scatters on the boundaries of the segment *2* with dimensions $d_{x,2}\times d_{y,2}\times d_{z,2}$. The specularity parameter p characterizes the phonon-boundary scattering. Depending on the boundary roughness, p can take values between $p = 0$ (pure diffusive scattering) and $p = 1$ (pure specular scattering).

In Fig. 3.6. we show the phonon thermal conductivity as a function of cross-section dimensions (a) and of temperature (b) for Si/Ge 1D-C-QDSLs.

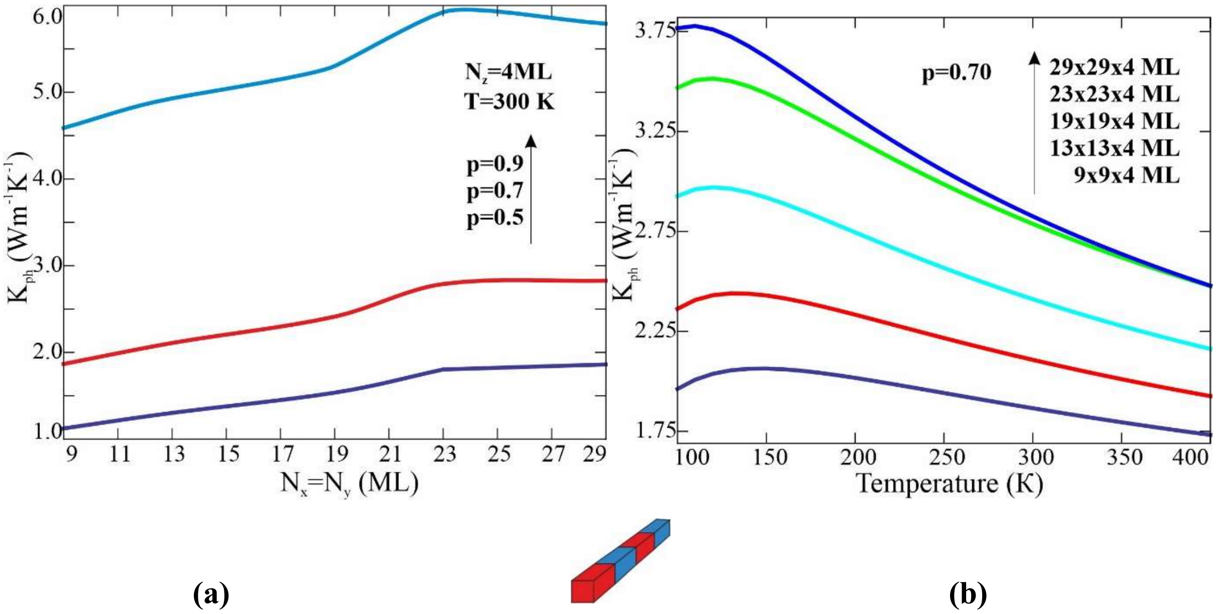

Fig. 3.6. Phonon thermal conductivity in segmented Si/Ge 1D-C-QDSLs
(a) Cross-section dependency; **(b)** Temperature dependency

The cross-section dependencies in Fig.3.6 (a) are shown for specularity parameters values $p = 0.9, 0.7, 0.5$ and temperature $T = 300\,\mathrm{K}$. Thermal conductivity is higher for higher values of the specularity parameter because boundary scattering becomes weaker. Increase of the cross-section dimensions firstly leads to growth of the thermal conductivity, but then it turns to saturation (approximatively at $21\,\mathrm{ML} \times 21\,\mathrm{ML}$) and slightly goes down at $23\ \mathrm{ML}\times 23\ \mathrm{ML}$. It happens due to interplay of two opposite mechanisms: increasing of the number of the phonon modes carrying heat, tending to increase of the thermal conductivity and increasing of phonon scattering with rise of QDSL cross-section, tending to decrease thermal conductivity.

The Fig. 3.6 (b) shows temperature dependencies for 1D-C-QDSL with different cross-section dimensions $9\ \mathrm{ML}\times 9\ \mathrm{ML}\times 4\ \mathrm{ML}$, $13\mathrm{ML}\times 13\mathrm{ML}\times 4\mathrm{ML}$, $19\mathrm{ML}\times 19\mathrm{ML}\times 4\mathrm{ML}$, $23\mathrm{ML}\times 23\mathrm{ML}\times 4\mathrm{ML}$ and $29\mathrm{ML}\times 29\mathrm{ML}\times 4\mathrm{ML}$, while specularity parameter value was fixed $p = 0.7$. The curves with cross-sections in the range $9\ \mathrm{ML} - 23\ \mathrm{ML}$ have higher conductivity values in all presented temperature range $100\mathrm{K} - 400\mathrm{K}$. The difference between thermal conductivity values of the Si/Ge 1D-C-QDSL with cross-section $29\mathrm{ML}\times 29\mathrm{ML}$ and with $23\ \mathrm{ML}\times 23\ \mathrm{ML}$ one are less than $10\,\%$ for low temperatures range $100\,\mathrm{K} - 150\,\mathrm{K}$ and becomes even smaller while the temperature grows. Dependencies nearly coincides at the temperatures higher than $\sim 330\,\mathrm{K}$. The process of the phonon's scattering with the temperature becomes more significant than the increase of the phonon modes' number in the case of the cross-section larger than $23\ \mathrm{ML}\times 23\ \mathrm{ML}$. The intensification of the Umklapp scattering and population of the higher phonon energy levels, which have near-zero phonon group velocity, due to the increase of the temperature contribute to the thermal conductivity drop. However, all presented temperature dependencies have maxima in the range $100\mathrm{K} - 150\mathrm{K}$. The maximum in temperature dependencies appears when the relaxation time of Umklapp and boundary scattering, which does not depend on temperature, became approximatively equal $\tau_u \approx \tau_b$. The maximums' position shift takes place because boundary scattering is stronger in smaller 1D-C-QDSL and it doesn't depend on the temperature as Umklapp scattering, so the condition $\tau_u \approx \tau_b$ is met at the lower temperature values in the case of 1D-QDSL s with larger cross-section.

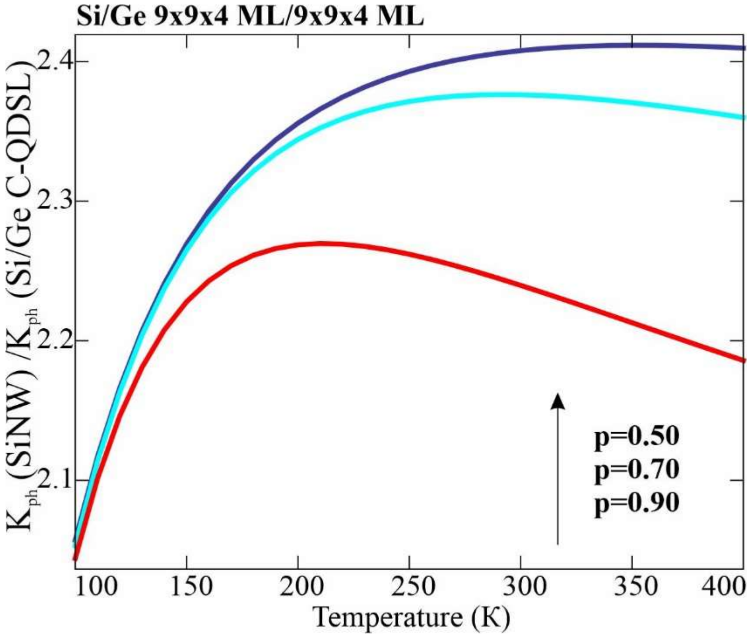

Fig. 3.7. Temperature dependence of the thermal conductivity ratio in Si/Ge 1D-C-QDSL

In Fig. 3.7 the ratio of thermal conductivities in Si/Ge C-QDSL and Si NW with the same cross-sections is shown as a function of the temperature. The curves are shown for three values of the specularity parameters: $p = 0.5, 0.7, 0.9$. The dimensions of Si and Ge segments are the same: $9\ \mathrm{ML} \times 9\ \mathrm{ML} \times 4\ \mathrm{ML}$. The curve for $p = 0.9$ has a prominent maximum at the $T \approx 190\,\mathrm{K}$. The Decrease of p leads to a shift of maximum to higher temperatures and to enlarge its width. The behavior of ratio curves is explained by a complicated interplay of different factors: (i) increase of phonon modes population with temperature, tending to enhance the phonon transport; (ii) increase of phonon Umklapp scattering, tending to suppress the phonon transport and (iii) different manifestation of these effects in the case of bare NW and 1D-C-QDSL.

In Fig. 3.8 the ratio of the thermal conductivity in Si/Ge 1D-C-QDSL to the homogeneous Si NW with the corresponding cross-section is provided. We varied specularity parameter values $p = 0.9, 0.7, 0.5$ and fixed temperature $T = 300\,\mathrm{K}$ for the dependencies in Fig. 3.8 (a), and vice versa, fixed the specularity parameter $p = 0.7$ and changed temperatures $T = 100\,\mathrm{K}$, $200\,\mathrm{K}$, $300\,\mathrm{K}$, $400\,\mathrm{K}$ in Fig. 3.8 (b). Translation period was $N_z = 4\,ML$ in both cases. The presented ratio dependencies on the QDSL cross-section have maximum. The continues increase of the cross-section means more atoms, and phonons as well, participating in heat propagation either in C-QDSL and in NW. The effect of the modes trapped in the QDSL segments and of additional phonon scattering become not so significant and ratio dependency goes throw its maximum in the range $17\,\mathrm{ML} \times 17\,\mathrm{ML} - 23\,\mathrm{ML} \times 23\,\mathrm{ML}$ at the temperature $T = 300\,\mathrm{K}$ (see, Fig. 3.8(a)). The maximum drop of thermal flux is up to $2.6 - 2.9$ times. The more significant drop corresponds to smaller specularity parameter value. The shift of the maxima toward larger cross section for smaller specularity parameter is the result of interplay of the increasing number of the phonon modes and boundary scattering. The curves in Fig. 3.8 (b) demonstrate the most significant drop of the thermal transport is reached at the higher temperatures. The thermal transport drop at $200\,\mathrm{K}$ is with $\sim 25\ \%$ more than at the $T = 100\,\mathrm{K}$. The difference between values at $200\,\mathrm{K}$, $300\,\mathrm{K}$, $400\,\mathrm{K}$ is in the range $1\% - 4\%$. With higher temperatures phonons start to populate higher energy levels with near-zero values of the phonon velocity that leads to the more essential drop of the thermal flux, but subsequent continues population doesn't influence the flux much. The intensification of the Umklapp scattering leads to the shift of the dependencies' maxima toward smaller cross-section with the increase of temperature.

The thermal flux in Si/Ge 1D-C-QDSL is lower than in the Si NWs due to different process that undergoes in 1D-C-QDSL: high energy phonon modes are trapped within Ge segments with lower sound velocity, Umklapp scattering and scattering at segments' interfaces.

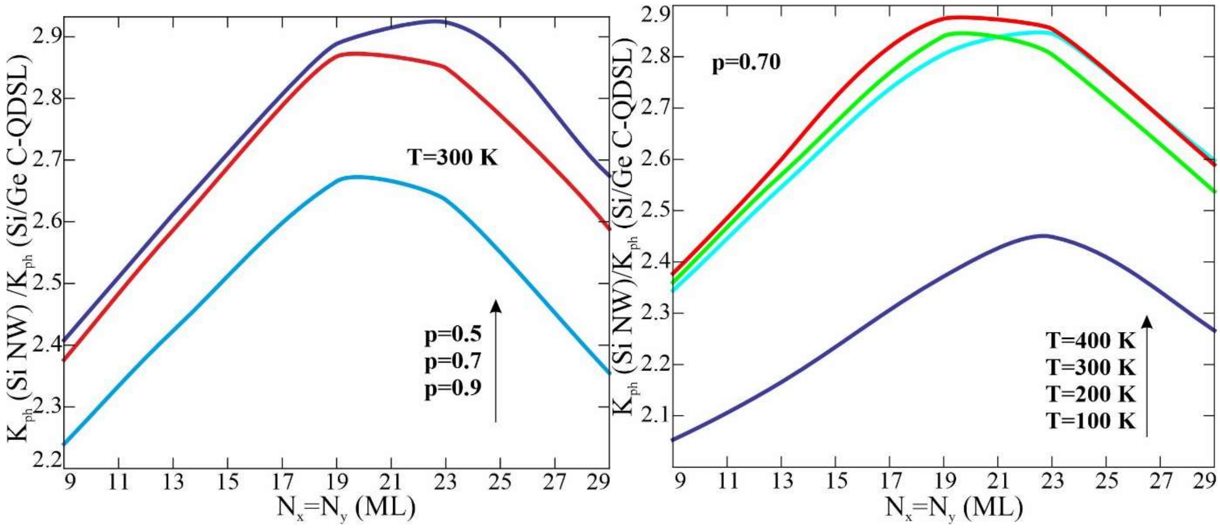

(a) **(b)**

Fig. 3.8. Cross-section influence on thermal conductivity ratio in Si/Ge 1D-C-QDSL (a) constant temperature value $T = 300\,\mathrm{K}$; **(b)** constant specularity parameter $p = 0.7$.

The Fig. 3.9 shows the influence of the translation period on thermal properties of the 1D-C-QDSL. In Fig. 3.9 (a) the dependence of thermal conductivity in the Si/Ge 1D-C-QDSL with different translation periods on temperature is shown. We fixed the cross-section of the 1D-C-QDSL at $9\,\mathrm{ML} \times 9\,\mathrm{ML}$ and the specularity parameter at $p = 0.7$. Translation period N_z values were taken as follows: $4\,\mathrm{ML}$, $8\,\mathrm{ML}$, $12\,\mathrm{ML}$, $16\ \mathrm{ML}$.

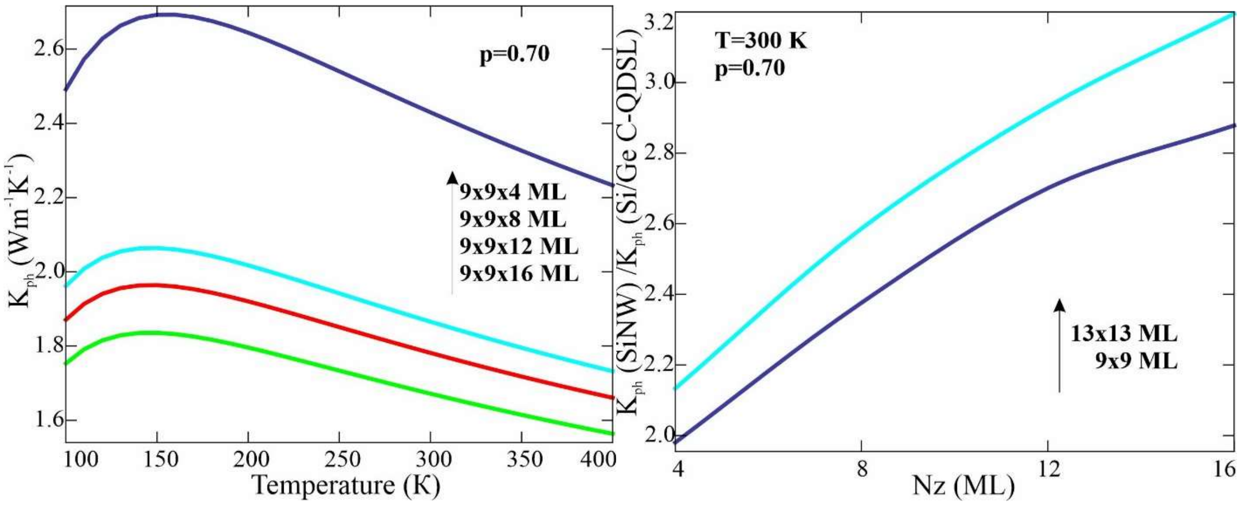

(a) (b)

Fig. 3.9. Influence of 1D-C-QDSL's period on thermal conductivity

(a) Temperature dependence of thermal conductivity for Si/Ge 1D-C-QDSL with cross-section $N_x \times N_y$: $9\,\mathrm{ML} \times 9\,\mathrm{ML}$ $(2.43\,\mathrm{nm} \times 2.43\,\mathrm{nm})$ and different translation period: green $- N_z =$ $16\,\mathrm{ML} = 4.32\,\mathrm{nm}$, red $- N_z =$ 12 $\mathrm{ML} = 3.24$ nm , cyan $- N_z =$ $8\,\mathrm{ML} = 2.16$ nm, blue $- N_z = 4\,\mathrm{ML} = 1.08$ nm ;

(b) Ratio of thermal conductivities in SN and 1D-C-QDSL as a function of 1D-C-QDSL's period N_z: blue – $N_x \times N_y$: $9\,\mathrm{ML} \times 9\,\mathrm{ML}$ $(2.43\,\mathrm{nm} \times 2.43\,\mathrm{nm})$, cyan – $N_x \times N_y$: $13\,\mathrm{ML} \times 13\,\mathrm{ML}$ (3.51 $\mathrm{nm} \times 3.51\,\mathrm{nm}$).

Thermal conductivity possesses higher values for 1D-C-QDSL with smaller N_z values. All dependencies demonstrate a maximum in the range of the temperatures $120\,\mathrm{K} - 150\,\mathrm{K}$. This maximum is explained by the intensification of the Umklapp scattering with the temperature. It slightly shifts toward higher temperatures because boundary scattering is stronger in the 1D-QDSL with a smaller translation period N_z, so the condition $\tau_u \approx \tau_b$ is met at higher temperatures. The thermal conductivity in 1D-C-QDSL with $N_z = 4\,\mathrm{ML}$ is ~ 1.25 times smaller than in 1D-C-QDSL with $N_z = 8\,\mathrm{ML}$ in the large interval of temperature ($100\,\mathrm{K} - 400\,\mathrm{K}$). The continuous increase of translation element length N_z reduces thermal conductivity, but the drop is not significant $\sim 1.0 - 1.1$ in comparison with 1D-C-QDSL with $N_z = 4$ ML.

Fig. 3.9 (b) shows the dependence of the room temperature thermal conductivity ratio on the translation period in 1D-C-QDSL. The results are shown for 2 different cross-sections: $N_x \times N_y$: $9\,\mathrm{ML} \times 9\,\mathrm{ML}$ and $N_x \times N_y$: $13\,\mathrm{ML} \times 13\,\mathrm{ML}$, and specularity parameter $p = 0.7$. The ratio between thermal conductivity in Si NW and Si/Ge 1D-C-QDSL increases together with translation period length N_z and is higher for larger cross-sections. However, we expect that thermal conductivity ratio as a function of C-QDSL sizes will reach maximal value for certain dimensions and then will start to decrease, approaching value of 1 for C-QDSL with micrometre dimensions. The latter is explained by weakening of phonon modes trapping with increase of N_x, N_y and/or N_z. In the range of $N_z = 4\,\mathrm{ML} - 16\,\mathrm{ML}$ ratio increases: $\sim 2.0 - 2.8$ for 1D-C-QDSLs with cross-section $9\,\mathrm{ML} \times 9\,\mathrm{ML}$ and $\sim 2.2 - 3.2$ 1D-C-QDSLs with cross-section $13\,\mathrm{ML} \times 13\,\mathrm{ML}$. Thermal conductivity in Si/Ge 1D-C-QDSL with $N_z = 16\,\mathrm{ML}$ is ~ 3.0 time lower than in Si NW for room temperature which thermal conductivity is ~ 20 time lower than in bulk Si. Thermal transport in Si/Ge 1D-C-QDSL is lower in comparison with bulk material due to the trapped phonon modes excluded from thermal transport.

It is already known that the thermal transport in cross-section-modulated nanowires is reduced in comparison with the smooth NW with constant cross-section due to stronger phonon confinement [24]. To enhance the suppression of thermal flux we investigated 1D-QDSL formed from different materials Si and Ge with different cross-sections of QD. In Fig. 3.10 a dependence of thermal flux on the temperature in Si/Ge 1D-M-QDSL is shown for temperatures $100K - 400K$. Specularity parameter took values $p = 0.5$ (blue lines), $p = 0.7$ (green lines), and $p = 0.9$ (red lines). We fixed the cross-section of the Si QDs for each panel of Fig 3.10, so the M-QDSL had the following geometric parameters of cross-section in panel **(a):** $\mathrm{Si}:7\,\mathrm{ML} \times 7\,\mathrm{ML} - \mathrm{Ge}:9\,\mathrm{ML} \times 9\,\mathrm{ML}$ ($1.89\,\mathrm{nm} \times 1.89\,\mathrm{nm} - 2.43\,\mathrm{nm} \times 2.43\,\mathrm{nm}$), $\mathrm{Si}:7\,\mathrm{ML} \times 7\,\mathrm{ML} -$ $\mathrm{Ge}:15\,\mathrm{ML} \times 15\,\mathrm{ML}$ ($1.89\,\mathrm{nm} \times 1.89\,\mathrm{nm} - 4.05\,\mathrm{nm} \times 4.05\,\mathrm{nm}$), and in panel **(b):** $\mathrm{Si}:9\,\mathrm{ML} \times 9\,\mathrm{ML} -$ $\mathrm{Ge}:11\,\mathrm{ML} \times 11\,\mathrm{ML}$ ($2.43\,\mathrm{nm} \times 2.43\,\mathrm{nm} -$ $2.97\,\mathrm{nm} \times 2.97\,\mathrm{nm}$), $\mathrm{Si}:9\ \mathrm{ML} \times 9\ \mathrm{ML} -$ $\mathrm{Ge}:15\ \mathrm{ML} \times 15\ \mathrm{ML}$ ($2.43\,\mathrm{nm} \times 2.43\,\mathrm{nm}$ $-$ $4.05\,\mathrm{nm} \times 4.05\,\mathrm{nm}$). Translation period of the M-QDSL length was $N_z =$ $8\,\mathrm{ML} = 2.16\,\mathrm{nm}$.

Thermal flux is more for higher values of the specularity parameter for the 1D-M-QDSL of the equal dimensions of Ge QDs because of less intensive boundary scattering. Thermal flux for specularity parameter $p = 0.9$ decreases with the temperature rise for all geometries presented in Fig. 3.10. The dependencies shown for specularity parameter $p = 0.7$ decreases uniformly in all temperature interval. However the slope of the M-QDSL with $N_{x,2} = N_{y,2} = 9$ ML demonstrates more rapid decline than with $N_{x,2} = N_{y,2} = 15$ ML. The curves with $p = 0.5$ and closer values for the cross-section of the Si and Ge QDs $N_{x,1} = N_{y,1} = 7$ ML and $N_{x,2} = N_{y,2} = 9$ ML, or $N_{x,1} = N_{y,1} = 9$ ML and $N_{x,2} = N_{y,2} = 11$ ML, are similar to the temperature dependencies for C-QDSL, there is a slight maximum near $T = 200$ K. The dependencies for $p = 0.5$, but with Ge QDs with cross-section $15\ \mathrm{ML} \times 15\ \mathrm{ML}$ do not have maxima, but the slope of the curve become smaller for temperatures greater than $T = 200$ K.

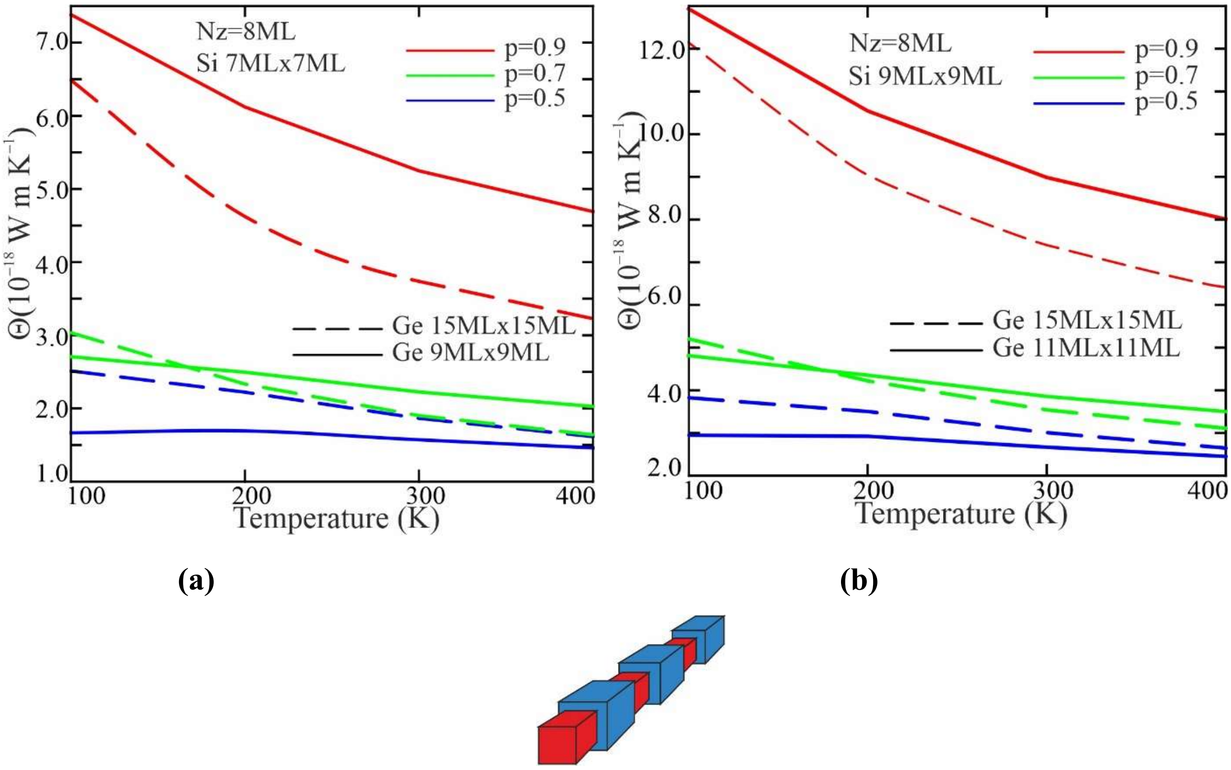

(a) **(b)**

Fig. 3.10. Thermal flux dependence on temperature in Si/Ge 1D-M-QDSL

Translation period $N_z = 8$ ML and specularity parameter $p = 0.5$ (blue lines), $p = 0.7$ (green lines), and $p = 0.9$ (red lines)

(a) *Si QD:* $N_{x,1} = N_{y,1} = 7$ ML. Dashed lines – *Ge QD*: $N_{x,2} = N_{y,2} = 15$ ML,

Continuous lines – $N_{x,2} = N_{y,2} = 9$ ML;

(b) *Si QD*: $N_{x,1} = N_{y,1} = 9$ ML, Dashed lines – *Ge QD*: $N_{x,2} = N_{y,2} = 15$ ML,

Continuous lines – $N_{x,2} = N_{y,2} = 11$ ML.

Number of phonon modes is obviously lager in the case of the 1D-QDSL with larger cross-section. The contribution of the different segments in the case of the 1D-M-QDSL into boundary scattering is inversely to their cross-section due to the factor $\left(\frac{1}{d_{x,i}} + \frac{1}{d_{y,i}} \right)$, see Eq. 3.9(d). So, if we fix dimension of the Si QD and will increase the dimension of the Ge one, we can suppose the higher values of the thermal flux in the case of the M-QDSL with $N_{x,2} = N_{y,2} = 15\text{ ML}$, rather than in the case of $N_{x,2} = N_{y,2} = 9\text{ ML}$ or $N_{x,2} = N_{y,2} = 11\text{ ML}$. This behaviour we see for the curves with $p = 0.5$. Though, in the case of the specularity parameter $p = 0.9$ thermal flux of the 1D-M-QDSL with $Si:7\text{ML}\times 7\text{ML}-Ge:15\text{ML}\times 15\text{ML}$ is lower than thermal flux in M-QDSL $Si:7\text{ML}\times 7\text{ML}-Ge:9\text{ML}\times 9\text{ML}$, and in the $Si:9\text{ ML}\times 9\text{ ML}-Ge:15\text{ ML}\times 15\text{ ML}$ is lower than in $Si:9\text{ML}\times 9\text{ML}-Ge:11\text{ML}\times 11\text{ML}$.

The dependencies obtained for the specularity parameter $p = 0.7$ demonstrates intermediate case: the thermal flux is more intensive for Ge QDs with a cross-section $N_{x,2} = N_{y,2} = 15\text{ ML}$ than with the smaller ones at temperatures less than 170K. But situation changes for the higher temperatures: the M-QDSL with Ge QDs $N_{x,2} = N_{y,2} = 9\text{ ML}$, in the case of Si QD $N_{x,1} = N_{y,1} = 7\text{ ML}$, or with Ge QDs $N_{x,2} = N_{y,2} = 11\text{ ML}$, in the case of Si QD $N_{x,1} = N_{y,1} = 9\text{ ML}$. It demonstrates that behaviour of the phonons is more complex. Despite the factor $\left(\frac{1}{d_{x,i}} + \frac{1}{d_{y,i}}\right)$ that decreases contribution of the 1D-M-QDSL segment into scattering inverse to its cross-section, we cannot predict the value of the integral $\int_{-d_{x,2}/2}^{d_{x,2}/2} \int_{-d_{y,2}/2}^{d_{y,2}/2} \int_{l_1+a/4}^{l_1+l_2} \left|\vec{w}_s(x,y,z;q_z)\right|^2 dxdydz$. The redistribution and deceleration of the phonon modes leads to more complex behaviour of the thermal flux dependencies, while thermal conductivity demonstrates increase with the increase of the atoms number in 1D-M-QDSL.

In Fig. 3.11 thermal flux dependencies are shown for 1D-M-QDSL with different geometric parameters. In Fig. 3.11 (a) we fixed dimensions of the Ge QDs at $N_{x,2} = N_{y,2} = 11\text{ ML}$ and value of specularity parameter $p = 0.7$. Red curves correspond to the Si QDs with $N_{x,1} = N_{y,1} = 9\text{ ML}$, while the blue to the $N_{x,1} = N_{y,1} = 7\text{ ML}$. Solid lines denote 1D-M-QDSL with translation period $N_z = 4\text{ ML}$, dashed lines are for $N_z = 8\text{ ML}$, and the dot-dashed lines to the $N_z = 12\text{ ML}$. Dependencies which correspond to 1D-M-QDSL with the larger cross-section have higher values for same translation period length. However, 1D-M-QDSL with larger Si QDs $N_{x,1} = N_{y,1} = 9\text{ ML}$ and translation period $N_z = 12\text{ ML}$ have lower values of thermal flux, than ones with smaller Si QD cross-section and $N_z = 4\text{ ML}$.

In Fig. 3.11 (b) the dependencies are presented for fixed values of Si QDs $N_{x,1}=N_{y,1}=9$ ML and translation period $N_z=4$ ML. The dimensions of Ge QDs varied: $N_{x,2}=N_{y,2}=11$ ML, 13 ML, 15 ML. Red lines are for $p=0.9$, while the blue ones are for $p=0.5$. Solid lines denote 1D-M-QDSL with Ge QDs cross-section $N_{x,2}=N_{y,2}=15$ ML, dashed lines are for $N_{x,2}=N_{y,2}=13$ ML, and the dot-dashed lines to the $N_{x,2}=N_{y,2}=11\,ML$. Thermal flux is more intensive for 1D-M-QDSL with $p=0.9$ for all presented values of Ge QDs cross-section. In the case of specularity parameter $p=0.9$ higher thermal flux values correspond to the larger Ge QDs because of the greater number of the phonon modes, while boundary scattering has low intensity. For the specularity parameter $p=0.5$ dependencies with 13 ML and 11 ML intersect at the temperatures ~120 K because boundary scattering and Umklapp contribute become more significant in comparison of the phonon number increase.

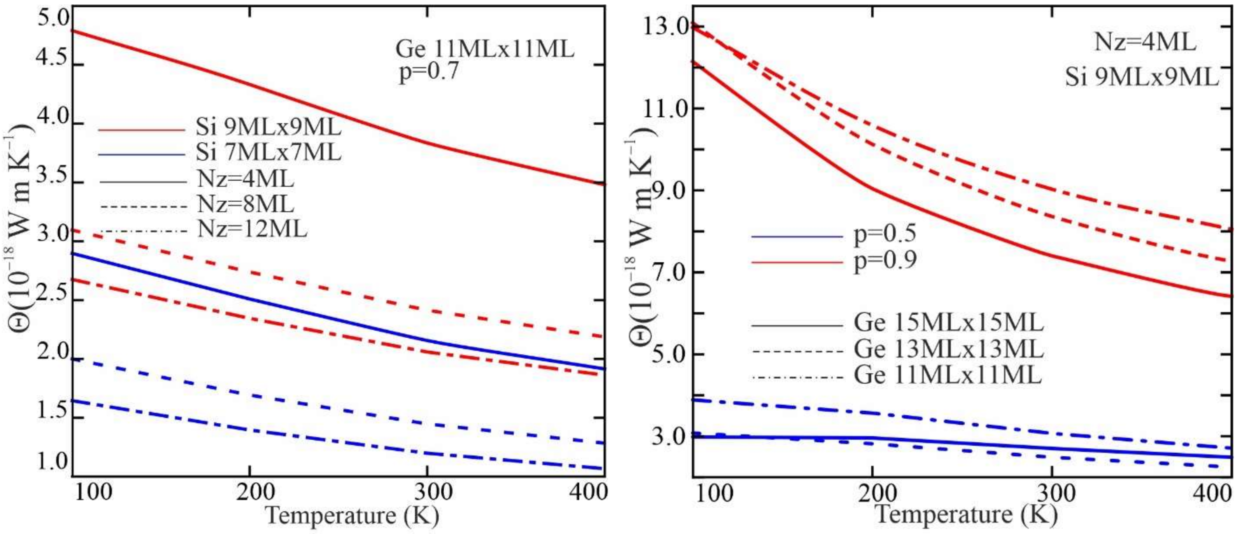

(a) **(b)**

Fig. 3.11. Thermal flux in Si/Ge 1D-M-QDSL.

(a) *Ge QD:* $N_{x,2}=N_{y,2}=11$ ML, $p=0.7$. Red lines *Si QD*: $N_{x,1}=N_{y,1}=9$ ML, Blue lines *Si QD*: $N_{x,1}=N_{y,1}=7$ ML; Continuous lines – $N_z=4$ ML; Dashed lines – $N_z=8$ ML, Dash-dotted lines – $N_z=12$ ML;

(b) *Si QD*: $N_{x,1}=N_{y,1}=9$ ML, $N_z=4$ ML. Red lines *Si QD*: $p=0.9$, Blue lines *Si QD*: $p=0.5$; Continuous lines – *Ge QD*: $N_{x,2}=N_{y,2}=15$ ML; Dashed lines – *Ge QD*: $N_{x,2}=N_{y,2}=13$ ML, Dash-dotted lines – *Ge QD*: $N_{x,2}=N_{y,2}=11$ ML ;.

In Fig. 3.12 ratios of thermal fluxes between 1D-M-QDSL and NW with corresponding cross-sections are shown. In Fig. 3.12 (a) the temperature dependencies are shown. We fixed values of the specularity parameter at $p = 0.7$, and cross-section of the Ge QDs at $11\ \text{ML} \times 11\ \text{ML}$. Dependencies are depicted with green lines for M-QDSL with Si QDs' cross-section $7\ \text{ML} \times 7\ \text{ML}$, but the green ones for M-QDSL with Si QDs' cross-section $9\ \text{ML} \times 9\ \text{ML}$. Continuous lines correspond to the translation period value $N_z = 4\ \text{ML}$, dashed lines to the $N_z = 8\ \text{ML}$, and dot-dashed lines to the $N_z = 12\ \text{ML}$. Ratio of the thermal fluxes in 1D-M-QDSL and Si NW grows together with temperature. Thermal flux ratio dependencies have no maxima for all presented cross-sections and translation period values, as the ratios in C-QDSL do. However curves' slope becomes less starting from the temperature $\sim 200\,\text{K}$. The slope becomes nearly zero for M-QDSL with $N_{x,1} = N_{y,1} = 9\ \text{ML}$ and translation period $N_z = 4\ \text{ML}$, the M-QDSL with $N_z = 8\ \text{ML}$ and $N_z = 12\ \text{ML}$ dependencies demonstrate saturation, as well. The slope in temperature interval $100\,\text{K} - 200\,\text{K}$ is more pronounced due to population of the high energy level in NW and M-QDSL, which have in the modulated nanostructure near 0 phonon velocities and their contribution in such structures to the thermal transport is rather small, while boundary scattering which is stronger in M-QDSL and does not depend on temperatures.

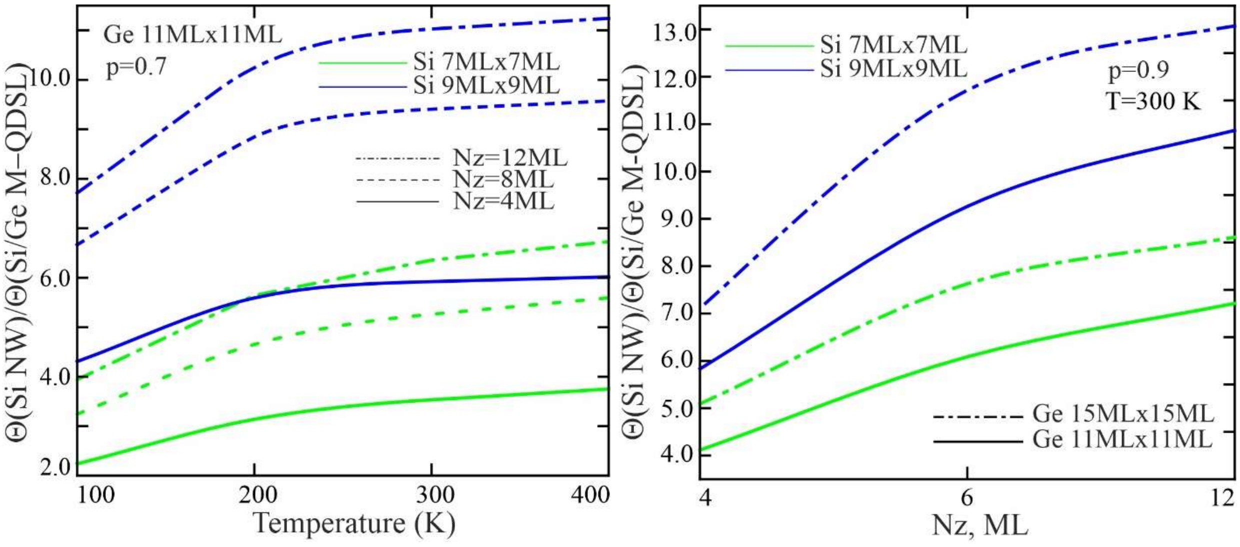

(a) (b)

Fig. 3.12. Thermal flux ratio in Si/Ge 1D-M-QDSL

(a) Temperature dependency for different translation period N_z;

(b) Thermal flux ratio dependency on translation period N_z

Fig. 3.12 (b) shows the dependencies of the thermal flux on translation period N_z for fixed temperature $T = 300\,K$ and specularity parameter $p = 0.7$. The green and blue lines have same meaning as in Fig. 3.12 (a). Here, continuous lines correspond to the Ge segments with $11\ \text{ML} \times 11\ \text{ML}$, and dot-dashed lines to the $15\ \text{ML} \times 15\ \text{ML}$. The drop of the thermal flux increases with the increase of the translation period. Our results show the drop of RT thermal flux up to ~ 13 times. The drop of the thermal flux in Si/Ge 1D-M-QDSL is stronger than in Si/Ge 1D-C-QDSL (up to ~ 3.5 times) because geometry that amplifies the effect of the material mismatch.

In Fig. 3.13 we show the ratio of the thermal flux in Si NW #1 and Si/SiO$_2$ coated and partially coated 1D-M-QDSL #2 - #7 as a function of temperature. The Table with nanostructures notations and dimensions is shown below. The heat flux increases with the temperature rise in wide interval of temperatures. Most of presented curves have minima at temperature $\sim 125\ \text{K}$, excepting the curve #5 where cross-section of the narrow and wide QDs are very close. These minima are explained by different temperature-dependencies f thermal flux in NWs and QDSLs. Overall, the heat flux in Si/SiO$_2$ 1D-M-QDSLs drops by a factor of 3 to 7 depending on their core and shell dimensions.

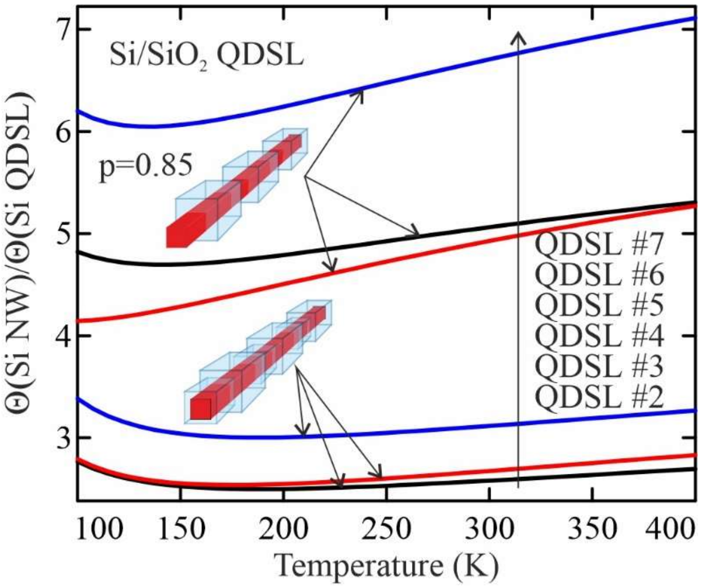

Fig. 3.13. Ratio of thermal fluxes in Si NW and Si/SiO$_2$ 1D-M-QDSLs as a function of temperature.

The reason for the thermal flux reduction is the decrease of the average phonon group velocity and trapping of phonon modes into the M-QDSL segments. In M-QDSL, partially coated with SiO$_2$ (1D-M-QDSLs #5, #6, #7), the heat propagates only through Si core, while in Si/SiO$_2$

M-QDSL fully coated (1D-M-QDSLs #2, #3, #4) it propagates also through SiO_2 shell. As a result, reduction of the heat flux is stronger in the 1D-M-QDSLs #5 - #7 in comparison with that in the 1D-M-QDSLs #2 - #4. In general, more complicated lattice dynamics models than the FCC model are needed for an accurate quantitative description of Si/SiO_2 1D-M-QDSLs. Therefore, our results presented here provide a qualitative description of their thermal properties. Nevertheless, we have checked that the FCC model only by a few (~2 to 10) percent overestimates the heat flux in Si NWs and 1D-M-QDSLs in comparison with the five-parameter BvK model due to the difference in phonon dispersion curves [24].

Dimensions of the 1D nanostructures

Nanostructure	Dimensions (all dimensions are indicated in monolayers 1 ML = 0.27 nm)	Notation in the present work
Si NW	28 ML × 28 ML	NW #1
Si/SiO_2 M-QDSL	QD1: Si(28 ML × 28 ML × 24 ML)/SiO_2(36 ML × 36 ML × 24 ML) QD2: Si(28 ML × 28 ML × 24 ML)/SiO_2(44 ML × 44 ML × 24 ML)	M-QDSL #2
Si/SiO_2 M-QDSL	QD1: Si(60 ML × 60 ML × 24 ML)/SiO_2(76 ML × 76 ML × 24 ML) QD2: Si(60 ML × 60 ML × 24 ML)/SiO_2(92 ML × 92 ML × 24 ML)	M-QDSL #3
Si/SiO_2 M-QDSL	QD1: Si(60 ML × 60 ML × 24 ML)/SiO_2(68 ML × 68 ML × 24 ML) QD2: Si(60 ML × 60 ML × 24 ML)/SiO_2(76 ML × 76 ML × 24 ML)	M-QDSL #4
Si/SiO_2 M-QDSL	QD1: Si(28 ML × 28 ML × 24 ML) – QD2: Si(28 ML × 28 ML × 24 ML)/SiO_2(52 ML × 52 ML × 24 ML)	M-QDSL #5
Si/SiO_2 M-QDSL	QD1: Si(28 ML × 28 ML × 24 ML) – QD2: Si(28 ML × 28 ML × 24 ML)/SiO_2(36 ML × 36 ML × 24 ML)	M-QDSL #6

Si/SiO2 M-QDSL	QD1: Si(60 ML × 60 ML × 24 ML) – QD2: Si(60 ML × 60 ML × 24 ML)/SiO2(76 ML × 76 ML × 24 ML)	M-QDSL #7

Phonons and thermal transport in multishell Si/SiO$_2$ nanotubes

It was already shown in this Chapter and in Ref. [139] that SiO$_2$ shell in Si NW and 1D-QDSL leads to drop of thermal transport up to 7 times due to acoustical mismatch of materials. Here we would like to investigate another 1D structure – the NT made of one or more “shells”, each shell is formed from Si and SiO$_2$ layer.

The schematic view of the Si/SiO$_2$ NT is presented in Fig. 3.14. The *X* and *Y* axes of the Cartesian coordinate system are located in the cross-sectional plane of the NT and are parallel to its sides, while the *Z* axis is directed along the structure axis. The origin of the coordinates is set in the centre of the nanotube cross-section. MNTs have square cross-section. We assume that investigated MNT are infinite along the *Z* axis. Multishell NTs have characteristic parameters, such as dimensions of cavity $d_{cavity} \times d_{cavity}$, thickness of silicon d_{Si} and silica d_{SiO_2} layers, which together form a shell, and number of Si/SiO$_2$ shells is L.

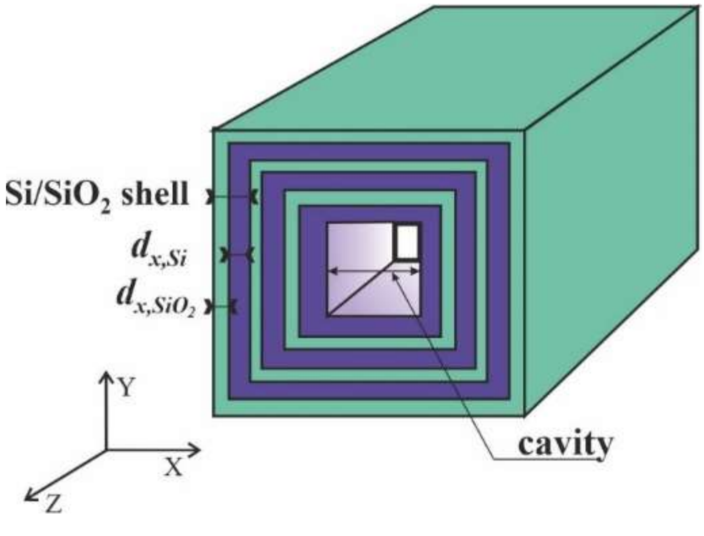

Fig. 3.14. Schematic view of the multishell NT.

Figure is adopted from Ref. [139]

In Fig. 3.15 the comparison of phonon spectra and DOS in Si NW and two Si NT with different number of shells parameters is provided. The phonon spectra were calculated resolving system from Eq. 3.4. In 1D case, the phonon density of states (DOS) per unit length in real space can be found from the relation: $g(\omega)d\omega = \frac{1}{2\pi}dq_z$. Hence,

$$g(\omega) = \frac{1}{2\pi}\frac{dq_z}{d\omega} = \frac{1}{2\pi v_z}. \tag{3.10}$$

The Si NW has dimensions $11\ \text{ML} \times 11\ \text{ML}$ ($2.97\ \text{nm} \times 2.97\ \text{nm}$). The geometric parameters of the Si/SiO$_2$ NTs are as follows: the cavity cross-section is $45\,\text{ML} \times 45\,\text{ML}$ ($12.15\ \text{nm} \times 12.15\ \text{nm}$), the thickness of the Si layer is $6\ \text{ML}$ ($1.62\ \text{nm}$) and the thickness of the SiO$_2$ layer is $4\,\text{ML}$ ($1.08\ \text{nm}$). Phonon dispersion curves and DOS are represented for a NT with a single shell, $L = 1$, in panel (**b**) and with two shells, $L = 2$, in panel (**c**). For the Si/SiO$_2$ NT with $L = 1$, we present phonon branches with s = 1–5, 30, 55, 480, 500, 550, …, 1000, 1075, …, 1600, 1661 for *Dilatational* polarization; s = 1–5, 30, 55, 480, 500, 550, …, 1000, 1075, …, 1600, 1640 for *Shear* polarization and s = 1–5, 30, 55, 480, 500, 550, …, 1000, 1075, …, 1600, 1650 for *Flexural1* and *Flexural2* polarizations. For the Si/SiO$_2$ NT with $L = 2$, the following phonon branches are depicted: s = 1–5, 80, 155, 230, 305, 380, 455, 500, 675, 850, …, 2950, 3000, 3100 …, 3900, 3920 for *Dilatational* polarization; s = 1–5, 80, 155, 230, 305, 380, 455, 500, 675, 850, …, 2950, 3000, 3100 …, 3800, 3880 for *Shear* polarization and s = 1–5, 80, 155, 230, 305, 380, 455, 500, 675, 850, …, 2950, 3000, 3100, …, 3900 for *Flexural1* and *Flexural2* polarizations.

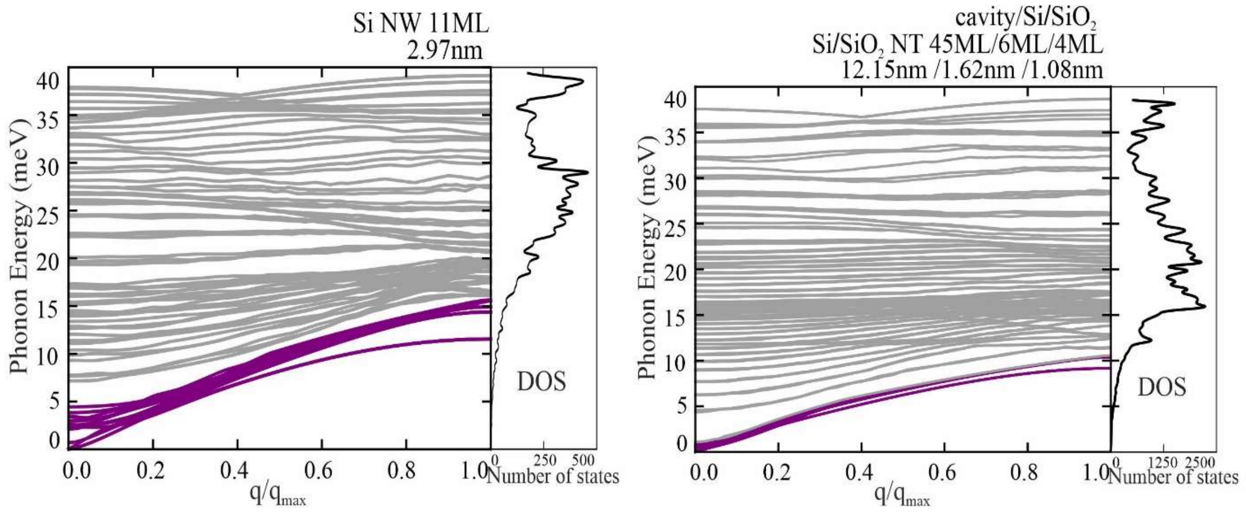

(a) **(b)**

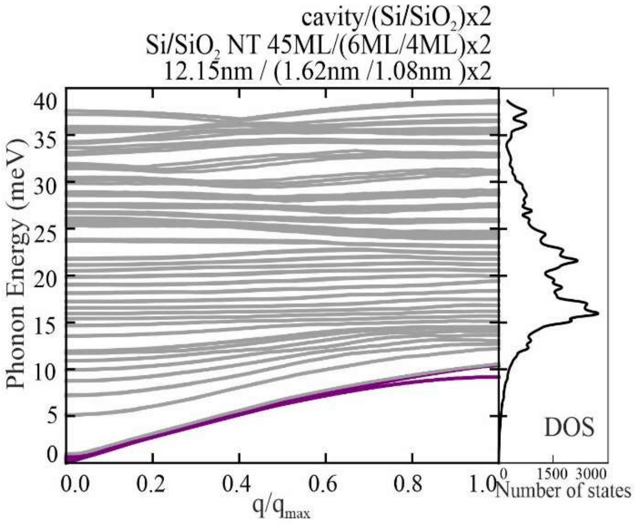

(c)

Fig. 3.15. Phonon acoustic mode dispersions and DOS in Si NW and Si/SiO₂ NT

(a) Si NW; **(b)** Si/SiO₂ NT with one shell; **(c)** Si/SiO₂ NT with two shells.

Figure is adopted from Ref. [139].

The number of quantized phonon branches in the NTs, 6600 for NT with single shell and 15600 for NT with double shell, is substantially larger as compared to NW, 1323. The slope of dispersions in NTs is less than in the NW for the lowest phonon branches due to acoustic mismatch between silicon and silicon dioxide. A great number of phonon modes in the NTs with energy $\hbar\omega > 10\ \text{meV}$ are nearly dispersionless and possess group velocities close to zero. The DOS maximum in NTs is shifted toward the lower energy interval than in the NW, where the drop of the phonon group velocity is more significant (see Fig. 3.16). The DOS maximum for two shells is more prominent, than for a single shell, due to a greater number of phonon modes concentrated in SiO$_2$, which has a lower maximal phonon energy than Si. However number of states in the energy range $20\ \text{meV} - 37\ \text{meV}$ decreases, that demonstrates the redistribution of phonon states in Si layers, too. The effect of the phonon deceleration in a NT is illustrated in Fig. 3.16.

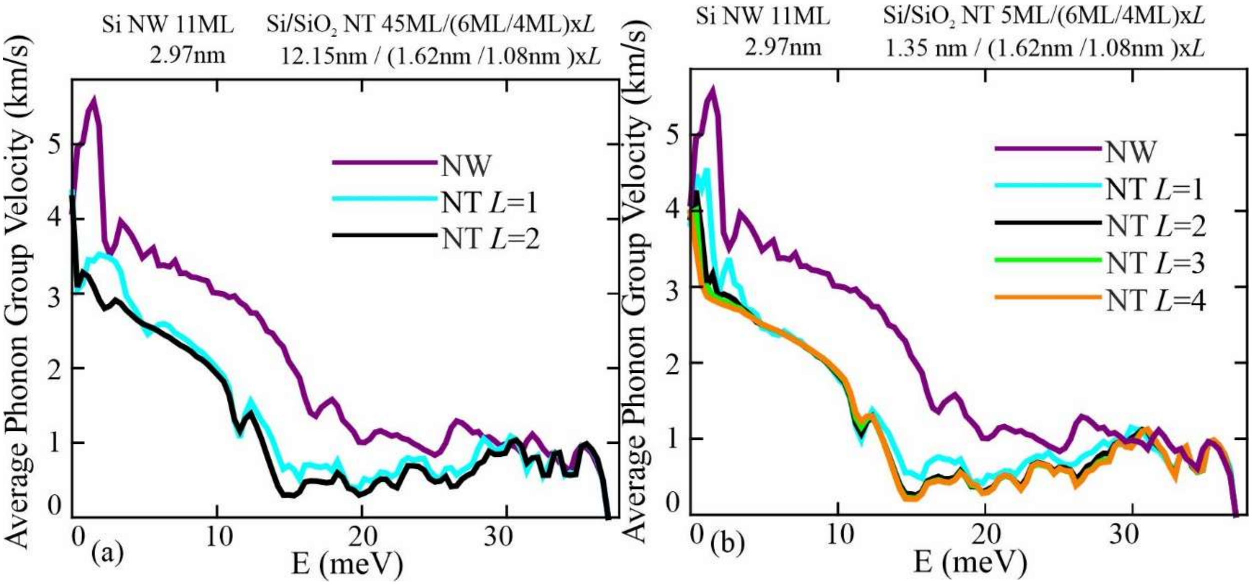

(a) **(b)**

Fig. 3.16. Phonon group velocities in NT with different numbers of shells

(a) Si/SiO2 NT with cavity dimensions $N_{cavity,x} \times N_{cavity,y} = 45\ \text{ML} \times 45\ \text{ML}$;

(b) Si/SiO2 NT with cavity dimensions $N_{cavity,x} \times N_{cavity,y} = 5\ \text{ML} \times 5\ \text{ML}$.

Figure is adopted from Ref. [139].

The phonon group velocities for NTs with the same cavity and Si- and SiO2-layer thicknesses, but different numbers of shells are shown in panels **(a)** and **(b)**. In Fig. 3.16 (a), the Si/SiO2 NTs with the following geometric parameters are represented: the cavity cross-section is $N_{cavity,x} \times N_{cavity,y} = 45\ \text{ML} \times 45\ \text{ML}$, $N_{Si,x} = N_{Si,y} = 6\ \text{ML}$, $N_{SiO_2,x} = N_{SiO_2,y} = 4\ \text{ML}$; blue line and black line correspond to a single shell ($L = 1$) and two shells ($L = 2$). In Fig. 3.16 (b), NTs have the following parameters: $N_{cavity,x} \times N_{cavity,y} = 5\ \text{ML} \times 5\ \text{ML}$, $N_{Si,x} = N_{Si,y} = 6\,\text{ML}$, $N_{SiO_2,x} = N_{SiO_2,y} = 4\ \text{ML}$; blue, red, green and orange lines correspond to single shell ($L = 1$), two ($L = 2$), three ($L = 3$) and four ($L = 4$) shells.

The phonon group velocity in NTs is smaller than in a NW over a large energy range (0 to $30\ \text{meV}$). In the interval of energies $30\ \text{meV}$ to $37\ \text{meV}$, the phonon group velocities vary near the same low values for all considered above geometric parameters of NTs. The reduction of the phonon group velocities is explained by an acoustic mismatch of materials, a stronger phonon confinement, and a redistribution of the phonons' DOS. The effect of the number of shells is more significant in NTs with a larger cavity: the decrease of phonon group velocities in two-shell NTs in comparison with single-shell NTs is stronger in NTs with cavity dimensions $45\ \text{ML} \times 45\ \text{ML}$ than in NTs with $N_{cavity,x} \times N_{cavity,y} = 5\ \text{ML} \times 5\ \text{ML}$. A further increase of the number of shells slightly reinforces the reduction of the phonon group velocities. This fact can be explained by weaker special phonon confinement in NT with more shells.

For calculation of the phonon thermal flux in multishell NT, we used the Boltzmann transport equation in the form presented in Eq. 3.6 [30–33] using Matthiessien rule for total relaxation time (Eq. 3.7). We used Eq. 3.8a for calculation of the thermal conductivity, as for 1D-C-QDSL. As in the case of the Si/Ge 1D-QDSL, for NT we have taken into account three-phonon Umklapp and impurity scatterings [31–38], [149]. Their relaxation times were calculated using Eqs. 3.9 (a-b). As the third scattering mechanism for NT we employed two different types: the "*effective scattering rate*" $\frac{1}{\tau_{SiO_2}}$ due to the diffusion of vibrational excitations in amorphous SiO2 [152]:

$$\frac{1}{\tau_X}=\frac{1}{\tau_{SiO_2}}=\frac{1}{\tau_{SiO_2,S}\left(q_z\right)}=v_{Z,s}^2\left(q\right)\frac{3\omega_s\left(q\right)}{a_{b.l.}^2F\left\langle\omega\right\rangle^2}\frac{d_{x,SiO_2}}{d_{x,Si}}, \tag{3.11a}$$

or the relaxation rate for the *boundary scattering* $\frac{1}{\tau_B}$:

$$\frac{1}{\tau_X}=\frac{1}{\tau_{B,S}\left(q_z\right)}=\frac{1-p}{1+p}\frac{\left|v_{Z,S}\left(q_z\right)\right|}{2}N\left(\frac{1}{d_{x,Si}}+\frac{1}{d_{y,Si}}+\frac{1}{d_{x,SiO_2}}+\frac{1}{d_{y,SiO_2}}\right). \tag{3.11b}$$

In Equations (3.11a) and (3.11b) $a_{b.l.}=0.235$ is the SiO2 bond length, $\left\langle\omega\right\rangle$ is the mean vibrational frequency (the mean vibrational energy $\hbar\left\langle\omega\right\rangle=34\ \mathrm{meV}$ is taken from Ref. [152], $F=0.33$ according to Ref. [153]).

A comparison of thermal conductivity in a Si NW and Si/SiO2 NTs as a function of temperature is provided in Fig. 3.17. Average phonon group velocities as a function of phonon energies in Si/SiO2 MNTs with the cavity cross-section $45\ \mathrm{ML}\times45\ \mathrm{ML}$ and $5\ \mathrm{ML}\times5\ \mathrm{ML}$, and different numbers of Si/SiO2 bilayer shells, formed by silicon layer with thickness 6 ML and silica layer with thickness $4\ \mathrm{ML}$. Results for Si NW with cross section $11\ \mathrm{ML}\times11\ \mathrm{ML}$ are also shown for comparison. Calculation of the thermal conductivity illustrated in Fig. 3.17 (a-b) takes into account diffusion transport in SiO2 (see Eq. (3.11a)), while Fig. 3.17 (c-d) includes the boundary scattering (see Eq. (3.11b)) with the specular parameter $p=0.6$. The values of the thermal conductivity in NTs (even for the NTs with a greater number of phonon modes, see Fig 3.17(c)) are lower than the thermal conductivity in the NW in the whole temperature range. This decrease of the thermal conductivity in the NTs occurs due to the acoustic mismatch of Si and SiO2, a DOS redistribution (Fig. 3.15), which leads to a decrease of the phonon group velocities, and an enhancement of the phonon scattering at interfaces.

The maxima on the thermal flux curves shown in Fig. 3.17 are determined by the interplay between the three-phonon Umklapp and the boundary or amorphous scattering. At low temperatures, the boundary scattering dominates, and the thermal flux increases with temperature due to the population of high-energy phonon modes and approaches the maximum value, when $\tau_U \gg \tau_B$. A subsequent rise of temperature leads to an enhancement of the Umklapp scattering and a diminution of the thermal flux. The lower values of the thermal conductivity and curves' slope for temperature dependences calculated considering the boundary scattering mechanism (Eq. 3.17 b). One can see that considering the boundary scattering mechanism instead of amorphous scattering mechanism leads to more significant reduction of thermal conductivity due to a big number of interfaces in multishell NTs, which leads to domination of the boundary scattering mechanism. The thermal conductivity of the NTs with $45\ \mathrm{ML}\times 45\ \mathrm{ML}$ is higher than with the $5\ \mathrm{ML}\times 5\ \mathrm{ML}$ because of a larger number of phonon modes in these structures. Additional interfaces between the shells effectively scatter phonons, hence the TC decreases with augmentation of the number of shells (see panels (b) and (d)) reaching values as low as $0.2\ {}^{\mathrm{W}}\!/_{\mathrm{m\cdot K}}$ at RT for Si/SiO_2 NT with smaller cavity and $L=4$. A similar dependence of TC on L was demonstrated experimentally for Si/SiO_2 rolled-up nanotubes of $1.9\ \mu\mathrm{m}$ to $3.2\ \mu\mathrm{m}$ radii and a 24-nm-thick shell [152], see Fig. 3.17(g).

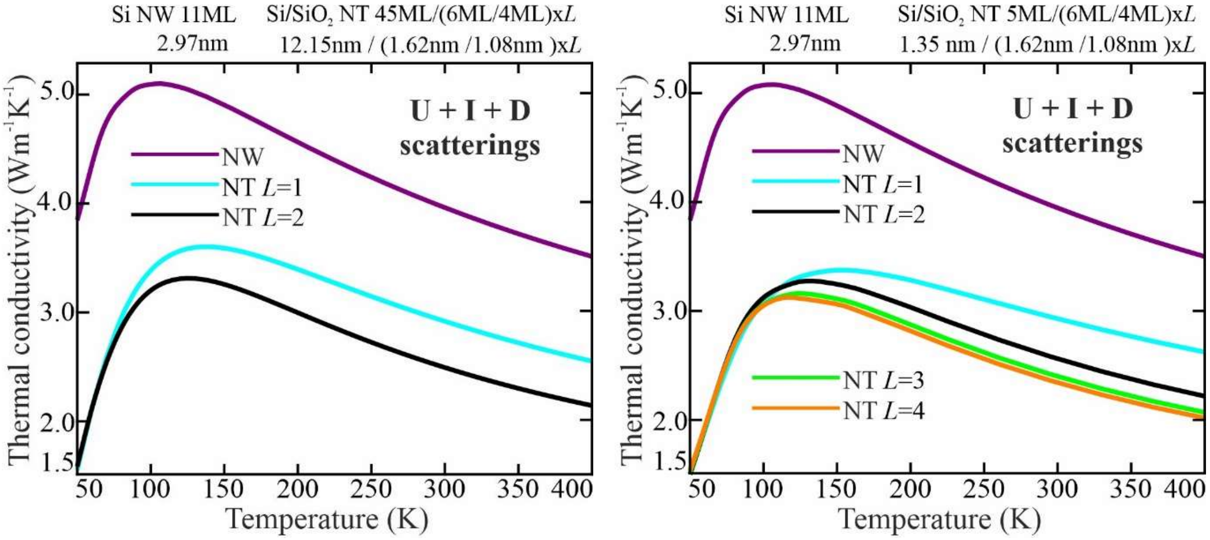

(a) **(b)**

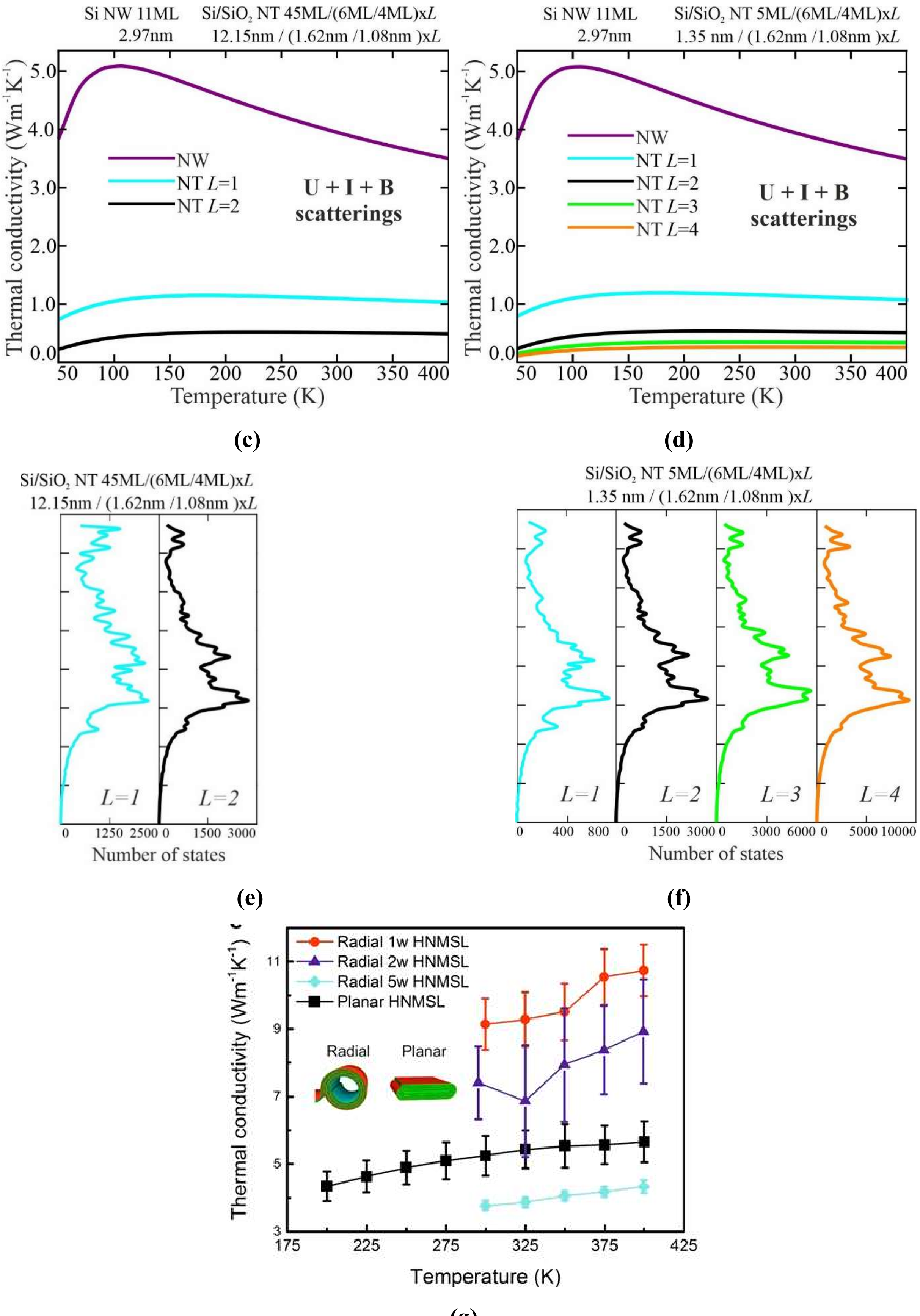

(c) (d)

(e) (f)

(g)

Fig. 3.17. Thermal conductivity in NTs.

Umklapp and diffusive scattering in Si/SiO_2 NT with cavity dimensions

(a) $N_{cavity,x} \times N_{cavity,y} = 45\ \mathrm{ML} \times 45\ \mathrm{ML}$ and **(b)** $N_{cavity,x} \times N_{cavity,y} = 5\ \mathrm{ML} \times 5\ \mathrm{ML}$

Umklapp and boundary scattering in Si/SiO_2 NT with cavity dimensions

(c) $N_{cavity,x} \times N_{cavity,y} = 45\ \mathrm{ML} \times 45\ \mathrm{ML}$ and **(d)** $N_{cavity,x} \times N_{cavity,y} = 5\ \mathrm{ML} \times 5\ \mathrm{ML}$

Density of states in Si/SiO_2 NT with cavity dimensions

(e) $N_{cavity,x} \times N_{cavity,y} = 45\ \mathrm{ML} \times 45\ \mathrm{ML}$ and **(f)** $N_{cavity,x} \times N_{cavity,y} = 5\ \mathrm{ML} \times 5\ \mathrm{ML}$

(g) Thermal conductivity in rolled-up structures.

Figure is adopted from Refs. [139] and [152]

To elucidate the dependence of TC in MNTs on *p*, we plot in Fig. 3.18, the TC of a single-shell Si/SiO_2 NT ($5\,\mathrm{ML}/6\ \mathrm{ML}/4\ \mathrm{ML}$) as a function of temperature for different values of *p*. A decrease of the specularity parameter suppresses TC over the entire considered range of temperatures. Thus, the boundary scattering plays an important role in limiting thermal transport even for $T > 150\ \mathrm{K}$, where the three-phonon Umklapp scattering becomes relatively strong. This results in decreasing TC with *T* for $T > 150\ \mathrm{K}$.

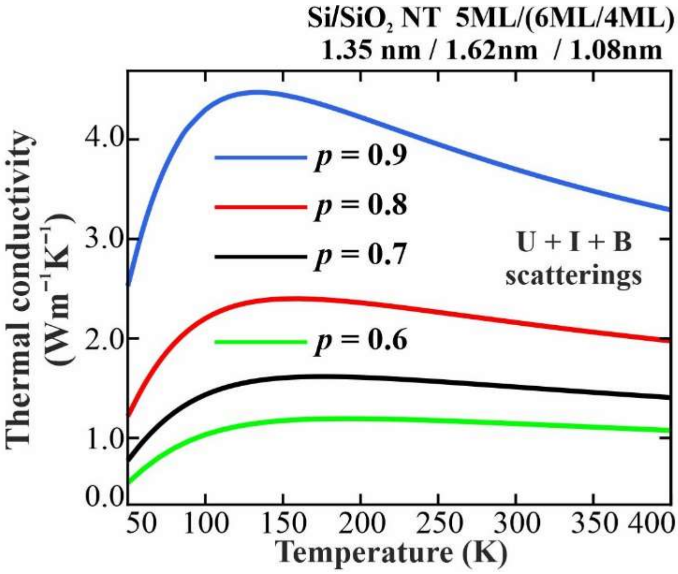

Fig. 3.18. Thermal conductivity in NTs

Figure is adoped from Ref. [139].

In Fig. 3.19 (a), we show how different values of *p* affect the drop of TC in MNTs as compared with NWs. The TC curves in Fig. 3.19 (a), were calculated taking into account both the phonon-boundary scattering and the diffusion of vibrational excitations in SiO_2 layers. Coexistence of the phonon-boundary scattering and the "*effective scattering*" due to the diffusion of vibrational excitations in SiO_2 layers results in lower values of TC in comparison with the cases of their separate action. At the same time, the TC reduction with rising number of shells remains manifested for different values of p (see Fig. 3.19 (a)). It is also worth noticing that for $p = 0.9$ the ratios between thermal conductivities in MNTs with different numbers of shells $\frac{\kappa_{ph}\left(N\right)}{\kappa_{ph}\left(1\right)}$ for $L = 2$ and $L = 5$ (see Fig. 3.19 (b) are close to experimental values [152] despite the fact that experimental multishell NTs possess much larger sizes. Thereby the multishell nanotubes are good candidates for efficient engineering of phonon and thermal properties similar to multilayer planar heterostructures, heterowires and acoustic metamaterials [140], [154–157].

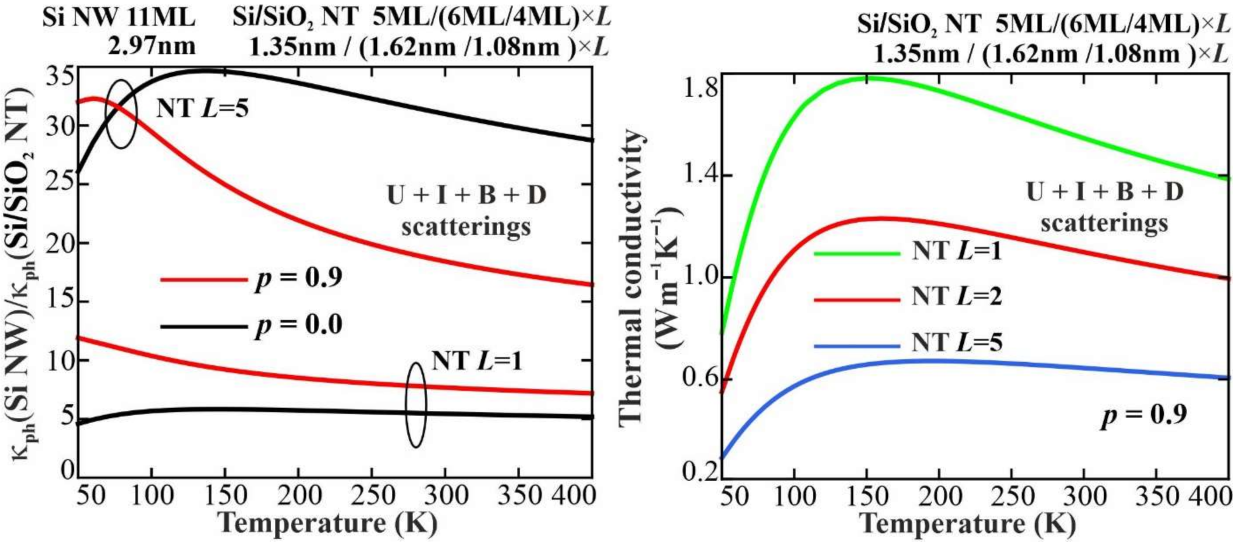

(a) **(b)**

Fig. 3.19. Thermal conductivity in NTs.

(a) Ratio of the thermal conductivity in Si NW and Si/SiO_2 NT as a function of temperature**;** **(b)** Temperature dependency of the thermal conductivity in Si/SiO_2 NT.

Figure is adopted from Ref. [139].

3.3. Conclusions to Chapter 3

In this Chapter, we have studied phonon and thermal properties of quasi-one-dimensional silicon-based nanostructures: 1D-QDSLs (with constant and periodically modulated cross-sections) and multi-shell nanotubes. The phonon energy dispersions were calculated using a face-centred-cubic cell model of lattice vibrations. The thermal flux and thermal conductivity were calculated employing the Boltzmann transport equation approach within relaxation time approximation taking into consideration the one-dimensional density of phonon states. The main mechanisms of phonon scattering were taken into account: impurity, boundary, and Umklapp. It has been demonstrated that:

- Phonon modes in Si/Ge 1D-QDSLs are trapped in their segments due to an acoustical mismatch of materials. The slope of the phonon dispersion in 1D-QDSLs is smaller than in Si nanowires. Many high energy modes in Si/Ge QDSLs are dispersionless and possess low group velocities close to 0 value.
- The average phonon group velocities in Si/Ge 1D-QDSLs are significantly lower than those in nanowires for all phonon energies in 1D-M-QDSLs and for phonon energies $\hbar\omega > 5$ meV in 1D-C-QDSLs. The effect of APGV drop is stronger in the case of 1D-M-QDSLs due to the interplay between segmentation and cross-section modulation.
- Thermal transport in Si/Ge 1D-QDSLs is significantly suppressed due to phonon deceleration and reinforcement of phonon scattering at Si/Ge interfaces. Up to 7-times (13.5-times) drop of TC was demonstrated for C-QDSLs (M-QDSLs) as a function of temperature. At room temperature, the thermal conductivity in Si/Ge 1D-C-QDSLs is by a factor of 2.6 – 2.9 lower than that in silicon nanowires with the same cross-section.
- Thermal conductivity and thermal flux in 1D-QDSL increase with the growth of the specularity parameter due to the weakening of phonon boundary scattering. At the same time drop of the thermal flux becomes stronger with the rise of the specularity parameter.
- In partially coated Si/SiO$_2$ M-QDSLs heat propagates through internal silicon channel only, while in the fully coated M-QDSLs, it propagates through both internal Si and external SiO$_2$ channels. As a result, the reduction of the thermal flux in partially coated Si/SiO$_2$ M-QDSLs is stronger than that in fully coated M-QDSLs: up to ~ 6.5 times at room temperature for fully-coated M-QDLs and ~ 3.5 times for partially-coated M-QDSLs.
- Phonon average group velocities in multi-shell Si nanotubes are close to 0 for phonon energies $\hbar\omega > 10$ meV.
- The thermal conductivity in the Si/SiO$_2$ nanotubes is lower than that in the Si nanowires with the same lateral dimensions due to acoustic mismatch of the materials and lower group velocities.
- The phonon boundary scattering plays an important role in limiting thermal transport in the Si/SiO$_2$ MNTs even for medium and high temperatures, where the three-phonon Umklapp scattering becomes relatively strong. At the same time Umklapp scattering stipulates decrease of thermal conductivity with rise of the temperature for $T > 150$ K.
- A large number of phonon modes in Si/SiO$_2$ MNTs are scattered on Si/SiO$_2$ interfaces. As a result, an L-fold drop of the thermal conductivity in a wide temperature range from 50 K to 400 K is predicted for Si/SiO$_2$ MNTs with L shells in comparison with one-shell Si/SiO$_2$

NT. A similar dependence of TC on the *number of shells* was demonstrated experimentally for Si/SiO$_2$ rolled-up nanotubes by G. Liu et al. in Ref. [152].

The obtained results confirm that considered Si-based one-dimensional quantum-dot-superlattices and Si/SiO$_2$ multi-shell nanotubes provide different opportunities for efficient phonon engineering. Ultra-low values of the thermal conductivities make these nanostructures prospective candidates for thermoelectric and thermal insulation applications.

GENERAL CONCULSIONS AND RECOMMENDATIONS

The detailed theoretical study of exciton, phonon, and thermal properties of the Si/Ge, Si/SiC, and Si/SiO$_2$ one-dimensional quantum-dot superlattices as well as phonon and thermal properties of the Si/SiO$_2$ multi-shell nanotubes is carried out in the Thesis. Below is the summary of the obtained results.

1. The effective mass approach was employed for the theoretical investigation of electron, hole, and exciton states in Si/SiO$_2$ and Si/SiO$_2$ 1D-QDSLs:
   - It has been shown that for the qualitative description of exciton states it is crucial to take into account the anisotropy of electron and hole effective masses, mixing of heavy, light, and split-off holes as well as mixing of different electron and hole states. Exciton energies calculated within this theoretical approach with a three-band hole Hamiltonian were in good agreement with experimental exciton energies reported for Si QDs.
   - It has been demonstrated that electron, hole, and exciton states in considered 1D-QDSLs can be effectively engineered by changing the QD's shape and size which is particularly important for optoelectronic and biomedical applications of 1D-QDSLs.
   - Conical QDs possess the lower values of ground exciton energy in comparison with cuboid and pyramidal QDs for the volumes $V < 32\,\mathrm{nm}^3$, while for $V > 32\,\mathrm{nm}^3$ cuboid QDs demonstrate the lower values of ground exciton energy.
   - The outer media parameters influence the electron and hole ground energy only for Si QDs with narrow SiC shells with thickness < 1 nm because maximal penetration of hole and electron wave functions into barrier media in considered Si/SiC/air or Si/SiC/water QDs is about 1 nm.
   - It has been also revealed that the broadening of photoluminescence lines in Si/SiO$_2$ QDSLs can be explained by the dispersion of QD's size and shape.
2. The face-centred cubic cell model of lattice vibrations was applied for the theoretical study of phonon modes in Si/Ge and Si/SiO$_2$ 1D-QDSLs and in Si/SiO$_2$ multi-shell nanotubes:
   - It has been theoretically shown that phonon modes in Si/Ge 1D-QDSLs are trapped in their segments due to an acoustical mismatch of materials. The slope of the phonon dispersion in 1D-QDSLs is smaller than that in Si nanowires.

- It has been revealed that many high energy phonon modes in Si/Ge QDSLs are dispersionless and possess low group velocities close to 0 value, resulting in the removal of these modes from heat flux.

3. Boltzmann transport equation within relaxation time approximation was employed for the theoretical study of thermal processes in Si-based 1D-QDSLs and Si/SiO_2 MNTs. All major phonon scattering mechanisms were taken into account: three-phonon Umklapp scattering, impurity, and boundary scatterings.

- It has been revealed that thermal transport in Si/Ge 1D-QDSLs is significantly suppressed in comparison with Si nanowires or bulk. Up to 7-times (13.5-times) drop of lattice thermal conductivity was demonstrated for Si/Ge 1D-QDSLs with constant (modulated) cross-section in dependence of the temperature.
- At room temperature, the thermal conductivity in Si/Ge 1D-C-QDSLs is by a factor of 2.6 – 2.9 lower than that in silicon nanowires with the same cross-section.
- In partially coated Si/SiO_2 1D-M-QDSLs heat propagates through internal silicon channel only, while in the fully coated M-QDSLs, it propagates through both internal Si and external SiO_2 channels. As a result, the reduction of the thermal flux in partially coated Si/SiO_2 M-QDSLs is stronger than that in fully coated M-QDSLs: up to ~ 6.5 times at room temperature for fully-coated M-QDSLs and ~ 3.5 times for partially-coated M-QDSLs.
- The thermal conductivity in the Si/SiO_2 multi-shell nanotubes is lower than that in the Si nanowires with the same lateral dimensions due to acoustic mismatch of the materials and lower group velocities.
- A large number of phonon modes in Si/SiO_2 MNTs are scattered at Si/SiO_2 interfaces. As a result, an L-fold drop of the thermal conductivity in a wide temperature range from $50\,\mathrm{K}$ to $400\,\mathrm{K}$ is predicted for Si/SiO_2 MNTs with L shells in comparison with one-shell Si/SiO_2 NT.

Based on the conclusions presented above, the following recommendations can be made:

1. For an accurate theoretical description of exciton states in Si/SiO_2, Si/SiC/air and Si/SiC/water 1D-QDSLs is crucial to take into consideration the mixing of different electron and hole states as well as mixing of different hole types: heavy, light and split-off (three-band Hamiltonian).

2. The Si/Ge and Si/SiO$_2$ 1D-QDSLs as well as Si/SiO$_2$ MNTs can be recommended as prospective candidates for thermoelectric and thermal insulation applications owing their ultra-low thermal conductivity.
3. Engineering of exciton and phonon states in 1D-QDSLs described in the Thesis can be useful for practical enhancement of their optical, thermal, and thermoelectric parameters.
4. Dispersion of quantum dot’s size and shape may be a key factor for the interpretation of experimental results in the field of exciton-related processes in silicon QDs with dimensions of several nanometers.

REFERENCES

[1] STROSCIO, M.A., DUTTA, M. Phonons in nanostructures. Cambridge: Cambridge University Press, 2001. DOI: 10.1017/CBO9780511534898.

[2] RUNGE, E. Excitons in semiconductor nanostructures. In: *Solid State Physics*. 2003, vol. 57, pp. 149–305. DOI: 10.1016/S0081-1947(08)60180-0

[3] WU, S., CHENG, L., WANG, Q. Excitonic effects and related properties in semiconductor nanostructures: roles of size and dimensionality. In: Materials Research Express. 2017 vol. 4, p. 085017. DOI: 10.1088/2053-1591/aa81da

[4] SCHOLES, G. D., RUMBLES, G. Excitons in nanoscale systems. In: *Nature Materials*. 2017, vol. 5, no. 9, pp. 683–696. DOI: 10.1038/nmat1710

[5] BALANDIN, A., POKATILOV, E., NIKA, D. Phonon engineering in hetero- and nanostructures. In: *Journal of Nanoelectronics and Optoelectronics*. 2007, vol. 2, pp. 140–170. DOI: 10.1166/jno.2007.201

[6] BALANDIN, A.A., NIKA, D.L. Phononics in low-dimensional materials. In: *Materials Today*. 2012, vol. 15, 266 – 275. DOI: 10.1016/S1369-7021(12)70117-7.

[7] HU, M., GIAPIS, K. P., GOICOCHEA, et al. Significant reduction of thermal conductivity in Si/Ge core-shell nanowires. In: *Nano Letters*. 2011, vol. 11, pp. 618–623. DOI: 10.1021/nl103718a.

[8] WINGERT, M. C., CHEN, Z.C.Y., DECHAUMPAI, E., et al., Thermal conductivity of Ge and Ge–Si Core–shell nanowires in the phonon confinement regime. In: *Nano Letters*. 2011, vol. 11, pp. 5507–5513. DOI: 10.1021/nl203356h

[9] LIANG, J., HUANG, C., GONG, X., Silicon nanocrystals and their composites: syntheses, fluorescence mechanisms, and biological applications. In: *ACS Sustainable Chemistry & Engineering*. 2019, vol. 7, pp. 18213–18227. DOI: 10.1021/acssuschemeng.9b04359

[10] SUN, W., QIAN, C., CHEN, K.K., et al. Silicon nanocrystals: it's simply a matter of size. In: *ChemNanoMat*. 2016, vol. 2, pp. 847–855. DOI: 10.1002/cnma.201600151.

[11] GONZÁLEZ-FERNÁNDEZ, A.A., ACEVES-MIJARES, M., PÉREZ-DÍAZ, O., et al. Embedded silicon nanoparticles as enabler of a novel CMOS-compatible fully integrated silicon photonics platform. In: *Crystals*. 2021, vol. 11, p. 630. DOI: 10.3390/cryst11060630

[12] NIKZAMIR, M., AKBARZADEH, A., PANAHI, Y. An overview on nanoparticles used in biomedicine and their cytotoxicity. In: *Journal of Drug Delivery Science and Technology*. 2021, vol. 61, p. 102316. DOI: 10.1016/j.jddst.2020.102316

[13] ZHIGUNOV, D.M., SEMINOGOV, V.N., TIMOSHENKO, V.Yu., et al. Effect of thermal annealing on structure and photoluminescence properties of silicon-rich silicon oxides. In: *Physica E.* 2009, vol. 41, pp. 1006-1009. DOI: 10.1016/j.physe.2008.08.026

[14] GUHA, S., QADRI, S.B., MUSKET, R.G., et al. Characterization of Si nanocrystals grown by annealing SiO_2 films with uniform concentrations of implanted Si. In: *Journal of Applied Physics.* 2000, vol. 88, pp.3954-3961. DOI: 10.1063/1.1308096

[15] LI, B., LIN, L., LIN, H., et al. Photosensitized singlet oxygen generation and detection: Recent advances and future perspectives in cancer photodynamic therapy. In*: Journal of Biophotonics*. 2016, vol. 9, pp. 1314–1325. DOI: 10.1002/jbio.201600055

[16] QIAN, X., ZHOU, J., Chen, G. Phonon-engineered extreme thermal conductivity materials. In: *Nature Materials*. 2021, vol. 20, p. 1188–1202. DOI: 10.1038/s41563-021-00918-3

[17] HOSSEINI, S.A., KHANNICHE, S., GREANEY, P. A., et al. In: Universal effective medium theory to predict the thermal conductivity in nanostructured materials. In: *International Journal of Heat and Mass Transfer*. 2022, vol. 183, p. 122040. DOI: 10.1016/j.ijheatmasstransfer.2021.122040.

[18] NIKA, D. L. *Phonon engineering in graphene and semiconductor nanostructures*. CEP USM, Chișinău, 2015. 183 p.

[19] ЗИНЧЕНКО, Н.Д. *Управление транспортными свойствами наноструктур методами фононной инженерии*: дис. д-ра физико-математических наук. CEP USM, Chișinau. 2010, p.135.

[20] PERNOT, G., STOFFEL, M., SAVIC, I. et al. Precise control of thermal conductivity at the nanoscale through individual phonon-scattering barriers. In: *Nature Materials.* 2010, vol. 9, pp. 491-495. DOI: 10.1038/nmat2752

[21] HOCHBAUM, A.I., CHEN, R., DELGADO R.D., et al. Enhanced thermoelectric performance of rough silicon nanowires. In: *Nature*. 2008, vol. 451, pp. 163-167. DOI: 10.1038/nature06381

[22] CRISMARI, D.V., NIKA, D.L. Thermal conductivity reduction in Si/Ge core/shell nanowires. In: *Journal of Nanoelectronics and Optoelectronics.* 2012, vol. 7, pp. 701–705. DOI: 10.1166/jno.2012.1421

[23] NIKA, D.L., COCEMASOV, A.I., CRISMARI, D.V., et al. Thermal conductivity inhibition in phonon engineered core-shell cross-section modulated Si/Ge nanowires. In: *Applied Physics Letters.* 2013, vol. 102, p. 213109. DOI: 10.1063/1.4807389

[24] NIKA, D.L., COCEMASOV, A., ISACOVA C., et al. Suppression of phonon heat conduction in cross-section modulated nanowires. In: *Physical Review B*. 2012, vol. 85, p. 205439. DOI: 10.1103/PhysRevB.85.205439

[25] NIKA, D.L., POKATILOV, E.P., BALANDIN, A.A., et al., Reduction of lattice thermal conductivity in one-dimensional quantum-dot superlattices due to phonon filtering. In: *Physical Review B*. 2011, vol. 84, p. 165415. DOI: 10.1103/PhysRevB.84.165415

[26] COCEMASOV, A.I., NIKA, D.L., V. M. FOMIN, et al. Phonon-engineered thermal transport in Si wires with constant and periodically modulated cross-sections: A crossover between nano- and microscale regimes. In: *Applied Physics Letters*. 2015, vol. 107, p. 011904. DOI: 10.1063/1.4926401

[27] FOMIN, V.M., NIKA, D.L., COCEMASOV, A.S., et al. Strong reduction of the lattice thermal conductivity in superlattices and quantum dot superlattices. In: *AIP Conf. Proc., Saloniki, Greece*. 2012, vol. 1449, pp. 33–36. DOI: 10.1063/1.4731490

[28] ИСАКОВА, К., Падение фононной теплопроводности в сегментированных Si/Ge нанонитях. In: *Studia Universitatis Moldaviae*, *Seria Științe exacte și economice.* 2015, vol. 2 (82), pp. 65–71. ISSN 1857-2073

[29] DAVIDSON, E.R., THOMPSON, W.J., Monster matrices: their eigenvalues and eigenvectors. In: *Computers in Physics*. 1993, vol. 7, pp. 519-522. DOI: 10.1063/1.4823212

[30] NIKA, D., POKATILOV, E., A. ASKEROV, et al. Phonon thermal conduction in graphene: role of Umklapp and edge roughness scattering. In: *Physical Review B*. 2009, vol. 79, p. 155413. DOI: 10.1103/PhysRevB.79.155413

[31] MINGO, N. Calculation of Si nanowire thermal conductivity using complete phonon dispersion relations. In: *Physical Review B*. 2003, vol. 68, p. 113308. DOI: 10.1103/PhysRevB.68.113308

[32] NIKA, D.L., ZINCENCO, N.D., POKATILOV, E.P. Lattice thermal conductivity of ultra-thin freestanding layers: Face-centered cubic cell model versus Continuum Approach. In: *Journal of Nanoelectronics and Optoelectronics*. 2009, vol. 4, p. 170-173. DOI: 10.1166/jno.2009.1018

[33] VOLZ, S.G., CHEN, G. Molecular dynamics simulation of thermal conductivity of silicon nanowires. In: *Applied Physics Letters*. 1999, vol. 75, pp. 2056-2058. DOI: 10.1063/1.124914

[34] POKATILOV, E., NIKA, D., FOMIN, V. et al. Excitons in wurtzite AlGaN/GaN quantum-well heterostructures. In: *Physical Review B*. 2008, vol. 77, p. 125328. DOI: 10.1103/PhysRevB.77.125328

[35] QIU, B., RUAN, X. Molecular dynamics simulations of lattice thermal conductivity of bismuth telluride using two-body interatomic potentials. In: *Physical Review B*. 2009, vol. 80, p. 165203. DOI: 10.1103/PhysRevB.80.165203

[36] LADD, A.J.C., MORAN, B., HOOVER, W.G. Lattice thermal conductivity: A comparison of molecular dynamics and anharmonic lattice dynamics. In: *Physical Review B*. 1986. vol. 34, p. 5058. DOI: 10.1103/PhysRevB.34.5058

[37] WARD, A., BROIDO, D.A. Intrinsic phonon relaxation times from first-principles studies of the thermal conductivities of Si and Ge. In: *Physical Review B*. 2010, vol. 81, p. 085205. DOI: 10.1103/PhysRevB.81.085205

[38] NIKA, D.L., ZINCENCO, N.D., POKATILOV, E.P. Engineering of thermal fluxes in phonon mismatched heterostructures. In: *Journal of Nanoelectronics and Optoelectronics*. 2009, vol. 4, pp. 180-185. DOI: 10.1166/jno.2009.1020

[39] TIMOSHENKO, V. Yu., LISACHENKO, M.G., KAMENEV, B.V., et al. Highly efficient sensitizing of erbium ion luminescence in size-controlled nanocrystalline Si/SiO_2 superlattice structures. In: *Applied Physics Letters.* 2004, vol. 84, pp. 2512-2514. DOI: 10.1063/1.1690465

[40] TIMOSHENKO, V. Yu., LISACHENKO, M.G., SHALYGINA, O.A., et al. Comparative study of photoluminescence of undoped and erbium-doped size-controlled nanocrystalline Si/SiO_2 multilayered structures. In: *Journal of Applied Physics.* 2004, vol. 96, pp. 2254–2260. DOI: 10.1063/1.1773383

[41] SCHÖLL, E. Theory of transport properties of semiconductor nanostructures. Ed. Boston, MA: Springer US. 1998, 391 p. DOI: 10.1007/978-1-4615-5807-1.

[42] ROSS, M.B., MIRKIN, C.A., SCHATZ, G.C. Optical properties of one-, two-, and three-dimensional arrays of plasmonic nanostructures. In: *The Journal of Physical Chemistry C*. 2016, vol. 120, pp. 816–830. DOI: 10.1021/acs.jpcc.5b10800

[43] LIU, X., MA, T., PINNA, N., et al. Two-dimensional nanostructured materials for gas sensing. In: *Advanced Functional Materials*. 2017, vol. 27, p. 1702168. DOI: 10.1002/adfm.201702168

[44] KOROTCENKOV, G. Current Trends in Nanomaterials for Metal Oxide-Based Conductometric Gas Sensors: Advantages and Limitations. Part 1: 1D and 2D Nanostructures. In: *Nanomaterials*. 2020, vol. 10, p. 1392. DOI: 10.3390/nano10071392

[45] KOROTCENKOV, G., TOLSTOY, V. P. Current trends in nanomaterials for metal oxide-based conductometric gas sensors: advantages and limitations—Part 2: porous 2d nanomaterials. In: *Nanomaterials*. 2023, vol. 13, p. 237. DOI: 10.3390/nano13020237

[46] WANG, L., REIPA, V., BLASIC, J. Silicon nanoparticles as a luminescent label to DNA. In: *Bioconjugate Chemistry*. 2004, vol. 15, no. 2, pp. 409–412. DOI: 10.1021/bc030047k

[47] LI, X., HE, Y., SWIHART, M.T. Surface functionalization of silicon nanoparticles produced by laser-driven pyrolysis of silane followed by HF−HNO_3 etching. In: *Langmuir*. 2004, vol. 20, pp. 4720–4727. DOI: 10.1021/la036219j

[48] LAUBE, J., GUTSCH, S., HILLER, D., et al., Formation of size controlled silicon nanocrystals in nitrogen free silicon dioxide matrix prepared by plasma enhanced chemical vapor deposition. In: *Journal of Applied Physics*. 2014, vol. 116, p. 223501. DOI: 10.1063/1.4904053

[49] YU, W., XU, Y., LI, H., et al. Synthesis of full-visible-spectrum luminescent silicon nanocrystals and the origin of the luminescence. In: *Applied Physics A*. 2013, vol. 111, pp. 501–507. DOI: 10.1007/s00339-013-7556-z

[50] TILLEY, R.D., WARNER, J.H., YAMAMOTO, K., et al., Micro-emulsion synthesis of monodisperse surface stabilized silicon nanocrystals. In: *Chemical Communications*. 2005, no. 14, pp. 1833–1835. DOI: 10.1039/B416069J

[51] LE, T.-H., JEONG, H.-D. Synthesis of silicon nanocrystal by magnesium directed reduction of the silica nanoparticle formed in micro-emulsion of reverse micelle. In: *Bulletin of the Korean Chemical Society*. 2014, vol. 35, pp. 3421–3422. DOI: 10.5012/bkcs.2014.35.12.3421

[52] ZHONG, Y., PENG, F., BAO, F., et al. Large-scale aqueous synthesis of fluorescent and biocompatible silicon nanoparticles and their use as highly photostable biological probes. In: *Journal of the American Chemical Society.* 2013, vol. 135, pp. 8350–8356. DOI: 10.1021/ja4026227

[53] WU, J., DAI, J., SHAO, Y., et al. One-step synthesis of fluorescent silicon quantum dots (Si-QDs) and their application for cell imaging. In: *RSC Advances*. 2015, vol. 5, pp. 83581–83587. DOI: 10.1039/C5RA13119G

[54] SU, Y., PENG, F., JIANG, Z. et al. In vivo distribution, pharmacokinetics, and toxicity of aqueous synthesized cadmium-containing quantum dots. In: *Biomaterials*. 2011, vol. 32, pp. 5855–5862. DOI: 10.1016/j.biomaterials.2011.04.063

[55] FUJII, M., YOSHIDA, M., HAYASHI, S., et al. Photoluminescence from SiO_2 films containing Si nanocrystals and Er: Effects of nanocrystalline size on the photoluminescence efficiency of Er^{3+}. In: *Journal of Applied Physics*. 1998, vol. 84, p. 4525. DOI: 10.1063/1.368678

[56] KANZAWA, Y., KAGEYAMA, T., TAKEOKA, S., et al. Size-dependent near-infrared photoluminescence spectra of Si nanocrystals embedded in SiO_2 matrices. In: *Solid State Communications.* 1997, vol. 102, pp. 533–537. DOI: 10.1016/S0038-1098(96)00774-0

[57] DELLEY, B., STEIGMEIER, E. F. Quantum confinement in Si nanocrystals. In: *Physical Review B*. 1993, vol. 47, pp. 1397-1400. DOI: 10.1103/PhysRevB.47.1397

[58] BRUS, L.E., SZAJOWSKI, P.F., WILSON, W.L., et al. Electronic spectroscopy and photophysics of Si nanocrystals: relationship to bulk c-Si and porous Si. In: *Journal of the American Chemical Society.* 1995, vol. 117, pp. 2915-2922. DOI: 10.1021/ja00115a025

[59] van den HOVEN, G. N., SHIN, J. H., POLMAN, A., et al. Erbium in oxygen-doped silicon: optical excitation. In: *Journal of Applied Physics*. 1995, vol. 78, pp. 2642-2650. DOI: 10.1063/1.360125

[60] GODEFROO, S., HAYNE, M., JIVANESCU, M., et al. Classification and control of the origin of photoluminescence from Si nanocrystals. In: *Nature Nanotechnology. 20*08, vol. 3, pp. 174-178. DOI: 10.1038/nnano.2008.7

[61] DELERUE, C., ALLAN, G., LANNOO, M. Theoretical aspects of the luminescence of porous silicon. In: *Physical Review B*. 1993, vol. 48, pp. 11024–11036. DOI: 10.1103/PhysRevB.48.11024

[62] AVERBOUKH, B., HUBER, R, CHEAH, K.W., et al. Luminescence studies of a Si/SiO2 superlattice. In: *Journal of Applied Physics*. 2002, vol. 92, pp. 3564–3568. DOI: 10.1063/1.1498960

[63] PUZDER, A., WILLIAMSON, A. J., GROSSMAN, J.C., et al. Surface chemistry of silicon nanoclusters. In: *Physical Review Letters.* 2002, vol. 8, p. 097401. DOI: 10.1103/PhysRevLett.88.097401

[64] HADJISAVVAS, G., KELIRES, P.C. Structure and energetics of Si nanocrystals embedded in a-SiO2. In: *Physical Review Letters.* 2004, vol. 93, p. 226104. DOI: 10.1103/PhysRevLett.93.226104

[65] WANG, X.X., Zhang, J.G., DING, L., et al. Origin and evolution of photoluminescence from Si nanocrystals embedded in a SiO_2 matrix. In: *Physical Review B*. 2005, vol. 72, p. 195313. DOI: 10.1103/PhysRevB.72.195313

[66] YI, L. X., HEITMANN, J., SCHOLZ, R., ZACHARIAS, M. Si rings, Si clusters, Si nanocrystals—different states of ultrathin SiO_x layers. In: *Applied Physics Letters.* 2002, vol. 81, pp. 4248–4250. DOI: 10.1063/1.1525051

[67] HEITMANN, J., MÜLLER, F., YI, L., et al. Excitons in Si nanocrystals: Confinement and migration effects. In: *Physical Review B*. 2004, vol. 69, p. 195309. DOI: 10.1103/PhysRevB.69.195309

[68] ZACHARIAS, M., YI, L. X., HEITMANN, J., et al. Size-controlled Si nanocrystals for photonic and electronic Applications. In: *Solid State Phenomena*. 2003, vol. 94, pp. 95–104. DOI: 10.4028/www.scientific.net/SSP.94.95

[69] CALCOTT, P.D. J., NASH, K.J., CANHAM, L.T. Identification of radiative transitions in highly porous silicon. In: *Journal of Physics: Condensed Matter*. 1993, vol. 5, p. L91. DOI: 10.1088/0953-8984/5/7/003

[70] KOVALEV, D., HECKLER, H., BEN-CHORIN, M., et al. Breakdown of the k-conservation rule in Si nanocrystals. In: *Physical Review Letters*. 1998, vol. 81, pp. 2803–2806. DOI: 10.1103/PhysRevLett.81.2803

[71] KOVALEV, D., HECKLER, H., POLISSKI, G., et al. Optical properties of Si nanocrystals. In: *Physica Status Solidi B*. 1999, vol. 215, pp. 871–932. DOI: 10.1002/(SICI)1521-3951(199910)215:2<871::AID-PSSB871>3.0.CO;2-9

[72] LEDOUX, G., GUILLOIS, O., PORTERAT, D., et al. Photoluminescence properties of silicon nanocrystals as a function of their size. In: *Physical Review B*. 2000, vol. 62, pp. 15942–15951. DOI: 10.1103/PhysRevB.62.15942

[73] ROMAN, H. E., PAVESI, L. Monte Carlo simulations of the recombination dynamics in porous silicon. In: *Journal of Physics: Condensed Matter*. 1996, vol. 8, p. 5161. DOI: 10.1088/0953-8984/8/28/003

[74] PAVESI, L. Influence of dispersive exciton motion on the recombination dynamics in porous silicon. In: *Journal of Applied Physics*. 1996, vol. 80, pp. 216–225. DOI: 10.1063/1.362807

[75] VALENTA, J., LALIC, N., LINNROS, J., Electroluminescence of single silicon nanocrystals. In: *Applied Physics Letters*. 2004, vol. 84, pp. 1459–1461. DOI: 10.1063/1.1655705

[76] LEDOUX, G., GONG, J., HUISKEN, F., et al. Photoluminescence of size-separated silicon nanocrystals: Confirmation of quantum confinement. In: *Applied Physics Letters*. 2002, vol. 80, pp. 4834-4836. DOI: 10.1063/1.1485302

[77] CHOI, S., DICKSON, R. M., YU, J. Developing luminescent silver nanodots for biological applications. In: *Chemical Society Reviews*. 2012, vol. 41, pp. 1867–1891. DOI: 10.1039/C1CS15226B

[78] RICHARDS, C. I. et al., Oligonucleotide-stabilized Ag nanocluster fluorophores. In: *Journal of the American Chemical Society*. 2008, vol. 130, pp. 5038–5039. DOI: 10.1021/ja8005644

[79] PATEL, S.A., RICHARDS, C.I., HSIANG, J.-C., et al., Water-soluble Ag nanoclusters exhibit strong two-photon-induced fluorescence. In: *Journal of the American Chemical Society*. 2008, vol. 130, pp. 11602–11603. DOI: 10.1021/ja804710r

[80] CHOI, S., YU, J., PATEL, S.A., et al., Tailoring silver nanodots for intracellular staining. In: *Photochemical & Photobiological Sciences.* 2011, vol. 10, pp. 109–115. DOI: 10.1039/C0PP00263A

[81] YU, J., CHOI, S., DICKSON, R.M., Shuttle-based fluorogenic silver-cluster biolabels. In: *Angewandte Chemie*. 2009, vol. 121, pp. 324–326. DOI: 10.1002/ange.200804137

[82] TIKHOMIROV, V.K., RODRÍGUEZ, V.D., KUZNETSOV, A., et al. Preparation and luminescence of bulk oxyfluoride glasses doped with Ag nanoclusters. In: *Optics Express*. 2010, vol. 18, pp. 22032–22040. DOI: 10.1364/OE.18.022032

[83] De CREMER, G., ANTOKU, Y., ROEFFAERS, M., et al., Photoactivation of silver-exchanged zeolite A. In: *Angewandte Chemie International Edition*. 2008, vol. 47, pp. 2813–2816. DOI: 10.1002/anie.200704861

[84] De CREMER, G., COUTIÑO-GONZALEZ, E., ROEFFAERS, M., et al., Characterization of fluorescence in heat-treated silver-exchanged zeolites. In: *Journal of the American Chemical Society*. 2009, vol. 131, pp. 3049–3056. DOI: 10.1021/ja810071s

[85] EACHUS, R.S., MARCHETTI, A.P., MUENTER, A.A., The photophysics of silver halide imaging materials. In: *Annual Review of Physical Chemistry*. 1999, vol. 50, pp. 117–144. DOI: 10.1146/annurev.physchem.50.1.117

[86] MARCHETTI, A.P., MUENTER, A.A., BAETZOLD, R.C., et al., Formation and spectroscopic manifestation of silver clusters on silver bromide surfaces. In: *The Journal of Physical Chemistry B*. 1998, vol. 102, pp. 5287–5297. DOI: 10.1021/jp980729i

[87] PEYSER, L. A., VINSON, A. E., BARTKO, A. P., et al. Photoactivated fluorescence from individual silver nanoclusters. In: *Science*. 2001, vol. 291, pp. 103–106. DOI: 10.1126/science.291.5501.103

[88] SHEN, Z., DUAN, H., FREY, H., Water-soluble fluorescent ag nanoclusters obtained from multiarm star poly(acrylic acid) as 'Molecular Hydrogel' Templates. In: *Advanced Materials*. 2007, vol. 19, pp. 349–352. DOI: 10.1002/adma.200601740

[89] DÍEZ, I., PUSA, M., KULMALA, S., et al., Color tunability and electrochemiluminescence of silver nanoclusters. In: *Angewandte Chemie International Edition.* 2009, vol. 48, pp. 2122–2125. DOI: 10.1002/anie.200806210

[90] YU, J., PATEL, S. A., DICKSON, R. M. In vitro and intracellular production of peptide-encapsulated fluorescent silver nanoclusters. In: *Angewandte Chemie International Edition*. 2007, vol. 46, pp. 2028–2030. DOI: 10.1002/anie.200604253

[91] PEYSER-CAPADONA, L., ZHENG, J., GONZÁLEZ, J. I., et al., Nanoparticle-free single molecule anti-Stokes Raman spectroscopy. In: *Physical Review Letters.* 2005, vol. 94, p. 058301. DOI: 10.1103/PhysRevLett.94.058301

[92] ZHENG, J., DING, Y., TIAN, B., et al., Luminescent and Raman active silver nanoparticles with polycrystalline structure. In: *Journal of the American Chemical Society*. 2008, vol. 130, pp. 10472–10473. DOI: 10.1021/ja803302p

[93] SHANG, L., DONG, S. Silver nanocluster-based fluorescent sensors for sensitive detection of Cu(II). In: *Journal of Materials Chemistry*. 2008, vol. 18, pp. 4636–4640. DOI: 10.1039/B810409C

[94] SU, Y.-T., LAN, G.-Y., CHEN, W.-Y., et al. Detection of copper ions through recovery of the fluorescence of DNA-templated copper/silver nanoclusters in the presence of mercaptopropionic acid. In: *Analytical Chemistry.* 2010, vol. 82, pp. 8566–8572. DOI: 10.1021/ac101659d

[95] FONOBEROV, V.A., POKATILOV, E.P., BALANDIN, A.A. Exciton states and optical transitions in colloidal CdS quantum dots: Shape and dielectric mismatch effects. In: *Physical Review B*. 2002, vol. 66, p. 085310. DOI: 10.1103/PhysRevB.66.085310

[96] FONOBEROV, V.A., POKATILOV, E.P., FOMIN, V.M., et al. Photoluminescence of tetrahedral quantum-dot quantum wells. In: *Physical Review Letters*. 2004, vol. 92, p. 127402. DOI: 10.1103/PhysRevLett.92.127402

[97] FONOBEROV, V.A., POKATILOV, E.P., BALANDIN, A.A. Interplay of confinement, strain, and piezoelectric effects in the optical spectrum of GaN quantum dots. In: *Journal of Nanoscience and Nanotechnology*. 2003, vol. 3, pp. 253–256. DOI: 10.1166/jnn.2003.169

[98] ИСАКОВА, К. Электронные, дырочные и экситонные состояния в кремниевых квантовых точках, помещенных в диэлектрическую среду оксида кремния. In: *Studia Universitatis Moldaviae. Seria științe exacte și economice.* 2011, vol. 7 (47), pp. 66–72. ISSN: 1857-2073.

[99] ИСАКОВА, К., НИКА, Д., ПОКАТИЛОВ Е. Экситонные состояния в квантовых точках Si/SiO$_2$. In: *Studia Universitatis Moldaviae. Seria științe reale și ale naturii.* 2008 vol. 2, pp. 232–236. ISSN: 1814-3237.

[100] BIENIEK, M., SADECKA, K., SZULAKOWSKA, L., et al. Theory of excitons in atomically thin semiconductors: tight-binding approach. In: *Nanomaterials*. 2022, vol. 12, p. 1582. DOI: 10.3390/nano12091582

[101] YIP, C. T., LO, Tsz. W., ZHU, S.-C., et al. Tight-binding modeling of excitonic response in van der Waals stacked 2D semiconductors. In: *Nanoscale Horizons*. 2019, vol. 4, no. 4, pp. 969–974. DOI: 10.1039/C9NH00042A

[102] ISHIDA, K., AOKI, H., CHIKYU, T. One-dimensional exciton in a two-band tight-binding model with long-range interactions. In: *Physical Review B*. 1993, vol. 47, pp. 7594–7597. DOI: 10.1103/PhysRevB.47.7594

[103] LEE, J.-C., CHAI, J.-D., LIN, S.-T. Assessment of density functional methods for exciton binding energies and related optoelectronic properties. In: *RSC Advances*. 2015, vol. 5, no. 123, pp. 101370–101376. DOI: 10.1039/C5RA20085G

[104] KÖNIG, D., HILLER, D., SMITH, S.C. Absorption and photoluminescence of silicon nanocrystals investigated by excited state DFT: role of embedding dielectric and defects. In: *Physica Status Solidi B*. 2022, vol. 259, p. 2100549. DOI: 10.1002/pssb.202100549

[105] FOMIN, V.M., POKATILOV, E.P. Excitons in multi-layer systems. In: *Physica Status Solidi B*. 1985, vol. 129, pp. 203–209. DOI: 10.1002/pssb.2221290120

[106] BALDERESCHI, A., LIPARI, N.O. Direct exciton spectrum in diamond and zinc-blende semiconductors. In*: Physical Review Letters*. 1970, vol. 25, pp. 373–376. DOI: 10.1103/PhysRevLett.25.373

[107] MIRELES, F., ULLOA, S.E. Ordered Hamiltonian and matching conditions for heterojunctions with wurtzite symmetry: GaN / $Al_xGa_{1-x}N$ quantum wells. In: *Physical Review B*. 1999, vol. 60, pp. 13659–13667. DOI: 10.1103/PhysRevB.60.13659

[108] VURGAFTMAN, I., MEYER, J.R., RAM-MOHAN, L.R. Band parameters for III–V compound semiconductors and their alloys. In: *Journal of Applied Physics*. 2001, vol. 89, pp. 5815–5875. DOI: 10.1063/1.1368156

[109] LANGER, R., SIMON, J., ORTIZ, V., et al. Giant electric fields in unstrained GaN single quantum wells. In: *Applied Physics Letters.* 1999, vol. 74, pp. 3827–3829. DOI: 10.1063/1.124193

[110] LEROUX, M., GRANDJEAN, N., MASSIES, J., et al. Barrier-width dependence of group-III nitrides quantum-well transition energies. In: *Physical Review B*. 1999, vol. 60, pp. 1496–1499. DOI: 10.1103/PhysRevB.60.1496

[111] POKATILOV, E.P., NIKA, D.L., BALANDIN, A.A. Phonon spectrum and group velocities in AlN/GaN/AlN and related heterostructures. In: *Superlattices and Microstructures*. 2003, vol. 33, pp. 155–171. DOI: 10.1016/S0749-6036(03)00069-7

[112] LI, D., WU, Y., KIM, P., et al. Thermal conductivity of individual silicon nanowires. In: *Applied Physics Letters.* 2003, vol. 83, pp. 2934–2936. DOI: 10.1063/1.1616981

[113] RYTOV, S.M. Acoustical properties of a thinly laminated medium. In: *Soviet Physics - Acoustics. 19*56, vol. 2, p. 68-80.

[114] LANDAU, L. D., LIFSHITS, E. M., KOSEVICH, A. M., LIFSHITZ, E. M., PITAEVSKII, L. P. Theory of Elasticity: Volume 7. Elsevier. 1986, 200 p. ISBN: 978-0-7506-2633-0

[115] FEDOROV, F. I. General theory of elastic waves in crystals based on comparison with an isotropic medium. In: *Theory of Elastic Waves in Crystals*, F. I. Fedorov, Ed., Boston, MA: Springer US. 1968, pp. 169–209. DOI: 10.1007/978-1-4757-1275-9_5

[116] POKATILOV, E.P., NIKA, D.L., BALANDIN, A.A. A phonon depletion effect in ultrathin heterostructures with acoustically mismatched layers. In: *Applied Physics Letters*. 2004, vol. 85, pp. 825-827. DOI: 10.1063/1.1775033

[117] POKATILOV, E.P., NIKA, D.L., BALANDIN, A.A. Acoustic-phonon propagation in rectangular semiconductor nanowires with elastically dissimilar barriers. In: *Physical Review B*. 2005, vol. 72, p. 113311. DOI: 10.1103/PhysRevB.72.113311

[118] POKATILOV, E.P., NIKA, D.L., BALANDIN, A.A. Acoustic phonon engineering in coated cylindrical nanowires. In: *Superlattices and Microstructures*. 2005, vol. 38, pp. 168-183. DOI: 10.1016/j.spmi.2005.06.001

[119] LIU, W., ASHEGHI, M. Thermal conductivity measurements of ultra-thin single crystal silicon layers. In: *J Journal of Heat Transfer*. 2005, vol. 128, pp. 75–83. DOI: 10.1115/1.2130403

[120] BALANDIN, A.A., GOSH, S., BAO, W., et al. Superior thermal conductivity of single-layer graphene. In: *Nano Letters. 20*08, vol. 8, pp. 902–907. DOI: 10.1021/nl0731872

[120] NICA, D. Kinetic effects determined by the interaction of electrons with acoustic oscillations in quantum heterostructures: tz. de doctor in științe fizico-matematice. Chisinau. 2006. 120 p.

[122] NIKA, D.L., POKATILOV, E.P., ASKEROV, A.S., et al. Phonon thermal conduction in graphene: role of Umklapp and edge roughness scattering. In*: Physical Review B*. 2009, vol. 79, p. 155413. DOI: 10.1103/PhysRevB.79.155413

[123] YEO, P.S. E., LOH, K.P., GAN, C.K. Strain dependence of the heat transport properties of graphene nanoribbons. In: *Nanotechnology*. 2012, vol. 23, p. 495702. DOI: 10.1088/0957-4484/23/49/495702

[124] MA, F., ZHENG, H.B., SUN, Y.J., et al. Strain effect on lattice vibration, heat capacity, and thermal conductivity of graphene. In: *Applied Physics Letters.* 2012, vol. 101, p. 111904. DOI: 10.1063/1.4752010

[125] BI, K., WANG, J., WANG, Yu., et al. The thermal conductivity of SiGe heterostructure nanowires with different cores and shells. In: *Physics Letters A*. 2012, vol. 376, pp. 2668–2671. DOI: 10.1016/j.physleta.2012.07.004

[126] COCEMASOV, A.I. Phonon processes in graphene and silicon-based nanostructures: tz. de doctor in ştiinte fizico-matematice. Chisinau. 2015, 140 p.

[127] XIA, B., ZHANG, W., BAO, W., et al. Photoluminescence enhancement of porous silicon particles by microwave-assisted activation. In: *Physica Status Solidi A*. 2012, vol. 209, pp. 2247–2250. DOI: 10.1002/pssa.201228309V

[128] TIAN, B., ZHANG, X., LIU, L. M., et al. Anneal effect on multipeak photoluminescence properties of porous silicon pillar arrays. In: *Optics Communications*. 2015, vol. 338, pp. 154–158. DOI: 10.1016/j.optcom.2014.10.063

[129] ИСАКОВА, К. Экситонные состояния в кремниевых точках. In: *Материалы XVIII международной научной конференции студентов, аспирантов и молодых учёных,* «Ломоносов», Москва, Россия. 2011. ISBN 978-5-317-03634-8

[130] “1.3.6. Зонная структура некоторых полупроводников.” StudFiles. [QUOTED: May 21. 2022]. Available: https://studfile.net/preview/8838954/page:3/

[131] CHELIKOWSKY, J. R., COHEN, M. L. Nonlocal pseudopotential calculations for the electronic structure of eleven diamond and zinc-blende semiconductors. In: *Physical Review B*. 1976, vol. 14, pp. 556–582. DOI: 10.1103/PhysRevB.14.556

[132] POKATILOV, E.P., FONOBEROV, V. A., FOMIN, V. M., et al. Development of an eight-band theory for quantum dot heterostructures. In: *Physical Review B*. 2001, vol. 64, p. 245328. DOI: 10.1103/PhysRevB.64.245328

[133] ИСАКОВА, К.Я., НИКА, Д.Л., ПОКАТИЛОВ, Е.П. Экситонные состояния в квантовых точках кристаллов кремния, помещенных в водную и воздушную среду. In: *Труды 11-ой международной научно-практической конференции «Современные информационные и электронные технологии»*, 24–28 Мая. 2010, Одесса, Украина, часть 2, p. 103.

[134] MOSKALENKO, A. S., BERAKDAR, J., et al. Single-particle states in spherical Si/SiO_2 quantum dots. In: *Physical Review B*. 2007, vol. 76, p. 085427. DOI: 10.1103/PhysRevB.76.085427

[135] WATANABE, K., FUJII, M., HAYASHI, S. Resonant excitation of Er^{3+} by the energy transfer from Si nanocrystals. In*: Journal of Applied Physics*. 2001, vol. 90, pp. 4761-4767. DOI: 10.1063/1.1409572

[136] KOVALEV, D., GROSS, E., KÜNZNER, N., et al. Resonant Electronic Energy Transfer from Excitons Confined in Silicon Nanocrystals to Oxygen Molecules. In: *Physical Review Letters*. 2002, vol. 89, p.137401.

[137] TIMOSHENKO, V. Yu., DITTRICH, TH., LYSENKO, V., et al. Free charge carriers in mesoporous silicon. In*: Physical Review B*. 2001, vol. 64, p. 085314.

[138] BAKALOVA, R., OHBA, H., ZHELEV, Z., et al. Quantum dot anti-CD conjugates: are they potential photosensitizers or potentiators of classical photosensitizing agents in photodynamic therapy of cancer? In*: Nano Letters.* 2004, vol. 4, pp. 1567–1573. DOI: 10.1021/nl049627w

[139] ISACOVA, C., COCEMASOV, A., NIKA, D.L., et al. Phonons and thermal transport in Si/SiO_2 multishell nanotubes: atomistic study. In*: Applied Sciences*. 2021, vol. 11(8), p. 3419. DOI: 10.3390/app11083419

[140] COCEMASOV, A.I., ISACOVA, C. I., NIKA, D.L. Thermal transport in semiconductor nanostructures, graphene, and related two-dimensional materials. In*: Chinese Physics B*. 2018, vol. 27(5), p. 056301. DOI: 10.3390/app11083419

[141] ИСАКОВА, К., ЗИНЧЕНКО, Н., НИКА, Д. Фононные моды и решеточная теплопроводность в сегментированных нанонитях и в нанонитях покрытых оболочкой. In: *Progrese în fizica teoretică*, CEP USM.Chișinău: CANȚER, V.; PALADI, F.; NICA, D. 2016, pp. 325–357. ISSN: 978-9975-71-817-2

[142] CHANG, C., ZHAO, L.-D. Anharmoncity and low thermal conductivity in thermoelectrics. In*: Materials Today Physics*. 2018, vol. 4, pp. 50–57. DOI: 10.1016/j.mtphys.2018.02.005

[143] NIKA, D.L., COCEMASOV, A.I., BALANDIN, A.A. Thermal conductivity of segmented nanowires. In: *Nanostructures and Thin Films for Multifunctional Applications*, I. Tiginyanu, P. Topala, and V. Ursaki, Eds., in NanoScience and Technology. Cham: Springer International Publishing. 2016, pp. 507–531. ISBN: 978-3-319-30197-6 978-3-319-30198-3

[144] BLONDER, G.E., TINKHAM, M., KLAPWIJK, T.M. Transition from metallic to tunneling regimes in superconducting microconstrictions: Excess current, charge imbalance, and supercurrent conversion. In*: Physical Review B*. 1982, vol. 25, pp. 4515–4532. DOI: 10.1103/PhysRevB.25.4515

[145] YAMASUE, E., SUSA, M., FUKUYAMA, H., et al. Thermal conductivities of silicon and germanium in solid and liquid states measured by non-stationary hot wire method with silica coated probe. In*: Journal of Crystal Growth.* 2002, vol. 234, pp. 121–131. DOI: 10.1016/S0022-0248(01)01673-6

[146] ANDERSON, E., BAI, Z., BISCHOF, L.S. *LAPACK users' guide*, Philadelphia: Society for industrial and applied mathematics. 1999, 430 p. – ISBN 978-0-89871-447-0

[147] GNU C Compiler. Free Software Foundation. 2020. [quoted: Apr. 05, 2021]. Available: https://gcc.gnu.org/gcc-8/

[148] NISHIGUCHI, N., ANDO, Y., WYBOURNE, M.N. Acoustic phonon modes of rectangular quantum wires. In*: Journal of Physics: Condensed Matter*. 1997, vol. 9, pp. 5751–5764. DOI: 10.1088/0953-8984/9/27/007

[149] WEBER, L., GMELIN, E. Transport properties of silicon. In: *Applied Physics A: Materials Science & Processing.* 1991, vol. 53, pp. 136–140. DOI: 10.1007/BF00323873

[150] GIANNOZZI, P., de GIRONCOLI, S., PAVONE, P., et al. Ab initio calculation of phonon dispersions in semiconductors. In*: Physical Review B*. 1991, vol. 43, pp. 7231-7242. DOI: 10.1103/PhysRevB.43.7231

[151] ZIMAN, J. M. *Electrons and Phonons: The Theory of Transport Phenomena in Solids*. New York, Oxford University Press. 2001, 554 p. ISBN 978-0-19-850779-6

[152] LI, G., YARALI, M., COCEMASOV, A., et al. In-plane thermal conductivity of radial and planar Si/SiO$_x$ hybrid nanomembrane superlattices. In: *ACS Nano*. 2017, vol. 11, pp. 8215–8222. DOI: 10.1021/acsnano.7b03219

[153] ALLEN, P. B., FELDMAN, J. L. Thermal conductivity of glasses: Theory and application to amorphous Si. In: *Physical Review Letters.* 1989, vol. 62, pp. 645-648. DOI: 10.1103/PhysRevLett.62.645

[154] LIU, Y., LI, Y., SHEN, K., et al. Further decrease of the thermal conductivity of superlattice through embedding nanoparticle. In: *International Journal of Heat and Mass Transfer*. 2023, Vol. 203, p. 123789. DOI: 10.1016/j.ijheatmasstransfer.2022.123789.

[155] Ma, J. Phonon engineering of micro- and nanophononic crystals and acoustic metamaterials: a review. In: *Small Science*. 2023, Vol. 3: p. 2200052. DOI: 10.1002/smsc.202200052

[156] Demić A., Valavanis A., Dean P., et al. Acoustic band engineering in terahertz quantum-cascade lasers and arbitrary superlattices. In: *Physical Review* B. 2023, vol. 107, p. 235411. DOI: 10.1103/PhysRevB.107.235411

[157] Balandin, A., Wang K.L. Significant decrease of the lattice thermal conductivity due to phonon confinement in a free-standing semiconductor quantum well. 1998, vol. 58, pp. 1544-1549. DOI: 10.1103/PhysRevB.58.1544

DECLARATION OF RESPONSIBILITY

Subsemnatul, declar pe răspundere personală că materialele prezentate în teza de doctorat sunt rezultatul propriilor cercetări şi realizări ştiinţifice. Conştientizez că, în caz contrar, urmează să suport consecinţele în conformitate cu legislaţia în vigoare.

Isacova Calina

Semnătura

Data 04.01.2024

Curriculum Vitae

Name:	Isacova
Surname	Calina
Date of birth:	December 30, 1983
Citizenship	Moldova, Rep. of

Education:

2006-2010: Moldova State University, Department of Physics, Subdepartment of Theoretical Physics, PhD student, Speciality: 01.04.02 –Theortical and Mathematical Physics
2005-2006: Moldova State University, Department of Physics, Master's degree programme, Speciality: Solid State Physics,
2000-2005: Moldova State University, Department of Physics,

Research interests:

Theory of exciton and photoluminescence properties of nanostructures
Theory of acoustic and thermal properties of nanostructures.
Numerical simulations and modeling of physical phenomena.

Place of employment:

Research associate, Moldova State University, Department of Physics, Scientific Research Laboratory "Physics and engineering of nanomaterials „E. Pokatilov"

Internship:

Bursa DAAD Leonhard-Euler 2010, Duisburg, Germany

Scientific trips:

2010 February, University of Duisburg-Essen, Duisburg, Germany
2018 May, Institute for Integrative Nanosciences, IFW, Dresden, Germany

Participation in scientific projects:

2020-2023 Moldova State institutional project: 20.80009.5007.02.
2019-2020 Moldova State project for young researchers: 19.80012.02.13F.
2018 International project DFG Grant FO 956/4-1
2017-2018 Moldova-Ukraine bilateral project: 17.80013.16.02.04/Ua
2015-2020 Moldova State institutional project: 15.817.02.29F.
2014-2015 Moldova State project for young researchers: 14.819.16.02F.
2012-2013 Moldova State project for young researchers: 12.819.05.18F.
2011-2014 Moldova State institutional project: 11.817.05.10F.
2010-2011 Moldova State project for young researchers: 10.819.05.02F.
2008-2009 Moldova-Russia bilateral project: 08.820.05.29RF

2008-2009 Moldova State project for young researchers: 08.819.05.08F.
2006-2008 International project INTAS 05-104-7656.
2006-2010 Moldova State institutional project: 06.408.036F.

Participation in conferences:

CMD2020GEFES, European Physical Society, 31 August – 4 September, 2020 (online)
DPG Spring Meeting, Dresden, Germany, 2014, 2019.
4th Central and Eastern European Conference on Thermal Analysis and Calorimetry (CEEC-TAC4). Chisinau, Moldova, 28–31 August 2017.
Int. Conf. on Materials Science and Condensed Mater Physics, MSCMP 2008, 2010, 2014, 2016
76th Annual Meeting of the DPG and DPG Spring Meeting, Berlin, Germany, March 25-30, 2012
International Conference of Young Scientists Condensed Matter Physics, Grodno, Belarus, editions 2008, 2009.
International Conference „Modern informational and electronic tehnologies”, Odessa, Ukraine, 19-23 May 2008-2013, 2015.
International Conference of Young Researchers, Chisinau, Republic of Moldova, 2007, 2008, 2009
Conference of Moldovan Physicists, Chisinau, Moldova, 2007, 2009
Conferinţa ştiinţifică naţională cu participare internaţională „Integrare prin cercetare şi inovare”. Chișinău, USM, ed. 2012, 2021, 2022
EMN Open Access Week, Chengdu, China, 2012.
9th European Conference on Thermoelectrics, Thessaloniki, Greece, 2011.
Lomonosov-2011, Moscow, Russia, 2011.
XIth International Young Scientists' Conference on Applied Physics, June 15-18, 2011, Kyiv, Ukraine
International Conference of Young Scientists „Computer Science and Engineering” Lvov, Ukraine, 4-6 October 2007

Publications:

8 articles
35 materials on international and national conferenes

Knowledge of languages:

Russian (native), Romanian (good), English (good)

Contacts:

Address: str. Alba-Iulia 202, ap. 169, Chişinău, MD-2071, R. Moldova

Telephone: +373 79284946

E-mail: isacova.calina@gmail.com